Topochemical Cation Exchange Reactions of Ruddlesden-Popper Oxides

Rachel Conway

University College
University of Oxford



A thesis submitted in partial fulfilment of the requirements for the degree of *Doctor of Philosophy*

August 2024

Abstract

Topochemical Cation Exchange Reactions of Ruddlesden-Popper Oxides

The work detailed in this thesis focuses on the low-temperature, topochemical cation exchange reactions of a series of some noncentrosymmetric $n = 2$ pseudo-Ruddlesden-Popper oxides.

The reaction between $Li_2CaTa_2O_7$ and anhydrous transition metal chlorides at elevated temperatures yielded single-phase samples of the metastable phases $FeCaTa_2O_7$, $CoCaTa_2O_7$, and $ZnCaTa_2O_7$. Structural analysis revealed that $FeCaTa_2O_7$ and $CoCaTa_2O_7$ adopt polar $a^-b^-c^+/b^-a^-c^+$ distorted $n = 2$ Ruddlesden Popper structures described in the $P2_1nm$ space group, where the interlayer transition metal cations adopt a chequerboard-ordered arrangement to minimise repulsion between the *A*'-cations. Upon cooling, $FeCaTa_2O_7$ and $CoCaTa_2O_7$ adopt G-type antiferromagnetically ordered structures below their respective magnetic transition temperatures. In contrast, $ZnCaTa_2O_7$ adopts a polar $a^-b^-c^+/-(a^-b^-)c^+$ distorted structure described in the $P2cm$ space group, where the Zn^{2+} cations order in a striped pattern within the interlayer tetrahedral coordination sites to optimise the bonding of the Ca^{2+} *A*-cations.

$MnSrNb_2O_7$ was synthesised by topochemical cation exchange from $Li_2SrNb_2O_7$ and adopts a polar, $a^-a^-c^+/a^-a^-c^+$ distorted structure described in superspace group $A2_1am(0\beta0)000$ with a propagation vector **q** = (0, 0.81, 0), consistent with an incommensurately modulated crystal structure. It was found that modulation of the Mn-site occupancy corresponds to a chequerboard ordering arrangement, which is coupled to the modulation of the equatorial oxygen ion site. $MnSrNb_2O_7$ undergoes a transition to an antiferromagnetically ordered state below $T_N = 39$ K, in which the Mn^{2+} magnetic moments are orientated parallel to the *z*-axis in a G-type arrangement. No evidence of strong magnetoelectric coupling was observed. The cation exchange chemistry of $Li_2SrNb_2O_7$ was further investigated in the synthesis of $MSrNb_2O_7$ (*M* = Fe, Co and Zn), which adopt complex structures that differ from the manganese analogue.

Finally, the structures and structural distortions of $Li_2SrNb_2O_7$, $Li_2SrTa_2O_7$ and $Li_2CaTa_2O_7$ were explored from a theoretical perspective using first-principles calculations to understand the transition from a trilinear-coupled stabilisation of the polar structure to a 'conventional' SOJT coupling as a function of the *A*-cation (Ca/Sr). Calculations revealed a shallow energy landscape between competing structures and were not able to account for the experimentally observed macroscopic polarisation in these phases.

Declaration

The work described in this thesis was carried out at the Inorganic Chemistry Laboratory at the University of Oxford between October 2019 and August 2024 under the supervision of Professor Michael A. Hayward. All the work presented in this thesis is my own except where I have either acknowledged help from a named person or given reference to a published source. None of the work has been submitted by the author for any degree at any other university.

Rachel Conway

August 2024

Acknowledgements

First and foremost, I would like to thank Prof. Mike Hayward for giving me the opportunity to join his group, and whose enthusiasm and seemingly unlimited knowledge of solid-state chemistry made this work possible. I couldn't have wished for a better DPhil supervisor.

Thank you to the EPSRC-funded OxICFM Centre for Doctoral Training for the financial support that made it possible for me to come to Oxford and complete this DPhil.

Thank you to my secondary supervisor, Prof. Stephen Blundell, for explaining muon spectroscopy and magnetism to a chemist and for giving me the opportunity to visit PSI. Thank you also to Hank and George from the Blundell group for showing me the ropes of GPS, being excellent company during the muon measurements, and analysing all the muon data included in this thesis.

I would like to thank Dr Fabio Orlandi and Dr Pascal Manuel for their assistance with collecting neutron diffraction data, for giving me a JANA crash course, and their help during the characterisation of the incommensurate structures described in this thesis. I would also like to thank Prof. Shiv Halasyamani and Dr Yujie Zhang for collecting SHG data, as well as Dr Simon Cassidy for the PXRD and SQUID training, and the instrument scientists at Diamond I11 beamline for their assistance in collecting synchrotron X-ray diffraction data.

I want to extend a huge thank you to Prof. Nicole Benedek for opening my eyes to the world of computational chemistry and for allowing me to briefly work in her group. Thank you to the entire Benedek group — Tucker, Jeff, Guru, Jalen and Sabrina — for making my four months at Cornell some of my favourites from my DPhil. Most of all, I would like to thank Tucker for his unwavering patience with me. The DFT work of this thesis would not have been possible without his continuous help.

It certainly wasn't easy starting in the lab during the height of the pandemic. Thank you to the Hayward group, especially Suraj and Ella, for your countless hours of help and for teaching me everything I know about solid-state synthesis and Rietveld refinements. Thank you also to James and Riju for always being willing to remind me how to use the SQUID, to Romain for his moral and scientific support, and to the rest of the Hayward group, past and present, for making these four and a half years in the lab a little less challenging. It has been a pleasure to work with you all.

Clara - Thank you for the countless cake trips and coffee breaks, mental health walks through University parks, comfort during my many tearful moments, unwavering support and encouragement throughout my job search, and the occasional scientific discussion. Your friendship has meant the world to me over the past four years, and I count myself very lucky to have been here in Oxford at the same time as you. You are an incredible person and scientist, and I cannot wait to hear about all the amazing chemistry you will do during your next adventure.

To my fellow Univites, Malitha and Ed, thank you for the absolute best times in Magpie Lane during our first year. I will never forget our late-night fast food runs that almost bankrupted me and the many bizarre but wonderful moments we experienced together in Oxford.

And of course, Mom, Dad and Annie, I need far more than an acknowledgement page in my thesis to express my gratitude to you. Thank you for always encouraging and supporting me, pushing me to achieve my full potential, and providing me with the opportunities that have gotten me to this point. I hope I've made you all proud.

Last, but certainly not least, Joël, thank you for trying your very best to understand what a perovskite is, and for believing in me even when I didn't believe in myself. I couldn't have done this without you.

Table of Contents

Topochemical Cation Exchange Reactions of Ruddlesden-Popper Oxides

Abstract ii

Declaration iv

Acknowledgements vi

Chapter 1: Introduction 1

1.1 Perovskites 1

1.2 Layered Perovskites: The Ruddlesden-Popper Structure 2

1.3 The Goldschmidt Tolerance Factor 3

1.4 Octahedral Tilting and The Glazer Notation System 6

1.5 Magnetoelectric Multiferroic Materials 8

1.5.1 Design Rules for Ferroelectric and Ferromagnetic Materials 9

1.6 Trilinear Coupling Mechanism 12

1.6.1 Breaking Inversion Symmetry Using Layered Perovskites 15

1.7 Traditional Ceramic Synthesis of Crystalline Solids 19

1.8 Low-temperature Topochemical Synthesis 20

1.9 Incommensurate Modulated Structures 22

1.10 Thesis Aims 23

Chapter 2: Experimental Techniques 25

2.1 Synthetic Methods 25

2.1.1 Ceramic Synthesis of Thermodynamic Precursors 25

2.1.2 Cation Exchange Reactions 25

2.1.3 Handling of Air-Sensitive Materials 26

2.1.3.1 Drying Anhydrous Chlorides 26

2.1.3.2 Reactions in Sealed Glass Ampules 27

2.1.3.3 Reactions Under Flowing Gas 27

2.2 Powder Diffraction 29

2.2.1 X-ray Powder Diffraction 31

2.2.1.1 Panalytical Empyrean and X'Pert Diffractometers 34

2.2.1.2 Synchrotron X-ray Diffraction 35
2.2.2 Neutron Powder Diffraction 37
2.2.2.1 Generation of Neutrons 39
2.2.2.2 Neutron Diffractometers: WISH (ISIS-TS2) 40
2.3 Rietveld and Pawley Refinements 41
2.4 DC SQUID Magnetometry 43
2.4.1 Paramagnetism 45
2.4.2 Curie-Weiss Law 45
2.5 Muon Spin Spectroscopy 47
2.5.1 General Purpose Surface-Muon Instrument (GPS) 48
2.6 Second Harmonic Generation 50
2.7 ISODISTORT symmetry analysis 52
2.8 Density Functional Theory 54
2.8.1 Symmetry-mode Analysis of Distorted Structures 55
Chapter 3: Synthesis and Characterisation of $M^{II}CaTa_2O_7$ (M = Fe, Co, Zn) 58
3.1 Introduction 58
3.2 Synthesis 58
3.2.1 Synthesis of $Li_2CaTa_2O_7$ 58
3.2.2 Synthesis of $M^{II}CaTa_2O_7$ (M = Fe, Co, Zn) 59
3.3 Results 59
3.3.1 Optical SHG Measurements 59
3.3.2 Structural Characterisation of $ZnCaTa_2O_7$ 61
3.3.2.1 Room temperature synchrotron X-ray diffraction data 61
3.3.2.2 100 K neutron powder diffraction data 62
3.3.3 Characterisation of $FeCaTa_2O_7$ 69
3.3.3.1 Room temperature synchrotron X-ray diffraction data 69
3.3.3.2 200 K neutron powder diffraction data 69
3.3.3.3 Magnetisation data 75
3.3.3.4 Low temperature (1.5 K) neutron powder diffraction data 77
3.3.3.5 Variable temperature neutron powder diffraction data 83

3.3.4 Characterisation of $CoCaTa_2O_7$ 87
3.3.4.1 Room temperature synchrotron X-ray diffraction data 87
3.3.4.2 100 K neutron powder diffraction data 87
3.3.4.3 Magnetisation data 93
3.3.4.4 Low temperature (1.5 K) neutron powder diffraction data 95
3.3.4.5 Variable temperature neutron powder diffraction data 99
3.4 Discussion 103
3.5 Conclusions 110
Chapter 4: Synthesis and Characterisation of $MnSrNb_2O_7$ 112
4.1 Introduction 112
4.2 Synthesis 112
4.2.1 Synthesis of $Li_2SrNb_2O_7$ 112
4.2.2 Synthesis of $MnSrNb_2O_7$ 113
4.3 Results 113
4.3.1 Optical SHG Measurements 113
4.3.2 Characterisation of $MnSrNb_2O_7$ 114
4.3.2.1 Room temperature synchrotron X-ray diffraction data 114
4.3.2.2 80 K neutron powder diffraction data 117
4.3.2.2.1 Commensurate structural model 117
4.3.2.2.2 Incommensurate structural model 118
4.3.2.3 Magnetisation data 124
4.3.2.4 Low temperature (1.5 K) neutron powder diffraction data 126
4.3.2.5 Variable temperature neutron powder diffraction data 131
4.3.2.6 Muon spectroscopy 134
4.4 Discussion 137
4.5 Conclusions 141
Chapter 5: Synthesis and Characterisation of $M^{II}SrNb_2O_7$ (M = Fe, Co, Zn) 142
5.1 Introduction 142
5.2 Synthesis 142
5.2.1 Synthesis of $M^{II}SrNb_2O_7$ (M = Fe, Co, Zn) 142

5.3 Results 143
5.3.1 Optical SHG Measurements 143
5.3.2 Characterisation of $CoSrNb_2O_7$ 144
5.3.2.1 Room temperature synchrotron X-ray diffraction data 144
5.3.2.2 50 K neutron powder diffraction data 144
5.3.2.2.1 Commensurate structural model 144
5.3.2.2.2 Incommensurate structural model 150
5.3.2.3 Magnetisation data 152
5.3.2.4 Low temperature (1.5 K) neutron powder diffraction data 154
5.3.3 Characterisation of $ZnSrNb_2O_7$ 156
5.3.3.1 Room temperature synchrotron X-ray diffraction data 156
5.3.3.2 100 K neutron powder diffraction data 157
5.3.4 Characterisation of $FeSrNb_2O_7$ 161
5.3.4.1 Room temperature synchrotron X-ray diffraction data 161
5.3.4.2 60 K neutron powder diffraction data 164
5.3.4.3 Magnetisation data 166
5.3.4.4 Low temperature (1.5 K) neutron powder diffraction data 168
5.4 Discussion 170
5.5 Conclusions 174
Chapter 6: Computational Studies of $Li_2AB_2O_7$ (A = Ca, Sr; B = Nb, Ta) 176
6.1 Introduction 176
6.2 Methods 179
6.3 Results 179
6.3.1 $Li_2CaTa_2O_7$ 179
6.3.1.1 Density functional perturbation theory calculations 179
6.3.1.2 Frozen phonon calculations 180
6.3.2 $Li_2SrTa_2O_7$ 186
6.3.2.1 Density functional perturbation theory calculations 186
6.3.2.2 Frozen phonon calculations 186
6.3.2.3 Varying the exchange-correlation functional 190

6.3.3 $Li_2SrNb_2O_7$ 191
6.3.3.1 Density functional perturbation theory calculations 191
6.3.3.2 Frozen phonon calculations 191
6.3.4 Influence of Artificial Strain 197
6.4 Discussion 202
6.4.1 Structure Decomposition 204
6.4.2 Future Work 210
6.5 Conclusions 211
Chapter 7: Conclusions 212
Appendix 1 – Index of Figures and Tables 218
Appendix 2 – Additional Data 230
A2.1 Additional data from the structural refinements in Chapter 3 230
A2.2 Additional data from the structural refinements in Chapter 4 246
A2.3 Additional data from the first principles calculations of Chapter 6 253
Appendix 3 – Bibliography 258

Chapter 1: Introduction

1.1 Perovskites

Complex transition-metal oxides are one of the largest and most technologically important families of materials. In particular, perovskites are conceivably the most widely studied, thanks to the extensive array of interesting physical behaviours these phases display, including colossal magnetoresistance, superconductivity, ferroelectricity, piezoelectricity, and metal-insulator transitions.[1–3] Their popularity is perhaps not so surprising, as the flexible structure is able to accommodate a wide range of elements with diverse sizes and formal charges, providing almost limitless variation of imaginable chemical compositions. Through thoughtful chemical design, desired functionalities can be established within the materials, and the ability to carefully tailor these properties makes perovskites applicable to many technologies.

The archetypal mineral perovskite $CaTiO_3$ was discovered in the Ural Mountains of Russia in 1839 by Gustav Rose and is named after the Russian count Lev Perovskii. It was not until 1926 that Victor Goldschmidt first described the perovskite structure, and many years later, in 1946, Helen D. Megaw first published the crystal structure from X-ray diffraction data.[4–6] The prototypical ABO_3 perovskite structure, illustrated in Figure 1.1, consists of a three-dimensional network of corner-sharing BO_6 octahedra, forming twelve coordinate cavities within which the larger *A*-cations sit. Typically, the *A*-site cations will be large, alkaline earth metals or lanthanides, whilst the *B*-site will be occupied by transition metal cations. The ideal cubic perovskite adopts a structure described in the $Pm\bar{3}m$ space group.

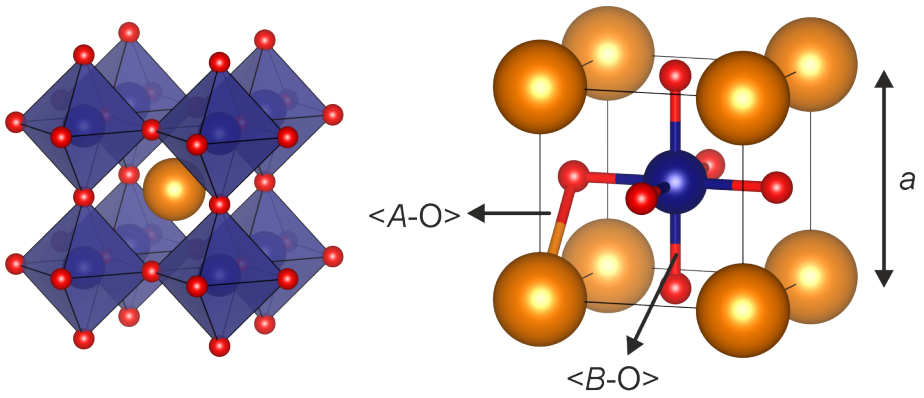


Figure 1.1 The cubic ABO_3 perovskite crystal structure, where the orange A-cation sits in a 12-coordinate site formed by the BO_6 octahedra shown in blue.

1.2 Layered Perovskites: The Ruddlesden-Popper Structure

Compounds that adopt the perovskite structure may form layered structures consisting of infinite 2D layers of the perovskite structure separated by some motif. One of the most well-studied layered structure types is the Ruddlesden-Popper family of materials. Ruddlesden-Popper oxides share the general formula $(AO)(ABO_3)_n = A_{n+1}B_nO_{3n+1}$, and consist of perovskite sheets separated by AO rock salt-type layers inserted every n sheets of octahedra, where the adjacent perovskite layers are related by a (½, ½, z) translation.[7] Typically, the A-cations are alkali, alkaline earth, or rare earth metals, and the B-cations are transition metal ions. The A_2BO_4 n = 1 and $A_3B_2O_7$ n = 2 Ruddlesden-Popper aristotype structures are given in Figure 1.2. The A-cations within the perovskite layers occupy the twelve-coordinate sites, and those within the interlayer A'O region sit inside a nine-coordinate environment. When the A'-cations are small, they may occupy four-coordinate tetrahedral coordination sites in the so-called pseudo-Ruddlesden-Popper structure (Figure 1.2, right), rather than the nine-coordinate sites that are occupied in conventional Ruddlesden–Popper frameworks.

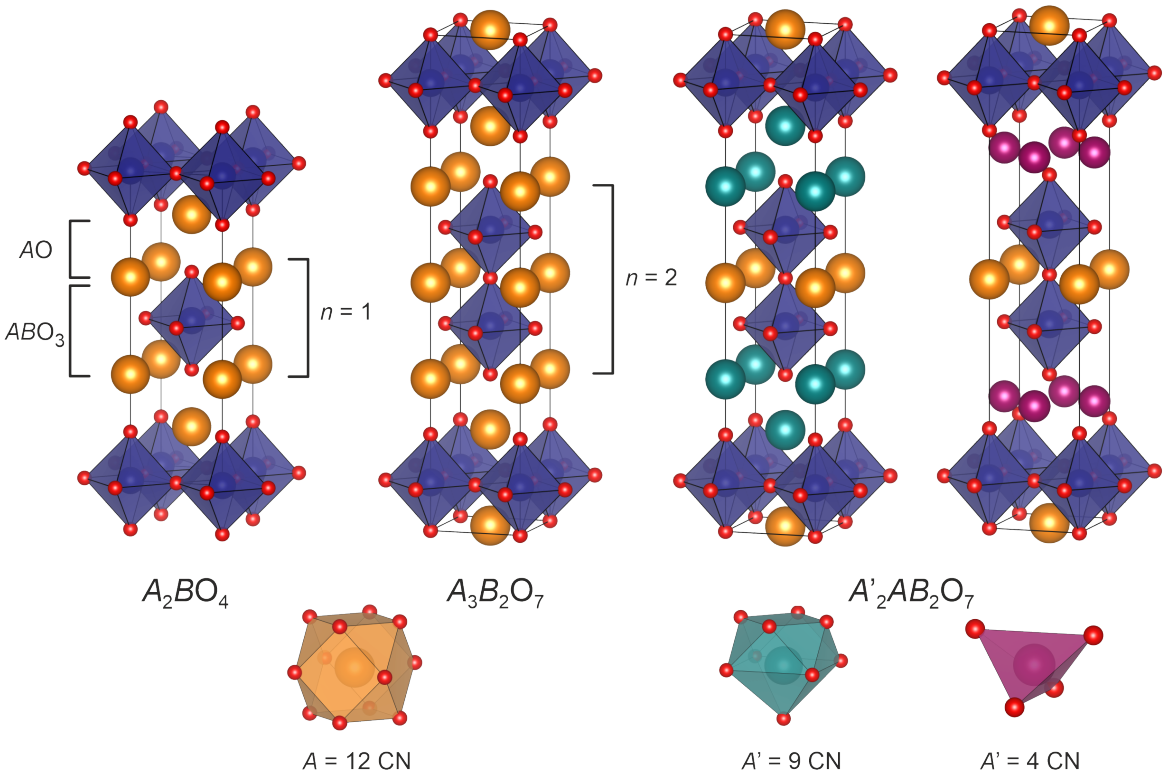


Figure 1.2 The general crystal structure of the aristotype A_2BO_4 $n = 1$ and $A_3B_2O_7$ and $A'_2AB_2O_7$ $n = 2$ Ruddlesden-Popper oxides. Orange, green, pink, blue and red spheres represent *A*, *A*', *B* and O atoms, respectively.

1.3 The Goldschmidt Tolerance Factor

Often, perovskites undergo structural distortions from the cubic aristotype to lower-symmetry phases as a way to lower their energy. The perovskite structure is able to tolerate deviations from the ideal cubic structure by employing complex cooperative rotations or deformations of the octahedra without losing their corner-sharing connectivity.[8] One way in which the degree of distortion within an ABO_3 perovskite structure can be quantified is through the calculation of the Goldschmidt tolerance factor *t*, which relates the *A*-O and *B*-O bond lengths to the stability of the crystal structure, where r_O, r_A and r_B are the ionic radii of O, *A* and *B*, respectively (Equation 1.1)[4].

$$t = \frac{< A - O >}{\sqrt{2} < B - O >} = \frac{r_A + r_O}{\sqrt{2}(r_B + r_O)} \qquad (1.1)$$

In the ideal, undistorted cubic perovskite structure, shown in Figure 1.1, t is equal to one. When the size of the A-cation is too large, t is greater than one, and the material crystallises in a hexagonal arrangement that sees an increase in the number of face-sharing octahedra in the structure. If the size of the A-cation is too small ($t < 1$), the perovskite structure will adjust to optimise the coordination environment of this cation, cooperatively rotating the BO_6 octahedra and reducing the B-O-B bond angle from the ideal value of 180° seen in the cubic structure (Figure 1.3). Therefore, the rotations of the octahedral units occur as a result of a size mismatch between the A-O and B-O bond lengths and are driven by the coordination preferences of the A-site cations.[9] These low-energy structural deformations allow the A-O bonds to contract without any change to the B-O bond length or coordination environment of the B-site cation.

The driving force which stabilises the rotations can be better understood by using bond valence sum (BVS) calculations. The bond valence sum model is based only on structural information and relates the bond lengths around a metal ion to its oxidation state. It is a useful empirical metric for the accuracy or reliability of crystal structure determination and

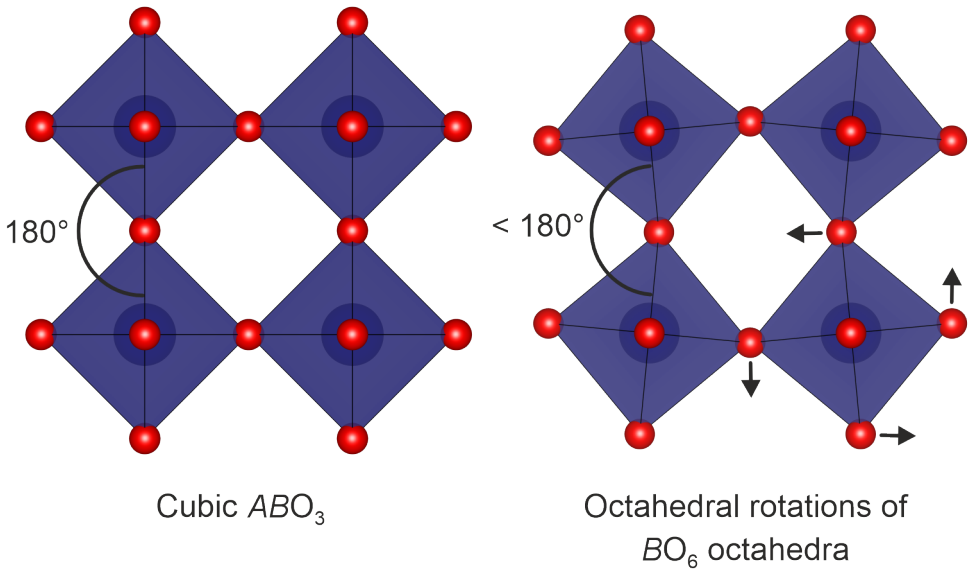


Figure 1.3 The cubic perovskite structure and a cooperative octahedral rotation of the BO_6 octahedra.

for rationalising structural differences between compounds. Altermatt and Brown proposed a general expression for the total bond valence of an atom i, V_i, and is given by:

$$V_i = \sum s_{ij} = \sum \exp\left[\frac{R_0 - r_{ij}}{b}\right] \quad (1.2)$$

where s_{ij} is the valence of the bond between atoms i and j, r_{ij} is the observed bond length between ions i and j, R_0 is a tabulated bond valence parameter, and b is an empirical constant equal to 0.37.[10,11] Since the sum of the individual bond valences around each atom should be equal to its oxidation state for any given MX_n coordination polyhedron, V_i is an approximation of the formal oxidation state of the central metal ion within the coordination sphere.

In a situation where the tolerance factor is less than one, BVS calculations indicate that the *A*-site cation is under-bonded and that the bonds it forms to oxygen are too long. A combination of octahedral rotations and polar distortions can relieve this under-bonding, shortening the length of the *A*-O bonds and optimising the coordination environment of the cation.

Tolerance factor calculations provide a valuable metric for understanding the stability of perovskite chemical compositions and their propensity to rotate. These calculations can be surprisingly accurate, and many perovskite oxides with tolerance factors of less than one adopt structures with octahedral rotations. Furthermore, control and manipulation of the tolerance factor through carefully considered substitutions of the cations allows for some degree of control over the structure and resulting properties in a material.

1.4 Octahedral Tilting and The Glazer Notation System

Several symmetry-lowering distortions of the cubic perovskite have been identified. The most common of these are the low-energy cooperative rotations of the BO_6 octahedra around one or more of their crystallographic axes.[12] The complex tilting distortions commonly observed in perovskite lattices can be conveniently denoted using Glazer notation.[13] Glazer describes the tilts around the $Pm\overline{3}m$ cubic axes of the aristotype perovskite structure using a set of three letters, each referring to rotations about each of the axes [100], [010] and [001]. A superscript is used to indicate the sense of the tilting between successive layers of octahedra along an axis. If the tilting of adjacent octahedra is of the same sense, or in phase, a positive (+) superscript is used, and a negative (-) superscript is used to denote out-of-phase tilting. A superscript of zero (0) is used to denote a zero tilt around any axis. The magnitude of each tilt is indicated symbolically by each of the three letters, where identical characters indicate tilting of the same magnitude. For example, $a^+a^+c^-$ would describe an in-phase tilt of equal magnitude about [100] and [010], but an out-of-phase tilting of a different magnitude about [001].

Figure 1.4a illustrates an example of an in-phase and an out-of-phase rotation of the octahedra around the [001] axes and highlights the cooperative and collective nature of the tilts between successive octahedra along the axes perpendicular to the tilt, which are constrained to tilt in the opposite sense about that axis due to the corner-sharing network. This means that a clockwise rotation of magnitude *c* around [001] in any chosen octahedron will result in an anti-clockwise rotation of equal magnitude around [001] of the four adjacent octahedra within that plane.

Glazer notation can similarly describe the tilting distortions observed in layered perovskite oxides. However, since the three-dimensional octahedral connectivity seen in perovskites is broken along one direction in the layered materials, adjacent perovskite layers do not necessarily have to adopt the same tilting distortions. For example, the $n = 2$ Dion-Jacobson

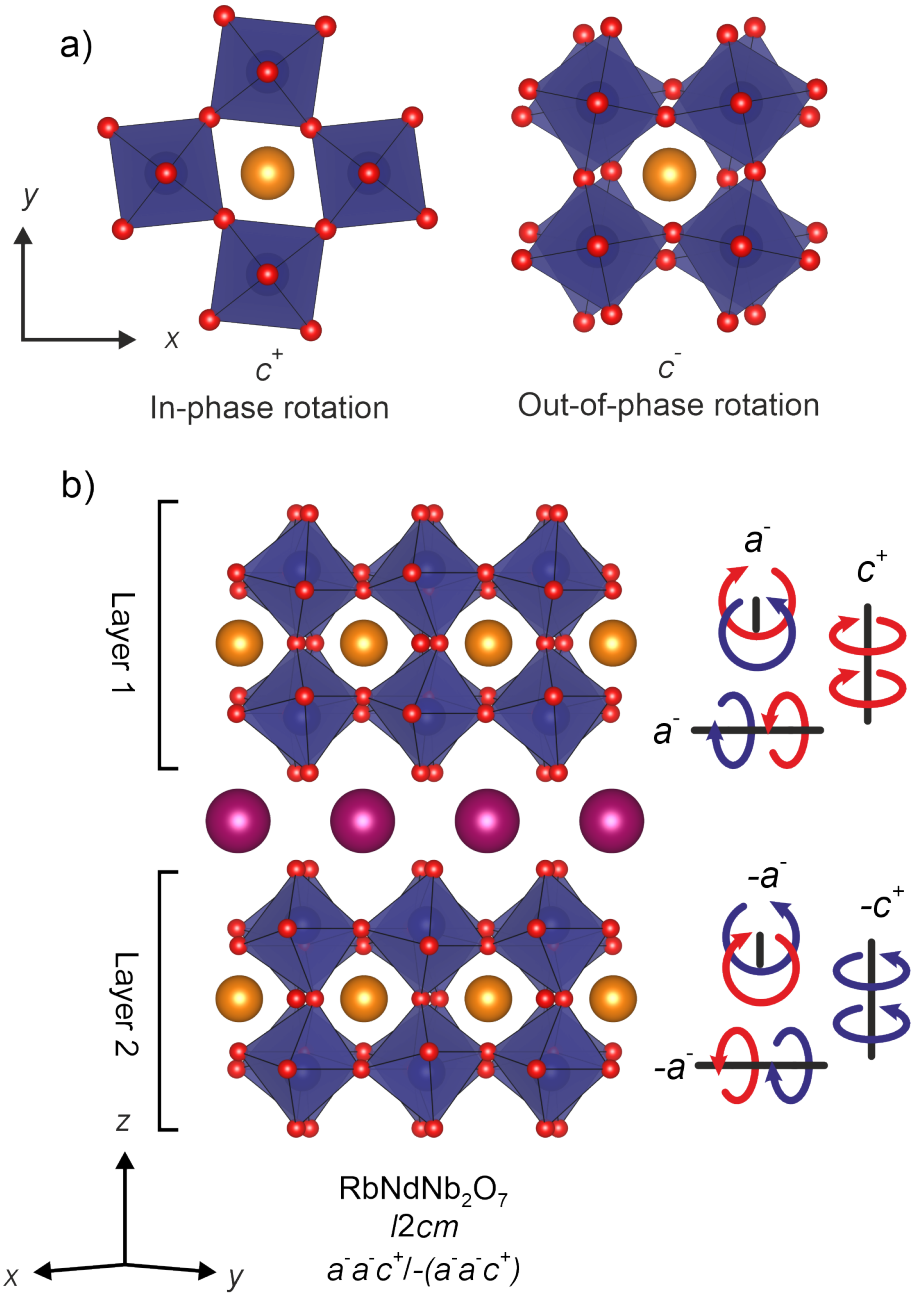


Figure 1.4 a) The in-phase and out-of-phase tilting distortions of the BO_6 octahedra of a 3D perovskite around the [001] axis. b) The *I*2*cm* structure adopted by $RbNdNb_2O_7$, exhibiting an $a^-a^-c^+/-(a^-a^-c^+)$ tilting distortion, where pink, orange, blue and red are used to represent Rb, Nd, Nb and O ions, respectively.

phase $RbNdNb_2O_7$ adopts an *I*2*cm* structure, described by an $a^-a^-c^+/-(a^-a^-c^+)$ tilting distortion, depicted in Figure 1.4b. Although the local tilting distortions within each perovskite layer are the same ($a^-a^-c^+$), the direction of each tilt is reversed along each of the three cartesian axes. In layered perovskite structures, the chemical reasonability of a particular rotation pattern must also be considered. Although the tilting distortions between each layer are no longer constrained to be the same, to be chemically plausible, chemically equivalent cations (those that are related by symmetry operations, e.g., rotational axis, plane of symmetry, centre of inversion) within different layers must share the same local environment. An example of a chemically implausible rotation pattern would be $a^-a^-c^+/a^-a^-c^0$.

1.5 Magnetoelectric Multiferroic Materials

Increasingly, combining useful and fascinating phenomena into a single, multifunctional material is driving the development of new advanced materials. The most interesting properties are those that interact mutually to result in cooperative effects. In particular, the design of multiferroic materials has attracted considerable interest in recent years. The term multiferroic is used to describe materials that exhibit more than one primary ferroic property in a single phase.[14] Specifically, magnetoelectric multiferroic materials exhibit both ferromagnetic and ferroelectric properties, having a spontaneous magnetisation that can be reoriented by an applied magnetic field, and a spontaneous electric polarisation that can be reoriented by an applied electric field.[15] Crucially, the magnetic and electric properties are coupled.

Besides scientific interest in their fundamental physical properties, novel multiferroic materials not only offer all the potential applications of ferromagnetic and ferroelectric materials but also open the door to a range of other multifunctional applications, such as

spintronics and low-power magnetoelectric devices.[14,16] The ability to control the magnetism using an electric field would be transformative, as the production of electric fields is less energy intensive than magnetic fields, which are currently standard in existing magnetic technologies. Furthermore, multiferroic bits may be used to create multiple-state memory devices in which data is stored in both the magnetic and electric polarisations.[17]

1.5.1 Design Rules for Ferroelectric and Ferromagnetic Materials

Combining ferroelectricity and ferromagnetism to prepare magnetoelectric multiferroic materials has proven to be extremely challenging. For a phase to exhibit ferromagnetic behaviour, the material must have unpaired electrons whose magnetic moments interact cooperatively to produce a spontaneous magnetisation in the absence of an applied field.[18] Many reliable methods can be used to induce and control ferromagnetism, as described by the Goodenough-Kanamori rules, which rationalise the magnetic interactions between neighbouring ions.[19–21]

On the other hand, ferroelectricity requires a phase to adopt a noncentrosymmetric polar crystal structure.[22] This can be difficult to achieve in a solid because asymmetric packing systems are less efficient than symmetric arrangements.[23] Therefore, noncentrosymmetric systems are usually energetically disfavoured, and unless specific measures are taken to break the inversion symmetry of a metal oxide phase, it will adopt a centrosymmetric structure.

The conventional approach taken towards breaking inversion symmetry in metal-oxide phases is to employ a second-order Jahn-Teller (SOJT) distortion resulting from the mixing of empty and filled orbitals.[24–26] A SOJT distortion is typically achieved by either of two methods. The first is the inclusion of post-transition metal cations having ‘lone-pair’ electrons (ns^2), such as Pb^{2+} and Bi^{3+}. This can be visualised by considering that the

stereoactive 'lone-pair' causes a displacement of the *A*-cation from the centre of the twelve-coordinate cuboctahedron.[27,28] This is driven by the mixing and subsequent hybridisation of the formally empty *p* states of the cation with the formally filled *s* states of the anionic ligands and leads to a shortening of the *A*-O bonds to optimise the coordination environment of the *A*-cation.

Polar distortions can also be induced by the inclusion of *B*-site cations with empty *d* shells, which are prone to displacement from the centre of the BO_6 octahedra.[29,30] As is seen with ns^2 post-transition metal cations, the onset of polarisation originates from the mixing of the empty *d* states of the cation with the oxygen ligand *p* states. The bonding preference of the *B*-site cation drives this type of off-centring distortion.

In proper ferroelectric materials, such as the two archetypal phases $PbTiO_3$ and $BaTiO_3$, the ferroelectric transition is driven by a single, zone-centre polar lattice distortion.[31] In the examples of both $PbTiO_3$ and $BaTiO_3$, the spontaneous polarisation results from a SOJT electronic distortion caused by the hybridisation of the empty Ti^{4+} 3*d* states with the formally full oxygen 2*p* states.[32–34] This distortion is further reinforced in $PbTiO_3$, where the 'lone-pair' on Pb^{2+} also contributes to the lifting of the inversion symmetry through hybridisation with oxygen 2*p* states.[35] Ferroelectricity results from a freezing-in or condensation of this polar lattice distortion. This is illustrated in Figure 1.5, where the ferroelectric tetragonal *P*4*mm* structure of $PbTiO_3$ is stabilised with respect to the paraelectric cubic $Pm\bar{3}m$ structure, which involves the displacement of the cations relative to the anions and the generation of a net dipole moment.[31] Both $PbTiO_3$ and $BaTiO_3$ are considered proper ferroelectrics because the distortion that breaks the symmetry of the high-symmetry phase at T_C also gives rise to the ferroelectric polarisation, that is, the polarisation is the primary order parameter. Conversely, paraelectric to ferroelectric transitions in which the distortion

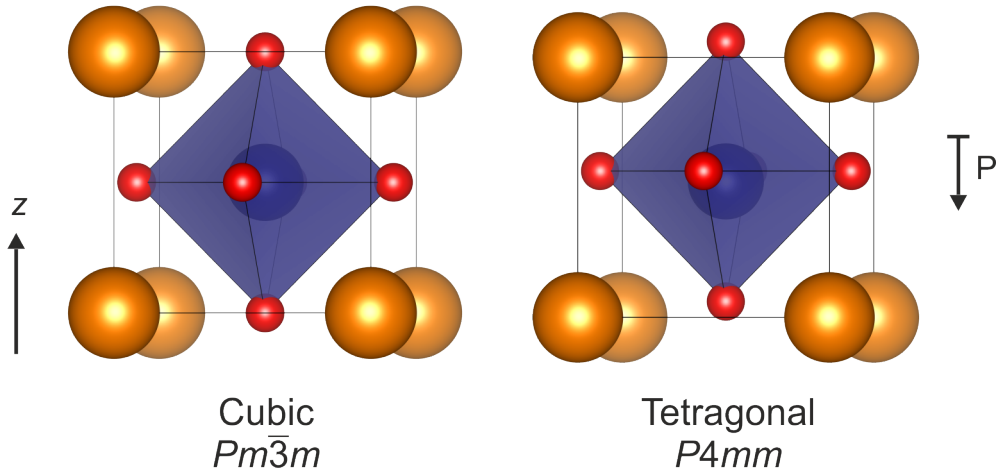


Figure 1.5 The high-temperature paraelectric $Pm\bar{3}m$ and ferroelectric tetragonal $P4mm$ structures of $PbTiO_3$. Orange, blue and red are used to represent Pb, Ti and O ions, respectively.

that generates the polarisation is the secondary order parameter are known as improper ferroelectrics.[36]

Clearly, ns^2 post-transition metal cations and d^0 transition metal cations are both diamagnetic. Polarisation induced through the exploitation of these electronic distortions is unlikely to coexist with magnetism since an absence of *d* electrons creating a localised magnetic moment means there can be no long-range magnetic ordering. Furthermore, cations with partially filled *d*-shells reduce the tendency for a ferroelectric displacement to occur.[14]

Despite the difficulty in combining ferroelectricity and ferromagnetism in the same material, notable successes have been achieved in the field. Perhaps the most exciting and well-studied of these is the antiferromagnetic ferroelectric perovskite $BiFeO_3$, which displays magnetoelectric coupling at room temperature.[37] The long-range spin cycloid structure in bulk $BiFeO_3$ that suppresses net magnetisation is alleviated in high-quality thin films, making them an excellent candidate for technological applications.[38] Similarly, ferroelectricity and antiferromagnetism are observed in $TbMnO_3$ as a result of spin

frustration caused by a combination of an $a^+b^-b^-$ $GdFeO_3$-type rotation and orbital ordering. Magnetoelectric coupling of the two ferroic properties is also observed.[39]

In response to the limitations described in this section, research in the field has been geared towards developing new approaches to designing materials capable of simultaneously exhibiting ferroelectricity and ferromagnetism. Recently, considerable effort has been made to exploit the cooperative rotations of the BO_6 octahedra since they are ubiquitous in the perovskite structure and can be rationally manipulated through chemical substitutions.

1.6 Trilinear Coupling Mechanism

Early theoretical analysis conducted by Woodward and co-workers anticipated that an alternative strategy which exploits a combination of two non-polar distortion modes, R_1 and R_2, could collectively lift the inversion symmetry of a paraelectric phase.[40,41] Building on this and the previous work of Bousquet and co-workers, Benedek and Fennie demonstrated that an octahedral rotation and tilting distortion couple linearly to the polar lattice mode in the layered perovskite $Ca_3Mn_2O_7$, forming a hybrid mode.[42,43] Materials which use this method to induce ferroelectricity contain a trilinear term in their free energies, $\mathcal{F}$, in which the polarisation, P, is trilinearly coupled to two non-polar structural distortions:

$$\mathcal{F} = \gamma Q_P Q_{R_1} Q_{R_2} \tag{1.3}$$

where γ is a coefficient, Q_P is the amplitude of the polarisation and Q_{R_1} and Q_{R_2} are the amplitudes of the non-polar rotational distortions.[31,36] This method of inducing polarity in a material has been coined the 'hybrid-improper' or trilinear coupling mechanism. Although each rotation leads to a non-polar space group individually, the combined rotation pattern breaks inversion symmetry and stabilises a polar distortion mode to enhance the macroscopic polarisation.

$Ca_3Mn_2O_7$ undergoes a structural phase transition from a paraelectric *I*4/*mmm* symmetry to the polar space group $A2_1am$. This polar structure can be related to the high-temperature tetragonal aristotype by applying two non-polar distortion modes (described by the X_2^+ and X_3^- irreducible representations) and a polar distortion mode, Γ_5^-, depicted in Figure 1.6. Figure 1.7 shows the total energy of the *I*4/*mmm* parent structure plotted as a function of the amplitude of each of the three modes.[43] Both the X_2^+ and the X_3^- rotation modes lower the energy of the *I*4/*mmm* phase, but individually, neither lead to the experimentally observed $A2_1am$ symmetry, nor do they break inversion symmetry. The Γ_5^- mode, however, does break inversion symmetry but raises the energy of the *I*4/*mmm* phase and is therefore stable, as shown in Figure 1.7b. In this situation, the X_2^+ and X_3^- modes establish the $A2_1am$ symmetry and couple together to form a hybrid mode that acts as the primary order

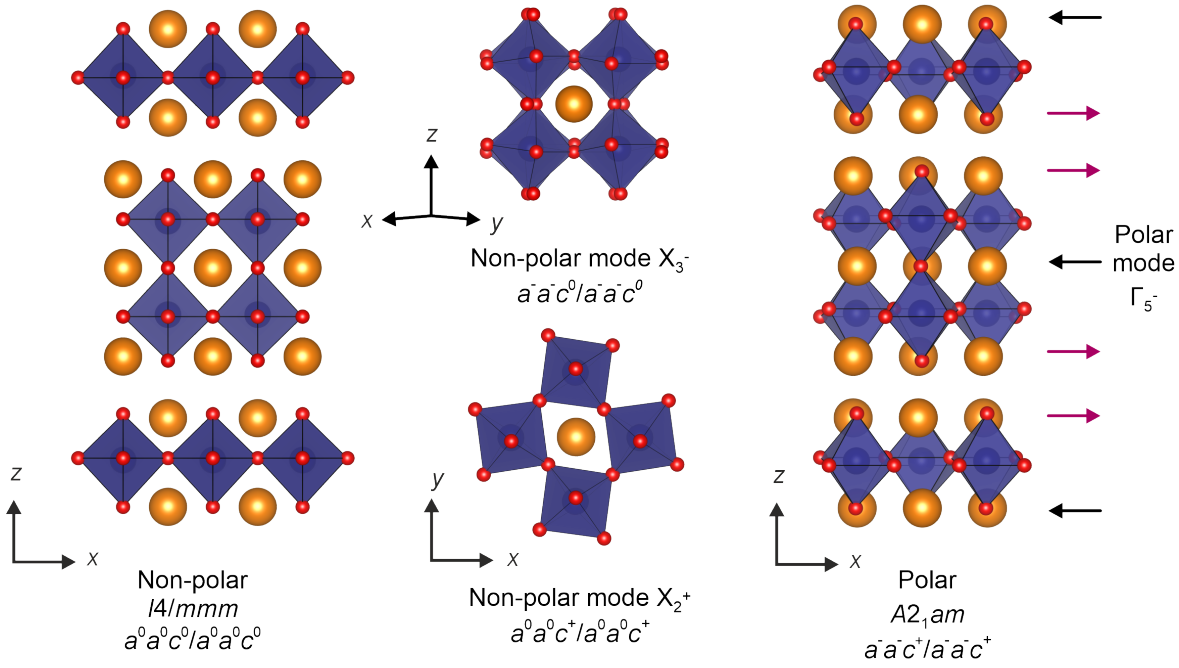


Figure 1.6 The non-polar *I*4/*mmm* aristotype structure of $Ca_3Mn_2O_7$ can be related to $A2_1am$ by the application of the two non-polar modes, X_2^+ and the X_3^-, which together couple to the polar Γ_5^- mode to generate a macroscopic polarisation. The net polarisation arises from the non-cancellation of *A*-site cation displacements in inequivalent *A*O layers. Orange, blue and red are used to represent Ca, Mn and O ions, respectively.

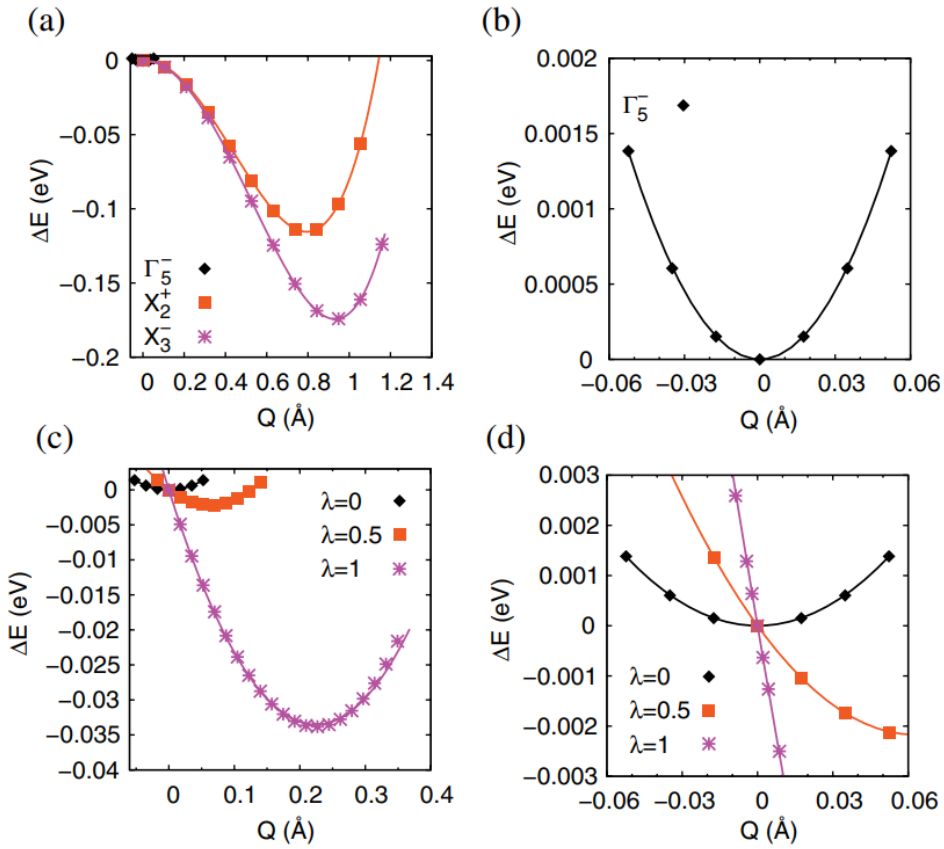


Figure 1.7 The change in energy per formula unit of the *I*4/*mmm* phase of $Ca_3Mn_2O_7$ as a function of the amplitude of a) the non-polar X_2^+ and X_3^- modes b) the polar Γ_5^- mode c) the polar Γ_5^- mode in the presence of the hybrid order parameter, $Q_{X_{23}} = \lambda Q_{X_3^-} Q_{X_2^+}$. d) shows a magnification of the region around $\Delta E = 0$. Figure is taken with permission from Reference 43.

parameter. Figure 1.7c demonstrates that in the absence of this hybrid parameter (when the coefficient $\lambda = 0$), the polarisation remains stable within an energy well. Only in the presence of the hybrid mode (when $\lambda > 0$) does the polarisation become unstable. The Γ_5^- mode couples to the hybrid mode to enhance the macroscopic polarisation, but does not drive the phase transition. Hence, $Ca_3Mn_2O_7$ is an improper ferroelectric, characterised by the single well with a minimum at $Q \neq 0$.

Unlike previous examples of phases which induce ferroelectricity in this way, Benedek and Fennie show that the coupling of the rotation modes can also be used to manipulate magnetic order in $Ca_3Mn_2O_7$ and, therefore, to control magnetoelectric coupling. In this example,

first-principles calculations indicate that the direction of the net magnetic moment can be flipped by reversing the tilting distortion. The X_3^- rotation mode induces a weak ferromagnetism but also forms part of the ferroelectric hybrid order parameter. Therefore, due to the form of the trilinear term in the free energy, the direction of the polarisation in the material will also be reversed.[43]

When considering the design and synthesis of magnetoelectric multiferroics, the hybrid improper mechanism presents the major advantage in that it does not require the inclusion of elements with specific electronic requirements, as is the case with proper ferroelectrics (such as $PbTiO_3$ and $BaTiO_3$) which rely on d^0 transition metals or ns^2 post-transition metal cations to induce polar displacements. Therefore, since these second-order Jahn-Teller distortions usually preclude the onset of magnetic order, the trilinear coupling mechanism offers greater flexibility in the choice of cations that can be included in the structure, expanding the scope for ferroelectric materials. Thus, the hybrid improper approach could be exploited as a fundamental design principle for synthesising magnetoelectric multiferroic materials.

1.6.1 Breaking Inversion Symmetry Using Layered Perovskites

Due to the corner-sharing, three-dimensional connectivity of the octahedra in a simple ABO_3 perovskite structure, octahedral rotations and tilting alone cannot induce ferroelectricity. This is because the octahedral connectivity ensures that the sign of the atomic displacements caused by rotations in neighbouring unit cells alternates, cancelling any local dipole moments and resulting in zero macroscopic polarisation.[44] The three-dimensional octahedral connectivity of the perovskite structure, which prevents rotations from lifting the inversion symmetry at the *B*-site, is broken in layered perovskites.[45] For example, in the Ruddlesden-Popper structure, when $n = 2$, the insertion of *A*O layers between the perovskite blocks

removes the octahedral connectivity along the [001] direction, creating two different *A*-cation coordination environments. The 12-coordinate *A*-site cations within the perovskite sheets become symmetry inequivalent to the 9-coordinate *A'*-site cations within the rock salt layer (Figure 1.2). Additionally, this leads to an odd number of *A*O sheets between the perovskite layers and ensures that an antipolar distortion that induces polarisation will not be exactly cancelled.

The family of layered perovskites contains several materials where the trilinear coupling mechanism induces the observed ferroelectricity. As previously discussed, the n = 2 Ruddlesden-Popper phase $Ca_3Mn_2O_7$ and the related materials $Ca_3Ti_2O_7$ and $Ca_3Ru_2O_7$ are all ferroelectric, despite their parent perovskite structures $CaMnO_3$, $CaTiO_3$ and $CaRuO_3$ being non-polar in bulk.[46–48] In both $Ca_3Mn_2O_7$ and $Ca_3Ti_2O_7$, the octahedral rotations transforming like the irreducible representations X_2^+ and the X_3^- (describing the $a^0a^0c^+/a^0a^0c^+$and $a^-a^-c^0/a^-a^-c^0$ tilting distortions, respectively) combine to give the $a^-a^-c^+/a^-a^-c^+$ tilt pattern, which transforms the aristotype *I*4/*mmm* space group to the polar $A2_1am$ space group.[43,49] Interestingly, this is the same tilt pattern seen in the *Pnma* space group of the parent perovskites. However, in those cases, the polarisation seen in each layer cancels due to the three-dimensional connectivity of the octahedra. The work of Oh and co-workers provided the first experimental confirmation of this, showing that the trilinear coupling mechanism was responsible for stabilising the polar structure in $Ca_3Ti_2O_7$ and that polarisation was switchable when an electric field was applied.[50] More recently, ferroelectricity was experimentally observed in $Ca_3Mn_2O_7$, and a switchable polarisation was demonstrated.[51]

Zhu and co-workers used cation-exchange reactions of the n = 2 *A'AB*$_2$O$_7$ Dion-Jacobson phases $RbNdNb_2O_7$ and $RbNdTa_2O_7$ to highlight the importance of controlling the mismatch

between the size of constituent cations and manipulating the tolerance factor in perovskites. The reaction of $LiNO_3$ and $NaNO_3$ with $RbNdNb_2O_7$ and $RbNdTa_2O_7$ yielded *A*'NdB_2O_7 (*A* = Li, Na, *B* = Nb, Ta) *n* = 2 Ruddlesden-Popper phases, where the identity of *A*' influenced the tilting distortion of the material formed.[52] Both $NaNdNb_2O_7$ and $NaNdTa_2O_7$ adopt a centrosymmetric structure described in the space group $P4_2/mnm$, whereas the Li analogues adopt polar structures described in space group *B*2*cm*. The differences in the structures formed occur as a result of the interplay between optimising the *A*'-cation coordination environment and minimising *A*'-*A*' cation repulsion.

Recent studies using first-principles calculations have suggested that several Dion-Jacobson phases previously reported as centrosymmetric could be polar, inspiring efforts to re-evaluate past work.[53] The *n* = 2 Dion-Jacobson phases $CsNdTa_2O_7$, $RbNdNb_2O_7$ and $RbNdTa_2O_7$ were re-examined using a combination of experimental and theoretical techniques.[54] Zhu and co-workers found that all three materials displayed particle size-dependent second-harmonic generation (SHG) activity, indicative of a noncentrosymmetric crystal structure, which contradicts the previously reported structures of these phases. First-principles calculations were used to identify the polar space groups adopted by each material and suggest that the macroscopic polarisation is a result of combinations of the cooperative rotations of the BO_6 octahedra. Polarisation switching using an electric field has since been used to demonstrate ferroelectricity in $RbNdNb_2O_7$.[55]

Similarly, whilst $CsBiNb_2O_7$ and $CsNdNb_2O_7$ were initially reported to crystallise in the noncentrosymmetric $P2_1am$ space group, electrical measurements of the dielectric constant suggested the phases were not ferroelectric.[56] Fennie and Rabe used group-theoretical analysis and first-principles calculations to calculate a considerable polarisation within $CsBiNb_2O_7$. They proposed that the material was, in fact, ferroelectric, and ferroelectric

switching has since been reported in $CsNdNb_2O_7$.[55,57] Likewise, ferroelectric behaviour has been observed in $RbBiNb_2O_7$ and was previously reported to adopt a structure described in an $A2_1am$ space group.[58] Recent work by Mallick and co-workers demonstrated that $RbBiNb_2O_7$ and the analogous phase $LiBiNb_2O_7$ instead adopt polar $I2cm$ and $B2cm$ crystal structures, respectively.[59]

Theoretical studies suggested that the centrosymmetric n = 2 Ruddlesden Popper phase $Sr_3Zr_2O_7$ could be ferroelectric, leading to the material's re-examination.[60,61] Indeed, the perovskite crystallises in the polar $A2_1am$ space group, utilising a series of nonpolar rotations and the trilinear coupling mechanism to induce ferroelectricity.[62] The chosen examples highlight the significance of revisiting Dion-Jacobson and Ruddlesden-Popper phases, which have formerly been characterised as non-polar, since further cases likely exist.

Finally, $n > 2$ layered oxide materials can exhibit additional tilting distortion modes that are not possible in the analogous n = 2 systems and, therefore, have the potential to display a range of complex coupled distortions. The ability to tune between a proper and hybrid improper stabilisation of the polarisation has been demonstrated in the n = 3 Dion Jacobson family of materials by adjusting their chemical compositions. A combined computational and experimental analysis of the $CsA_2Ti_2NbO_{10}$ (A = Bi, La, Nd) series revealed that $CsBi_2Ti_2NbO_{10}$ is a proper ferroelectric, in which a SOJT-like distortion of the Bi^{3+} cations stabilises the polar structure. In contrast, $CsLa_2Ti_2NbO_{10}$ and $CsNd_2Ti_2NbO_{10}$ are observed to adopt polar structures driven by a trilinear coupling of non-polar distortion modes.[63,64]

Many of these examples emphasise that while the trilinear coupling mechanism can stabilise noncentrosymmetric crystal structures without including ions with local electronic instabilities, large B-site cations are necessary to stabilise the highly distorted frameworks required for this mechanism to operate. This becomes evident when we consider that in the

majority of the materials reported to employ a trilinear coupling mechanism to stabilise a polar structure, the *B*-site cation is an early transition metal ion in its group oxidation state (Ti^{4+}, Zr^{4+}, Nb^{5+} or Ta^{5+}). The presence of these particular d^0 transition metals, which are themselves prone to SOJT distortions, could lead to confusion about the origin of the polar structure in many of these phases and suggests a possible competition between the SOJT mechanism and the trilinear coupling mechanism.

When attempting to overcome the chemical constraints imposed by the conventional approach taken to break inversion symmetry in oxides, we have encountered a further restriction: the size constraint, when combined with the requirement for high *B*-site charges in these frameworks, effectively excludes a large number of paramagnetic transition-metal cations. To overcome these thermodynamic limitations, it is necessary to apply alternative synthetic strategies to access metastable polar phases containing paramagnetic cations capable of displaying both ferroelectric and ferromagnetic behaviours.

1.7 Traditional Ceramic Synthesis of Crystalline Solids

Most traditional ceramic methods used to prepare solids use high temperatures to overcome the substantial diffusion barriers that limit the mobility of the reagents in solid-state reactions. The low mobility of ions is a universal feature of solid-state reactions, resulting from the strong bonding interactions between the constituent ions of the precursor reagents. Since the mass transport of ions accounts for the majority of the activation barrier in typical solid-state reactions, the activation energies of competing reactions are often comparable in size.[65] Therefore, at the high temperatures necessary for solid-state reactions to occur, the products of these competing reactions are energetically accessible. This results in the formation of the most thermodynamically stable phase, as the structure adopts a particular geometry which minimises the free energy of the system. This often precludes the formation

of a large number of metastable phases with low thermal stability. Usually, it is these metastable products that form noncentrosymmetric structures and, therefore, exhibit interesting magnetic and electronic properties. For this reason, it is necessary to utilise an alternative approach that makes use of low temperatures to access the kinetic products that cannot be synthesised using conventional high-temperature ceramic techniques.[66]

1.8 Low-temperature Topochemical Synthesis

In extended solids, one type of ion is often considerably more mobile than the rest of the species that comprise the phase.[66] This enables the selective insertion, removal or exchange of the more mobile ions whilst the host lattice remains unchanged.[67] This is known as a topochemical or topotactic reaction and has proven to be a valuable and reliable method for synthesising metastable transition metal-oxide phases.[68,69] This thesis makes use of topochemical cation exchange reactions of thermodynamically stable precursor phases, which are an example of a redox-neutral process, often driven by the formation of stable by-products such as binary metal halides or water.

Layered perovskite materials, such as Ruddlesden-Popper and Dion-Jacobson phases, have proven to be excellent candidate materials for such topochemical exchange reactions because the transition metal cations occupying the *B*-site sit within tightly bound oxide octahedra and are effectively immobile relative to other cations under the lower temperatures utilised in topochemical reactions. By contrast, the cations within the low coordinate sites of the interlayer region are kinetically more mobile than the host lattice and can be exchanged at modest reaction temperatures. This is demonstrated in the cation exchange reactions of the n =3 Ruddlesden-Popper phase $Na_2La_2Ti_3O_{10}$, shown in Figure 1.8.[70] In this example, nine-coordination Na^+ cations occupying the interlayer space between the perovskite sheets were substituted for relatively smaller Co^{2+} cations, which occupy 50%

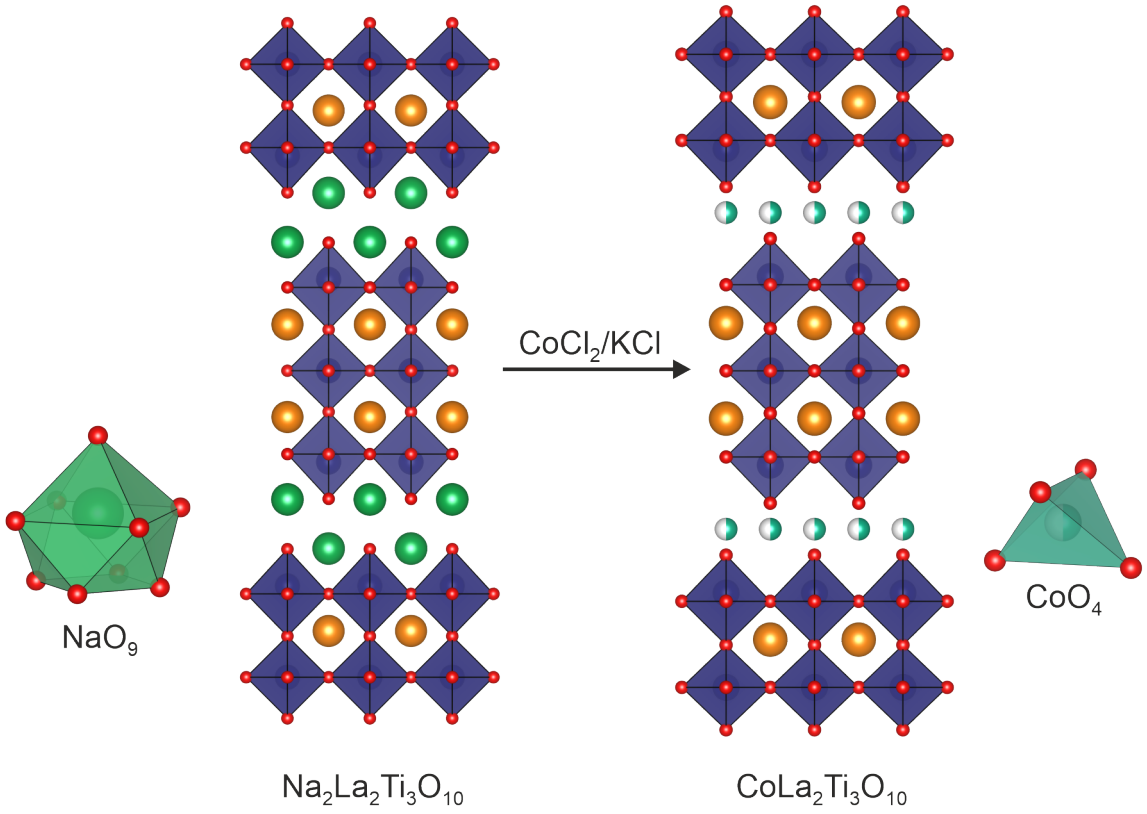


Figure 1.8 The topochemical cation exchange reaction of $Na_2La_2Ti_3O_{10}$ using a molten mixture of $CoCl_2$ and KCl results in the exchange of the 9-coordinate Na^+ ions with Co^{2+} ions, which occupy 50% of the available tetrahedral coordination sites. Orange, blue, green, mint and red are used to represent La, Ti, Na, Co and O ions, respectively.

of the available tetrahedral coordination sites, using a flux of KCl and $CoCl_2$. Analogous exchange reactions were performed using the corresponding metal chlorides to synthesise $CuLa_2Ti_3O_{10}$ and $ZnLa_2Ti_3O_{10}$.

Topochemical synthesis allows chemists some degree of control over the structure and resulting properties in a material and offers the opportunity to rationally design and synthesise new compounds using multistep, directed synthetic strategies. It can be envisioned that through thoughtful selection of thermodynamic precursor phases and chemical design, topochemical exchange reactions can be used to target metastable or low-temperature phases with specific functionalities and properties. [66]

1.9 Incommensurate Modulated Structures

A crystal is a three-dimensional array of atoms or molecules with periodic translational symmetry.[71] Modulations, whether incommensurate or not, can lower the symmetry of a structure and govern the observed physical properties of the phase. Here, modulation is used to describe a periodic deformation of the basic crystal structure.[72] The modulation can be a displacive or positional modulation, where the atomic positions of one or more atoms in the structure differ from the basic structure, or an occupational modulation, in which the occupancy of one or more atoms varies periodically. If the ratio of the periodicity of the modulation and the periodicity of the underlying basic lattice is irrational, then the modulated crystal structure is said to be incommensurate.[73] These incommensurate modulations break the translational symmetry of the 3D structure along at least one crystallographic axis. Although incommensurate structures lack 3D translational symmetry, the long-range order of the crystal structure is preserved, and it is possible to describe the structure using higher-order crystallography. Higher dimension space groups, known as superspace groups, are necessary to describe the symmetry of incommensurate modulated structures.[74]

In the diffraction pattern of an incommensurately modulated crystal, sharp peaks are observed for both the fundamental reflections generated by the average 3D structure and for the characteristic satellite reflections that are a consequence of the modulation. The periodicity of the modulation can be described in (3+1)D or higher space, in which the additional dimensions contain information about the modulation. Therefore, indexing of the pattern requires four or more Miller indices to account for the observed satellite reflections. The reflections can be indexed using the lattice parameters of the average periodic 3D lattice

and up to three modulation vectors. Reflections in four-dimensional reciprocal space can be described by:

$$\boldsymbol{H} = ha^* + kb^* + lc^* + m\boldsymbol{q} \quad (1.4)$$

where **H** is the scattering vector of the Bragg reflection, *m* is an additional integer, the fourth-dimension equivalent of the indices *h*, *k* and *l*, and **q** is the modulation vector:[75,76]

$$\boldsymbol{q} = \alpha a^* + \beta b^* + \gamma c^* \quad (1.5)$$

For an incommensurately modulated structure, at least one component of the modulation vector, α, β, γ, is an irrational number.

1.10 Thesis Aims

The thesis aims to explore the synthesis of new ferroelectric and magnetoelectric perovskite materials, exploiting the trilinear coupling mechanism to induce ferroelectricity and low-temperature 'soft' synthetic routes to obtain metastable phases that would not be accessible using traditional ceramic methods.

The previously reported polar $n = 2$ Ruddlesden-Popper phases $Li_2CaTa_2O_7$ and $Li_2SrNb_2O_7$ have been revisited with the aim of topochemically exchanging the more kinetically mobile *A*'-site Li^+ cations within the interlayer region of these structures. The proximity of the *A*'-site cations to each other suggests that inserting magnetic cations, such as transition metals, into these sites could introduce magnetic exchange interactions into these phases. Chemical substitution of the interlayer cations and subsequent structural characterisation of this family of layered perovskites will allow us to better understand the relationship between the octahedral distortions of these materials and their physical properties, which will, in turn, lead to a more rational design strategy of new materials in the future.

This thesis also attempts to develop an understanding of the mechanisms through which the ground-state structures of a series of $n = 2$ pseudo-Ruddlesden Popper phases emerge. Using a combination of symmetry principles and density functional theory (DFT) calculations, the symmetry-lowering distortions of $Li_2SrTa_2O_7$, $Li_2CaTa_2O_7$, and $Li_2SrNb_2O_7$ from the *I*4/*mmm* parent structure were studied to establish a physical reasoning behind the differing ground-state structures of each phase.

Chapter 2: Experimental Techniques

2.1 Synthetic Methods

2.1.1 Ceramic Synthesis of Thermodynamic Precursors

A direct ceramic method was the standard approach used to synthesise the thermodynamic precursor phases discussed in this thesis. As explained in Chapter 1, high-temperature ceramic synthesis techniques are required to overcome the substantial diffusion barriers that limit the mobility of the reagents in solid-state reactions.[65] Traditionally, this involves mixing and grinding binary metal oxides and/or metal salts (nitrates, carbonates, etc.), pressing the mixture into dense pellets, and heating at elevated temperatures.[77] A reaction initially occurs at the contact points between the metal precursors, after which the reaction proceeds via slow ionic diffusion between reactant particles. Reaction rates can be increased by regular cycles of mechanical processing, such as grinding of the reactants to improve homogenous mixing and compression of powders into pellets to improve inter-grain contact, followed by further heating cycles for extended periods of time. High-temperature ceramic reactions can take multiple days to reach completion, after which the product phase may only be partially homogenous since low levels of impurities are typical. It is often necessary to include an excess of reactants with high vapour pressures (typically 5-10%) to compensate for mass loss at high temperatures.

2.1.2 Cation Exchange Reactions

Cation exchange reactions were performed by mixing the thermodynamically stable precursor phases (layered perovskite oxides) with anhydrous 3*d* transition metal chlorides and heating the reaction mixture to a temperature considerably lower than those used in ceramic synthesis, typically 250 °C to 400 °C. At these temperatures, the cations occupying

the rock-salt interlayer region between the perovskite sheets are much more mobile than the host lattice and can be selectively removed from the material and replaced with different ions.[65,68] The cation exchange reactions performed in this thesis were completed in sealed glass ampules or under flowing argon.

2.1.3 Handling of Air-Sensitive Materials

Although the phases discussed in this thesis are air-stable at room temperature, using an inert atmosphere during the cation exchange reactions was necessary since anhydrous transition metal chlorides are hygroscopic and readily react with oxygen to form transition metal oxides when heated in air. To overcome these issues, all reactant mixtures were handled inside an argon-filled dry glovebox, and all reactions took place in air-free environments.

2.1.3.1 Drying Anhydrous Chlorides

Anhydrous transition metal chlorides were used to perform the cation exchange reactions. In practice, it was often necessary to dry these 'anhydrous' transition metal chlorides before use in subsequent exchange reactions, as small amounts of water were observed condensing inside the sealed tubes upon cooling if an effective drying procedure had not been completed. An unknown quantity of water inside a sealed reaction vessel raises two critical concerns. Firstly, when heated at high temperatures, water inside the sealed tube may react with the precursor material to form stable binary metal oxides and will introduce impurities into the reaction mixture. Secondly, an unknown amount of water vapour within a sealed reaction vessel could be dangerous if the pressure becomes too high. The transition metal chlorides were heated under flowing argon at a temperature of 150 °C for 2 hours to eliminate any absorbed water before being transferred to an argon-filled dry glovebox, where they were stored before use in subsequent reactions. This drying procedure was necessary for successful cation exchange reactions.

2.1.3.2 Reactions in Sealed Glass Ampules

The cation exchanged reactions were performed inside sealed Pyrex ampules. The thermodynamically stable precursors were combined with ten molar equivalents of anhydrous transition metal chloride and ground into a homogenous mixture using an agate pestle and mortar inside an argon-filled dry glovebox. The mixture was then loaded into a 9 mm Pyrex tube and sealed with a Young's tap. The tube was removed from the glovebox, evacuated, and sealed using a blowtorch. The samples were then heated in a horizontal low-temperature furnace at a ramp rate of 2 °C min^{-1} to the reaction temperature and held at this temperature for several days before cooling to room temperature (Figure 2.1a). When reactants with a melting point below the reaction temperature were used ($ZnCl_2$, for example), the sealed tubes were placed into vertically orientated low-temperature furnaces to ensure the reactants remained mixed when heated (Figure 2.1b). X-ray diffraction was used to monitor the reaction progress between each cycle, where the reaction ampule was opened and the sample washed with distilled water to remove unreacted transition metal chloride and LiCl by-product.

2.1.3.3 Reactions Under Flowing Gas

Exchange reactions were also performed under flowing argon conditions as an alternative to rigorously pre-drying the chlorides. This method allows for in situ drying of the chlorides and eliminates the risk of the reaction tube exploding. The thermodynamically stable precursors were combined with 10 molar equivalents of anhydrous transition metal chloride and ground into a homogenous mixture using an agate pestle and mortar inside an argon-filled dry glovebox. The mixture was loaded into a 9 mm Pyrex tube and placed inside an open-ended silica tube. The silica tube was secured with end caps fitted with T-junction taps, as shown in Figure 2.2. The entire apparatus setup was placed into a flowing tube furnace

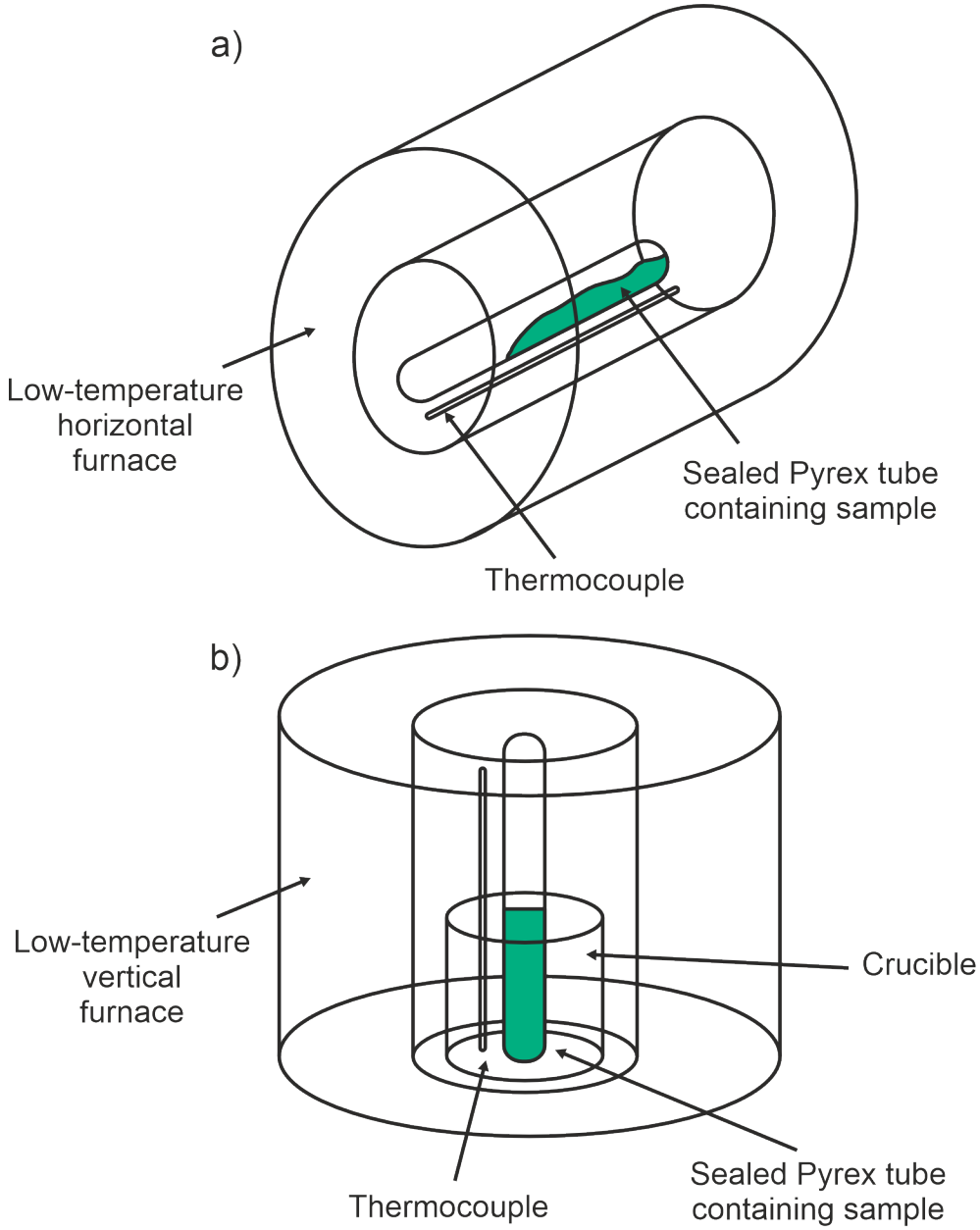


Figure 2.1 Schematic of the furnace setup used for air-sensitive cation-exchange reactions performed in sealed Pyrex tubes, where the furnace is orientated a) horizontally and b) vertically, for reactions involving reagents with melting points below the reaction temperature ($ZnCl_2$).

and connected to a continuous argon flow. The system was purged for approximately 30 minutes before being heated to the desired reaction temperature at a ramp rate of 2 °C min^{-1} and held at this temperature for the appropriate reaction time. Once cooled to room temperature, the flowing tube was opened, and the reaction progress was assessed using X-

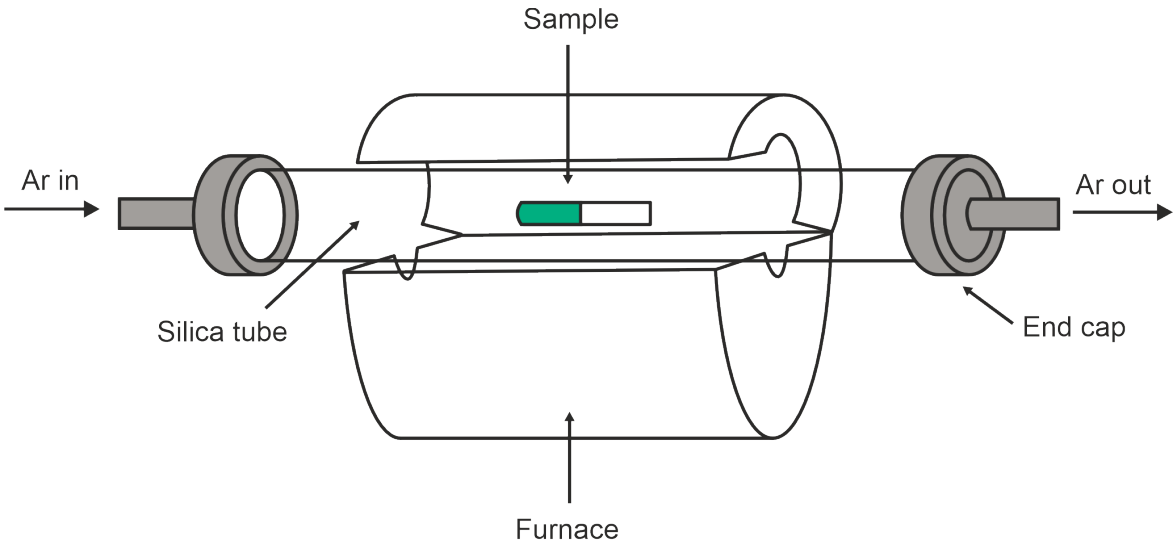


Figure 2.2 Schematic representation of the flowing tube apparatus used in cation-exchange reactions taking place under flowing argon gas.

ray diffraction. Once the reaction was complete, the sample was washed with distilled water to remove unreacted transition metal chloride and LiCl by-product.

A similar setup was used to hydrogen-treat samples when it was important to remove potential ferro- or ferrimagnetic impurities by reduction to diamagnetic impurities. The sample was loaded into an alumina boat and placed inside the silica flowing tube. The silica tube was secured with end caps fitted with T-junction taps and the entire apparatus setup was placed into a flowing tube furnace and heated to 350 °C under a continuous flow of 10% H_2 gas in argon.

2.2 Powder Diffraction

Diffraction occurs when a monochromatic beam of radiation interacts with a crystalline material. A crystalline material is a three-dimensional array of atoms or molecules with periodic translational symmetry.[71] This periodic array can act as a diffraction grating if the wavelength of the radiation is of the same order of magnitude as the lattice spacing.

Bragg's Law can be used to predict when diffraction will take place and defines the relationship between the angle at which a beam of radiation of a particular wavelength, λ, diffracts from a crystalline material with an interplanar spacing, d_{hkl}:

$$n\lambda = 2d_{hkl}sin\theta$$

where θ is the angle between the incident radiation and the crystal plane, and n is an integer number. Bragg's Law is schematically depicted in Figure 2.3.[78] When a monochromatic beam of radiation enters a crystal lattice, it interacts with a scattering object (e.g., the electron cloud of an atom), producing a diffracted beam of radiation. In most directions, the diffracted radiation reflecting from scattering objects in different lattice planes will interfere destructively because the waves are out of phase, altogether cancelling each other out. However, when Bragg's Law is satisfied, radiation scattered from objects in successive planes of the crystal lattice will be in phase and interact constructively to produce a diffracted beam with an increased amplitude.

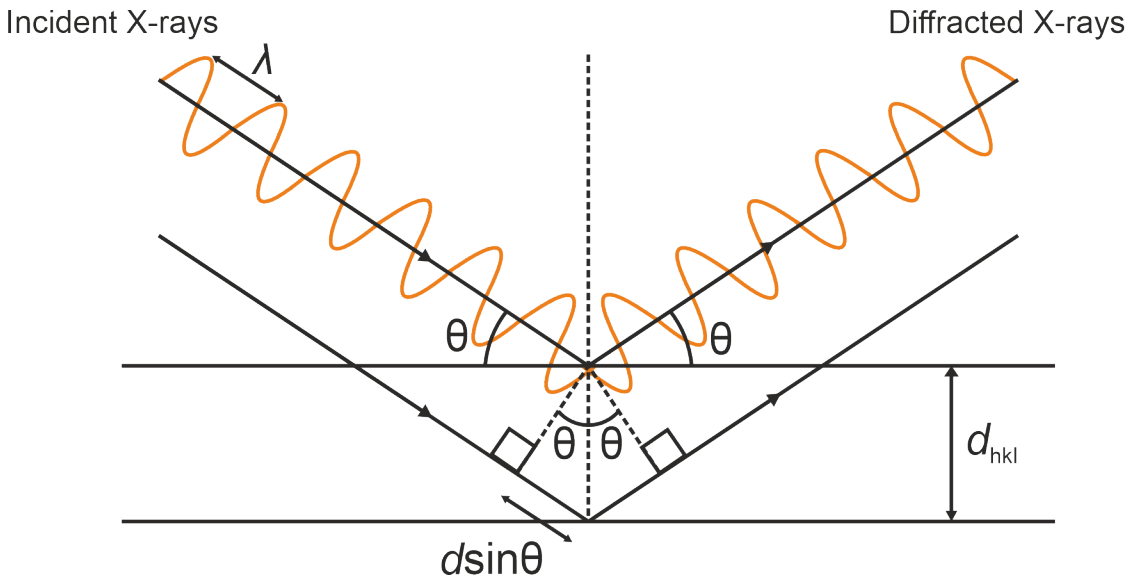


Figure 2.3 Schematic representation of Bragg's Law.

Polycrystalline powders were used in the diffraction experiments detailed in this thesis. A polycrystalline powder consists of many millions of individual crystallites, each randomly orientated along a different direction. Statistically, some of these crystallites will be correctly orientated to the Bragg angle, allowing for the constructive interference of the X-ray beam.

2.2.1 X-ray Powder Diffraction

X-ray powder diffraction is a routine structural analysis technique. X-ray radiation, with a wavelength of approximately 0.1-100 Å, satisfies the necessary conditions of diffraction since it is of the same magnitude as the lattice spacing, typically in the 1-20 Å range.[79] X-ray diffraction is a consequence of the interaction of a beam of X-ray radiation with the electron density of each atom within a crystalline lattice.

In a standard powder diffraction experiment, a beam of monochromatic X-rays is shone on a polycrystalline sample and the intensity of the diffracted radiation is monitored as a function of θ. Intensity is observed at discrete values of θ which satisfy Bragg's law. A great deal of quantitative information can be extracted from the observed experimental diffraction pattern of a material. The size and symmetry of the unit cell determine the 2θ positions of the observed reflections. Such information can be extracted by assigning Miller indices to each reflection and interpreting any systematic absences within a diffraction pattern. Systematic absences describe the absence of diffraction intensity at specific sets of reciprocal lattice points and arise due to translational symmetry elements, namely lattice centering, screw axes and glide planes. Information about the identities of atoms and their fractional coordinates can be obtained from the relative intensities of the different peaks within a diffraction pattern.

For the case of X-ray diffraction, the intensity of a given reflection, I_{hkl}, is proportional to the square of the structure factor F_{hkl} and is given by:

$$I_{hkl} \propto L \times m \times A \times |F_{hkl}|^2 \tag{2.1}$$

where L is the sample-independent Lorentz-polarisation function, which accounts for the geometric factors of the diffractometer, m is the multiplicity term, and A is the absorption factor that accounts for any reduction in intensity that results from competing absorption processes. The structure factor contains information about the fractional atomic coordinates and is given by:

$$F_{hkl} = \sum_j f_j \times q_j \times \exp\left[2\pi i\left(hx_j + ky_j + lz_j\right)\right] \tag{2.2}$$

where f_j is the X-ray scattering factor for atom j, x_j, y_j, and z_j are the fractional atomic coordinates of atom j in the unit cell, and q_j is the Debye-Waller factor, sometimes referred to as the temperature factor and is given by:

$$q_j = exp\left[\frac{-B_j \sin^2\theta_{hkl}}{\lambda^2}\right] \tag{2.3}$$

where B_j is the atomic displacement parameter. The Debye-Waller factor accounts for the reduction in scattering intensity due to the thermal motion of atoms relative to their equilibrium positions. These lattice vibrations act to smear out the electron density of an atomic site, causing a fall-off in the observed intensity. Furthermore, the Debye-Waller factor describes the dependence of the intensity on the scattering angle θ. As the scattering angle increases, the exponential term decreases, reducing the intensity to a greater extent at large values of Q (where $Q = 2\pi/d$).

The X-ray scattering factor, f_j, contains a form factor that describes the fall-off of intensity at large values of Q that occurs as a consequence of the destructive interference between electrons of the same atom. This angular dependence is a consequence of the finite size of the electron cloud. Different regions of the electron cloud within the same atom may diffract X-ray photons and will emerge from the sample with a slightly different path length. This difference in path length will result in destructive interference. Figure 2.4 presents the atomic scattering factors of some common atoms plotted against scattering angle.[80]

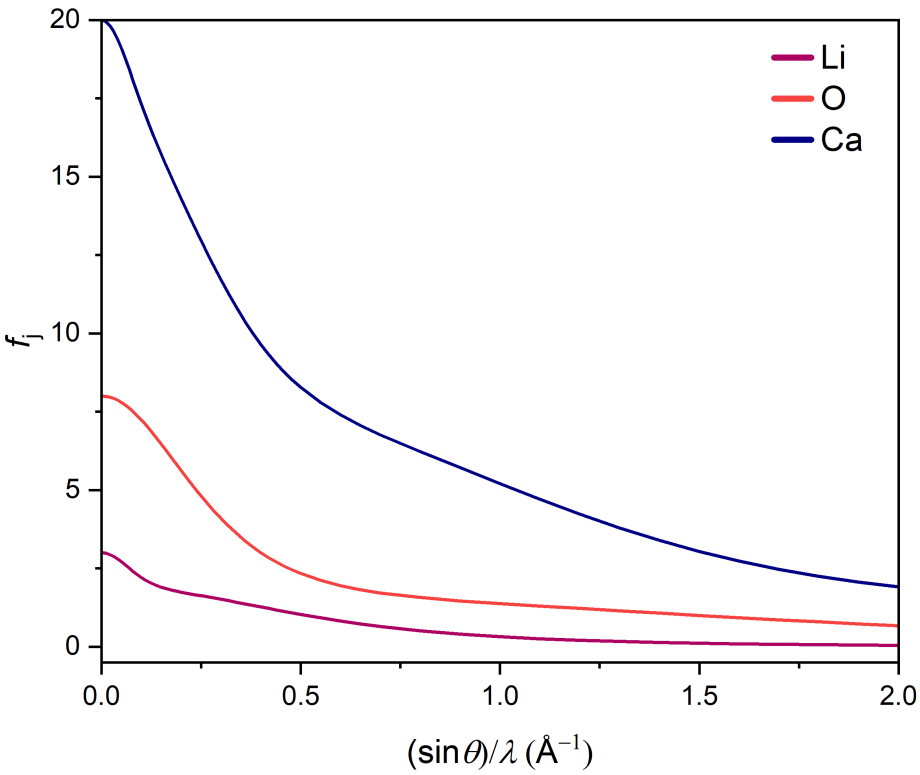


Figure 2.4 The atomic scattering factor of Li, O and Ca atoms as a function of scattering angle.

2.2.1.1 Panalytical Empyrean and X'Pert Diffractometers

In-house X-ray powder diffraction was used as a routine technique to perform initial structural analysis and to monitor reaction progress. Malvern Panalytical Empyrean and X'Pert diffractometers were used since they provide high-resolution data with peak intensities appropriate for detailed structural characterisation.

In conventional diffractometers, a filament is heated to produce electrons, which are accelerated in a vacuum towards the surface of a metal target, the most common of which is copper.[81] When these high-energy electrons strike the metal anode, they ionise electrons from the 1*s* orbitals of the metal ion and form holes. Electrons in higher energy orbitals drop into the vacant 1*s* holes, emitting X-rays as they do so. The wavelength of the emitted X-ray radiation is characteristic of the metal anode and is determined by the energy difference between the two orbitals. Three distinct lines are observed in the copper X-ray spectrum. The Kα lines ($K\alpha_1$ and $K\alpha_2$) result from transitions from Cu 2*p* to 1*s* orbitals and are split due to spin-orbit coupling. The Kβ line corresponds to transitions from Cu 3*p* to 1*s*.

A monochromatic beam of X-ray radiation is required to obtain useful information from a laboratory diffraction experiment. This is typically achieved using a single-crystal monochromator. The Panalytical Empyrean and X'pert diffractometers adopt a Bragg-Brentano reflection geometry, as shown in Figure 2.5, and generate Cu $K\alpha_1$ radiation through the inclusion of a Ge(111) single-crystal monochromator positioned between the incident beam and the sample.[82] Divergence slits, or Soller slits, are used to control the divergence of both the incident and scattered radiation by collimating the beam.

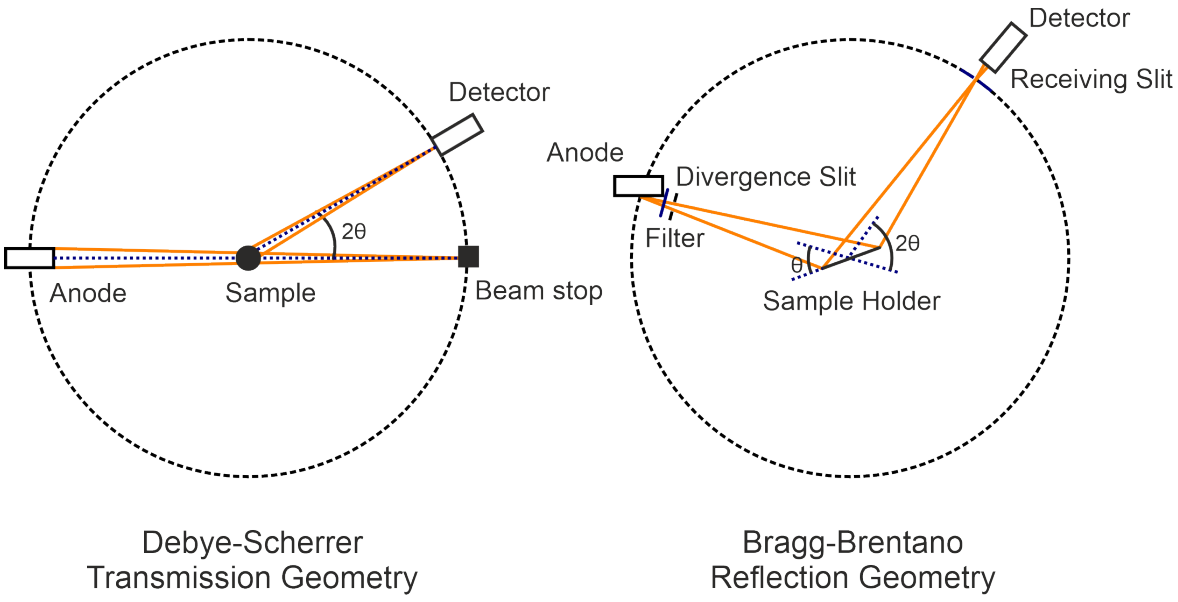


Figure 2.5 X-ray optics of the Debye-Scherrer transmission geometry and Bragg-Brentano reflection geometry.

The sample preparation procedure was identical for both diffractometers. A thin layer of vacuum grease was applied to the surface of a microscope slide. The powder to be measured was then evenly dispersed onto the grease, ensuring a secure, thin and uniform distribution of the sample. The microscope slide was then loaded into the flat bracket stage of the diffractometer.

2.2.1.2 Synchrotron X-ray Diffraction

Synchrotron radiation is generated by the acceleration of charged particles and the resulting emission of electromagnetic radiation. Synchrotrons consist of a circular arrangement of dipole magnets (Figure 2.6).[83] A dipole magnet will produce a vertical magnetic field, *H*, and an electron travelling perpendicular to the direction of the magnetic field will experience a force perpendicular to both the magnetic field and its incident direction of travel. The force will cause the centripetal acceleration of the electron, driving it to continue travelling in a circular orbit. By positioning a series of dipole magnets in a circle, it is possible to make an

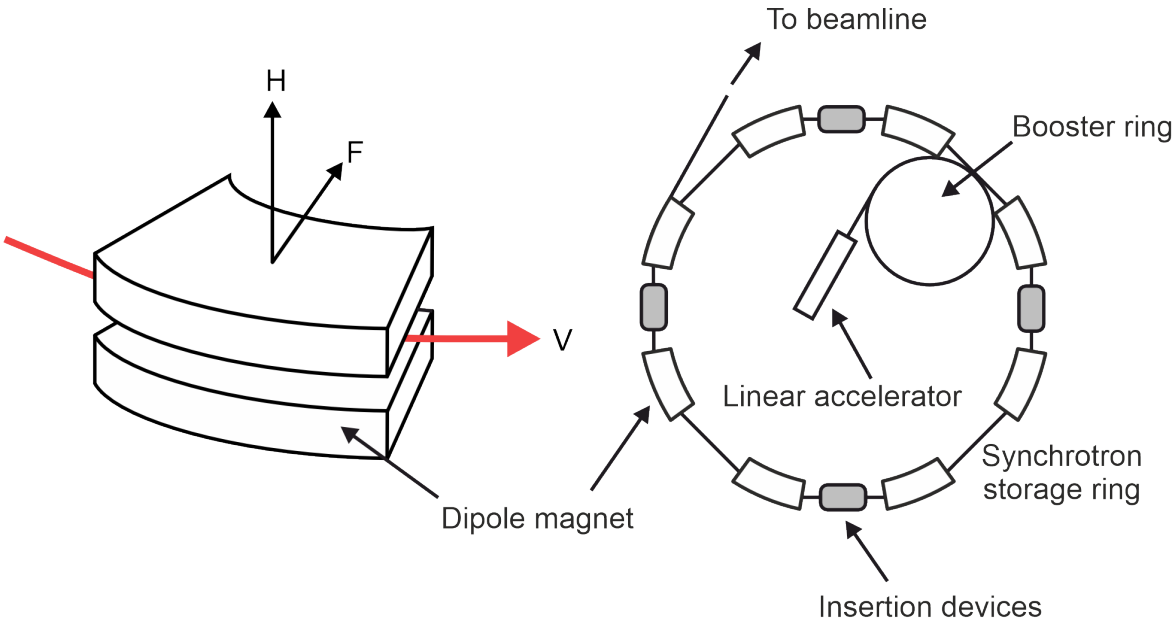


Figure 2.6 Left: Schematic diagram of the dipole magnets used to accelerate electrons inside a synchrotron. **V** represents the direction of travel of an electron, **H** is the magnetic field, and **F** is the force experienced by the electron. Right: Schematic diagram of a typical synchrotron.

electron accelerate around a closed ring. The accelerating electron will emit electromagnetic radiation as it is forced to change direction by the magnetic field as it travels around the ring.

Figure 2.6 illustrates a characteristic synchrotron.[83] In a typical synchrotron, electrons are generated by an electron gun and accelerated through a linear accelerator and booster ring before being fed into the storage ring. Once inside the ring, each electron will travel close to the speed of light and produce radiation that extends from the radio-frequency to the X-ray region of the electromagnetic spectrum. Several insertion devices, known as undulators and wigglers, are located in the straight sections of the storage ring and act to improve the brightness of select wavelengths of X-rays.

The photon flux of X-ray radiation generated in a synchrotron is incredibly high compared to in-house diffractometers. The greater brightness of the radiation ensures that measurements can be conducted more quickly, with superior counting statistics and a better signal-to-noise ratio. Since the intensity of the emitted beam arriving at the monochromator

is exceptionally high, it can afford to be highly wavelength-selective to produce a monochromatic beam of X-rays. A narrower wavelength range and a more controlled beam dispersion ensure the radiation is highly collimated, resulting in greater spatial precision during measurements and better resolution.

The synchrotron X-ray powder diffraction data presented in this thesis were collected using the I11 beamline at the Diamond Light Source Facility in Didcot, Oxfordshire. Each sample was diluted with a low-absorption amorphous material to account for absorption. Polycrystalline samples were combined with approximately 2/3 by volume of ground glass and ground into homogenous mixtures. The mixtures were loaded into 0.3 or 0.5 mm glass capillaries and sealed using a blowtorch. The sealed capillaries were mounted into brass sample pins and secured with superglue. Each brass pin was then screwed into a numbered magnetic base which was loaded onto a pre-aligned magnetic stage. Each capillary is aligned in the beam and spinning during the measurement to account for any preferred orientation. Data was collected using the Position Sensitive Detector (PSD) because it gives an excellent signal-to-noise ratio, and data is typically collected in a matter of seconds.[84]

2.2.2 Neutron Powder Diffraction

Neutrons are subatomic particles possessing both particle-like and wave-like properties as a consequence of wave-particle duality. Hence, neutrons have a wavelength, which can be related to their momentum using the de Broglie equation:

$$\lambda = \frac{h}{p} = \frac{h}{mv} \tag{2.4}$$

where λ is the de Broglie wavelength, h is Planck's constant, p is momentum, m is the mass of the particle, and v is the velocity of the particle.[85] A slow-moving neutron will have a wavelength comparable to the atomic spacing within a crystal lattice, so it is able to undergo

diffraction. Complementary information can be obtained from X-ray and neutron diffraction experiments, and often both are required to gain a complete structural understanding of a material.

The scattering process in X-ray diffraction occurs via the interaction of X-rays with the electron clouds of atoms, whereas neutrons interact directly with the nucleus of an atom. It is often difficult to accurately deduce the position of lighter atoms using X-rays, especially in the presence of heavy elements, because heavy atoms scatter more strongly and dominate the diffraction pattern.[85] Since there is no correlation between atomic number and the scattering power of an atom, nor any periodic trend, the position and occupancy of light elements, such as oxygen, can be more easily determined using neutron diffraction.[86] Similarly, neutron diffraction can help distinguish between atoms with a similar number of electrons and, therefore, similar scattering power, even isotopes.

As was demonstrated in Section 2.2.1, in the instance of X-ray diffraction, the intensity of an observed reflection is proportional to the square of the structure factor, F_{hkl}. This is also true of neutron diffraction, where the structure factor is given by an analogous expression to that of X-ray diffraction, except the X-ray scattering factor is replaced by the neutron scattering length, b_j, and describes how strongly atom j scatters neutrons. The neutron structure factor is given by:

$$F_{hkl} = \sum_j b_j \times \exp\left[2\pi i\left(hx_j + ky_j + lz_j\right)\right] \tag{2.5}$$

Unlike a diffuse electron cloud, an atom's nucleus is relatively small and acts as a pin-point scatterer. The consequence of this is that b_j does not include a form factor and is independent

of the scattering angle. Thus, neutron diffraction is ideal for studies where scattering at high angles is required to obtain short *d*-spacing information, such as atomic thermal parameters.

Neutrons are spin-½ particles and, therefore, interact with magnetic moments. As a consequence, neutron diffraction can reveal information about both the crystal and magnetic structures of magnetic materials. Magnetic scattering arises from the interactions between neutrons and unpaired electrons located in the diffuse outer shells of atoms and requires a form factor. Consequently, the intensity of the magnetic contribution to the diffraction peaks will fall off rapidly with increasing Q in a similar way to X-ray diffraction.

2.2.2.1 Generation of Neutrons

Neutron powder diffraction data presented in this thesis were collected using the WISH instrument at the ISIS Neutron and Muon Source in Oxfordshire. ISIS uses a spallation source to generate neutrons of sufficient intensity for powder diffraction experiments.[87] Pulsed neutron sources accelerate H^- ions using a linear accelerator, which are then fired through a thin alumina foil that strips off the electrons to produce a beam of protons. The protons are further accelerated around a synchrotron before they are diverted towards a tungsten metal target. The protons collide with the nuclei and produce high-energy neutrons via a process called spallation. The neutrons are slowed down by a hydrogenous moderating material (for example, solid methane at ISIS-TS2), which absorbs some of the excess energy of the neutrons and generates a pulse of thermal neutrons to be transported down beamlines to different instruments.

The spallation process produces neutrons with a large distribution of wavelengths. Unlike during an X-ray diffraction experiment, when monochromatic radiation of a fixed wavelength is required and the angle θ is varied, the wavelength is varied and the angle is fixed throughout a time-of-flight experiment. During a typical time-of-flight experiment, a

pulse of neutrons is fired towards a sample, where they undergo a scattering process and are finally detected by one or more fixed-angle detector banks.

Bragg's law can be related to the de Broglie equation via Equation 2.6 to calculate *d*-spacing:

$$\lambda = \frac{h}{mv} = \frac{ht}{mL} = 2dsin\theta \quad (2.6)$$

where *t* is the time-of-flight, and *L* is the neutron path length. Since the start time can be fixed by the pulsed generation of the neutron beam, recording the time taken for the diffracted neutron to reach the detector will provide valuable information about the wavelength of the scattered neutron and, therefore, the *d*-spacings of the material being studied.

2.2.2.2 Neutron Diffractometers: WISH (ISIS-TS2)

WISH is a long-wavelength diffractometer primarily designed to characterise systems with large magnetic or nuclear unit cells. Diffraction data are collected using 10 fixed-angle detector banks, covering neutron scattering angles between 10 and 170°.[88] The data from each pair of detectors located at the same angle are summed together to improve the signal-to-noise ratio of the data. High-resolution data is provided over a *d*-spacing range of 0.7 to 17 Å, and the total *d*-spacing coverage extends to 50 Å.[89] The broad *d*-spacing range and excellent resolution at high *d*-spacings make WISH an ideal diffractometer for studying complex magnetic structures and large unit cell systems.

Typically, the neutron flux produced by spallation is much lower than at X-ray sources. Neutrons also interact weakly with matter and are very penetrating, and as such, the volume of sample necessary for successful neutron diffraction experiments is very large in contrast

to X-ray measurements. Large samples (> 2 g) were synthesised for the neutron experiments detailed in this thesis.

Vanadium is often the chosen material for the sample cans used in neutron powder diffraction experiments since vanadium has a small coherent scattering length for neutrons and does not significantly contribute to the Bragg scattering, although it does result in a small amount of incoherent background scattering. Approximately 2 g of material was loaded into a thin cylindrical vanadium sample can and sealed with a cap. The sample can was then screwed onto the end of a sample stick. A thin sheet of cadmium metal was wrapped around the outside of the empty section of the can (located closest to the stick) to absorb neutrons and prevent scattering from vanadium and the cap, and secured using copper wire. The stick was then inserted into a low background cryostat to facilitate the low-temperature measurements.

2.3 Rietveld and Pawley Refinements

Rietveld refinement is a powerful technique for extracting quantitative information from experimental powder diffraction data and was used to analyse the X-ray and neutron diffraction data collected in this thesis.[90] The general approach involves constructing a suitable structural model close to the true structure and calculating an expected diffraction pattern. The simulated pattern is compared to the experimentally observed data by calculating the difference between the two. The model is then modified to minimise the difference between the two patterns until the simulated pattern adequately matches the experimental data. This process applies a least-squares algorithm, whereby the weighted sum of the squared differences between the observed and calculated intensities, S, is minimised by least-squares refinement:

$$S = \sum_{i=1}^{N} w_i \left(y_{obs,i} - y_{calc,i}\right)^2 \tag{2.7}$$

where w_i is the weighting factor, $y_{obs,i}$ is the observed intensity at point i and $y_{calc,i}$ is the calculated intensity.[91] The statistical quality of the fit of the model to the data is assessed using the weighted profile R factor, R_{wp}, and the Goodness-of-fit (GoF), given by:

$$R_{wp} = \sqrt{\frac{\sum_{i=1}^{N} w_i \left(y_{obs,i} - y_{calc,i}\right)^2}{\sum_{i=1}^{N} w_i {y_{obs,i}}^2}} \times 100\% \tag{2.8}$$

$$GoF = \chi = \frac{R_{wp}}{R_{exp}} = \sqrt{\frac{\sum_{i=1}^{N} w_i \left(y_{obs,i} - y_{calc,i}\right)^2}{N - P}} \tag{2.9}$$

R_{wp} is directly related to the quantity being minimised and is given by the weighted sum of the squared differences between the observed and calculated intensities, divided by the sum of the weighted squared observed intensities. The GoF parameter is related to χ^2, and is given by R_{wp} divided by the statistically expected R factor, R_{exp}, where N is the number of data points, and P is the number of parameters. The GoF ought to tend towards 1 as the refinement progresses, since R_{exp} can be thought of as the best possible value of R_{wp}.[91]

It is often helpful to perform a Pawley fitting before a Rietveld refinement. The Pawley method involves a structure-independent fitting of powder diffraction data and provides an indication as to the best possible fit from a subsequent structural refinement. The intensity is not constrained to a structural model and is treated as a free, refinable parameter during a Pawley fitting, in contrast to a Rietveld refinement, where the intensity of a diffraction peak is directly related to the structure factor. Useful information can be extracted from a Pawley fitting, such as unit cell parameters and peak-shape parameters, and used as a suitable starting point for a structure solution.

The structural refinements presented in this thesis were performed in TOPAS Academic version 7.[92,93] When the powder diffraction pattern was found to contain an incommensurately modulated phase, the JANA2020 software package was used instead.

2.4 DC SQUID Magnetometry

The magnetisation of a sample can be measured using a Superconducting Quantum Interference Device (SQUID). The magnetic susceptibility measurements performed in this thesis were measured using a Quantum Design Magnetic Property Measurement System (MPMS-3) SQUID magnetometer. A SQUID magnetometer contains a superconducting loop intersected by two thin strips of an insulating material that form two parallel Josephson junctions (Figure 2.7). Applying a small current across the junction causes Cooper pairs of electrons to tunnel through the insulating barrier with zero resistance. A current will continue to flow through the SQUID so long as the total current does not exceed the critical current of the Josephson junctions. Therefore, the critical current is the current at which a

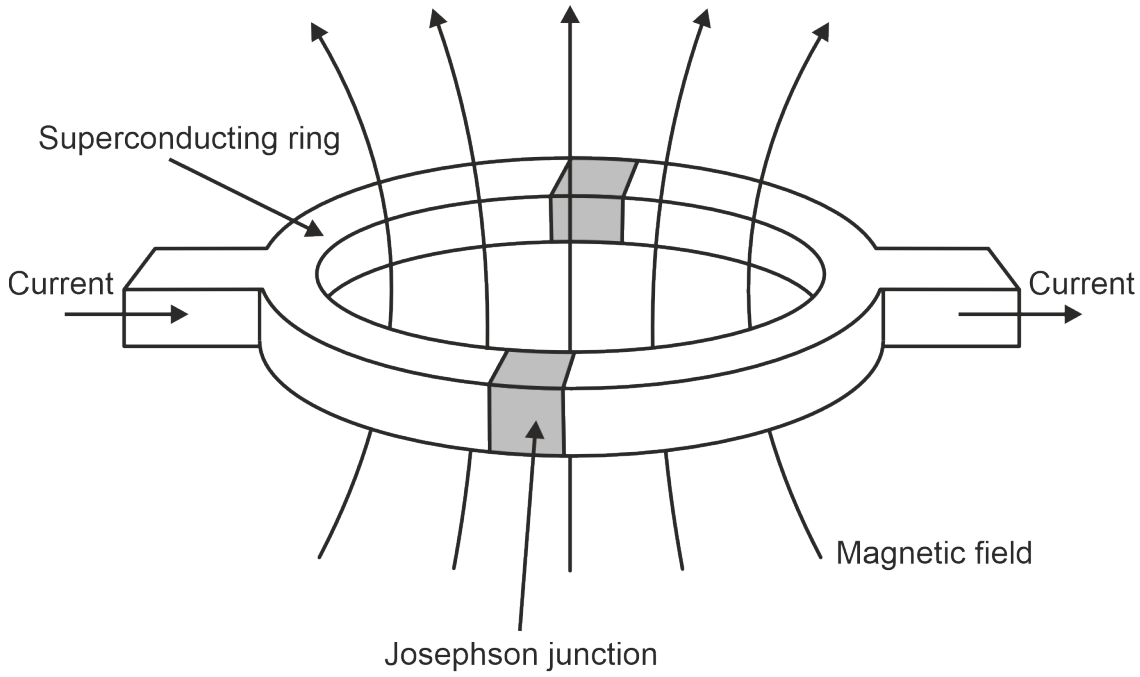


Figure 2.7 Schematic representation of the SQUID component of a magnetometer.

voltage would be generated across the ring. During a magnetisation measurement, the sample is moved vertically through an induction coil, and a current is generated in the superconducting ring to produce a magnetic field that opposes the direction of the applied field, effectively cancelling out the net magnetic flux in the ring. The magnitude of this induced current is proportional to the magnetisation of the measured sample. If the current exceeds the critical current of the superconducting ring, the superconducting state is lost. The SQUID becomes resistive, and a voltage is established across the device. Since the current is quantised, it can only take on discrete values, and very small variations in the external magnetic field can be measured with high precision by monitoring the voltage.[94]

Approximately 30 mg of the sample to be measured was weighed and loaded into a gelatine capsule and inserted into a plastic straw. Three empty capsules were placed inside the straw on either side of the sample to ensure the sample sat at the appropriate height inside the magnetometer. To prevent the sample capsule from moving during the measurement, a layer of diamagnetic Kapton tape was wrapped around the final capsule, and a plastic tip was inserted into the straw. The sample straw was then attached to a rod and mounted within a cryostat chamber surrounded by an induction coil. The sample was magnetised by a He-cooled superconducting magnet and translated vertically to induce a current in the induction coil, which is coupled to the SQUID.

Field and temperature-dependent susceptibility measurements were performed, whereby magnetisation data were collected as a function of temperature at a constant field or as a function of applied field at a fixed temperature. Zero-field-cooled (ZFC) and field-cooled (FC) measurements were performed from 5 K to 300 K in an applied field of 100 Oe. Measurements as a function of an applied field were conducted at a constant temperature over a field range of $-5\ \text{T} \leq H \leq 5\ \text{T}$.

2.4.1 Paramagnetism

Magnetic susceptibility, χ, is a quantity that relates a material's magnetisation, M, to the strength of the applied magnetic field, H, and describes how a material responds to an applied magnetic field.

$$\chi = \frac{\partial M}{\partial H} \tag{2.10}$$

Paramagnetism is a property of materials with unpaired electrons. At some temperature of comparable magnitude to the strength of the magnetic correlations between unpaired electrons, the material may undergo a transition to a magnetically ordered state. At temperatures above this transition, the thermal fluctuations of the magnetic ions are greater than the exchange interactions between them. The material behaves as a paramagnet, where the spins of the unpaired electrons are non-interacting and disordered.

2.4.2 Curie-Weiss Law

The Curie law describes the relationship between the susceptibility of a paramagnet and temperature and is given by:

$$\chi = \frac{C}{T} \tag{2.11}$$

where C is known as the Curie constant (with units of emu K mol^{-1} in cgs), directly related to the number of unpaired electrons and a sample's magnetic moment, and T is the temperature (with units of K).[95] The Curie law is only applicable to magnetically dilute systems where interactions between local magnetic moments are negligible. In reality, this is often not true, and the Curie law can rarely be applied directly to a system without the use of a correction, since the magnetic moments in many materials will experience a significant

internal magnetic field. The Curie-Weiss law was derived to account for the interactions between magnetic moments and is given by:

$$\chi = \frac{C}{T - \theta} \tag{2.12}$$

where θ is often referred to as the Weiss temperature (with units of K). The magnitude and sign of the Weiss temperature is related to the average strength and type of magnetic interactions between ions.[16] Positive values of θ imply the presence of ferromagnetic interactions between spins, whereas a negative value of θ indicates antiferromagnetic interactions.

The Curie constant can be used to calculate the effective magnetic moment per ion, μ_{eff}, in units of Bohr magnetons, using the relationship given in Equation 2.13. This equation only holds for cgs units, but can be modified for SI.

$$\mu_{eff} = \sqrt{8C} \tag{2.13}$$

In 3*d* transition metal ions, the orbital contribution to the moment is believed to be negligible due to the quenching of orbital angular momentum, and so the magnetic moment is well approximated by the spin-only moment. The observed moment can be directly compared to the calculated spin-only moment of an ion given by:

$$\mu_{calc} = g\sqrt{S(S+1)} \tag{2.14}$$

where g is the gyromagnetic factor ($g = 2$). S is the spin quantum number and can be deduced by counting the number of unpaired *d* electrons in the sample.

2.5 Muon Spin Spectroscopy

Muon spin spectroscopy, commonly known as muon spin rotation or relaxation (μSR) spectroscopy, is an experimental technique based on the implantation of spin-polarised muons into a sample.[96] The subsequent precession and relaxation of their spins can give an insight into their local environment and can be used to investigate a variety of static and dynamic effects in a material. Therefore, muons can act as a local probe to better understand magnetic interactions and ordering in materials of interest.

The muon is a lepton particle with a spin-1/2. Muons are generated by the collision of high-energy protons with carbon nuclei in the stationary target (usually graphite), and the positive pions produced by these interactions decay into spin-polarised muons. If the incident proton collides with a neutron, a positive muon, μ+, is formed.[97] For experiments in condensed matter physics, it is predominantly the positive muon which is used, since μ+ will implant itself away from the nucleus in a region of electron density, making them more sensitive to the physics of electrons. The muon is guided to the individual beamlines using a series of magnets, where it will stop in the sample of interest and decay via a three-body process, emitting a positron and two neutrinos. Detection of the emitted positron allows the spin precession of the muon to be studied.

The positive muons that are implanted into the sample are spin-polarised and sensitive to their local magnetic environment. If there is an internal magnetic field at the point where a muon comes to a standstill in a material, the muon spin will undergo Larmor precession around the direction of the local field.[98] When a muon eventually decays and emits a positron, it is emitted preferentially along the direction of the muon spin at the moment of decay. Hence, the direction along which the positron is emitted directly relates to the direction of the muon spin at the moment of its decay.[99]

2.5.1 General Purpose Surface-Muon Instrument (GPS)

μSR experiments are conducted at large-scale facilities using intense beams of muons produced by particle accelerators. The muon experiments described in this thesis were carried out on the General Purpose Surface-Muon Instrument (GPS) at the Paul Scherrer Institute (PSI) in Switzerland. PSI uses a continuous wave (CW) muon beam, generated by a cyclotron that produces a continuous proton beam.[97]

Figure 2.8 shows a schematic of the GPS instrument at PSI.[100] The detector arrangement consists of six positron detectors placed around the sample to measure the time evolution of the muon spin polarisation: forward-backward, left-right and up-down. Muons produced by a continuous beam arrive intermittently at the sample, with each muon individually counted and serving as the start signal for the positron detectors. The muon spectrometer also features a forward and backward veto detector, used to focus the muon beam to the sample and reject muons that have not stopped in the sample.

The quantity of interest in a muon spectroscopy experiment is the time evolution of the muon polarisation, which is proportional to the asymmetry function $A(t)$, given by:

$$A(t) = \frac{N_B(t) - N_F(t)}{N_B(t) + N_F(t)} \tag{2.15}$$

where $N_B(t)$ and $N_F(t)$ are the number of positrons detected in the backwards and forwards detectors, respectively.[96]

For the muon spectroscopy measurements detailed in this thesis, approximately 200 mg of polycrystalline sample was loaded into a foil packet and mounted onto a silver fork on the sample stick, which was then loaded into the instrument.

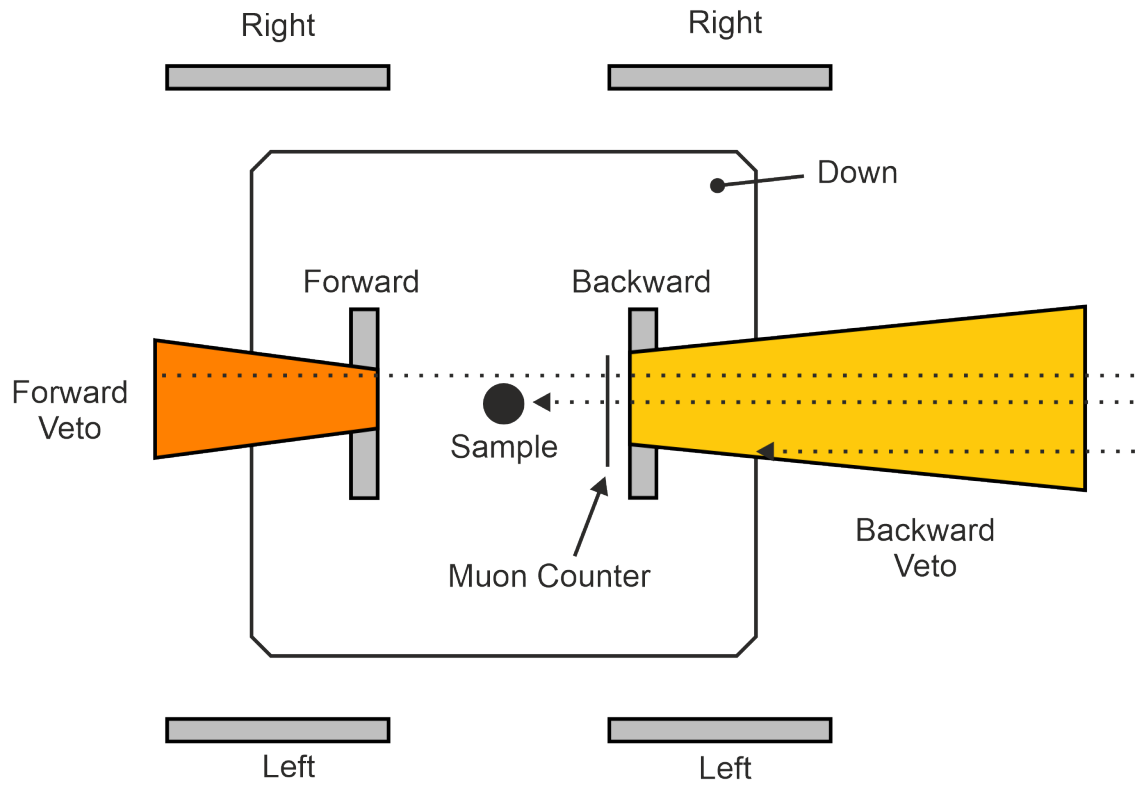


Figure 2.8 Schematic top view of the detector arrangement of the GPS instrument at PSI. The up detector is not shown because it sits above the sample. Figure adapted from Reference 100.

2.6 Second Harmonic Generation

Second harmonic generation (SHG) is a non-linear optical process in which two photons with the same wavelength interact with a non-linear material to produce a photon with half the wavelength of the original photons, or twice the energy.[101] The powder SHG technique is commonly used to characterise non-centrosymmetric compounds.

Figure 2.9 shows a schematic of a standard SHG setup. Typically, a Nd-YAG laser with a wavelength of 1064 nm is used, and any SHG activity will appear in the visible region at 532 nm. Many of the phases synthesised in this thesis were intensely coloured, and therefore, it was necessary to use an IR NLO setup. The SHG signals of the samples and benchmark $AgGaS_2$ were investigated under incident laser radiation of 2090 nm (Q-switched Tm fiber laser pumped Ho: YAG laser (HLPN-2090-20-10)) by modified Kurtz-Perry method,

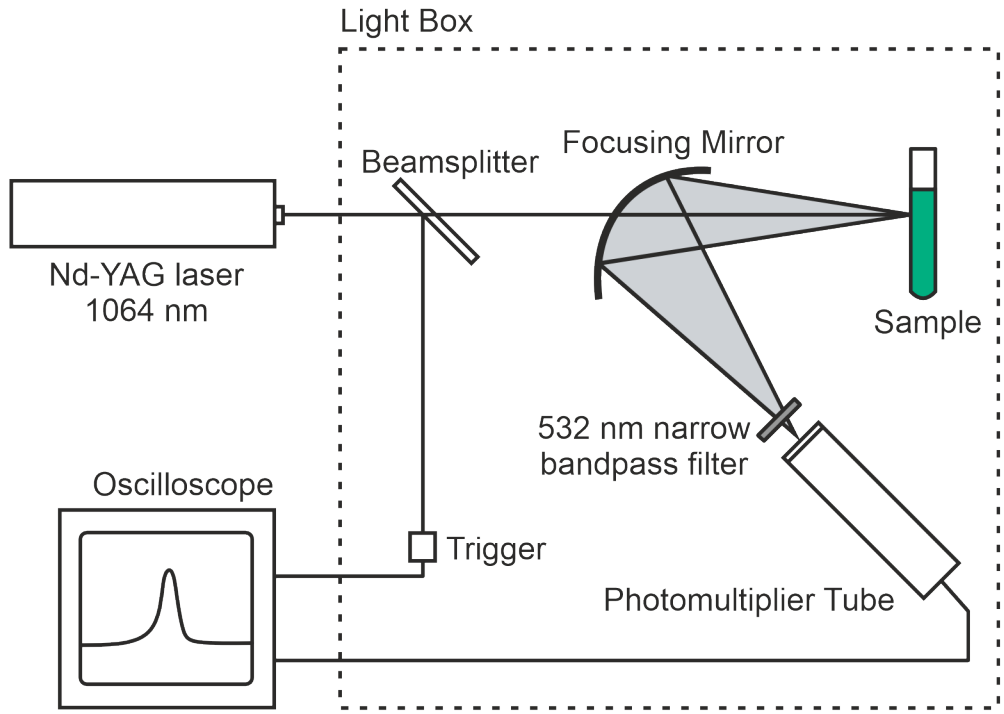


Figure 2.9 Schematic representation of a modified Kurtz-Powder Laser system adapted from Reference 101.

respectively.[102] $AgGaS_2$ was used as a standard against which the measured SHG activity were compared. The SHG signals were detected by a charge-coupled device.

A pulsed laser is used for SHG measurements, and as such, the intensity of the SHG signal is also pulsed with time. The data are plotted against time to demonstrate that the emitted SHG is synchronous with the incident laser pulse and decays at the same rate. The laser pulse is incident on the sample at zero time, and negative time values are included to show the background intensity level. A photomultiplier tube (PMT) serves as the detector, converting optical signals into electrical signals by producing photoelectrons when SHG hits the PMT. The generated photoelectrons are negatively charged, hence, the measured SHG intensities are also negative.

The SHG data reported in this thesis were collected by Dr. Yujie Zhang and Prof. Shiv Halasyamani from the Department of Chemistry at the University of Houston. For these measurements, approximately 200 mg of polycrystalline powder was sealed in 4 mm silica capillaries and loaded into the setup.

2.7 ISODISTORT symmetry analysis

The ISODISTORT tool of the ISOTROPY software suite allows the user to identify and explore physical symmetry-lowering distortions of structural phase transitions, such as atomic displacements, atomic ordering, magnetic moments, and lattice strain.[103] For a given parent space group, ISODISTORT is able to describe a series of operations, or atomic displacement patterns, induced by irreducible representations. The software tabulates each of the possible distortion symmetries or subgroups of the high symmetry space group in a more subtle way than simply losing symmetry operations.

The ISODISTORT tool was used to perform a detailed symmetry analysis of the aristotype $n = 2$ Ruddlesden-Popper structure to generate a series of chemically plausible structural tilting distortions (cooperative tilts between adjacent octahedra) and their space groups.[103–105] Here, 'chemically plausible' is used to refer to distortions whose corresponding arrangement of atoms retains their equivalence of BO$_6$ octahedra between adjacent perovskite double layers; that is, topologically equivalent cations are related by symmetry and share the same local environment between each layer.

The chemically plausible symmetry-lowering structural distortions and their space groups listed in Table 2.1 were each generated by applying one or two independent irreducible representations to the undistorted aristotype *I*4/*mmm* space group. We assume that the $n = 2$ Ruddlesden-Popper phases synthesised in this thesis adopt one of the chemically plausible structures described below.

Table 2.1 The chemically plausible distortions of the $n = 2$ Ruddlesden-Popper structure.

Glazer Tilts	Space group in standard setting	Stacking axis in standard setting	Space group (*c*-stacking)	Irreducible representation	NCS?
$a^0b^0c^0/a^0b^0c^0$	*I*4/*mmm* (139)	c	*I*4/*mmm*		No
$a^0a^0c^+/a^0a^0c^+$	*Cmca* (64)	a' = c	*Acam*	X_2^+ (a;0)	No
$a^0a^0c^-/a^0a^0c^-$	*Ccca* (68)	b' = c	*Acaa*	X_1^- (a;0)	No
$a^-b^0c^0/b^0a^-c^0$	*P*4$_2$/*mnm* (136)	c' = c	*P*4$_2$/*mnm*	X_3^- (a;a)	No
$a^-a^-c^0/a^-a^-c^0$	*Cmcm* (63)	a' = c	*Amam*	X_3^- (a;0)	No
$a^-b^-c^0/b^-a^-c^0$	*Pnnm* (58)	c' = c	*Pnnm*	X_3^- (a;b)	No
$a^-b^0c^0/b^0$-a^-c^0	*P*4$_2$/*mcm* (132)	c' = c	*P*4$_2$/*mcm*	X_4^- (a;a)	No
$a^-a^-c^0$/-$(a^-a^-)c^0$	*Cmma* (67)	b' = c	*Acmm*	X_4^- (a;0)	No
$a^-b^-c^0$/-$(b^-a^-)c^0$	*Pccm* (49)	c' = c	*Pccm*	X_4^- (a;b)	No
$a^-a^-c^+/a^-a^-c^+$	*Cmc*2$_1$ (36)	a' = c	*A*2$_1$*am*	$X_2^+ \bullet X_3^-$ (a;0|b;0)	Yes
$a^-a^-c^+/a^-a^-$-c^+	*Pnma* (62)	b' = c	*Pnam*	$X_2^+ \bullet X_3^-$ (a;0|0;b)	No
$a^-a^-c^+/a^-a^-$-c^+	*Pna*2$_1$(33)	c' = c	*Pna*2$_1$	$X_2^+ \bullet X_3^- \bullet \Gamma_3^-$ (a;0|0;b|c)	Yes
$a^-b^-c^+/b^-a^-c^+$	*Pmn*2$_1$ (31)	a' = c	*P*2$_1$*nm*	$X_2^+ \bullet X_3^-$ (a;0|b;c)	Yes
$a^-a^-c^+$/-$(a^-a^-c^+)$	*Abm*2 (39)	b' = c	*B*2*cm*	$X_2^+ \bullet X_4^-$ (a;0|b;0)	Yes
$a^-a^-c^+$/-$(a^-a^-)c^+$	*Pbcm* (57)	c' = c	*Pbcm*	$X_2^+ \bullet X_4^-$ (a;0|0;b)	No
$a^-b^-c^+$/-$(a^-b^-)c^+$	*Pma*2 (28)	a' = c	*P*2*cm*	$X_2^+ \bullet X_4^-$ (a;0|b;c)	Yes
$a^-a^-c^-/a^-a^-c^-$	*C*2/*c* (15)	a' = c	*A*2/*a*	$X_1^- \bullet X_3^-$ (a;0|b;0)	No
$a^-a^-c^-/a^-a^-$-c^-	*Pbcn* (60)	a' = c	*Pnab*	$X_1^- \bullet X_3^-$ (a;0|0;b)	No
$a^-a^-c^-/a^-a^-$-c^-	*Pna*2$_1$ (33)	c' = c	*Pna*2$_1$	$X_1^- \bullet X_3^- \bullet \Gamma_3^-$ (a;0|0;b|c)	Yes
$a^-b^-c^-/b^-a^-c^-$	*P*2$_1$/*c* (14)	c' = c	*P*2$_1$/*c*	$X_1^- \bullet X_3^-$ (a;0|b;c)	No
$a^-a^-c^-$/-$(a^-a^-)c^-$	*Pcca* (54)	a' = c	*Pcaa*	$X_1^- \bullet X_4^-$ (a;0|0;b)	No
$a^-b^-c^-$/-$(a^-b^-)c^-$	*P*2/*c* (13)	c' = c	*P*2/*c*	$X_1^- \bullet X_4^-$ (a;0|b;c)	No
$a^-a^-c^-$	*P*2/*c* (13)	a' = ½ c	*P*2/*a*	$X_1^- \bullet X_4^-$ (a;b|c;0)	No

2.8 Density Functional Theory

Density functional theory (DFT) is one of the most widely applied and important computational techniques used to study the structure and properties of crystalline materials. The ground state energy, *E*, of a system may be computed by the solution of the Schrödinger equation, which is given by:

$$\hat{H}\Psi = E_{tot}\Psi \tag{2.16}$$

where *H* is the Hamiltonian operator and Ψ is the ground-state wavefunction. The many-body Hamiltonian operator for a system of interacting electrons and nuclei is given by:[106]

$$H = -\sum_i \frac{\hbar^2}{2m_e}\nabla_i^2 - \sum_I \frac{\hbar^2}{2M_I}\nabla_i^2 + \frac{e^2}{4\pi\epsilon_0}\left[\frac{1}{2}\sum_{i\neq j}\frac{1}{|\boldsymbol{r}_i-\boldsymbol{r}_j|} + \frac{1}{2}\sum_{I\neq J}\frac{Z_I Z_J}{|\boldsymbol{R}_i-\boldsymbol{R}_j|} - \sum_{i\neq j}\frac{Z_I}{|\boldsymbol{r}_i-\boldsymbol{R}_I|}\right] \tag{2.17}$$

The Hamiltonian consists of five terms, three of which are quantum mechanical and depend on the wave-like properties of the electron. Here, $\sum_i \frac{\hbar^2}{2m_e}\nabla_i^2$ and $\sum_I \frac{\hbar^2}{2M_I}\nabla_i^2$ are the quantum kinetic energy of the electrons and nuclei, respectively, $\sum_{i\neq j}\frac{e^2}{4\pi\epsilon_0}\frac{Z_I}{|\boldsymbol{r}_i-\boldsymbol{R}_I|}$ is the Coulombic attraction between the electrons and the nuclei, $\frac{1}{2}\sum_{i\neq j}\frac{e^2}{4\pi\epsilon_0}\frac{1}{|\boldsymbol{r}_i-\boldsymbol{r}_j|}$ is the Coulombic electron-electron repulsion, and $\frac{1}{2}\sum_{I\neq J}\frac{e^2}{4\pi\epsilon_0}\frac{Z_I Z_J}{|\boldsymbol{R}_i-\boldsymbol{R}_j|}$ is the classical Coulombic electrostatic nucleus-nucleus repulsion. Since the Coulombic electron-electron interactions are a many-body quantum mechanical problem, it makes solving the Schrödinger equation and determining the wavefunction, Ψ, non-trivial, even for simple systems.

Several approximations must be introduced to simplify this problem and to obtain an approximate solution to the Schrödinger equation. The first of these is the Born-Oppenheimer approximation. Since the mass of the nuclei is so great in comparison to the mass of an electron, the motion of the nuclei is assumed to be negligible when describing

the electrons. Therefore, electrons can be treated as quantum particles in the field of fixed or very slowly moving nuclei and the nuclear kinetic energy term of Equation 2.17 can be ignored.

The Hohenberg-Kohn theorems form the foundation of density functional theory, which state that the ground-state energy of a system is a functional of the electron density.[107] Since the electron density is only a function of *x*, *y* and *z*, this reduces the many-body problem of considering *N* electrons of a system, with 3*N* cartesian coordinates, to one with only three variables.

2.8.1 Symmetry-mode Analysis of Distorted Structures

The structural distortions of a crystal structure can be decomposed into individual contributions from different phonon modes with specific symmetry properties. Phonon modes are the collective atomic displacements, or lattice vibrations, within a crystal, and their symmetries are given by irreducible representations of the higher-symmetry parent space group.[108] In this thesis, a symmetry-mode approach was used to relate the structure of a distorted phase to a higher-symmetry reference structure using symmetry-allowed modes.

Although a distortion mode may be allowed by symmetry, it does not necessarily follow that the distortion is energetically favourable. The energy, *E*, of the reference structure is given by:

$$E(u) = E^0 + \sum_n \frac{\partial E}{\partial u_n} + \frac{1}{2}\sum_{n,m} \frac{\partial^2 E}{\partial u_n \partial u_m} u_n u_m \qquad (2.18)$$

Here, E_0 is the energy of the reference structure at equilibrium and u_n and u_m are the displacements of atoms *n* and *m* from their equilibrium positions in the reference structure.[53] The term reference structure is used to describe the higher-symmetry structure undergoing

mode decomposition. The linear term of Equation 2.18 describes the force on atom *n* and is equal to zero when the reference structure is unperturbed. The coefficient of the quadratic term is defined as the force constant, *J*:

$$J_{mn} = \left(\frac{\partial^2 E}{\partial u_n \partial u_m} \right) \tag{2.19}$$

The force constants form a $3N \times 3N$ matrix in three dimensions, where *N* is equal to the number of atoms in the computational unit cell. The elements of the force constant matrix are given by:

$$J_{mn}^{\alpha\beta} = \frac{\partial^2 E}{\partial u_{m\alpha} \partial u_{n\beta}} \tag{2.20}$$

where $u_{m\alpha}$ is the displacement of atom *m* in the cartesian direction α. The eigenvalues of the force constant matrix are equal to the force constants of the distortion mode, not of discrete atoms. Therefore, the force constant matrix can be used to infer information about the curvature of the energy surface around the reference structure. A positive value of a force constant indicates that the high-symmetry structure is at a local minimum, that is, it is stable with respect to the distortion mode. A negative force constant indicates that the high-symmetry structure is unstable with respect to the atomic displacements of the distortion mode. In other words, perturbing the reference structure in such a way as defined by the symmetry of the distortion mode will lower the energy of the reference structure. Therefore, the force constant matrix provides a description of the energy surface around the reference structure.

In practice, the symmetry-mode approach involves first determining the symmetry-allowed modes for a given parent group–subgroup pair using the ISOTROPY software suite and then manually constructing a new set of basis vectors that transform according to the specific

irreducible representations of interest, also referred to as symmetry-adapted modes.[104] That is to say, each symmetry-adapted mode describes how each atom in the unit cell moves according to each irreducible representation. A small amplitude of the symmetry-adapted mode is then frozen into the reference structure to generate a set of distorted fractional coordinates. The force experienced by each atom in the unit cell as it undergoes the distortion is computed to construct the force constant matrix. From this, the frequency and force constant of each individual phonon mode can be calculated to determine which distortions are energetically favourable.

The density functional theory calculations detailed in this thesis were performed using the Vienna ab initio Software Package (VASP) using a PBEsol hybrid functional. Further computational details are described more thoroughly in Chapter 6.[109–113]

Chapter 3: Synthesis and Characterisation of $M^{II}CaTa_2O_7$ (M = Fe, Co, Zn)

3.1 Introduction

The synthesis of metastable phases using low-temperature topochemical exchange reactions has been widely studied.[52,59,65,66,68,114–118] As described in Chapter 1, the interlayer cations located between the perovskite sheets in the Ruddlesden-Popper family of materials are more mobile than the surrounding host lattice and can thus participate in low-temperature exchange reactions with cations of a similar ionic radius.

The cation-exchange chemistry of the n = 2 Ruddlesden-Popper phases $Li_2SrTa_2O_7$ and $Li_2CaTa_2O_7$ has previously been exploited to prepare $MnSrTa_2O_7$ and $MnCaTa_2O_7$, respectively, where Mn^{2+} cations are exchanged for Li^+ cations, which occupy half of the available interlayer cation coordination sites.[119,120] It is, therefore, conceivable that analogous cation-exchange reactions can be used to exchange other divalent first-row transition metal cations for Li^+ in these phases. Following this approach, this chapter explores the synthesis and characterisation of $FeCaTa_2O_7$, $CoCaTa_2O_7$ and $ZnCaTa_2O_7$, prepared via a facile cation-exchange reaction from $Li_2CaTa_2O_7$.

3.2 Synthesis

3.2.1 Synthesis of $Li_2CaTa_2O_7$

Polycrystalline samples of $Li_2CaTa_2O_7$ were prepared by combining suitable stoichiometric ratios of $CaCO_3$ (99.997%) and Ta_2O_5 (99%, dried at 900 °C) with a 3% stoichiometric excess of Li_2CO_3 (99.99%) to compensate for lithium loss due to volatility at high temperatures. The mixture was ground in an agate pestle and mortar, placed in an alumina

crucible and heated at 800 °C in air for 12 h. The mixture was reground, pressed into 13 mm pellets, and heated to 1200 °C at a heating rate of 5 °C/min for two periods of 2 h. The samples were reground and pressed into pellets between each heating cycle, placed in an alumina crucible and directly inserted into a furnace at 1200 °C before being quenched to room temperature.

3.2.2 Synthesis of $M^{II}CaTa_2O_7$ (M = Fe, Co, Zn)

Polycrystalline samples of $FeCaTa_2O_7$, $CoCaTa_2O_7$ and $ZnCaTa_2O_7$ were prepared via cation exchange reactions from $Li_2CaTa_2O_7$. 4.0 g of $Li_2CaTa_2O_7$ was combined with 10-molar equivalents of anhydrous $FeCl_2$ (99.5%), $CoCl_2$ (99.7%) or $ZnCl_2$ (99.99%). The mixtures were ground in an agate pestle and mortar in an argon-filled glovebox, loaded into Pyrex tubes and sealed under vacuum. The samples were heated at a ramp rate of 2 °C/min to 350 °C, 360 °C and 400 °C, respectively, for two periods of 48 h, followed by cooling at 5 °C/min to room temperature. The reaction tube containing $ZnCl_2$ was placed vertically in a furnace because $ZnCl_2$ has a melting point of 290 °C. Between each heating cycle, the sample was washed with distilled water to remove any unreacted chloride and LiCl byproduct and then combined with fresh anhydrous chloride for the following cycle. The resulting samples of $FeCaTa_2O_7$, $CoCaTa_2O_7$ and $ZnCaTa_2O_7$ were brown, blue and off-white in colour, respectively.

3.3 Results

3.3.1 Optical SHG Measurements

The SHG signals of $ZnCaTa_2O_7$ and KDP (potassium dihydrogen phosphate) were investigated under incident laser radiation of 1064 nm. Powder SHG data collected from $ZnCaTa_2O_7$ indicates that the material is SHG active, with an activity that was 0.07 times that of KDP (Figure 3.1a). This observation reveals that $ZnCaTa_2O_7$ adopts a non-

centrosymmetric structure. The SHG signals of $FeCaTa_2O_7$ and $CoCaTa_2O_7$ and benchmark $AgGaS_2$ were investigated under incident laser radiation of 2090 nm. The second harmonic efficiencies of the $FeCaTa_2O_7$ and $CoCaTa_2O_7$ powders were compared to that of $AgGaS_2$ powder with the same particle size, with efficiencies that were approximately 0.4 and 0.7

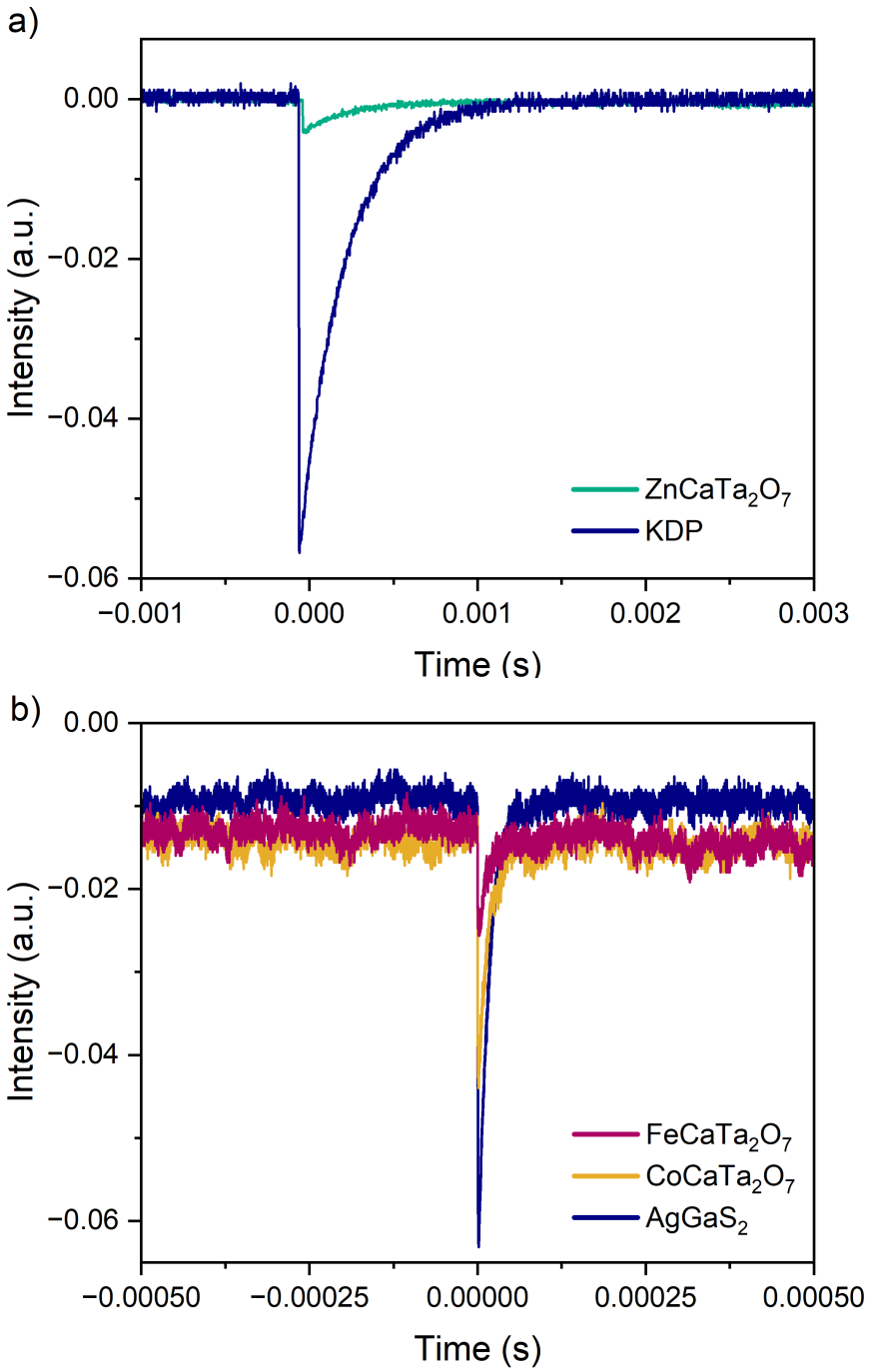


Figure 3.1 a) Plot of SHG intensity of $ZnCaTa_2O_7$ as a function of time under incident radiation of 1064 nm, compared to that of KDP standard. b) Plot of SHG intensity of $FeCaTa_2O_7$ and $CoCaTa_2O_7$ as a function of time under incident radiation of 2090 nm, compared to that of $AgGaS_2$ standard.

times that of the $AgGaS_2$ standard used for IR NLO measurements, respectively (Figure 3.1b). This indicates that both phases adopt non-centrosymmetric crystal structures.

3.3.2 Structural Characterisation of $ZnCaTa_2O_7$

3.3.2.1 Room temperature synchrotron X-ray diffraction data

Synchrotron X-ray diffraction data collected from $ZnCaTa_2O_7$ at room temperature could be indexed using a primitive orthorhombic unit cell (a = 5.38294(3) Å, b = 5.53804(4) Å, c = 19.76472(15) Å) consistent with a $\sim\sqrt{2} \times \sim\sqrt{2} \times 1$ geometric expansion of an undistorted n = 2 Ruddlesden-Popper unit cell. A Pawley fitting revealed that the sample was single-phase, indicating a successful cation exchange reaction had taken place (Figure 3.2).

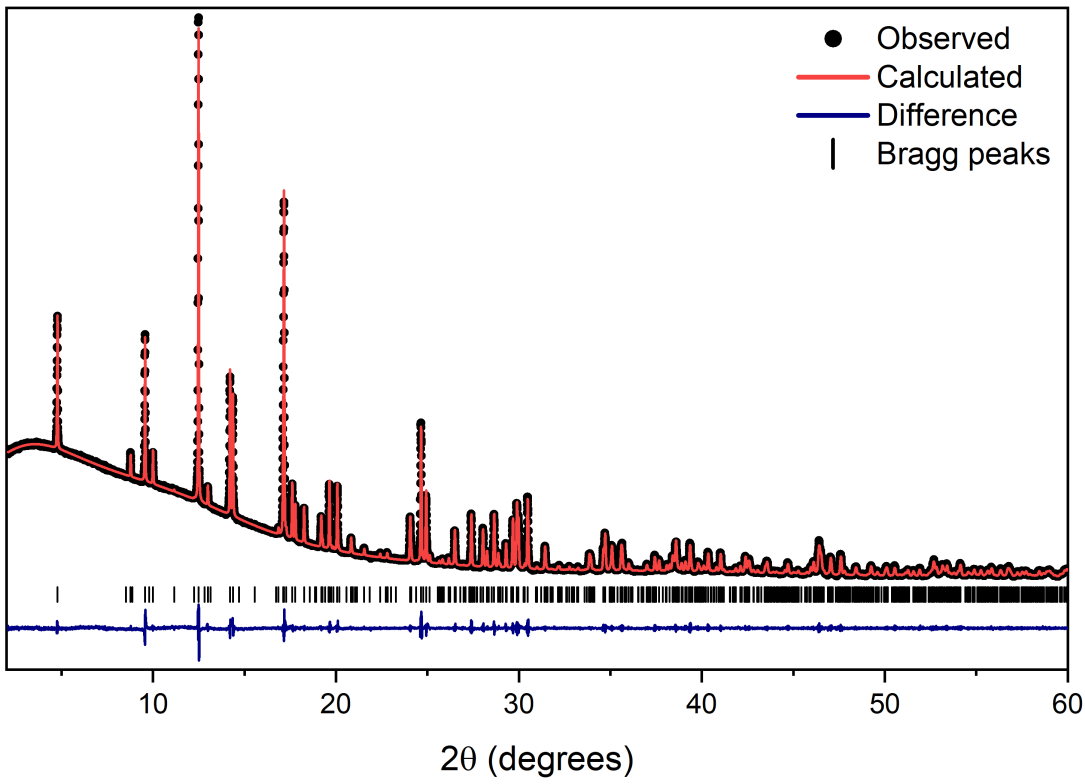


Figure 3.2 Observed, calculated and difference plots from the Pawley fitting of a primitive unit cell against SXRD data collected from $ZnCaTa_2O_7$ at room temperature.

3.3.2.2 100 K neutron powder diffraction data

Neutron powder diffraction data collected from $ZnCaTa_2O_7$ at 100 K could be indexed using a primitive orthorhombic unit cell (a = 5.38116(7) Å, b = 5.54170(7) Å, c = 19.78286(25) Å) consistent with a $\sim\sqrt{2} \times \sim\sqrt{2} \times 1$ geometric expansion of an undistorted n = 2 Ruddlesden-Popper unit cell. A detailed symmetry analysis of the aristotype n = 2 Ruddlesden-Popper structure was used to generate a series of chemically plausible structural models based on the tilting distortions of the Ta–O framework and to deduce their space groups. Close inspection of the diffraction data revealed four candidate structures described in space groups consistent with the observed reflection conditions: $a^-b^-c^0/-(b^-a^-)c^0$ (*Pccm)*, $a^-b^-c^+/b^-a^-c^+$ (*P*2$_1$*nm)*, $a^-b^-c^+/-(a^-b^-)c^+$ (*P*2*cm)*, and $a^-b^-c^-/-(a^-b^-)c^-$ (*P*2/*c)*. As noted above, $ZnCaTa_2O_7$ is SHG active and hence adopts a non-centrosymmetric crystal structure, so both *Pccm* and *P*2/*c* could be eliminated from the list of potential models. Full structural models were constructed for $ZnCaTa_2O_7$ with $a^-b^-c^+/b^-a^-c^+$ and $a^-b^-c^+/-(a^-b^-)c^+$ tilting distortions, described in space groups *P*2$_1$*nm* and *P*2*cm* respectively, and refined against the NPD data collected at 100 K. A markedly better fit to the observed data was achieved using the *P*2*cm* symmetry model compared to the *P*2$_1$*nm* model.

Since divalent Zn^{2+} cations are exchanged with monovalent Li^+ cations, the number of available coordination sites in the substituted phase is twice the number of transition metal cations present. Therefore, only half of the existing interlayer coordination sites between the perovskite double-layers of $ZnCaTa_2O_7$ will be occupied by Zn^{2+} cations, and as a result, Zn can adopt either an ordered or disordered arrangement across these sites. A fundamental difference between the *P*2*cm* and *P*2$_1$*nm* symmetry models is the possible ordering arrangements of the interlayer Zn^{2+} cations in each structure. The *P*2*cm* model has four

potential crystallographically distinct Zn coordination sites (2*a*, 2*a,* 2*b* and 2*b*). An ordering across half of these sites will result in a striped arrangement of the Zn cations, depicted in Figure 3.3. On the other hand, there are only two distinct Zn coordination sites (4*b*, 4*b*) in the $P2_1nm$ structure, and ordering of the interlayer cations will result in a chequerboard arrangement of the Zn cations.

During the initial refinement of the *P*2*cm* structural model against the neutron diffraction data, the Zn-site occupancies were constrained to each be 0.5, consistent with a disordered arrangement of the Zn cations across all four sites. The fit to the data was significantly improved when the total occupancy across Zn sites was constrained to 2.0 per unit cell, but the site occupancies were refined freely within this constraint. The occupancy of one 2*a* and one 2*b* site converged to 0.98 each, whilst the remaining 2*a* and 2*b* sites converged to an occupancy of 0.02. Fixing the occupancy of the 2*a* and 2*b* sites to unity did not change the

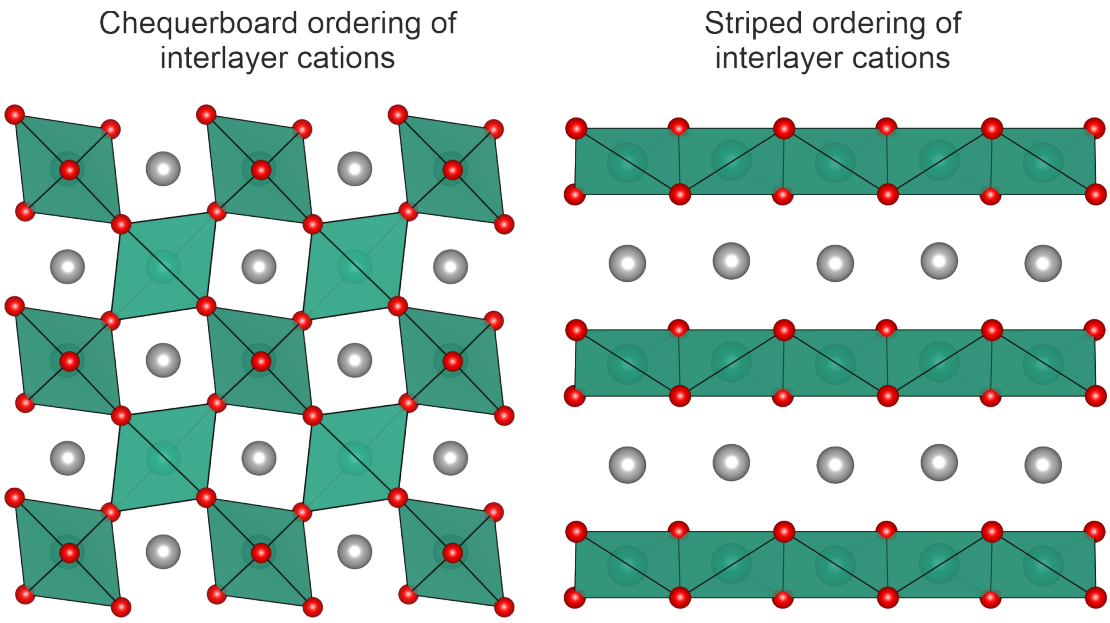


Figure 3.3 The two possible ordering schemes adopted by the interlayer cations in the $P2_1nm$ (left) and *P*2*cm* (right) Ruddlesden-Popper structure of *A*'$CaTa_2O_7$. Mint and red spheres represent *A*' and O, respectively. Grey spheres represent the positions of empty *A*'-sites.

fitting statistics, indicating that the Zn cations adopt an ordered arrangement within the *P*2*cm* structure. A similar approach was taken when refining the $P2_1nm$ model against the data, but in this case, when their site occupancy was allowed to refine freely, the Zn cations showed no preference for either site, instead maintaining a disordered arrangement across both sites. This observation can be used to rationalise the noticeably improved fitting statistics achieved by using the *P*2*cm* symmetry model, where the Zn cations are able to order correctly. In contrast, the Zn cations showed no preference to order when the $P2_1nm$ model was used since a better fit was achieved with a disordered arrangement over the sites compared to an incorrect chequerboard-ordered arrangement in the refinement. The observed, calculated and difference plots from the refinement of the ordered *P*2*cm* model of $ZnCaTa_2O_7$ against the bank 2 and bank 4 NPD data collected at 100 K are shown in Figure 3.4. Full details of the refined structure are given in Table 3.1. Selected bond lengths and bond valence sum values for the cations are reported in Table 3.2.

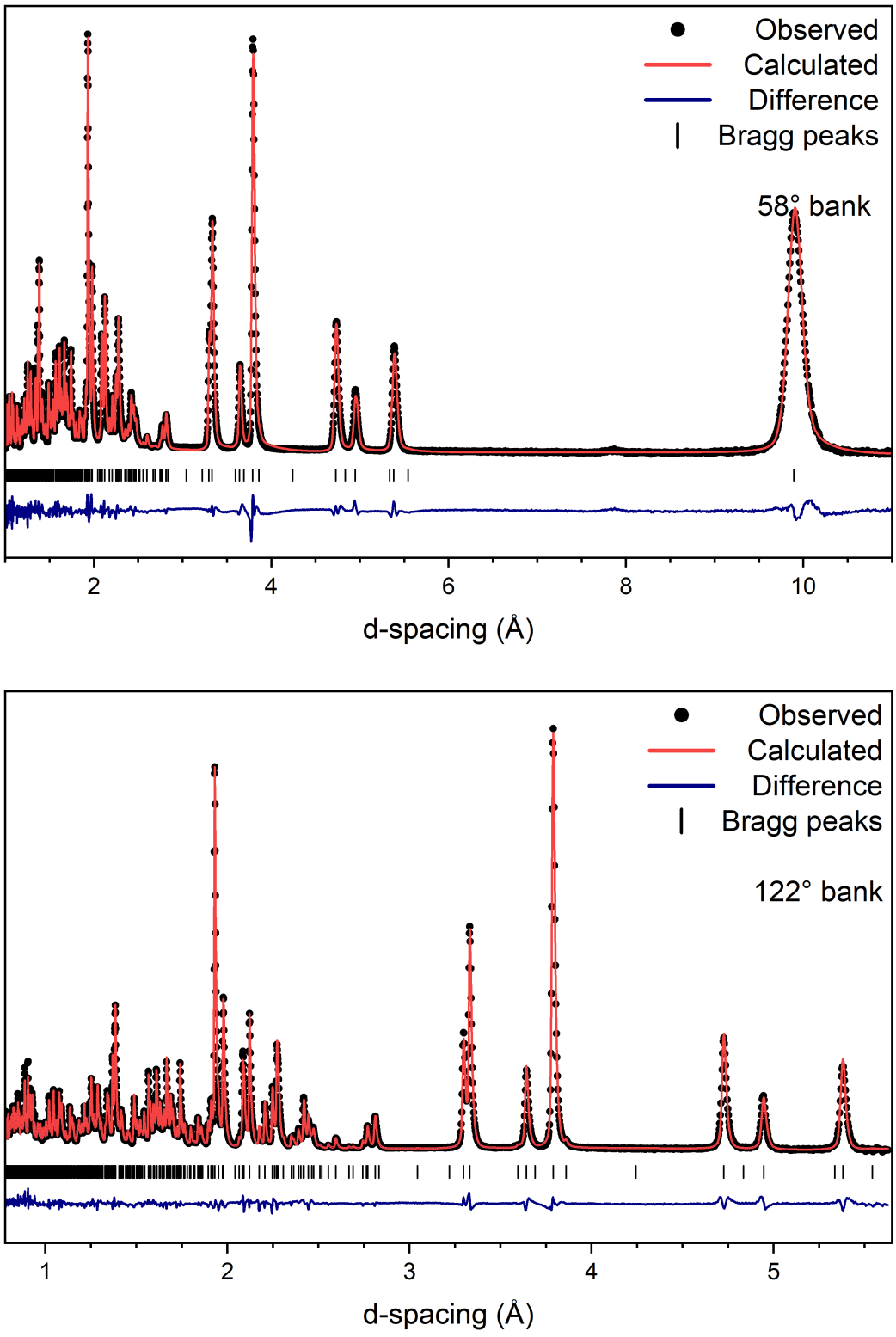


Figure 3.4 Observed, calculated and difference plots from the structural refinement of the ordered *P*2*cm* model of $ZnCaTa_2O_7$ against the NPD data collected from 2-9 (58°) and bank 4-7 (122°) of the WISH diffractometer at 100 K.

Table 3.1 Parameters from the structural refinement of the ordered *P*2*cm* model of $ZnCaTa_2O_7$ against the NPD data collected at 100 K.

Atom	Site	*x*	*y*	*z*	Occ.	B_{iso} / Å^2
Zn1	2*a*	0.9597(20)	0.00000	0.00000	1.0	0.39(14)
Zn2	2*b*	0.9720(20)	1/2	0.00000	1.0	0.92 (18)
Ca1	2*c*	0.1963(14)	0.2788(15)	1/4	1.0	0.29 (12)
Ca2	2*c*	0.7056(15)	0.7930(15)	1/4	1.0	0.98 (17)
Ta1	4*d*	0.2231(9)	0.7584(9)	0.1495(3)	1.0	0.34(75)
Ta2	4*d*	0.7143(9)	0.7480(9)	0.8541(2)	1.0	0.29 (78)
O1	2*c*	0.3003(12)	0.7363(17)	1/4	1.0	0.17 (11)
O2	2*c*	0.6583(13)	0.2192(18)	1/4	1.0	1.29 (17)
O3	4*d*	0.0100(12)	0.9667(8)	0.8293(3)	1.0	0.16 (72)
O4	4*d*	0.9468(14)	0.5069(9)	0.3268(3)	1.0	0.65(90)
O5	4*d*	0.5197(12)	0.9424(10)	0.3586(4)	1.0	0.22 (87)
O6	4*d*	0.4279(13)	0.5417(12)	0.8565(4)	1.0	1.02(11)
O7	4*d*	0.1290(9)	0.7541(14)	0.0552(4)	1.0	0.59 (10)
O8	4*d*	0.8019(10)	0.7468(15)	0.9470(4)	1.0	0.81(11)

$ZnCaTa_2O_7$ - Space group *P*2*cm* (#28)

a = 5.38116(7) Å, *b* = 5.54170(7) Å, *c* = 19.78286(25) Å

Volume = 589.940(13) Å^3

Formula weight = 579.36 g mol^{-1}, Z = 4

Radiation source: Neutron Time of Flight, Instrument: WISH

Temperature: 100 K

R_p = 4.01 % $_wR_p$ = 4.76 %

Table 3.2 Selected bond lengths and cation bond valence sums from the structural refinement of the *P*2*cm* model of $ZnCaTa_2O_7$ against the NPD data collected at 100 K.

Cation	Anion	Bond length	BVS
Zn1	O8 × 2	1.945(9)	+ 2.014
	O7 × 2	1.971(9)	
Zn2	O8 × 2	1.950(10)	+ 1.995
	O7 × 2	1.973(9)	
Ca1	O3 × 2	2.306(9)	+ 2.172
	O4 × 2	2.391(9)	
	O2 × 1	2.508(11)	
	O1 × 1	2.597(13)	
	O6 × 2	2.644(9)	
Ca2	O1 × 1	2.204(11)	+ 2.064
	O2 × 1	2.376(13)	
	O5 × 2	2.510(9)	
	O4 × 2	2.552(9)	
	O3 × 2	2.630(9)	
Ta1	O5 × 1	1.901(8)	+ 5.114
	O7 × 1	1.931(9)	
	O3 × 1	1.951(8)	
	O6 × 1	1.999(9)	
	O1 × 1	1.035(5)	
	O4 × 1	2.090(9)	
Ta2	O8 × 1	1.899(9)	+ 5.047
	O6 × 1	1.920(9)	
	O4 × 1	1.963(8)	
	O5 × 1	2.012(8)	
	O3 × 1	2.059(8)	
	O2 × 1	2.089(5)	

As a final step, both the ordered and disordered *P*2*cm* models were refined against the room-temperature synchrotron X-ray diffraction data. Ordering of the Zn cations vastly improved both the visual fit to the data as well as the fitting statistics. A comparison of the fit of the disordered and ordered models is shown in Figure 3.5, where arrows indicate peaks corresponding to the ordering of Zn^{2+} cations. The intensity of these peaks is only accounted for when the ordering of the zinc cations is introduced to the refinement.

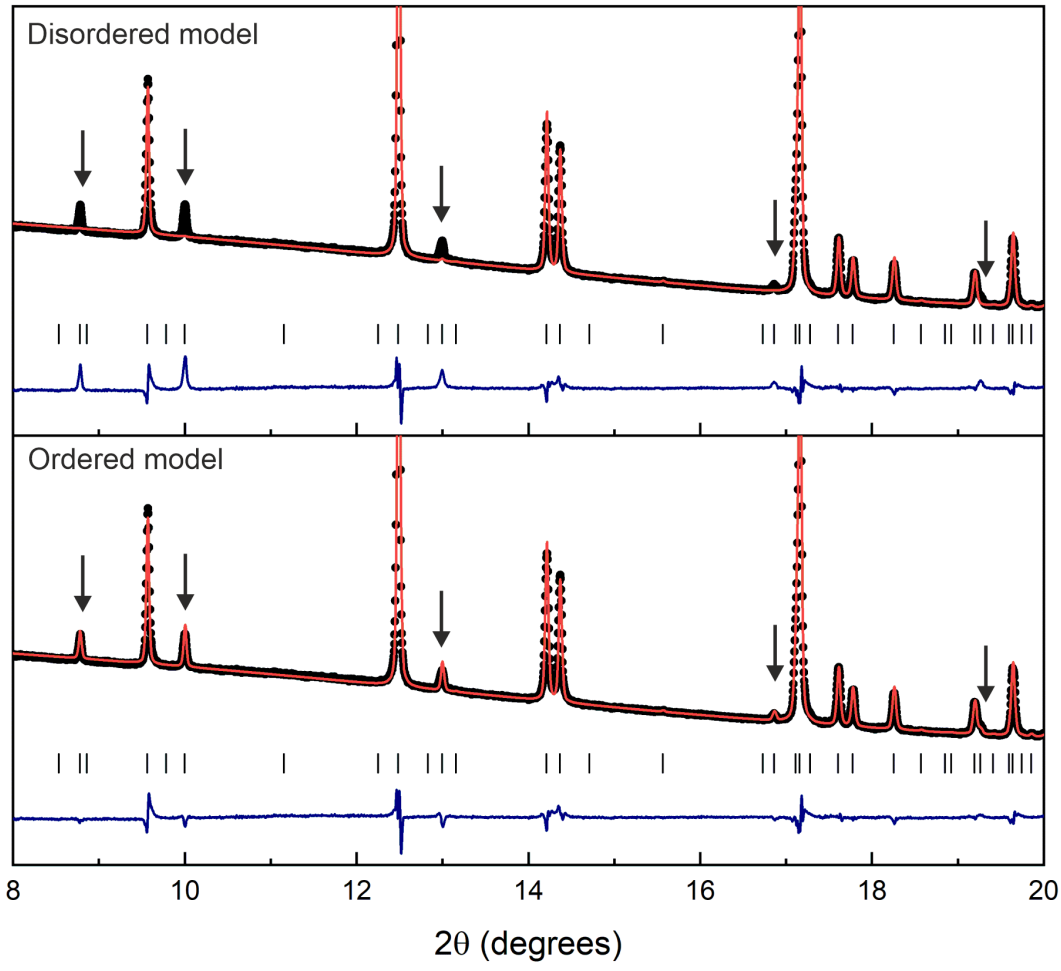


Figure 3.5 A comparison between the refinements of the disordered (top) and ordered (bottom) Zn-site *P*2*cm* models against SXRD data collected from $ZnCaTa_2O_7$ at room temperature. Black arrows indicate peaks which correspond to the ordering of Zn^{2+} ions.

3.3.3 Characterisation of $FeCaTa_2O_7$

3.3.3.1 Room temperature synchrotron X-ray diffraction data

Synchrotron X-ray diffraction data collected from $FeCaTa_2O_7$ at room temperature could be initially indexed using an almost metrically tetragonal, primitive unit cell (a = 5.51498(9) Å, b = 5.51392(9) Å, c = 18.658278(74) Å), consistent with a $\sqrt{2} \times \sqrt{2} \times 1$ geometric expansion of an undistorted n = 2 Ruddlesden-Popper unit cell. A Pawley fitting revealed that the sample is single-phase, indicating a successful cation exchange reaction had taken place (Figure 3.6).

3.3.3.2 200 K neutron powder diffraction data

Neutron powder diffraction data collected from $FeCaTa_2O_7$ at 200 K could be initially indexed using a similar, almost metrically tetragonal unit cell, consistent with a

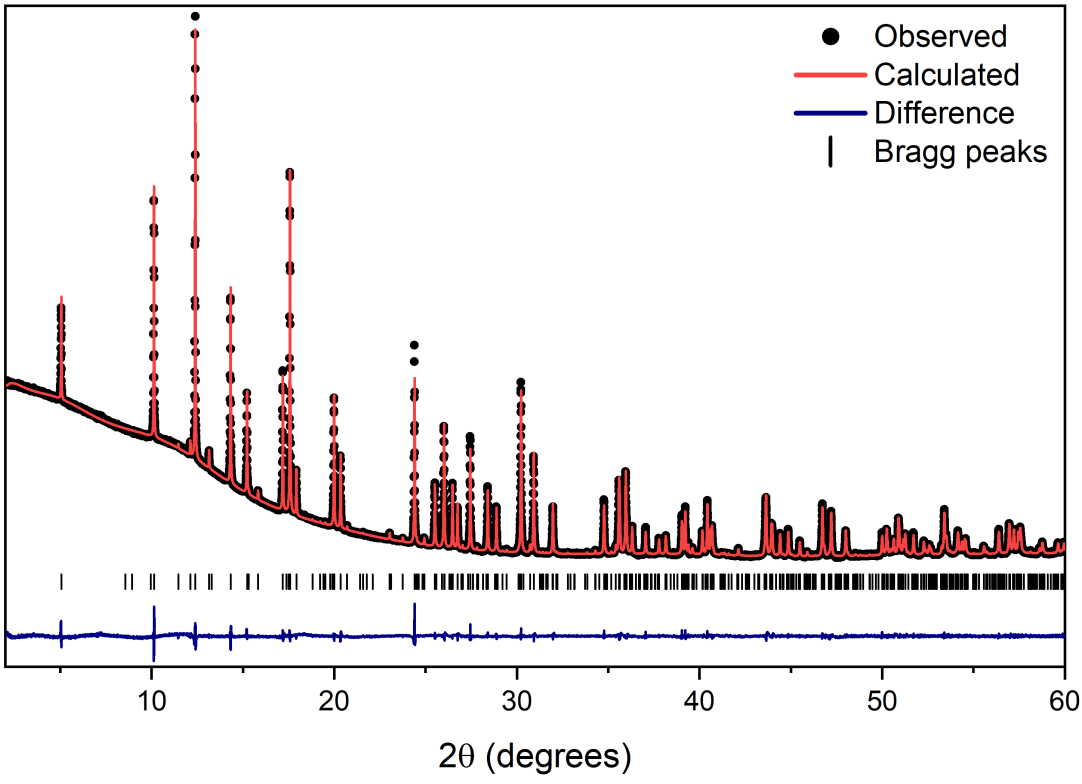


Figure 3.6 Observed, calculated and difference plots from the Pawley fitting of a primitive unit cell against SXRD data collected from $FeCaTa_2O_7$ at room temperature.

$\sqrt{2} \times \sqrt{2} \times 1$ geometric expansion of an undistorted n = 2 Ruddlesden-Popper unit cell. Systematic absences indicated that a primitive unit cell was necessary to index all the peaks of the diffraction pattern. Symmetry analysis revealed only two tilting distortions were consistent with a tetragonal unit cell: $a^-b^0c^0/b^0a^-c^0$ described in space group $P4_2/mnm$ and $a^-b^0c^0/b^0{-}a^-c^0$ described in space group $P4_2/mcm$. The $P4_2/mcm$ model could be eliminated based on extinction conditions of the diffraction data. Refinement of the $a^-b^0c^0/b^0a^-c^0$ structural model against the NPD data gave a reasonable fit. As noted above, powder second harmonic generation measurements revealed that $FeCaTa_2O_7$ is SHG active and, therefore, adopts a non-centrosymmetric crystal structure. Since the $P4_2/mnm$ space group is centrosymmetric, it cannot be the correct symmetry.

There remained a possibility that $FeCaTa_2O_7$ crystallises in an orthorhombic space group but with metrically tetragonal lattice parameters since this is commonly observed in similar cation-exchanged phases.[54] To explore this possibility, the symmetry of the $P4_2/mnm$ structural model was lowered to an orthorhombic lattice. The $P4_2/mnm$ space group is consistent with an $a^-b^0c^0/a^0b^-c^0$ tilting scheme. Lowering the crystal symmetry from tetragonal to orthorhombic indicates a more complex tilting pattern is adopted. Further symmetry analysis indicates $a^-b^-c^0/b^-a^-c^0$ (*Pnnm)*, $a^-b^-c^+/b^-a^-c^+$ ($P2_1nm$), $a^-b^-c^+/-(a^-b^-)c^+$ (*P2cm)*, $a^-b^-c^-/b^-a^-c^-$ ($P2_1/c$) and $a^-b^-c^-/-(a^-b^-)c^-$ (*P2/c)* are consistent with the observed reflection conditions. The *Pnnm*, $P2_1/c$ and *P2/c* structural models could be eliminated since they are centrosymmetric. Structural models were constructed based on $P2_1nm$ and *P2cm* and refined against the NPD data collected at 200 K. Refinement of the $P2_1nm$ model against the NPD data considerably improved the fitting statistics compared to the *P2cm* model.

A $P4_2/mnm$ structural model ($a^-b^0c^0/b^0a^-c^0$) can be used to describe a special case of the $P2_1nm$ structural model ($a^-b^-c^+/b^-a^-c^+$) where the magnitude of the tilting along the *b* and *c* direction is zero. To ensure that the improvement of the fit on changing from a tetragonal to an orthorhombic model was not simply an artifact of the increased number of refinable parameters, the magnitude of the tilts along each direction were measured. The *a* tilt is of a significant magnitude (20.3(4)°), whilst the *b* and *c* tilts are considerably smaller (2.1(4)° and 5.7(8)°, respectively). Although these rotations are small, they are larger than the calculated errors. This suggests that the rotations are real and that $FeCaTa_2O_7$ does indeed adopt a $P2_1nm$ structure at 100 K.

Fe^{2+} cations occupy half of the available pseudo-tetrahedral sites within the interlayer region of the layered perovskite structure to satisfy the stoichiometry of the phase. In the $P2_1nm$ model, there are two crystallographically distinct 4*b* sites. During initial refinements, the occupancies of the Fe-sites were constrained to be 0.5, such that the Fe^{2+} cations were disordered across both sites. A visual inspection of the fitting showed that this model did not correctly account for the intensity of some reflections. Refinement of the Fe-site occupancies within the constraint of the total occupancy across both sites being equal to one visibly improves the refinement and fitting statistics, where the occupancy of one 4*b* site converges to 1.0, whilst the other site converges to 0.0. This indicates that the Fe-cations adopt an ordered chequerboard arrangement within the interlayer region, in contrast to the striped arrangement adopted by the Zn^{2+} cations in $ZnCaTa_2O_7$. The observed, calculated and difference plots of the refinement of the ordered $P2_1nm$ model of $FeCaTa_2O_7$ against the bank 2 and bank 4 NPD data collected at 200 K are shown in Figure 3.7. Full details of the refined structure are given in Table 3.3. Selected bond lengths and bond valence sum values for the cations are reported in Table 3.4.

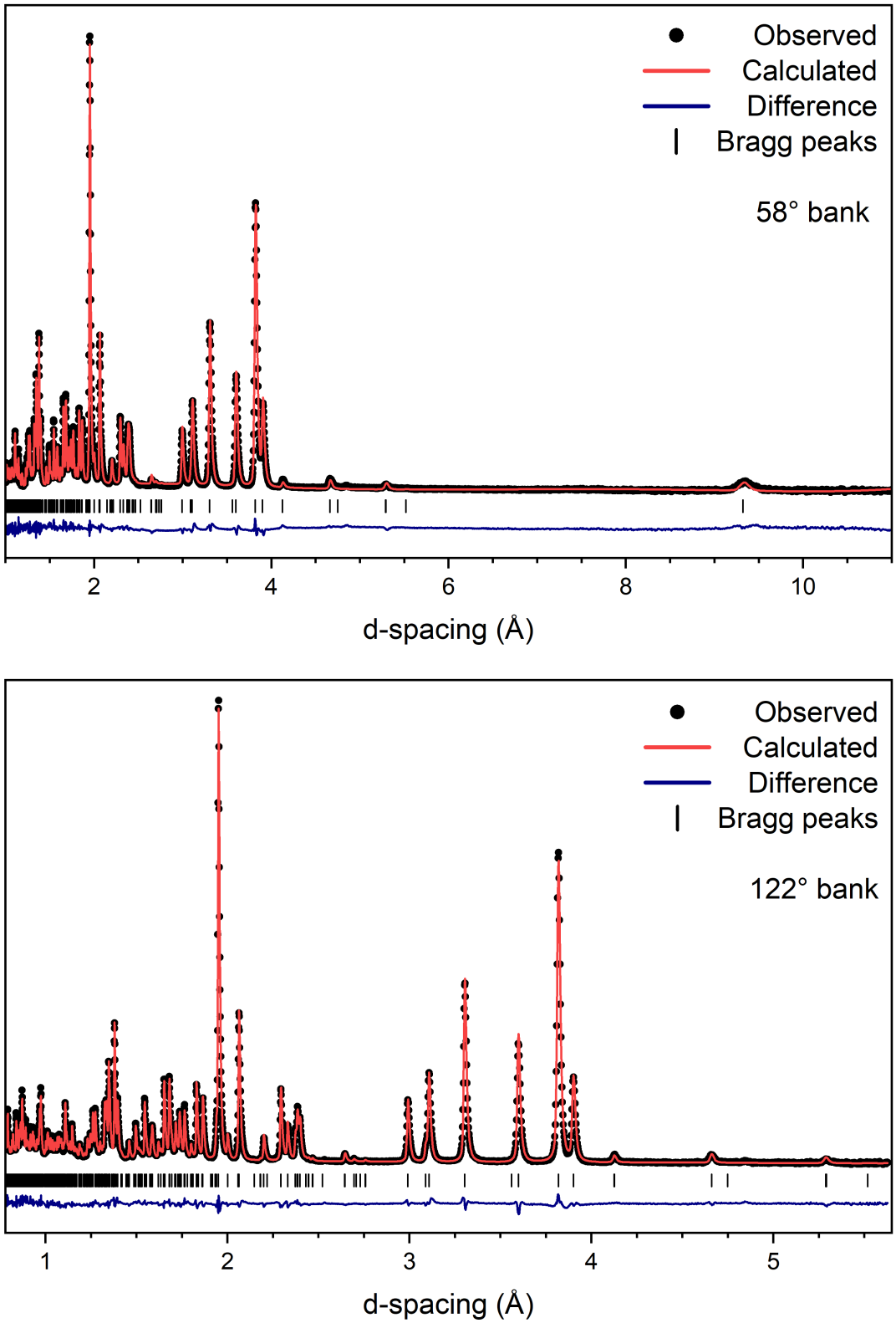


Figure 3.7 Observed, calculated and difference plots from the structural refinement of the *P*2$_1$*nm* model of $FeCaTa_2O_7$ against the NPD data collected from bank 2-9 (58°) and bank 4-7 (122°) of the WISH diffractometer at 200 K.

Table 3.3 Parameters from the structural refinement of the ordered $P2_1nm$ model of $FeCaTa_2O_7$ against the NPD data collected at 200 K.

Atom	Site	*x*	*y*	*z*	Occ.	B_{iso} / Å^2
Fe1	4*b*	0.7615(20)	0.7459(14)	0.26281(8)	1.0	1.79(4)
Ca1	2*a*	0.0575(16)	0.0152(16)	0.00000	1.0	0.47(6)
Ca2	2*a*	0.5259(20)	0.5091(17)	0.00000	1.0	0.47(6)
Ta1	4*b*	0.0188(11)	0.5062(10)	0.89383(38)	1.0	0.19(11)
Ta2	4*b*	0.5217(10)	0.0027(10)	0.10921(38)	1.0	0.38(12)
O1	2*a*	0.0547(19)	0.4303(14)	0.00000	1.0	0.29(17)
O2	2*a*	0.4527(19)	0.0612(16)	0.00000	1.0	0.65(19)
O3	4*b*	0.2645(24)	0.7385(13)	0.59064(21)	1.0	0.16(7)
O4	4*b*	0.2544(20)	0.2598(15)	0.42000(9)	1.0	0.39(5)
O5	4*b*	0.2738(20)	0.2521(15)	0.12419(11)	1.0	0.36(5)
O6	4*b*	0.2582(27)	0.7666(15)	0.90467(24)	1.0	0.88(9)
O7	4*b*	0.9838(9)	0.5371(14)	0.79443(49)	1.0	0.49(13)
O8	4*b*	0.5405(15)	0.0357(16)	0.20819(16)	1.0	1.06(15)

$FeCaTa_2O_7$ - Space group $P2_1nm$ (#31)

a = 5.5143(1) Å, b = 5.5187(1) Å, c = 18.64255(18) Å

volume = 567.333(18) Å^3

Formula weight = 569.81 g mol^{-1}, Z = 4

Radiation source: Neutron Time of Flight, Instrument: WISH

Temperature: 200 K

R_p = 4.25 % $_wR_p$ = 4.93 %

Table 3.4 Selected bond lengths and cation bond valence sums from the structural refinement of the ordered $P2_1nm$ model of $FeCaTa_2O_7$ against the NPD data collected at 200 K.

Cation	Anion	Bond length	BVS
Fe1	O7 × 1	1.988(12)	+ 1.817
	O8 × 1	2.006(13)	
	O5 × 1	2.103(3)	
	O7 × 1	2.254(12)	
	O8 × 1	2.291(12)	
Ca1	O2 × 1	2.136(15)	+ 2.045
	O1 × 1	2.304(14)	
	O6 × 2	2.473(12)	
	O4 × 2	2.725(13)	
	O3 × 2	2.748(15)	
Ca2	O4 × 2	2.367(11)	+ 1.796
	O2 × 1	2.479(13)	
	O3 × 2	2.537(13)	
	O1 × 1	2.618(15)	
	O6 × 2	2.713(13)	
Ta1	O7 × 1	1.862(15)	+ 5.227
	O3 × 1	1.960(15)	
	O6 × 1	1.970(15)	
	O4 × 1	2.006(13)	
	O5 × 1	2.012(13)	
	O1 × 1	2.045(8)	
Ta2	O8 × 1	1.856(15)	+ 5.199
	O6 × 1	1.960(15)	
	O4 × 1	1.985(12)	
	O5 × 1	1.987(12)	
	O3 × 1	1.998(15)	
	O2 × 1	2.090(8)	

3.3.3.3 Magnetisation data

Magnetisation data were collected from $FeCaTa_2O_7$ in an applied field of 100 Oe in the temperature range $5 \leq T/K \leq 300$ K. The zero-field-cooled (ZFC) and field-cooled (FC) data, shown in Figure 3.8, can be fit to the Curie-Weiss law in the region $100 \leq T/K \leq 300$ K, yielding a Curie constant of $C = 4.21$ cm^3 K mol^{-1} and a Weiss constant of $\theta_{CW} = -107.27$ K. The Curie constant was used to calculate the effective magnetic moment, $\mu_{eff} = 5.80$ μ_B, which can be directly compared to the calculated moment for Fe^{2+} (4.90 μ_B), and is notably higher than the spin-only moment expected for a single tetrahedral Fe^{2+} (S=2) ion per formula unit. The observed moment exceeds the calculated, implying a second-order spin-orbit coupling effect and an incomplete quenching of the orbital angular momentum. This behaviour is characteristic of tetrahedrally coordinated Fe^{2+} cations, attributed to low-lying

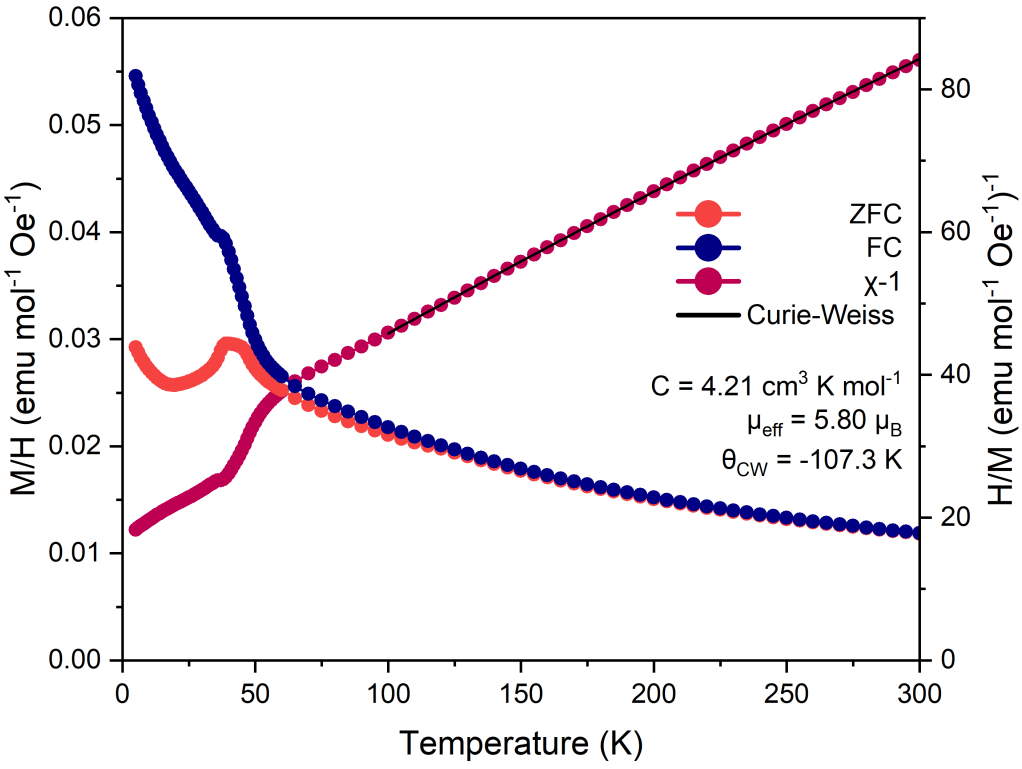


Figure 3.8 Zero-field-cooled and field-cooled magnetisation data collected from $FeCaTa_2O_7$ as a function of temperature in an applied field of 100 Oe.

excited states that can mix with the ground state. The excitation of an electron from an *e* orbital to t_2 orbital produces a *T* state, which can mix with the ground state and contributes to orbital angular momentum. However, the observed magnetic moment of the material exceeds predictions, even after accounting for second order spin-orbit coupling effects. The negative value of the Weiss constant is indicative of the onset of antiferromagnetic ordering. The ZFC and FC data sharply diverge at approximately T_N = 38 K (antiferromagnetic in character), but show a deviation before this temperature, which suggests the possible onset of 2D magnetic ordering before the eventual onset of 3D ordering. The magnetisation-field isotherm collected at 300 K is linear and passes through the origin, with data collected at 5 K exhibiting very weak hysteresis that is shifted above the origin (Figure 3.9). This suggests that the Fe^{2+} ions adopt a canted antiferromagnetic arrangement below the transition temperature, but is also indicative of some spin glass behaviour. This is consistent with the

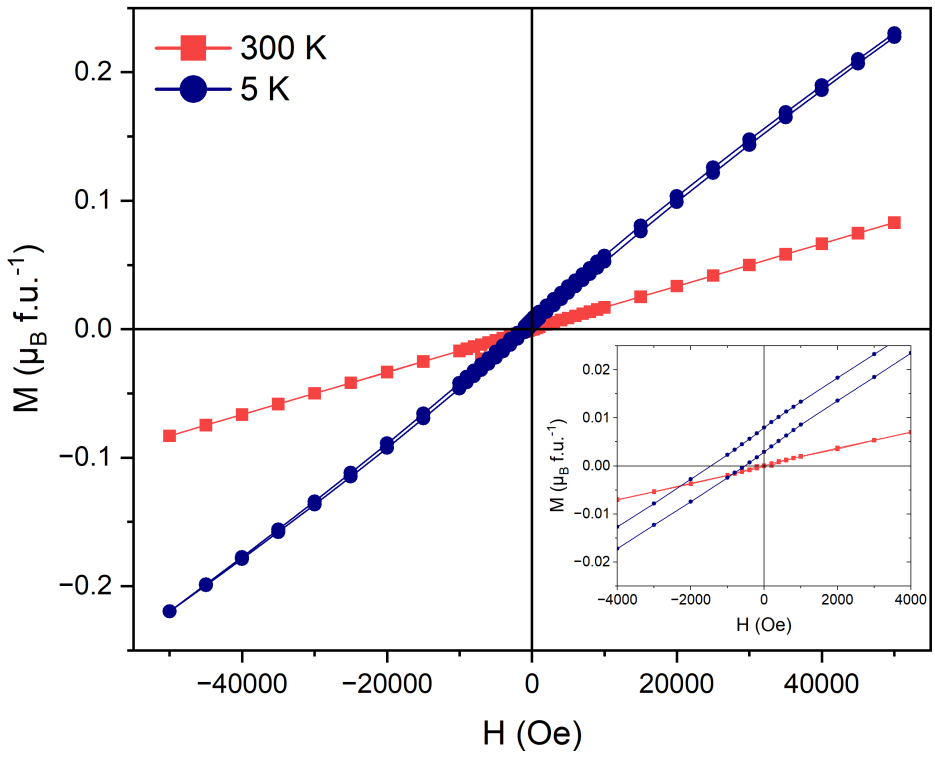


Figure 3.9 Magnetisation-field data collected from $FeCaTa_2O_7$ at 300 K and 5 K. The inset shows an expanded view of the origin.

small divergence of the ZFC and FC data above the magnetic ordering temperature, since some local magnetic domains may persist. To investigate this glassy behaviour further, AC susceptibility measurements were performed around the magnetic transition temperature. Figure 3.10 demonstrates that there is no strong frequency dependence to the data.

3.3.3.4 Low temperature (1.5 K) neutron powder diffraction data

Neutron powder diffraction data collected from $FeCaTa_2O_7$ at 1.5 K exhibit a series of additional diffraction peaks not present in the data collected at 100 K, which can be attributed to magnetic order in the phase. These additional diffraction features can be indexed using a single magnetic propagation vector (**k** = 0, 0, 0) of the crystallographic unit cell. A series of possible magnetic models were constructed based on the ordered $P2_1nm$ symmetry crystal structure using the ISODISTORT software package and were refined against the 1.5 K neutron diffraction data. The best fit was obtained by using a $P2_1n'm'$

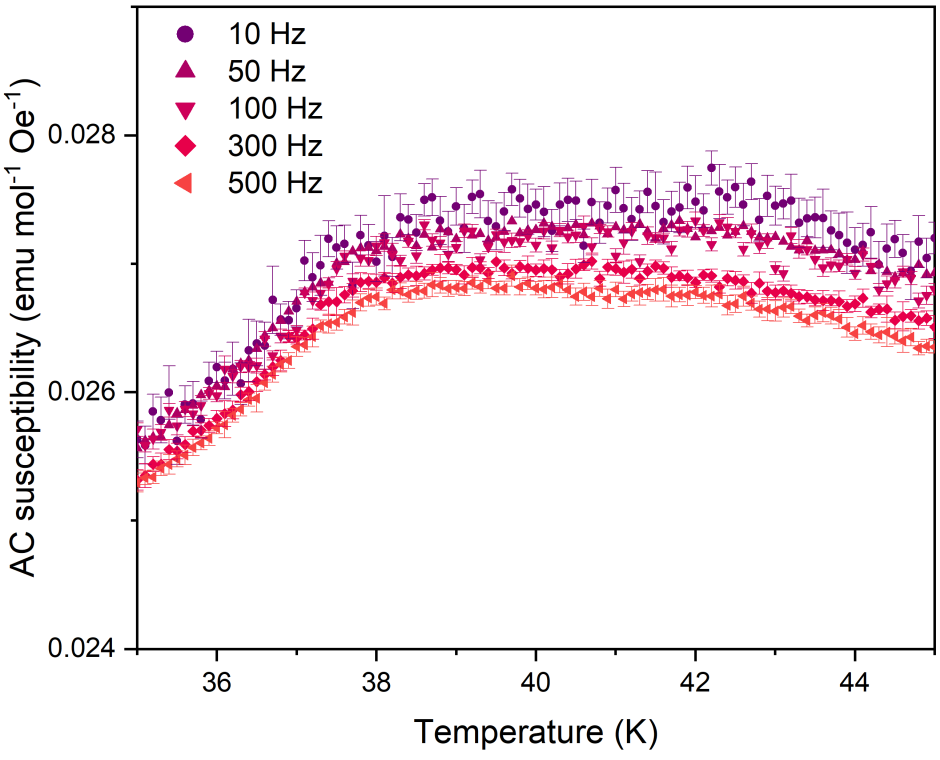


Figure 3.10 AC susceptibility data collected from $FeCaTa_2O_7$, showing the frequency dependence of the magnetic transition temperature, T_N, from 10 Hz to 500 Hz.

symmetry magnetic model, which can be constructed by applying the mΓ2 distortion mode to the $P2_1nm$ crystallographic structure. This mode permits the magnetic moment to have components in the *x*-, *y*- and *z*-directions, and so these three parameters were allowed to refine freely. Both the ordered moments along the *x*- and *y*-directions converged to zero within error and henceforth were constrained to be zero in the refinement. The moment along the *z*-direction refined to a value of 3.09(1) μ_B, approximately 75% of the spin-only moment expected for a single S=2 tetrahedral Fe^{2+} cation. This discrepancy could be understood by observing that a significant proportion of the additional scattering is not accounted for by the magnetic model, particularly around the magnetic diffraction peak at a *d*-spacing of 5.3 Å. This additional scattering is most clearly seen in the bank 2 data, shown in Figure 3.11. The observed, calculated, and difference plots of the refinement of the ordered $P2_1n'm'$ magnetic model of $FeCaTa_2O_7$ against the bank 2 and bank 4 NPD data collected at 1.5 K are shown in Figure 3.12. Full details of the refined structure are given in Table 3.5. Selected bond lengths and bond valence sum values for the cations are reported in Table 3.6.

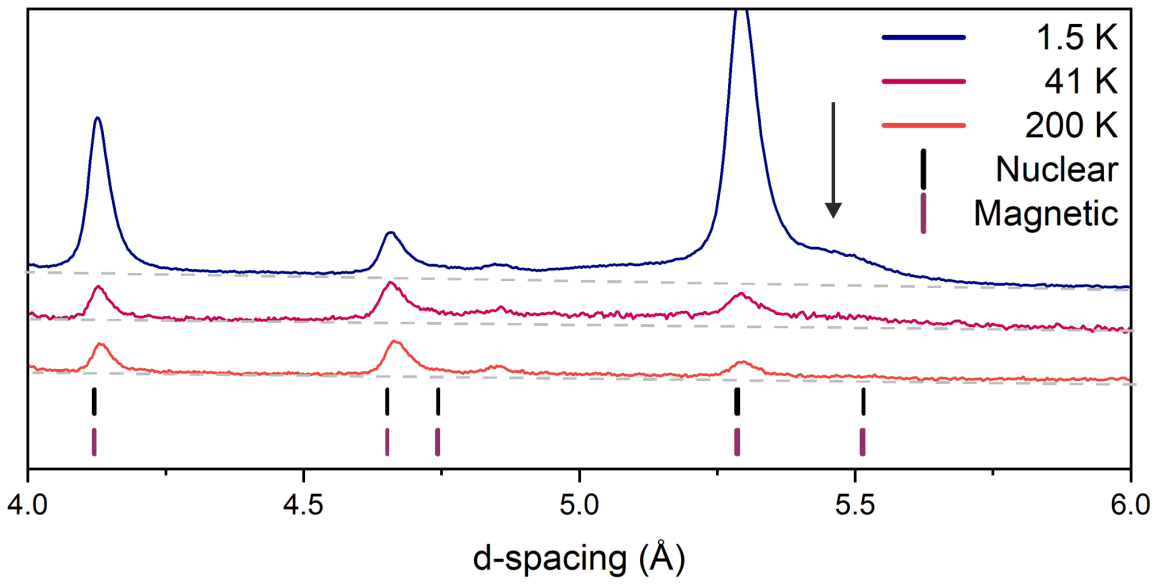


Figure 3.11 NPD data collected from $FeCaTa_2O_7$ at 1.5 K, 41 K and 200 K, where additional magnetic scattering can be seen below the magnetic diffraction peak at 5.3 Å, labelled with an arrow. Grey lines are used to guide the reader's eye.

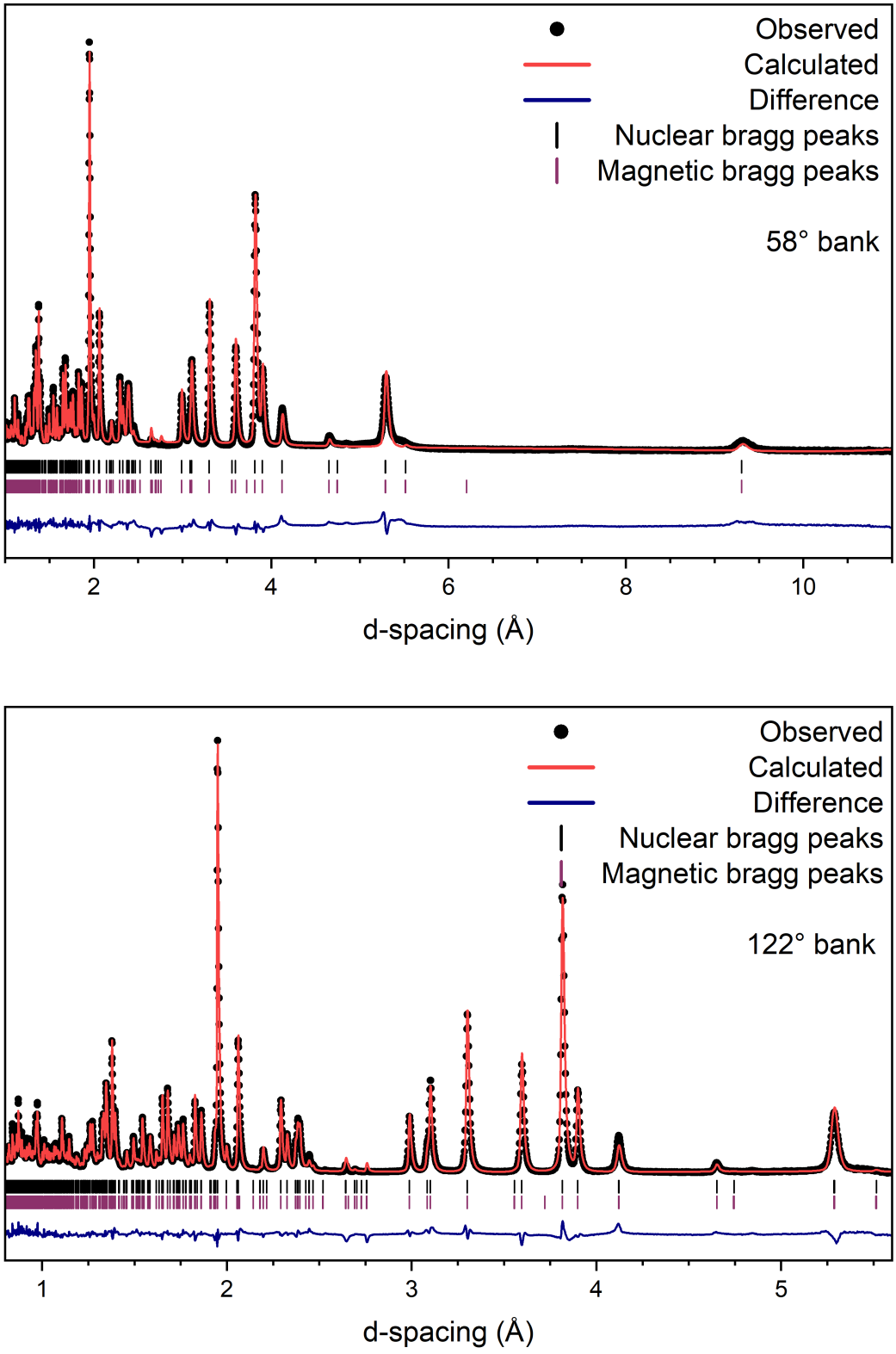


Figure 3.12 Observed, calculated and difference plots from the structural refinement of the magnetically ordered $P2_1n'm'$ model of $FeCaTa_2O_7$ against the NPD data collected from bank 2-9 (58°) and bank 4-7 (122°) of the WISH diffractometer at 1.5 K.

Table 3.5 Parameters from the structural refinement of the magnetically ordered $P2_1n'm'$ model of $FeCaTa_2O_7$ against the NPD data collected at 1.5 K.

Atom	Site	*x*	*y*	*z*	Occ.	B_{iso} / Å^2
Fe1	4*b*	0.8077(19)	0.7414(11)	0.26353(9)	1.0	1.80(4)
		$M_x = 0$	$M_y = 0$	$M_z = 3.08(1)$		
Ca1	2*a*	0.1106(35)	0.0073(19)	0.00000	1.0	0.56(7)
Ca2	2*a*	0.5682(35)	0.5074(21)	0.00000	1.0	0.56(7)
Ta1	4*b*	0.0586(30)	0.5091(11)	0.89530(24)	1.0	0.24(7)
Ta2	4*b*	0.5668(30)	0.9980(11)	0.11081(24)	1.0	0.39(9)
O1	2*a*	0.0939(33)	0.4371(12)	0.00000	1.0	0.12(9)
O2	2*a*	0.4919(34)	0.0706(14)	0.00000	1.0	0.40(14)
O3	4*b*	0.3218(31)	0.7381(12)	0.59201(19)	1.0	0.48(13)
O4	4*b*	0.2967(29)	0.2636(14)	0.42059(9)	1.0	0.14(9)
O5	4*b*	0.3308(30)	0.2548(14)	0.12481(10)	1.0	0.53(6)
O6	4*b*	0.3055(31)	0.7687(11)	0.90698(18)	1.0	0.39(7)
O7	4*b*	0.0274(32)	0.5298(14)	0.79425(39)	1.0	0.46(9)
O8	4*b*	0.5851(31)	0.9687(16)	0.20993(41)	1.0	1.33(11)

$FeCaTa_2O_7$ - Space group $P2_1n'm'$ (#31.127)

a = 5.51195(9) Å, b = 5.51556(9) Å, c = 18.60627(19) Å

volume = 565.658(15) Å^3

Formula weight = 569.81 g mol^{-1}, Z = 4

Radiation source: Neutron Time of Flight, Instrument: WISH

Temperature: 1.5 K

R_p = 5.82 % $_wR_p$ = 6.16 %

Table 3.6 Selected bond lengths and cation bond valence sums from the structural refinement of the magnetically ordered $P2_1n'm'$ model of $FeCaTa_2O_7$ against the NPD data collected at 1.5 K.

Cation	Anion	Bond length	BVS
Fe1	O7 × 1	1.986(14)	+ 1.840
	O8 × 1	2.037(14)	
	O5 × 1	2.085(3)	
	O7 × 1	2.194(16)	
	O8 × 1	2.299(15)	
Ca1	O2 × 1	2.15(3)	+ 2.095
	O1 × 1	2.365 (14)	
	O6 × 2	2.389(14)	
	O4 × 2	2.70(2)	
	O3 × 2	2.768(18)	
Ca2	O4 × 2	2.372(15)	+ 1.780
	O2 × 1	2.447(13)	
	O1 × 1	2.56(3)	
	O3 × 2	2.611(15)	
	O6 × 2	2.686(15)	
Ta1	O7 × 1	1.855(10)	+ 5.378
	O3 × 1	1.915(18)	
	O6 × 1	1.937(18)	
	O4 × 1	1.979(19)	
	O1 × 1	2.051(7)	
	O5 × 1	2.074(18)	
Ta2	O8 × 1	1.875(11)	+ 5.057
	O5 × 1	1.951(18)	
	O6 × 1	1.993(19)	
	O4 × 1	1.994(17)	
	O3 × 1	2.035(19)	
	O2 × 1	2.089(8)	

The refined magnetic model shows that the Fe cations adopt a G-type antiferromagnetic arrangement with moments orientated along the *z*-direction (Figure 3.13). It is important to note at this stage that although the moments along the *x*- and *y*- directions refined to a value of zero, a ferromagnetic alignment (canting) along *x* is allowed by symmetry in the $P2_1n'm'$ magnetic space group. Further symmetry analysis confirms that there are no possible centrosymmetric space groups which permit both a G-type antiferromagnetic arrangement and a canting of the Fe^{2+} magnetic moments by symmetry. This is significant because it confirms that the choice of space group is correct, as will be further discussed in Section 3.4.

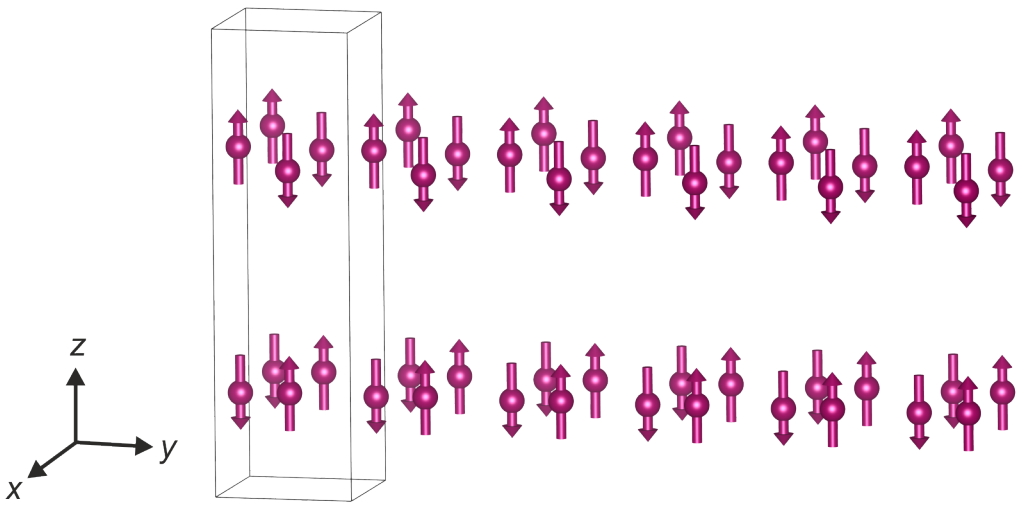


Figure 3.13 The G-type antiferromagnetic arrangement of Fe^{2+} ions adopted by $FeCaTa_2O_7$.

3.3.3.5 Variable temperature neutron powder diffraction data

Neutron powder diffraction data was collected from $FeCaTa_2O_7$ at 1.5 K, 5 K, 10 K, 20 K, 30 K to 50 K at 1 K temperature increments, 60 K, 150 K and 200 K. A magnetically ordered *P*21*n*'*m*' model was sequentially refined against the data collected at each temperature, where the output file from the first refinement became the input file for the next. After the first refinement, all variables were turned off and only the lattice parameters and the magnetic moment along the *z*-direction were allowed to freely vary in subsequent refinements. Figure 3.14 illustrates the evolution of the neutron powder diffraction data as a function of temperature. The intensity of the magnetic Bragg peaks, indicated by white arrows, decreases as the temperature increases, until 41 K, after which the intensity no longer changes. This is clearer in Figure 3.15, where it can be seen that the magnetic diffraction peaks appear to sit on top of nuclear diffraction peaks.

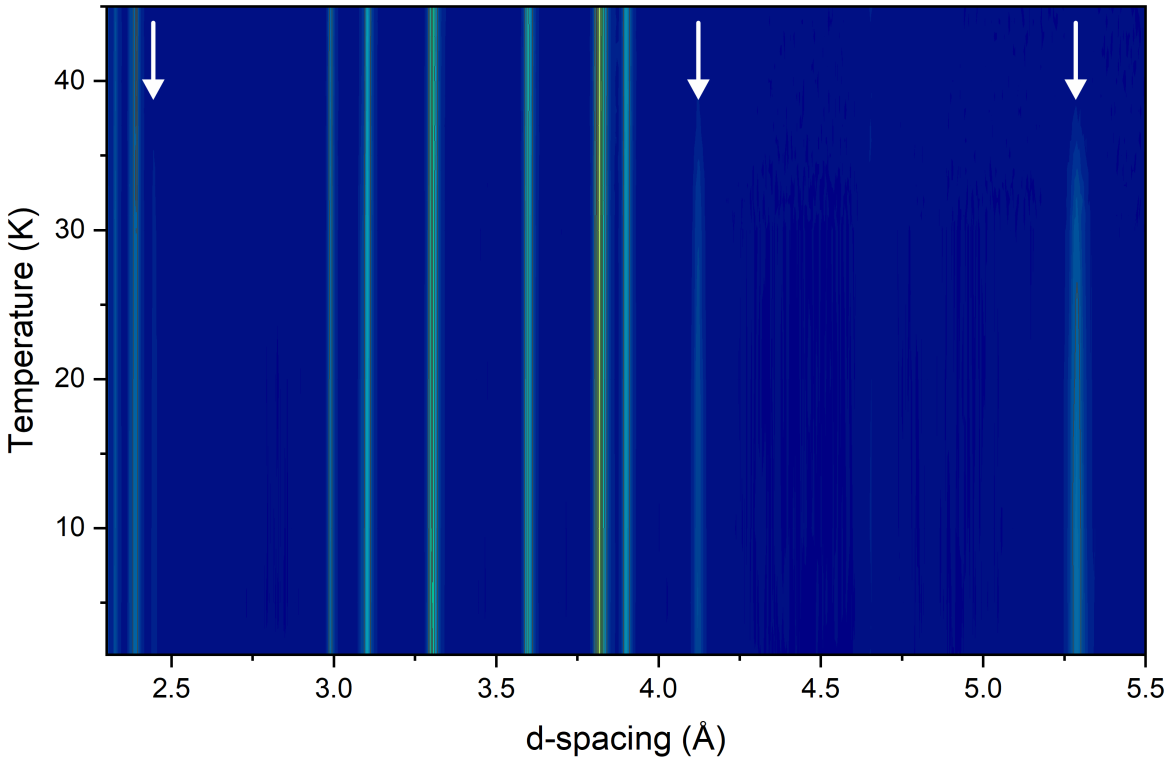


Figure 3.14 Evolution of the intensity of the neutron diffraction data collected from $FeCaTa_2O_7$ as a function of temperature. Magnetic peaks are labelled with arrows.

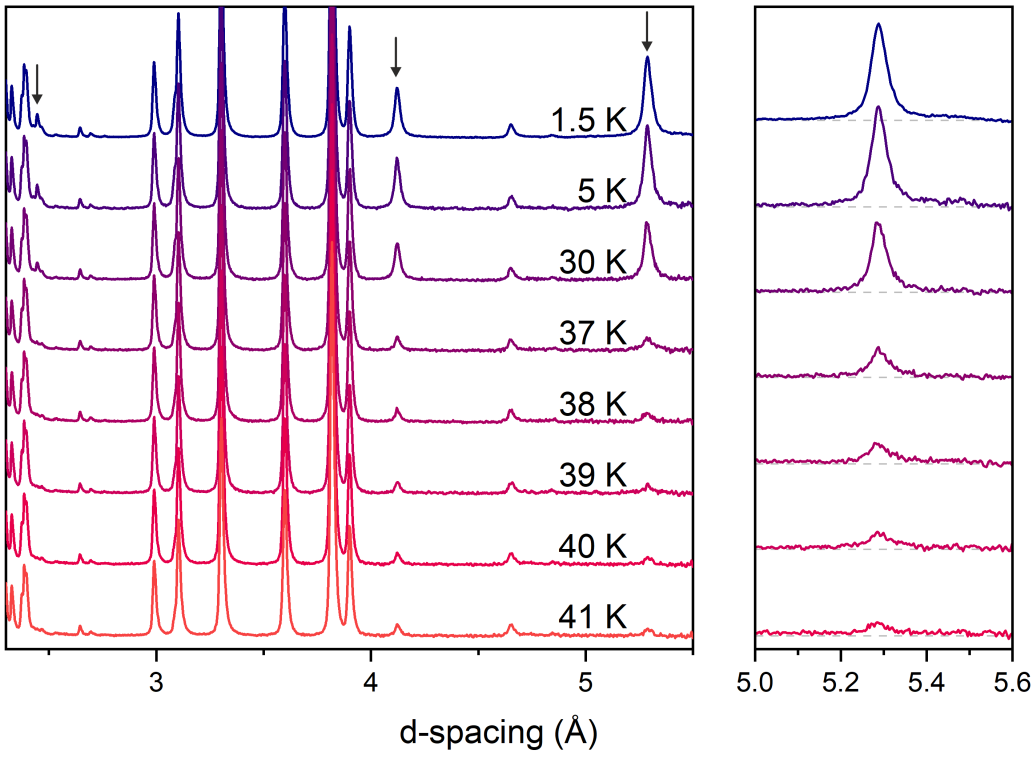


Figure 3.15 NPD data collected from $FeCaTa_2O_7$ as a function of temperature, from bank 4-7 (122°). Black arrows indicate magnetic scattering peaks. The right-hand image shows the region around the magnetic peak at ~ 5.3 Å at a greater magnification. The grey-line is used to guide the reader's eye.

Figure 3.16 shows the temperature dependence of the ordered moment obtained from the neutron powder diffraction data. A power law, $M = M_0(1 - \frac{T}{T_N})^{\beta}$, can be approximately fit to the data to yield a transition temperature, T_N, of 37.05(5) K, a value which is significantly lower than the magnetic transition temperature indicated by magnetisation data and from a visual inspection of the magnetic scattering seen in NPD. Indeed, Figure 3.16 shows a residual moment of approximately 1 μ_B above the inferred value of T_N. The extracted value of β = 0.172(1) is lower than expected for a material displaying two-dimensional ordering of the magnetic moment in the *xy* plane, where a value of β = 0.23 is regarded as a signature of 2D XY behaviour.[121] Although it is possible to extract reasonable values from the fitting of the power law, it is noted that the fit is only approximate, which may suggest that the 2D magnetic interactions are not strong in $FeCaTa_2O_7$. Figure 3.15 demonstrates that the

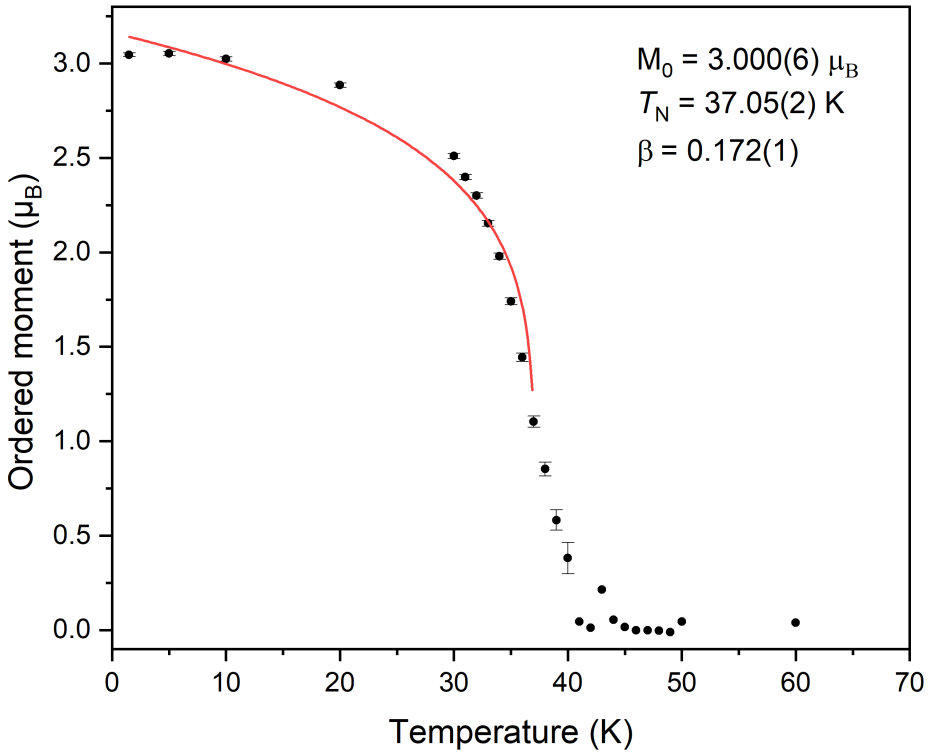


Figure 3.16 The ordered magnetic moment extracted from the refinement of the ordered $P2_1n'm'$ model against NPD data collected from $FeCaTa_2O_7$ in the temperature range 1.5 K ≤ T/K ≤ 60 K.

magnetic scattering peaks do not significantly broaden as the temperature increases, nor do any diffuse scattering features appear above T_N, unlike in the analogous $MnCaTa_2O_7$ phase. These diffraction features can usually be taken as an indication of the presence of strong 2D magnetic interactions in the *xy* plane above the magnetic transition temperature, and their absence suggests this behaviour is not present in $FeCaTa_2O_7$.

Figure 3.17 shows the evolution of the lattice parameters as a function of temperature, which increase with temperature. There are no clear lattice parameter anomalies that coincide with the onset of magnetic order, which indicates that the electric and magnetic polarisations are not strongly coupled within $FeCaTa_2O_7$, in contrast to the analogous $MnCaTa_2O_7$ phase.[119]

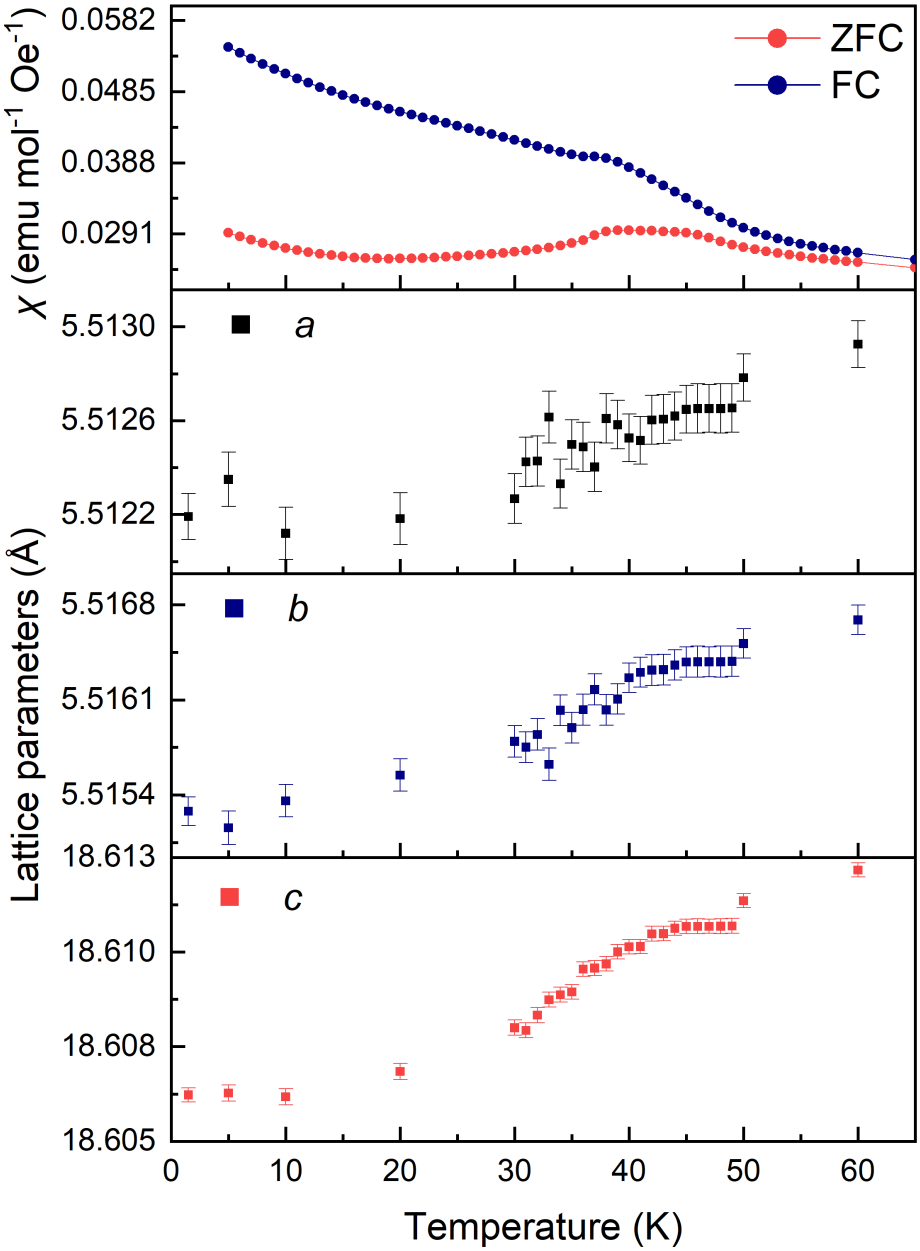


Figure 3.17 Zero-field cooled and field cooled magnetisation data and the lattice parameters extracted from NPD data collected from $FeCaTa_2O_7$, plotted as a function of temperature in the range $1.5 \leq T/K \leq 60$.

3.3.4 Characterisation of $CoCaTa_2O_7$

3.3.4.1 Room temperature synchrotron X-ray diffraction data

Synchrotron X-ray diffraction data collected from $CoCaTa_2O_7$ at 100 K could be initially indexed using an almost metrically tetragonal, primitive unit cell (a = 5.51363(1) Å, b = 5.5157(1) Å, c = 18.6077(1) Å) consistent with a $\sqrt{2} \times \sqrt{2} \times 1$ geometric expansion of an undistorted n = 2 Ruddlesden-Popper aristotype unit cell. A Pawley fitting revealed that the sample was single-phase, indicating that a successful cation exchange reaction had taken place (Figure 3.18).

3.3.4.2 100 K neutron powder diffraction data

Neutron powder diffraction data collected from $CoCaTa_2O_7$ at 100 K could also be initially indexed using a similar, almost metrically tetragonal unit cell, consistent with a

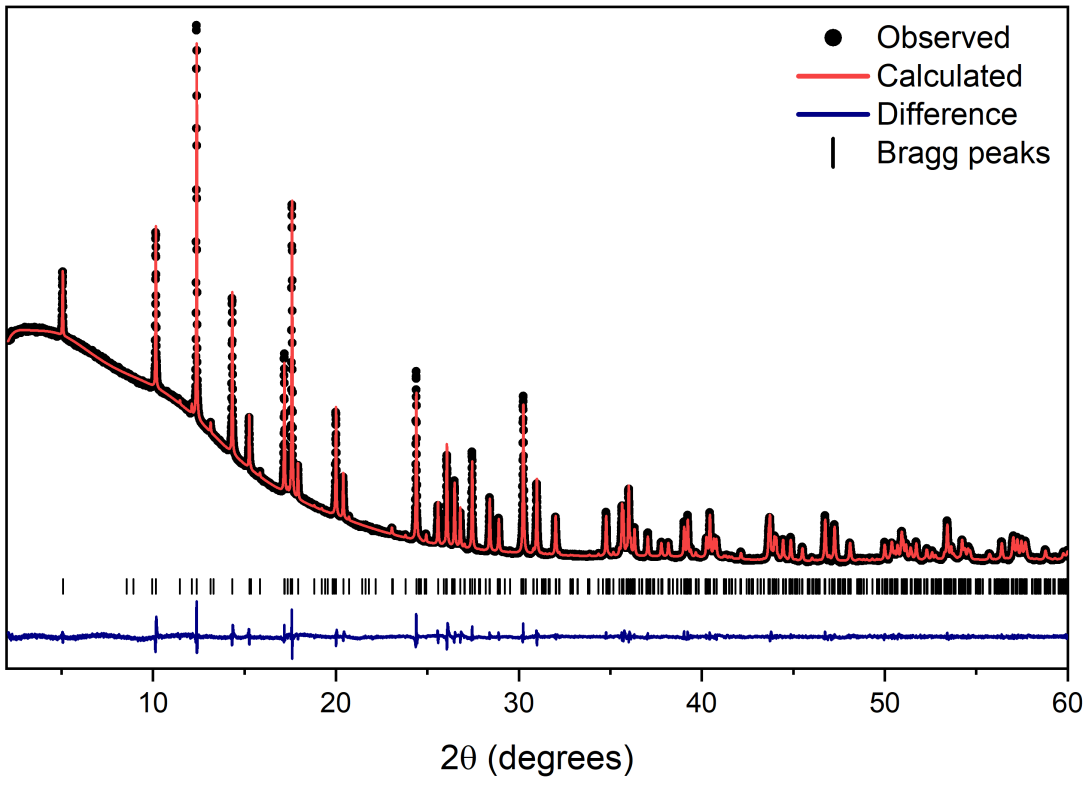


Figure 3.18 Observed, calculated and difference plots from the Pawley fitting of a primitive unit cell against SXRD data collected from $CoCaTa_2O_7$ at room temperature.

$\sqrt{2} \times \sqrt{2} \times 1$ geometric expansion of an undistorted n = 2 Ruddlesden-Popper unit cell. Systematic absences indicated that a primitive unit cell was necessary to index all the peaks of the diffraction pattern. Symmetry analysis revealed only two tilting distortions were consistent with a tetragonal unit cell: $a^-b^0c^0/b^0a^-c^0$ described in space group $P4_2/mnm$ and $a^-b^0c^0/b^0{-}a^-c^0$ described in space group $P4_2/mcm$. The $P4_2/mcm$ model could be eliminated based on extinction conditions of the diffraction data. Refinement of the $a^-b^0c^0/b^0a^-c^0$ structural model against the NPD data gave a reasonable fit. As noted above, powder second harmonic generation measurements revealed that $CoCaTa_2O_7$ is SHG active and, therefore, adopts a non-centrosymmetric crystal structure. Since the $P4_2/mnm$ space group is centrosymmetric, it cannot be the correct symmetry.

There remained a possibility that $CoCaTa_2O_7$ crystallises in an orthorhombic space group but with metrically tetragonal lattice parameters since this is commonly observed in similar cation-exchanged phases.[54] To explore this possibility, the symmetry of the $P4_2/mnm$ structural model was lowered to an orthorhombic lattice. The $P4_2/mnm$ space group is consistent with an $a^-b^0c^0/a^0b^-c^0$ tilting scheme. A lowering of the crystal symmetry from tetragonal to orthorhombic indicates a more complex tilting pattern is adopted. Further symmetry analysis indicates $a^-b^-c^0/b^-a^-c^0$ (*Pnnm)*, $a^-b^-c^+/b^-a^-c^+$ ($P2_1nm$), $a^-b^-c^+/{-}(a^-b^-)c^+$ (*P2cm)*, $a^-b^-c^-/b^-a^-c^-$ ($P2_1/c$) and $a^-b^-c^-/{-}(a^-b^-)c^-$ ($P2/c$) are consistent with the observed reflection conditions. Since they are centrosymmetric, the *Pnnm*, $P2_1/c$, and $P2/c$ structural models could be eliminated.

The neutron scattering length of Co^{2+} is small (2.49 fm) compared to the other elements in the phase, which makes it difficult to accurately determine atomic positions of the Co ion from neutron diffraction data alone.[86] Instead, a combined synchrotron X-ray and neutron refinement was necessary to locate both the cobalt ions and light oxygen ions. Structural

models were constructed based on $P2_1nm$ and $P2cm$ and refined against the NPD data collected at 200 K. Refinement of the $P2_1nm$ model against the NPD data considerably improved the fitting statistics compared to the $P2cm$ model and gave chemically realistic atomic positions for all atom types, although the thermal displacement parameter for Co remained unreasonably large.

To ensure that the improvement of the fit on changing from a tetragonal to an orthorhombic model was not simply an artifact of the increased number of parameters, the magnitude of the tilts along each direction were measured. The a tilt is of a significant magnitude (23.0(3)°), whilst the b and c tilts are considerably smaller (1.1(3)° and 1.7(7)°, respectively). Therefore, the $a^-b^-c^+/b^-a^-c^+$ tilting pattern described in space group $P2_1nm$ can effectively be described as $a^-b^{0-}c^0/b^0a^-c^0$ in which the b and c tilts have zero magnitude. This structural analysis highlights that in this case it is difficult to distinguish between $P4_2/mnm$ and $P2_1nm$ symmetries using diffraction data alone, although the lower symmetry is necessary to describe the non-centrosymmetric structure indicated by a positive SHG signal, and as we will see, the ferromagnetic component (canting) of the magnetisation data.

Co^{2+} cations occupy half of the available pseudo-tetrahedral sites within the interlayer region of the layered perovskite structure. In the $P2_1nm$ model, there are two crystallographically distinct 4b sites. During initial refinements, the occupancies of the Co sites were constrained to be 0.5, such that the Co^{2+} cations were disordered across both sites. A visual inspection of the fitting showed that this model did not correctly account for the intensity of some reflections. Refinement of the Co-site occupancies within the constraint of the total occupancy across both sites being equal to one visibly improved the refinement and fitting statistics, where the occupancy of one 4b site converged to 1.0, whilst the other site

converged to 0.0. This indicates that the Co-cations adopt a chequerboard ordered arrangement within the interlayer region, analogous to the ordering of the Fe-cations in $FeCaTa_2O_7$. The observed, calculated and difference plots from the refinement of the ordered $P2_1nm$ model of $CoCaTa_2O_7$ against the bank 2 and bank 4 NPD data collected at 100 K are shown in Figure 3.19. Full details of the refined structure are given in Table 3.7. Selected bond lengths and bond valence sum values for the cations are reported in Table 3.8.

Table 3.7 Parameters from the structural refinement of the ordered $P2_1nm$ model of $CoCaTa_2O_7$ against the NPD data collected at 100 K.

Atom	Site	*x*	*y*	*z*	Occ.	B_{iso} / Å^2
Co1	4*b*	0.820(11)	0.7620(123)	0.2331(6)	1.0	19.99(53)
Ca1	2*a*	0.078(11)	0.9854(18)	0.000000	1.0	0.44(12)
Ca2	2*a*	0.572(11)	0.5108(25)	0.000000	1.0	1.45(19)
Ta1	4*b*	0.075(11)	0.4964(7)	0.8905(1)	1.0	0.29(6)
Ta2	4*b*	0.570(11)	0.9999(8)	0.1067(1)	1.0	0.37(7)
O1	2*a*	0.984(11)	0.5426(18)	0.000000	1.0	2.77(17)
O2	2*a*	0.611(11)	0.9284(7)	0.000000	1.0	1.02(3)
O3	4*b*	0.318(11)	0.7460(16)	0.5889(2)	1.0	0.58 (3)
O4	4*b*	0.322(11)	0.2512(18)	0.3720(1)	1.0	0.93(4)
O5	4*b*	0.320(11)	0.2442(15)	0.0782(1)	1.0	0.58(3)
O6	4*b*	0.325(10)	0.7441(16)	0.9020(2)	1.0	0.93(4)
O7	4*b*	0.089(11)	0.4480(10)	0.7939(3)	1.0	1.48(11)
O8	4*b*	0.521(11)	0.0505(14)	0.2066(4)	1.0	1.29 (11)

$CoCaTa_2O_7$ - Space group $P2_1nm$ (#31)

a = 5.51504(17) Å, b = 5.51841(17) Å, c = 18.59118(22) Å

volume = 565.807(25) Å^3

Formula weight = 572.90 g mol^{-1}, Z = 4

Radiation source: Neutron Time of Flight, Instrument: WISH

Temperature: 100 K

R_p = 2.07 % $_wR_p$ = 2.89 %

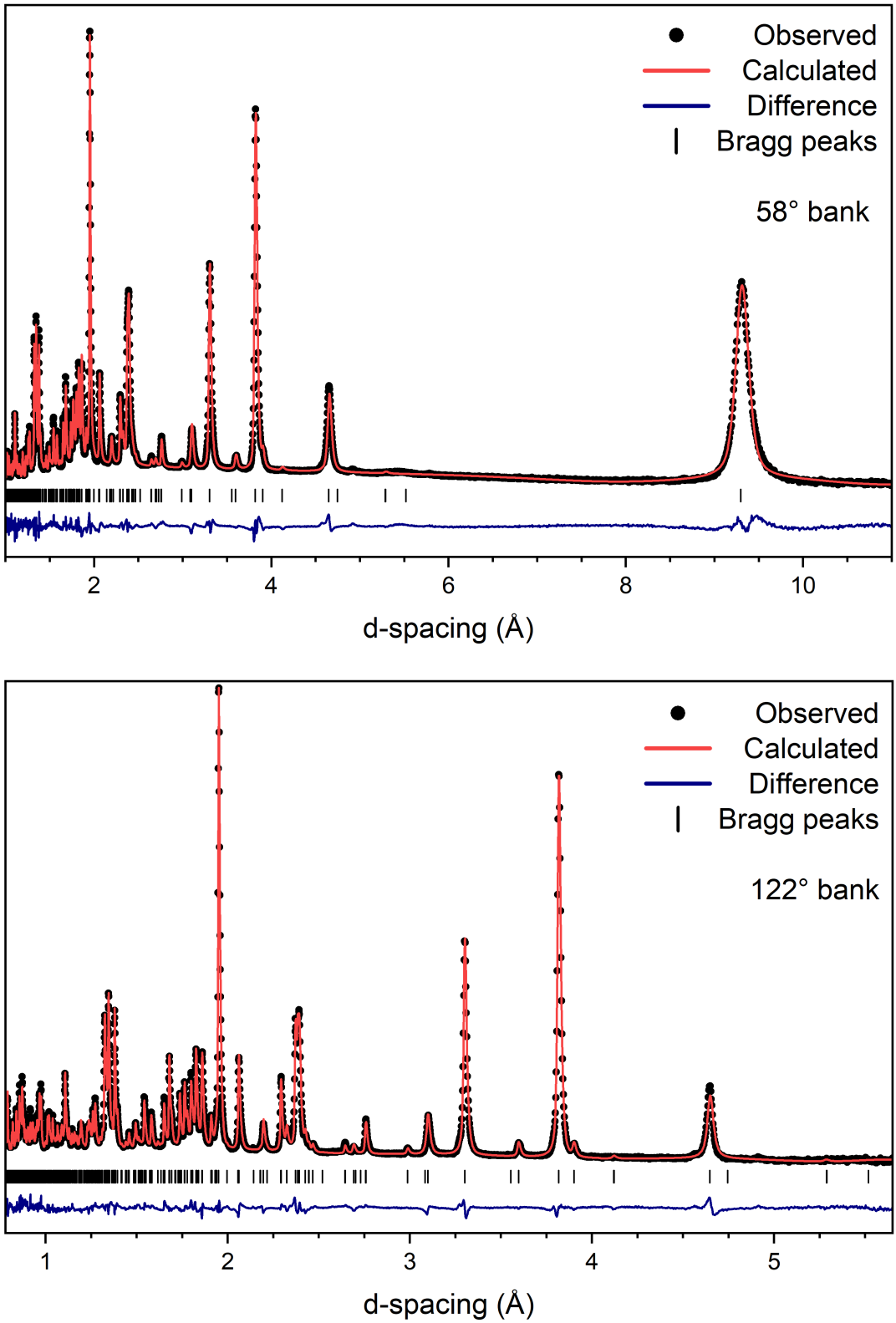


Figure 3.19 Observed, calculated and difference plots from the structural refinement of the ordered $P2_1nm$ model of $CoCaTa_2O_7$ against the NPD data collected from bank 2-9 (58°) and bank 4-7 (122°) of the WISH diffractometer at 100 K.

Table 3.8 Selected bond lengths and cation bond valence sums from the structural refinement of the ordered $P2_1nm$ model of $CoCaTa_2O_7$ against the NPD data collected at 100 K.

Cation	Anion	Bond length	BVS
Co1	O8 × 1	1.88(6)	+ 1.803
	O4 × 1	1.954(12)	
	O7 × 1	2.06(6)	
	O7 × 1	2.34(7)	
	O8 × 1	2.35(7)	
Ca1	O5 × 2	2.437(11)	+ 1.635
	O1 × 1	2.497(15)	
	O2 × 1	2.595(12)	
	O6 × 2	2.634(10)	
	O3 × 2	2.643(11)	
Ca2	O1 × 1	2.278(19)	+ 2.052
	O2 × 1	2.313(12)	
	O5 × 2	2.493(14)	
	O3 × 2	2.565(13)	
	O6 × 2	2.614(13)	
Ta1	O7 × 1	1.818(7)	+ 5.224
	O6 × 1	1.949(10)	
	O3 × 1	1.988(10)	
	O4 × 1	2.004(11)	
	O5 × 1	2.023(10)	
	O1 × 1	2.112(4)	
Ta2	O8 × 1	1.898(8)	+ 5.127
	O6 × 1	1.962(10)	
	O3 × 1	1.988(11)	
	O5 × 1	1.999(10)	
	O4 × 1	2.003(11)	
	O2 × 1	2.035(3)	

3.3.4.3 Magnetisation data

Magnetisation data were collected from $CoCaTa_2O_7$ in an applied field of 100 Oe in the temperature range $5 \leq T/K \leq 300$ K. The zero-field-cooled (ZFC) and field-cooled (FC) data, shown in Figure 3.20, can be fit to the Curie-Weiss law in the region $100 \leq T/K \leq 300$ K, yielding a Curie constant of $C = 2.29$ cm^3 K mol^{-1} and a Weiss constant of $\theta_{CW} = -51.8$ K. The Curie constant was used to calculate the effective magnetic moment, $\mu_{eff} = 4.28$ μ_B, which can be directly compared to the calculated moment for Co^{2+} (3.88 μ_B), and is somewhat higher than the spin-only moment expected for a single tetrahedral Co^{2+} (S=3/2) ion per formula unit. The slight discrepancy between the observed and calculated moment can be attributed to second-order spin-orbit coupling. The negative value of the Weiss constant is indicative of the onset of antiferromagnetic ordering. The ZFC and FC data

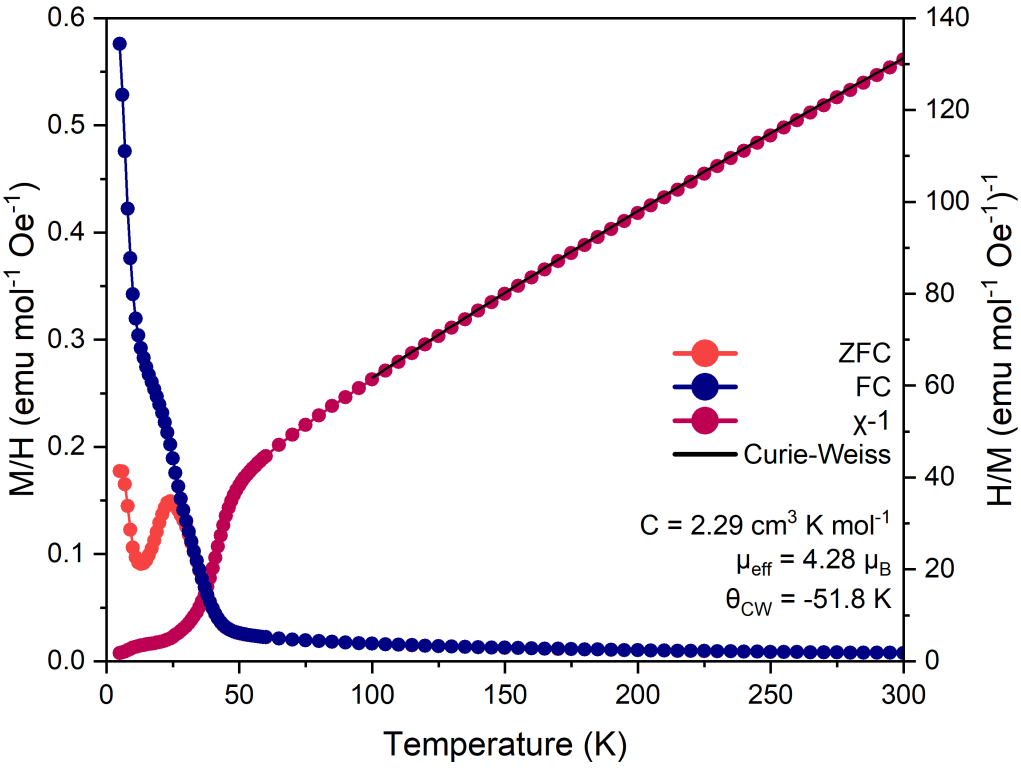


Figure 3.20 Zero-field-cooled and field-cooled magnetisation data collected from $CoCaTa_2O_7$ as a function of temperature in an applied field of 100 Oe.

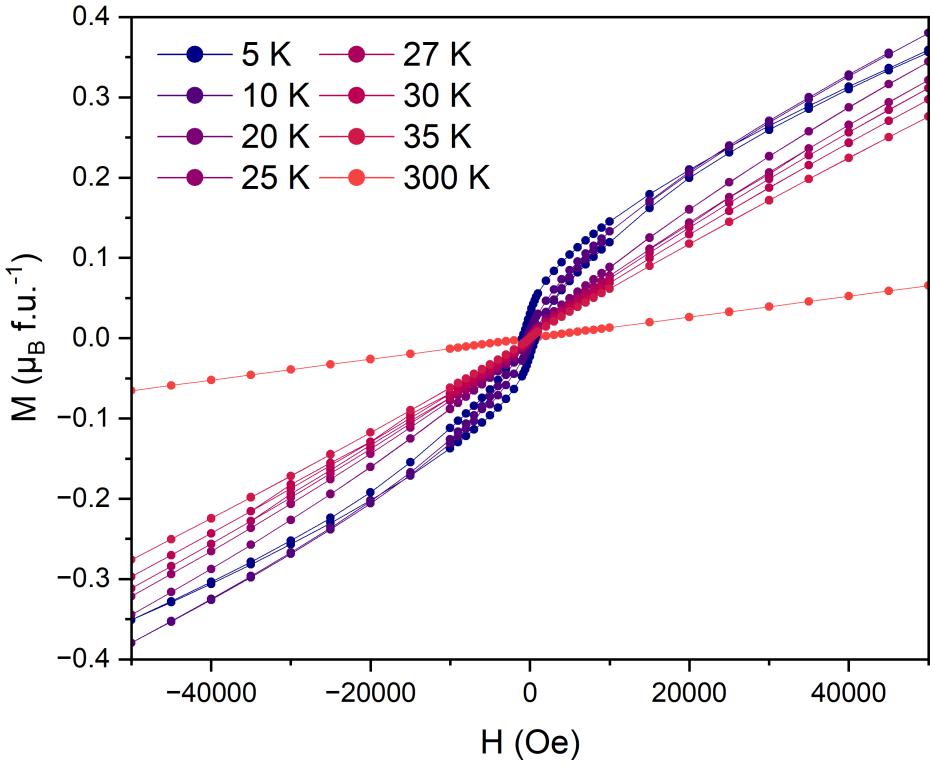


Figure 3.21 Magnetisation-field data collected from $CoCaTa_2O_7$ at the indicated temperatures.

sharply diverge at approximately T_N = 28 K (antiferromagnetic in character), and a second feature is observed at T_A = 10 K where the susceptibility increases once again as the temperature decreases. The magnetisation-field isotherm collected at 300 K is linear and passes through the origin, with data collected at 5 K exhibiting weak hysteresis that is symmetric about the origin (Figure 3.21). This suggests that the Co^{2+} ions adopt a canted antiferromagnetic arrangement at low temperatures. Similarly, the field-dependent magnetisation data collected at temperatures between T_N and the second inflection point at T_A are non-linear but do not exhibit hysteresis. Below T_A, however, the magnitude of the coercive field and remnant magnetisation increase, consistent with an increase in the canting or ferromagnetic component to the magnetic moment.

3.3.4.4 Low temperature (1.5 K) neutron powder diffraction data

Neutron powder diffraction data collected from $CoCaTa_2O_7$ at 1.5 K exhibit a series of additional diffraction peaks not present in the data collected at 100 K, which can be attributed to magnetic order in the phase. These additional diffraction features can be indexed using a single magnetic propagation vector (**k** = 0, 0, 0) of the crystallographic unit cell. A series of possible magnetic models were constructed based on the ordered $P2_1nm$ symmetry crystal structure using the ISODISTORT software package and were refined against the 1.5 K neutron diffraction data. The best fit was obtained by using a $P2_1n'm'$ symmetry magnetic model, which can be constructed by applying the mΓ2 distortion mode to the $P2_1nm$ crystallographic structure. This mode permits magnetic moments to be orientated along the *x*-, *y*- and *z*-directions, and so these three parameters were allowed to refine freely. Both the ordered moments along the *x*- and *y*-directions converged to zero within error and henceforth were constrained to be zero in the refinement. The moment along the *z*-direction refined to a value of 3.07(1) μ_B, consistent with the spin-only moment expected for a single tetrahedral $S = 3/2$ Co^{2+} cation. The refined model shows that the Co cations adopt a G-type antiferromagnetic arrangement with moments orientated along the *z*-direction.

The observed, calculated, and difference plots of the refinement of the ordered $P2_1n'm'$ magnetic model of $CoCaTa_2O_7$ against the bank 2 and bank 4 NPD data collected at 1.5 K are shown in Figure 3.22. Full details of the refined structure are given in Table 3.9. Selected bond lengths and bond valence sum values for the cations are reported in Table 3.10.

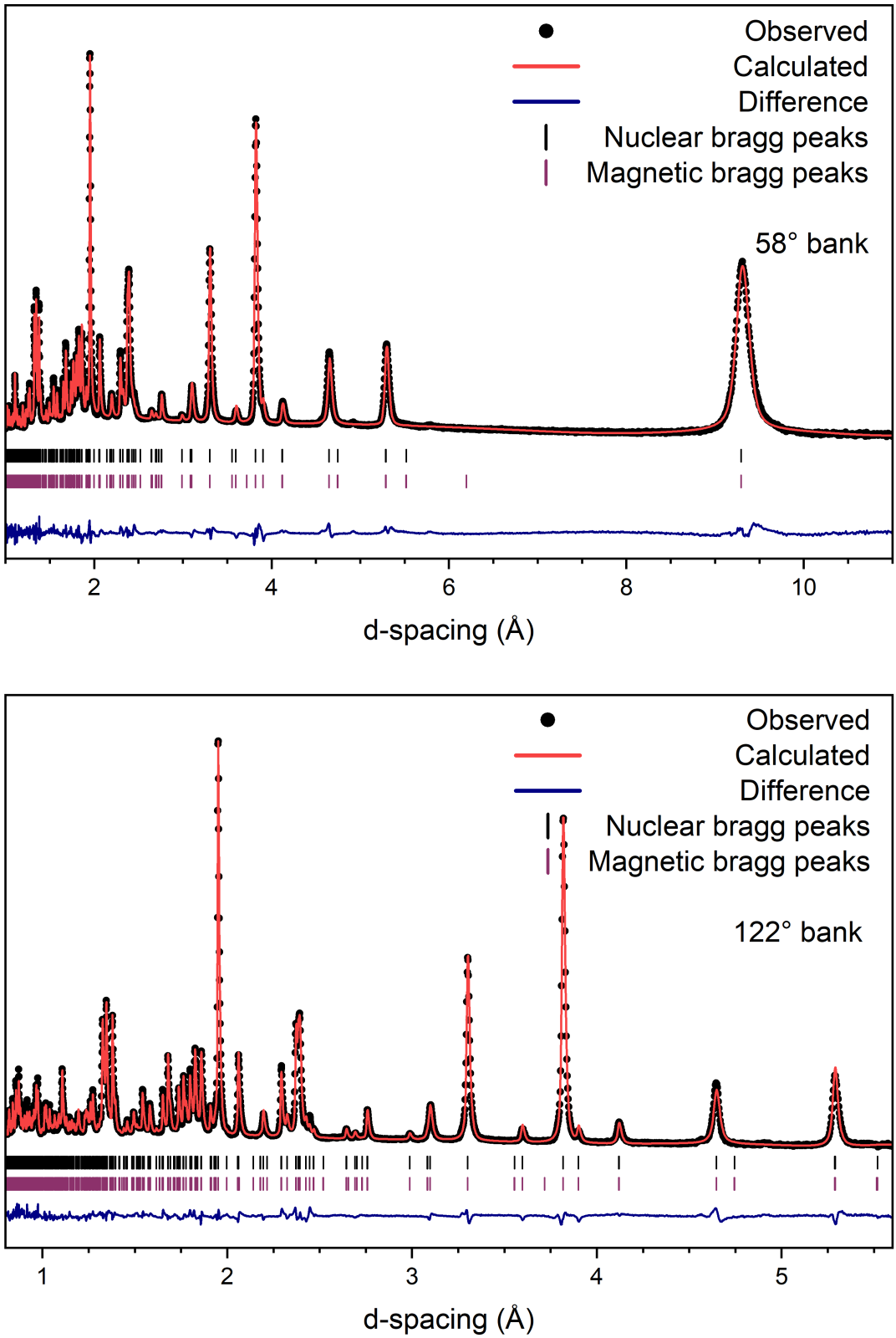


Figure 3.22 Observed, calculated and difference plots from the structural refinement of the magnetically ordered $P2_1n'm'$ model of $CoCaTa_2O_7$ against the NPD data collected from bank 2-9 (58°) and bank 4-7 (122°) of the WISH diffractometer at 1.5 K.

Table 3.9 Parameters from the structural refinement of the magnetically ordered $P2_1n'm'$ model of $CoCaTa_2O_7$ against the NPD data collected at 1.5 K.

Atom	Site	*x*	*y*	*z*	Occ.	B_{iso} / Å^2
Co1	4*b*	0.820(11) $M_x = 0$	0.7620(12) $M_y = 0$	0.2331(6) $M_z = 3.05(2)$	1.0	19.99(46)
Ca1	2*a*	0.057(14)	0.9767(28)	0.0000	1.0	0.75(6)
Ca2	2*a*	0.557(14)	0.5106(32)	0.0000	1.0	0.75(6)
Ta1	4*b*	0.066(14)	0.4975(10)	0.8908(3)	1.0	0.19(10)
Ta2	4*b*	0.557(14)	0.9973(12)	0.1070(3)	1.0	0.49(12)
O1	2*a*	0.984(14)	0.5523(16)	0.0000	1.0	0.22(12)
O2	2*a*	0.583(14)	0.9194(16)	0.0000	1.0	1.42(17)
O3	4*b*	0.302(14)	0.7461(21)	0.5889(2)	1.0	0.38(4)
O4	4*b*	0.321(14)	0.2509(20)	0.3719(1)	1.0	0.81(5)
O5	4*b*	0.302(14)	0.2387(19)	0.0775(1)	1.0	0.38(4)
O6	4*b*	0.321(14)	0.7437(17)	0.9020(2)	1.0	0.81(5)
O7	4*b*	0.090(14)	0.4444(15)	0.7924(5)	1.0	0.84(14)
O8	4*b*	0.511(14)	0.0426(19)	0.2047(6)	1.0	1.82(18)

$CoCaTa_2O_7$ - Space group $P2_1n'm'$(#31.127)

a = 5.51487(14) Å, b = 5.51863(14) Å, c = 18.58723(22) Å

volume = 565.693(21) Å^3

Formula weight = 572.90 g mol^{-1}, Z = 4

Radiation source: Neutron Time of Flight, Instrument: WISH

Temperature: 1.5 K

R_p = 4.04 % $_wR_p$ = 5.01 %

Table 3.10 Selected bond lengths and cation bond valence sums from the structural refinement of the magnetically ordered $P2_1n'm'$ model of $CoCaTa_2O_7$ against the NPD data collected at 1.5 K.

Cation	Anion	Bond length	BVS
Co1	O8 × 1	1.89(6)	+ 1.806
	O4 × 1	1.949(3)	
	O7 × 1	2.05(6)	
	O8 × 1	2.33(7)	
	O7 × 1	2.36(7)	
Ca1	O1 × 1	2.46(4)	+ 1.603
	O5 × 2	2.46(8)	
	O2 × 1	2.57(14)	
	O6 × 2	2.65(8)	
	O3 × 2	2.67(8)	
Ca2	O1 × 1	2.23(13)	+ 2.130
	O2 × 1	2.31 (2)	
	O5 × 2	2.52 (8)	
	O3 × 2	2.53(7)	
	O6 × 2	2.59(7)	
Ta1	O7 × 1	1.814(15)	+ 5.218
	O4 × 1	1.97(10)	
	O6 × 1	1.98 (10)	
	O3 × 1	1.99(10)	
	O5 × 1	2.03(9)	
	O1 × 1	2.11(4)	
Ta2	O8 × 1	1.90(3)	+ 5.139
	O6 × 1	1.95(10)	
	O3 × 1	1.97(9)	
	O4 × 1	2.01(10)	
	O5 × 1	2.02(10)	
	O2 × 1	2.032(14)	

3.3.4.5 Variable temperature neutron powder diffraction data

Neutron powder diffraction data was collected from $CoCaTa_2O_7$ at 1.5 K, 5 K, 7.5 K, 10 K to 30 K at 1 K temperature increments, 35 K, 40 K, 50 K and 100 K. A magnetically ordered $P2_1n'm'$ model was sequentially refined against the data collected at each temperature, where the output file from the first refinement became the input file for the next. After the first refinement, all variables were turned off, and only the lattice parameters and the magnetic moment along the *z*-direction were allowed to vary freely during subsequent refinements. Figure 3.23 illustrates the evolution of the neutron powder diffraction data as a function of temperature. The intensity of the magnetic Bragg peaks decreases as the temperature increases, completely disappearing above 25 K. This can be more clearly seen in Figure 3.24.

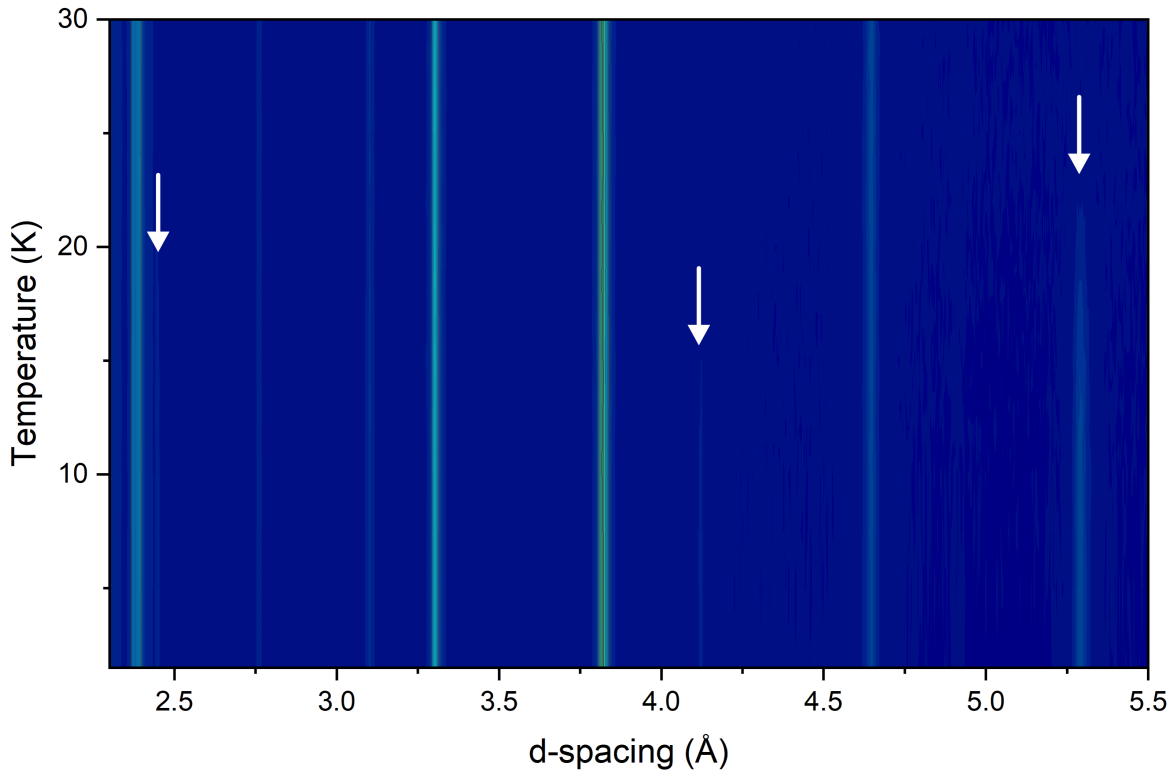


Figure 3.23 Evolution of the intensity of the neutron diffraction data collected from $CoCaTa_2O_7$ as a function of temperature. Magnetic peaks are labelled with arrows.

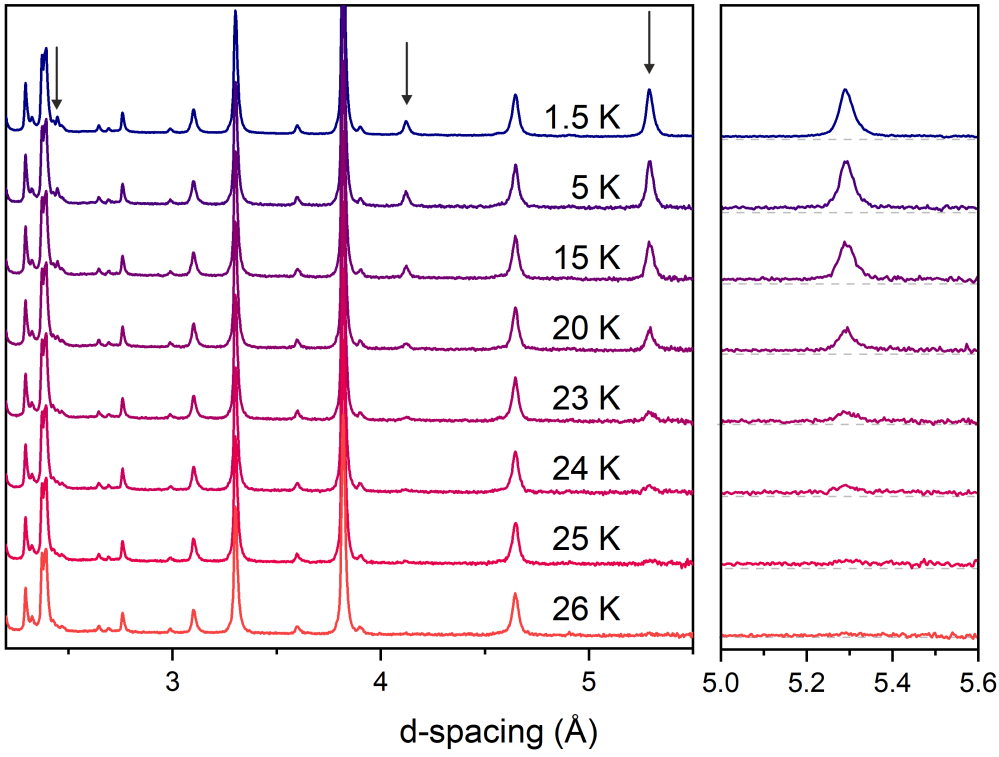


Figure 3.24 NPD data collected from $CoCaTa_2O_7$ as a function of temperature (bank 4-7 (122°)). Black arrows indicate magnetic scattering peaks. The right-hand image shows the region around the magnetic peak at ~ 5.3 Å at a greater magnification. The grey line is used to guide the reader's eye.

Figure 3.25 shows the temperature dependence of the ordered moment obtained from the neutron powder diffraction data. The power law, $M = M_0(1 - \frac{T}{T_N})^{\beta}$, could not be fit to the data. In comparison to $FeCaTa_2O_7$ and $MnCaTa_2O_7$, where the moment falls off rapidly at the transition temperature, the magnitude of the ordered moment decreases more gradually in $CoCaTa_2O_7$, suggesting that the moments do not align simultaneously in one step. Instead, the onset of order occurs over a reasonable temperature window below the magnetic transition temperature. Therefore, the magnetic transition temperature of $CoCaTa_2O_7$ is considered to be approximately 24 K, based on visual inspection of the magnetic scattering features around this temperature in NPD data and magnetisation data.

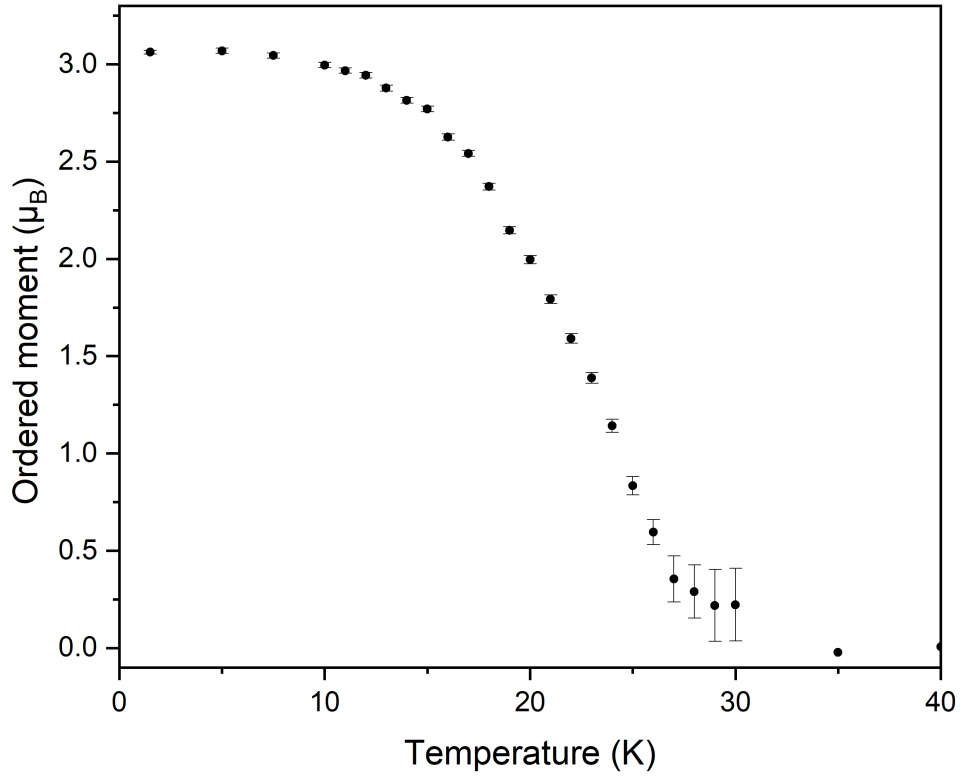


Figure 3.25 The ordered magnetic moment extracted from the refinement of the ordered P2$_1$*n*'*m*' model against NPD data collected from $CoCaTa_2O_7$ in the temperature range 1.5 K ≤ *T*/K ≤ 40 K.

The evolution of the lattice parameters as a function of temperature is shown in Figure 3.26. Surprisingly, there is not a strong correlation between the lattice parameters and temperature, as would be expected, although the *c* parameter does increase with temperature. Instead, the lattice parameters remain approximately constant with varying temperature, especially in *a* and *b*, which are essentially temperature-independent. This may be because the WISH instrument does not provide the required resolution to accurately extract very small differences in the values of the lattice parameters. In this case, it is not possible to extract any meaningful information about the presence or absence of lattice parameter anomalies that coincide with an increase in the magnetisation at T_N.

As noted above, $CoCaTa_2O_7$ exhibits a second feature in the magnetisation data at T_A. However, there are no signatures of this event in the crystallographic data. For example, the

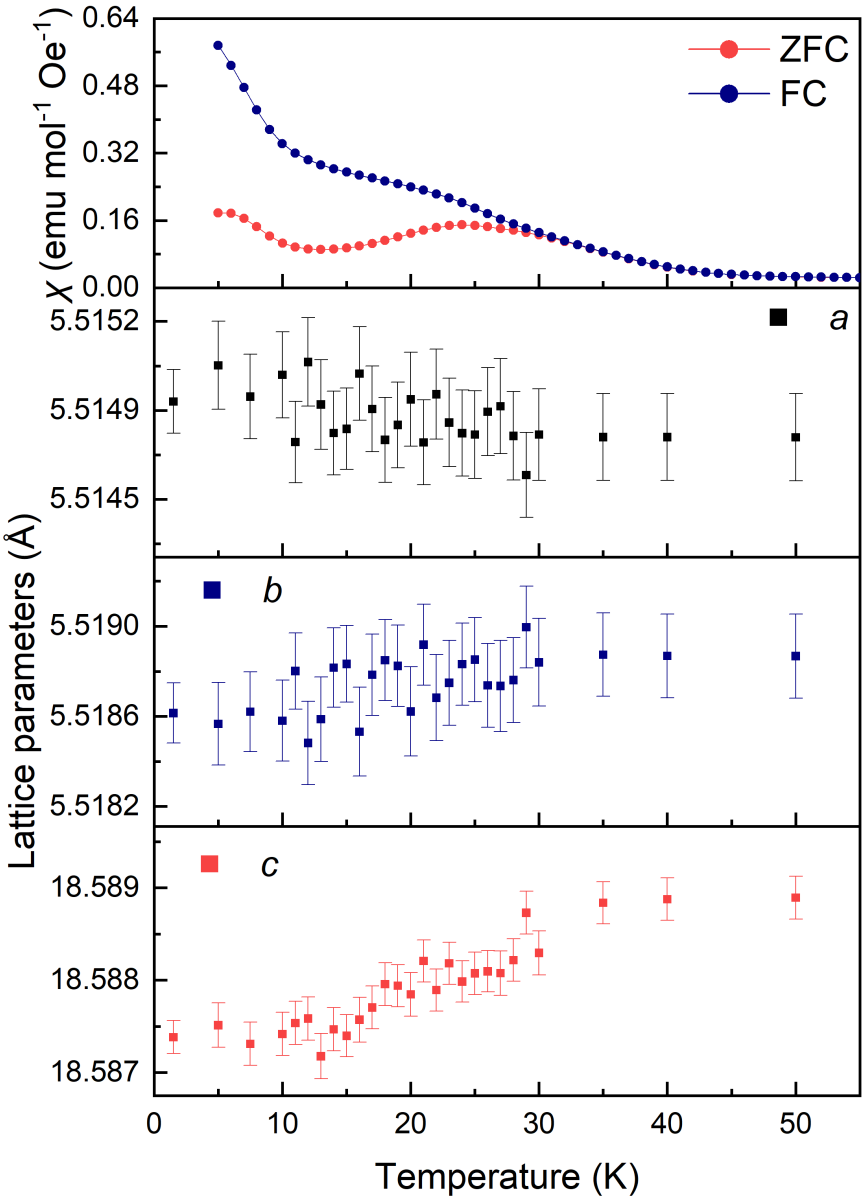


Figure 3.26 Zero-field cooled and field cooled magnetisation data and the lattice parameters extracted from NPD data collected from $CoCaTa_2O_7$, plotted as a function of temperature in the range $1.5 \leq T/K \leq 55$.

ordered moment does not change at this temperature, and there (appear to be) no lattice parameter anomalies, which suggests that this feature is not related to a structural change. Indeed, it is more likely that this second feature at T_A occurs as a result of the onset of the canted component to the magnetic structure, which is allowed by the symmetry of the unit cell but does not have any structural consequences. The magnitude of this ferromagnetic component is minimal, and a value could not be extracted from the neutron diffraction data.

This indicates that the electric and magnetic polarisations are not strongly coupled within $CoCaTa_2O_7$, unlike the analogous $MnCaTa_2O_7$ phase.[119]

3.4 Discussion

The reaction of $Li_2CaTa_2O_7$ with anhydrous 3*d* transition metal chlorides results in the topochemical cation exchange of the host lattice and formation of $FeCaTa_2O_7$, $CoCaTa_2O_7$ and $ZnCaTa_2O_7$. $ZnCaTa_2O_7$ adopts a polar *P*2*cm* $n = 2$ Ruddlesden-Popper structure described by an $a^-b^-c^+/-(a^-b^-)c^+$ tilting distortion (Figure 3.27). This symmetry is established by applying the X_2^+ and the X_4^- symmetry modes (describing the $a^0a^0c^+/a^0a^0c^+$ and $a^-b^-c^0/-(b^-a^-)c^0$ tilting distortions, respectively) to the undistorted *I*4/*mmm* aristotype structure. This is in contrast to the $n = 2$ Ruddlesden-Popper

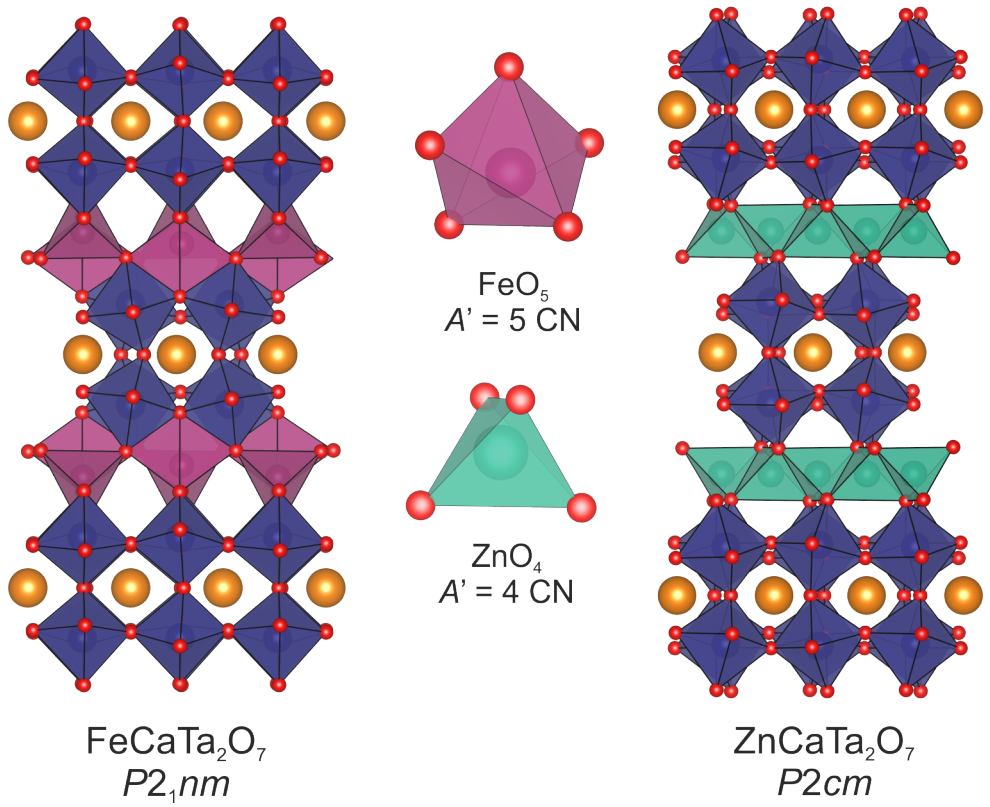


Figure 3.27 Crystal structures and the coordination environments of the *A*' cations in $FeCaTa_2O_7$ and $ZnCaTa_2O_7$. Pink, mint, orange, blue and red spheres represent Fe, Zn, Ca, Ta and O, respectively.

phases $FeCaTa_2O_7$ and $CoCaTa_2O_7$, which both adopt a $P2_1nm$ structure, described by an $a^-b^-c^+/b^-a^-c^+$ tilting distortion pattern and established by applying the X_2^+ ($a^0a^0c^+/a^0a^0c^+$) and X_3^-, ($a^-b^-c^0/b^-a^-c^0$) symmetry modes to $I4/mmm$ (Figure 3.27).

A modified tolerance factor, *t*', can be calculated for the tetrahedral *A*' coordination sites according to $t' = r_{A'} + r_O/(\sqrt{3}/\sqrt{2})\, r_B + r_O$ to quantify the magnitude of the size mismatch between the *A*' interlayer cations and the *B*-cations.[52] Using tabulated values of the Shannon radii for each ion (Ta^{5+} = 0.64 Å, Fe^{2+} = 0.63 Å, Co^{2+} = 0.58 Å, Zn^{2+} = 0.6 Å and O^{2-} = 1.4 Å), we can obtain values of *t'* = 0.812, *t*' = 0.792 and *t*' = 0.800 for $FeCaTa_2O_7$, $CoCaTa_2O_7$ and $ZnCaTa_2O_7$, respectively. The tolerance factor of the zinc phase is smaller than that of the iron phase, suggesting that the former will have a more distorted structure than the latter. This is experimentally confirmed since the magnitudes of each of the three tilts in $ZnCaTa_2O_7$ are greater than in $FeCaTa_2O_7$. Interestingly, the tolerance factor of the cobalt phase is the smallest in the series, which would typically suggest that $CoCaTa_2O_7$ would adopt the most distorted structure. This is not the case, since the $P2_1nm$ crystal structure adopted by $CoCaTa_2O_7$, described by an $a^-b^-c^+/b^-a^-c^+$ tilting distortion, can be approximately described using a $P4_2/mnm$ ($a^-b^0c^0/b^0a^-c^0$) model, assuming that the magnitude of the tilting distortions around the *b* and *c* directions are close to being zero.

Table 3.11 A comparison of the calculated modified tolerance factor, *t*', and the magnitude *a*, *b* and *c,* of the rotations around each axis extracted from the $P2_1nm$ and $P2cm$ crystal structure models of $FeCaTa_2O_7$, $CoCaTa_2O_7$ and $ZnCaTa_2O_7$.

Phase	Space Group	Glazer Tilt	*t'*	*a* / °	*b* / °	*c* / °
$FeCaTa_2O_7$	$P2_1nm$	$a^-b^-c^+/b^-a^-c^+$	0.812	20.3(4)	2.1(4)	5.7(8)
$CoCaTa_2O_7$			0.792	23.0(3)	1.1(3)	1.7(7)
$ZnCaTa_2O_7$	$P2cm$	$a^-b^-c^+/-(a^-b^-)c^+$	0.800	21.3(3)	19.4(3)	19.9(5)

The zinc cations in $ZnCaTa_2O_7$ occupy the four-coordinate tetrahedral coordination sites located between the perovskite double-layers to form a striped arrangement of edge-sharing ZnO_4 tetrahedra. In comparison, the iron and cobalt cations in $FeCaTa_2O_7$ and $CoCaTa_2O_7$ sit in five-coordinate sites and are ordered within a network of corner-linked $(Fe/Co)O_5$ pseudo-tetrahedra. This results in a chequerboard arrangement of the cations within the interlayer region. A comparison of the two types of ordering is shown in Figure 3.28.

Bond-valence sum (BVS) calculations of the iron and cobalt cations suggest that in both structures, iron and cobalt are under-bonded (BVS Fe = 1.82, Co = 1.80), indicating that the Fe and Co coordination sites are larger than ideal. On the other hand, the BVS values obtained from the zinc cations indicate that the bonding environment of Zn has been optimised (BVS Zn = 2.014).

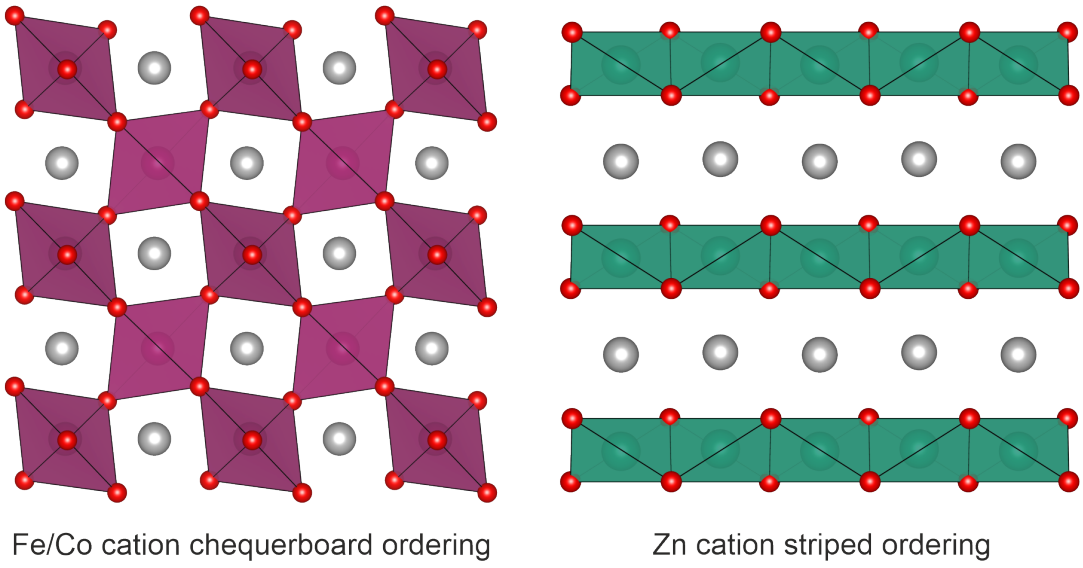


Figure 3.28 The ordering schemes adopted by Fe and Co (left) and Zn (right) within the interlayer coordination sites. Pink, mint and red spheres represent Fe/Co, Zn and O, respectively. Grey spheres represent the positions of empty *A*'-sites.

According to Pauling's third rule of ionic crystals, the corner-sharing nature of the (Fe/Co)O_5 pseudo-tetrahedra minimises the cation-cation repulsion between adjacent *A*'-cations, because cations will be furthest apart if they only share one anion.[122] This collective arrangement of polyhedra means that it is not possible to use octahedral rotations to optimise the bonding environment of the *A*'cations, since minimising one *A*'–O bond length in a particular tetrahedron will increase the length of another *A*'–O bond in adjacent tetrahedra. Therefore, in both $FeCaTa_2O_7$ and $CoCaTa_2O_7$, it is energetically more favourable to minimise the Coulombic repulsion between the interlayer cations than optimising their coordination environment. In this situation, the ordering of the cations is prioritised over the optimum octahedral tilting arrangement, and the Fe and Co cations adopt a chequerboard pattern. In $ZnCaTa_2O_7$, the striped configuration of edge-sharing ZnO_4 tetrahedra does not optimise the cation-cation repulsion to the same extent as chequerboard ordering, but does permit the optimisation of the zinc coordination environment via octahedral tilting.

The difference between the chosen ordering patterns can be understood by considering that within each system, there is a competition between minimising the cation-cation repulsion of the *A*'-cations and optimising the size of the *A*'-cations coordination site via octahedral tilting. Generally, the ionic radius of the 3*d* transition metal cations in tetrahedral coordination environments decreases moving across the period from left to right (Table 3.12). Smaller *A*' cations will be under-bonded to a greater extent than larger cations, and optimising their coordination environment outweighs the energetic gain of minimising the Coulombic repulsion. Therefore, the striped and chequerboard ordering schemes are the optimum solution for smaller and larger cations, respectively. Similar behaviour has been observed in related layered perovskite phases. For example, in the $n = 2$ Ruddlesden-Popper phases $LiNdM_2O_7$ and $NaNdM_2O_7$, where M = Nb or Ta, and in $LiBiNb_2O_7$ and $NaBiNb_2O_7$,

Table 3.12 Ionic radii of Li^+ and M^{2+} cations in a tetrahedral coordination geometry.

Cation	Mn^{2+}	Fe^{2+}	Co^{2+}	Ni^{2+}	Cu^{2+}	Zn^{2+}
Ionic Radius (Å)	0.66	0.63	0.58	0.55	0.57	0.60

an analogous competition between minimising the *A*'–*A*' repulsion and optimising the *A*' coordination environment has been studied, where the smaller Li^+ cations adopt a striped arrangement and Na^+ cations a chequerboard arrangement.[52,59]

Crystal field effects may also influence the ordering pattern adopted by each phase. Tetragonal Co^{2+} (d^7) cations and Fe^{2+} (HS d^6) cations are anisotropic (Figure 3.29) and will experience crystal field effects. Furthermore, the Co^{2+} and Fe^{2+} cations occupy pseudo-tetrahedral, five-coordinate sites, whereas Zn occupies a truly tetrahedral site. Therefore, the crystal field splitting of the *d*-orbitals of Co^{2+} and Fe^{2+} will differ from that of Zn^{2+} due to the coordination of a fifth oxygen atom. Since the local environment of Co^{2+} and Fe^{2+} has deviated from the ideal tetrahedral geometry, the crystal field splitting will differ from that depicted in Figure 3.29. Instead, a relative increase in the energy of the d_{z^2} orbital might be expected for Co^{2+} and Fe^{2+}. In comparison, the 3*d* orbitals of Zn^{2+} (d^{10}) are fully occupied,

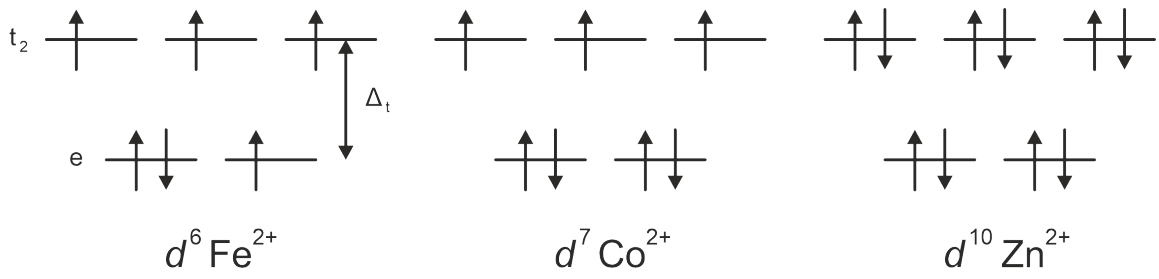


Figure 3.29 Crystal field splitting of *d*-orbitals in a tetrahedral coordination environment. The ground state electronic configuration of Fe^{2+} (left), Co^{2+} (middle) and Zn^{2+} (right) are compared.

and hence, the Zn^{2+} cations experience zero ligand field effects and would not exhibit an electronically-driven preference for a specific geometry.

Although it was not possible to synthesise the nickel and copper analogues in this work, the same reasoning can be extrapolated to predict the structures adopted by $NiCaTa_2O_7$ and $CuCaTa_2O_7$. Tetrahedrally coordinated Ni^{2+} and Cu^{2+} cations have an ionic radius of 0.55 Å and 0.57 Å, respectively. $NiCaTa_2O_7$ would, therefore, have the smallest tolerance factor of the series and adopt the most distorted structure. Based on this, the nickel ions would be expected to order in a striped arrangement to optimise their coordination environment. In comparison, Cu^{2+} has a tetrahedral ionic radius comparable to that of Co^{2+}, and hence, the Cu^{2+} cations in the interlayer region of $CuCaTa_2O_7$ might be expected to adopt a chequerboard ordered arrangement. Both Ni^{2+} and Cu^{2+} would also experience crystal field effects since they are d^8 and d^9. Therefore, $NiCaTa_2O_7$ and $CuCaTa_2O_7$ might be expected to adopt crystal structures described in space group $P2cm$ and $P2_1nm$, respectively.

The iron and cobalt cations in $FeCaTa_2O_7$ and $CoCaTa_2O_7$ adopt a canted G-type antiferromagnetic structure below their respective magnetic transition temperatures. However, $FeCaTa_2O_7$ shows some spin glass-like behaviour. The magnetisation-field isotherm at 5 K shows weak hysteresis slightly shifted above the origin, and magnetic diffuse scattering is observed below the transition temperature. This spin-glass behaviour in the *xy* plane is likely the result of some short-range disorder or frustration within the layered perovskite structure. There are several possibilities as to the origin of this disorder. First, a small amount of site occupancy disorder or anti-site disorder of the chequerboard arrangement may result in localised domains of randomised spins. Similarly, even a very small percentage of Fe^{3+} in the structure could cause frustration. Interestingly, the cobalt analogue does not show this spin glass behaviour. This may be because the Li^+ for Co^{2+}

exchange is more robust than Li^+ for Fe^{2+}, or more likely that it is easier to oxidise Fe^{2+} to Fe^{3+} than Co^{2+} to Co^{3+}, and so a small impurity, either inherited from the $FeCl_2$ precursor or formed during the cation-exchange, is more likely to have formed in the synthesis of $FeCaTa_2O_7$.

The analogous phase $MnCaTa_2O_7$ adopts the same polar $P2_1nm$ space group as $FeCaTa_2O_7$ and $CoCaTa_2O_7$.[119] On cooling, $MnCaTa_2O_7$ undergoes a transition to a G-type antiferromagnetic state at T_N = 56 K. Unlike in the iron and cobalt materials, $MnCaTa_2O_7$ exhibits a lattice parameter anomaly at T_A = 50 K associated with a sharp increase in the magnitude of its polar distortion, but this is not accompanied by an increase in the ferromagnetic moment of the phase. This reveals that these properties are not strongly coupled in this material. Similar behaviour is also seen in the iron and cobalt phases of this family since no anomalies in the lattice parameters or magnitude of the distortion modes are observed at the magnetic ordering temperature or, indeed, at any temperature. Furthermore, there is no evidence of weak ferromagnetism in $MnCaTa_2O_7$. The magnetisation vs. field isotherm collected at 5 K does not exhibit hysteresis, unlike $FeCaTa_2O_7$ and $CoCaTa_2O_7$, suggesting that the moments are not canted in the manganese phase. Similarly, the same broadening of the magnetic scattering features above the magnetic transition temperature is not observed in the NPD data collected from $FeCaTa_2O_7$ and $CoCaTa_2O_7$, which can be attributed to the 2D-like behaviour of the magnetic moments in $MnCaTa_2O_7$.

The work detailed in this chapter can also serve as a cautionary tale for using a standard non-linear optic setup to measure the SHG activity of intensely coloured materials. During initial SHG measurements using a typical Nd:YAG laser apparatus, no SHG signal was observed for $FeCaTa_2O_7$ and $CoCaTa_2O_7$, suggesting that both samples adopt centrosymmetric space groups. However, magnetometry undoubtedly demonstrates that

$FeCaTa_2O_7$ and $CoCaTa_2O_7$ adopt canted antiferromagnetic structures below their magnetic ordering temperatures. A detailed symmetry analysis of the $n = 2$ Ruddlesden-Popper structure showed that no centrosymmetric space groups permit both a G-type antiferromagnetic arrangement of the magnetic cations and a canting of the moments. Therefore, the presence of a small ferromagnetic component to the magnetic order of the materials contradicts the initial SHG data. How can these seemingly inconsistent observations be explained? Both samples are intensely coloured, and UV-vis data indicate they absorb strongly across the visible region ($FeCaTa_2O_7$ is brown and $CoCaTa_2O_7$ is blue in colour). SHG from a 1064 nm laser appears in the visible at 532 nm, hence, it is possible that the samples may absorb any SHG, since both samples absorb at this wavelength. The SHG measurements were repeated using an IR NLO system with a 2090 nm laser and demonstrated that the phases adopt non-centrosymmetric crystal structures.

3.5 Conclusions

Single phase samples of $FeCaTa_2O_7$, $CoCaTa_2O_7$ and $ZnCaTa_2O_7$ were successfully synthesised from the topochemical cation-exchange reaction of $Li_2CaTa_2O_7$ using anhydrous transition metal chlorides. Structural characterisation reveals the materials retain the polar Ruddlesden-Popper framework of the parent phase, with $FeCaTa_2O_7$ and $CoCaTa_2O_7$ adopting a crystal described in the $P2_1nm$ space group, and $ZnCaTa_2O_7$ adopting a $P2cm$ structure. In the $P2_1nm$ structure, the *A*' cations order in a chequerboard arrangement to minimise interionic repulsion, whereas in the $P2cm$ structure, these interlayer cations adopt a striped arrangement to optimise their coordination environments via octahedral tilting. This difference highlights the importance of the interplay between different stabilisation mechanisms within this family of compounds and suggests that by carefully selecting the substituting *A*'-cation, the tilting distortions can be rationally tuned.

Upon cooling, both $FeCaTa_2O_7$ and $CoCaTa_2O_7$ undergo transitions to antiferromagnetically ordered states below their transition temperatures, with their magnetic moments ordered parallel to the *z*-axis in a G-type arrangement. Both phases also display small hysteresis in the magnetisation vs. field isotherm measured at 5 K, indicative of a ferromagnetic component to the magnetic order. $FeCaTa_2O_7$ shows some evidence of spin-glass order. In both compounds, no lattice parameter anomalies coincide with the onset of magnetic order and suggests that the electric and magnetic polarisations are not strongly coupled in these materials.

Chapter 4: Synthesis and Characterisation of $MnSrNb_2O_7$

4.1 Introduction

In the previous chapter, low-temperature cation-exchange reactions were employed to substitute paramagnetic cations into the non-centrosymmetric phase $Li_2CaTa_2O_7$. To extend this work further, this chapter explores the synthesis and characterisation of $MnSrNb_2O_7$, achieved through the topochemical cation exchange reaction of the related phase $Li_2SrNb_2O_7$, to investigate how the magnetoelectric coupling in this family of materials changes as a function of *A*-site and *B*-site cation.

4.2 Synthesis

4.2.1 Synthesis of $Li_2SrNb_2O_7$

Polycrystalline samples of $Li_2SrNb_2O_7$ were prepared by combining suitable stoichiometric ratios of $SrCO_3$ (99.997%) and Nb_2O_5 (99%, dried at 900 °C) with a 5% stoichiometric excess of Li_2CO_3 (99.99%) to compensate for lithium loss due to volatility at high temperature. The mixture was ground in an agate pestle and mortar, placed in an alumina crucible and heated at 600 °C in air for 12 h. The mixture was reground and pressed into 13 mm pellets and heated to 1150 °C at a heating rate of 5 °C/min for three periods of 30 minutes. The samples were reground and pressed into pellets between each heating cycle, placed in an alumina crucible and directly inserted into a furnace at 1150 °C before being quenched to room temperature.

4.2.2 Synthesis of $MnSrNb_2O_7$

Polycrystalline samples of $MnSrNb_2O_7$ were prepared via cation exchange reactions from $Li_2SrNb_2O_7$. 4.0 g of $Li_2SrNb_2O_7$ was combined with 10-molar equivalents of anhydrous $MnCl_2$ (98 %), and the mixture was ground in an agate pestle and mortar in an argon-filled glovebox, loaded into a Pyrex tube and heated at a ramp rate of 2°C/min to 350 °C under flowing argon for three periods of 5 days. The sample was washed with distilled water between each heating cycle to remove any unreacted $MnCl_2$ or LiCl byproduct, dried thoroughly, and combined with fresh anhydrous chloride for the following cycle. After the final washing step, the material was placed in an alumina boat and heated at 300 °C under flowing hydrogen gas to ensure any ferromagnetic manganese oxide impurities were reduced to manganese metal.

4.3 Results

4.3.1 Optical SHG Measurements

The SHG signals of $MnSrNb_2O_7$ and benchmark $AgGaS_2$ were investigated under incident laser radiation of 2090 nm. The second harmonic efficiency of $MnSrNb_2O_7$ powder was compared to that of $AgGaS_2$ powder with the same particle size and displayed an efficiency that was extremely weak in comparison to the $AgGaS_2$ standard used for IR NLO measurements but does indicate that the sample is SHG active (Figure 4.1). These results reveal that $MnSrNb_2O_7$ adopts a non-centrosymmetric crystal structure.

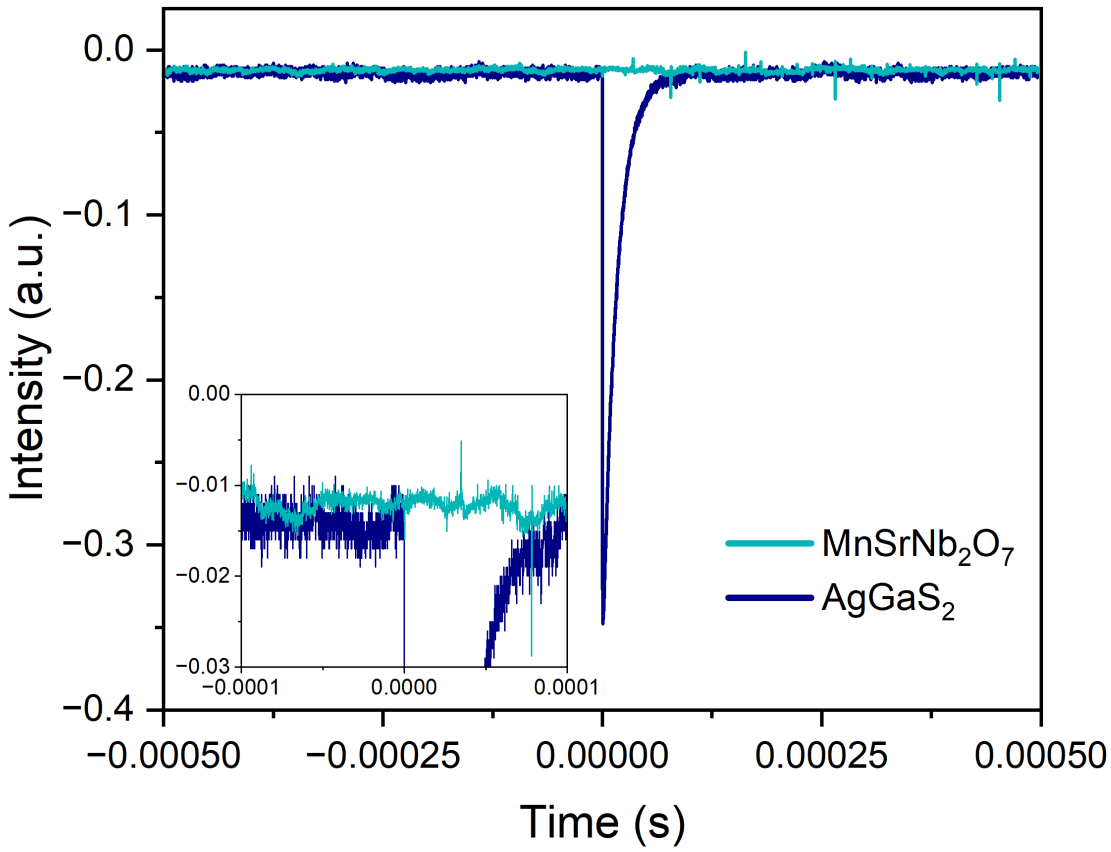


Figure 4.1 Plot of SHG intensity of $MnSrNb_2O_7$ as a function of time under incident radiation of 2090 nm, compared to that of $AgGaS_2$ standard. The inset shows the region around $t = 0$ at greater magnification.

4.3.2 Characterisation of $MnSrNb_2O_7$

4.3.2.1 Room temperature synchrotron X-ray diffraction data

Synchrotron X-ray diffraction data collected from $MnSrNb_2O_7$ at room temperature could be indexed using an orthorhombic unit cell (a = 5.5970(2) Å, b = 5.5930(2) Å, c = 18.84281(38) Å) consistent with a $\sim\sqrt{2} \times \sim\sqrt{2} \times 1$ geometric expansion of an undistorted $n = 2$ Ruddlesden-Popper unit cell (Figure 4.2). A close inspection of the Pawley refinement revealed a series of weak diffraction peaks that could be accounted for by a tetragonal unit cell ($a = b = 3.957$ Å, $c = 26.591$ Å), consistent with an undistorted $n = 3$ Ruddlesden-Popper

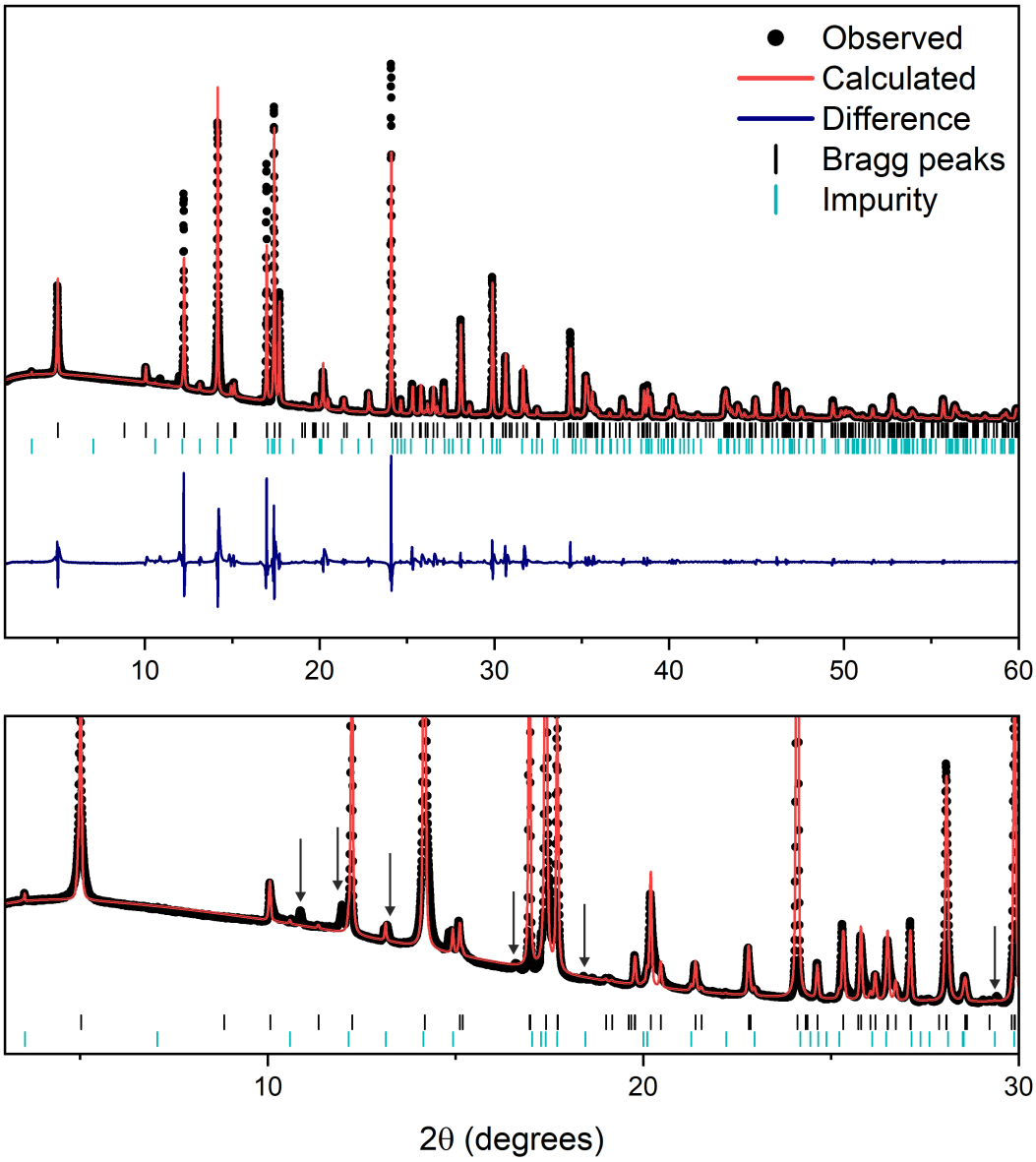


Figure 4.2 Observed, calculated and difference plots from the Pawley refinement of an *A*-centred unit cell against SXRD data collected from $MnSrNb_2O_7$ at room temperature (top) and an expanded region showing weak diffraction peaks that cannot be accounted for with a commensurate expansion of the unit cell, labelled with black arrows (bottom).

unit cell. Finally, several weak diffraction peaks, labelled with arrows in the bottom pane of Figure 4.2, could not be indexed by either of the proposed unit cells or any expansion of the unit cells. These satellite peaks provided the initial evidence of a potential incommensurate modulation of the $MnSrNb_2O_7$ crystal structure.

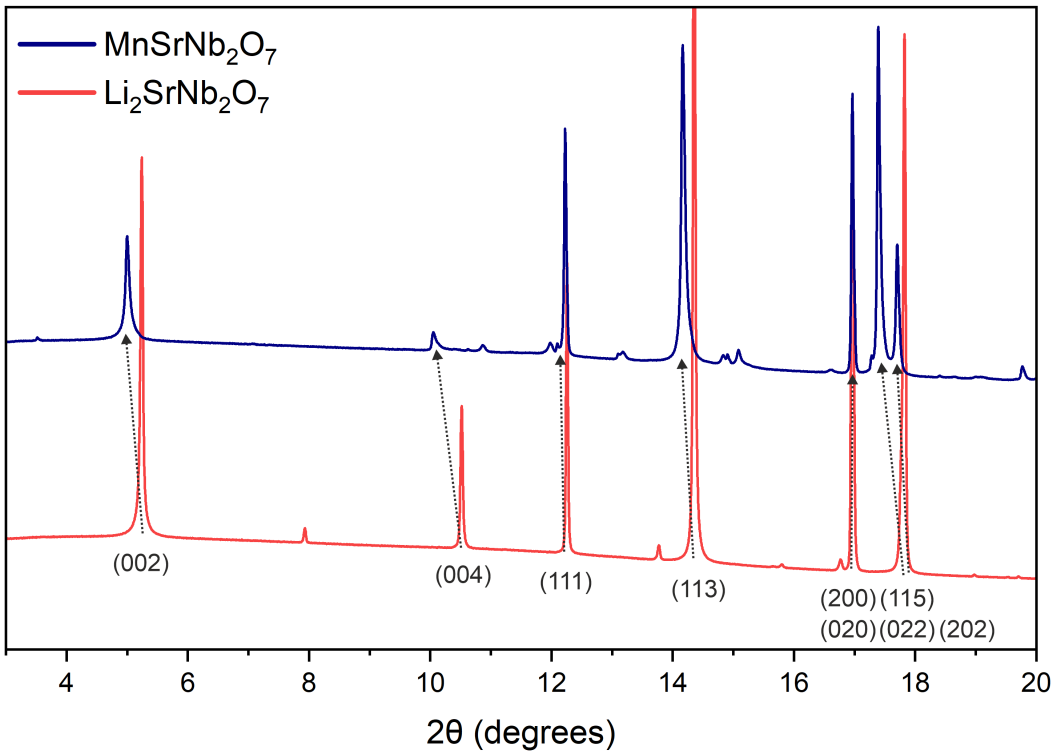


Figure 4.3 Plots of raw SXRD data collected from $MnSrNb_2O_7$ and $Li_2SrNb_2O_7$.

In addition, many of the peak shapes of the synchrotron data were also asymmetric in a way which could not be easily modelled using anisotropic broadening or peak shape functions. These irregular peak shapes are inherited from the precursor material, $Li_2SrNb_2O_7$, whose synchrotron X-ray diffraction data show a similar, strong, *hkl*-dependent broadening, shown in Figure 4.3. Indeed, it proved difficult to make a high-quality sample of $Li_2SrNb_2O_7$, particularly when scaling up the synthesis to produce the large sample sizes necessary for neutron powder diffraction experiments. This is likely because the $n = 2$ Ruddlesden Popper phase competes with the $n = 1$ RP oxide and the ABO_3 perovskite and undergoes some degree of phase separation during the synthesis.[123]

Importantly, the success of low-temperature topochemical cation-exchange reactions depends on the stability and robustness of the precursor phase undergoing the exchange. The data above show that the $Li_2SrNb_2O_7$ precursor does not serve as a stable starting point for

subsequent reactions, significantly impacting the quality of the manganese-exchanged material produced. The observation of *hkl*-dependent broadening in the $MnSrNb_2O_7$ diffraction data is consistent with extensive stacking disorder in the phase and suggests that the cation exchange is incomplete.

4.3.2.2 80 K neutron powder diffraction data

4.3.2.2.1 Commensurate structural model

Neutron powder diffraction data collected from $MnSrNb_2O_7$ at 80 K could be indexed using a primitive orthorhombic unit cell (a = 5.599(1) Å, b = 5.604(2) Å, c = 18.824(6) Å) consistent with a $\sim\sqrt{2} \times \sim\sqrt{2} \times 1$ geometric expansion of an undistorted n = 2 Ruddlesden-Popper unit cell. A detailed symmetry analysis of the aristotype n = 2 Ruddlesden-Popper structure was used to generate a series of chemically plausible structural models based on the tilting distortions of the Nb–O framework and to deduce their space groups. As noted above, $MnSrNb_2O_7$ is SHG active and hence adopts a non-centrosymmetric crystal structure, so any centrosymmetric space groups could be eliminated from the list of potential space groups on this basis. Close inspection of the diffraction data revealed several possible candidate structures based on distortions of the n = 2 RP structure, consistent with the observed reflection conditions: $a^-a^-c^+/a^-a^-c^+$ ($A2_1am$), $a^-a^-c^+/a^-a^--c^+$ ($Pna2_1$), $a^-b^-c^+/b^-a^-c^+$ ($P2_1nm$), $a^-a^-c^+/-(a^-a^-c^+)$ ($B2cm$) and $a^-b^-c^+/-(a^-b^-)c^+$ ($P2cm$). Structural models were constructed for $MnSrNb_2O_7$ with these tilting patterns and refined against the NPD data collected at 80 K. The best fit to the observed data was achieved using an $A2_1am$ symmetry model.

Since divalent Mn^{2+} cations are exchanged with monovalent Li^+ cations, the number of available coordination sites in the substituted phase is twice the number of transition metal cations present. Therefore, only half of the interlayer coordination sites between the

perovskite double-layers of $MnSrNb_2O_7$ will be occupied by Mn^{2+} cations. There is only one possible crystallographic Mn coordination site (8*b*) in the $A2_1am$ model. As a result, Mn can only adopt a disordered arrangement across these sites to maintain the stoichiometry of the phase.

Closer inspection of the refinement of the commensurate model to the NPD data revealed a series of satellite peaks which could not be indexed by this unit cell or a rational expansion of the unit cell and could not be accounted for by any logical impurities, but are consistent with those observed in the synchrotron X-ray diffraction data. However, these peaks could be indexed by an incommensurate unit cell described in space group $A2_1am(0\beta0)000$ with a propagation vector **q** = (0, 0.81, 0), in which the translational symmetry has been broken along the *y*-axis. This behaviour is consistent with the analogous tantalum compound, $MnSrTa_2O_7$, which also adopts an incommensurately modulated structure.[120]

4.3.2.2.2 Incommensurate structural model

A structural model was constructed with an $a^-a^-c^+/a^-a^-c^+$ tilting distortion, described in space group $A2_1am(0\beta0)000$, and refined against the NPD data collected at 80 K to establish which constituents of $MnSrNb_2O_7$ contribute to the structural modulation. The best fit to the observed data was achieved when a crenel modulation of the Mn^{2+} site occupancy was applied to the model. The refined model indicates that the Mn^{2+} cations adopt a chequerboard-ordered arrangement across the tetrahedral interlayer coordination sites to form a network of corner-linked MnO_5 pseudo-tetrahedra. As described in Chapter 3, this chequerboard arrangement minimises the cation-cation repulsion between adjacent Mn cations. Figure 4.4 illustrates the two possible, local chequerboard ordering patterns, A and B, related by inverting the occupied and unoccupied coordination sites of the 50% occupied interlayer region. The incommensurate modulation of the Mn cations results in an

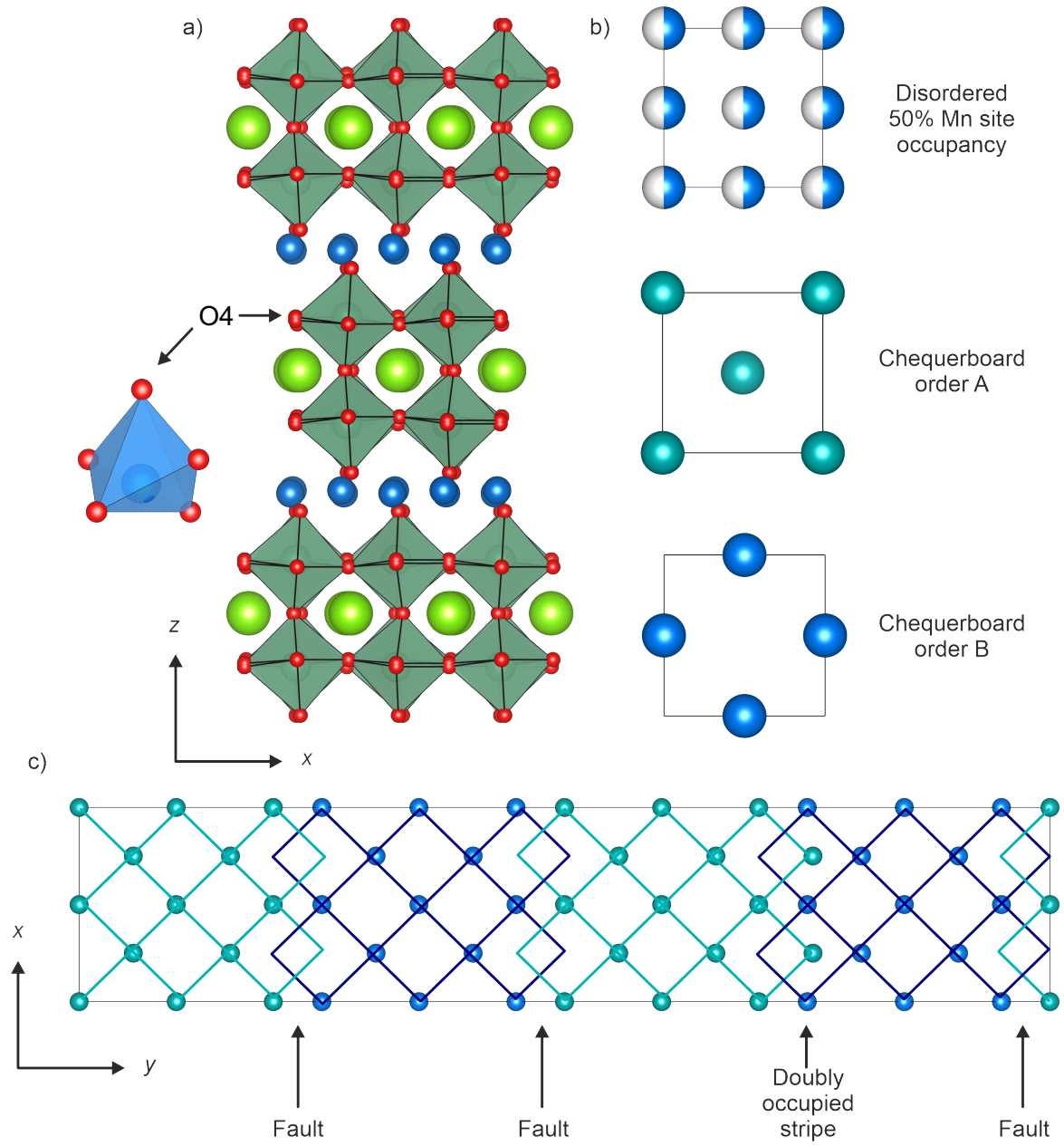


Figure 4.4 a) The average incommensurately modulated crystal structure of $MnSrNb_2O_7$, described in the superspace group $A2_1am(0\beta0)000$. Blue, lime, green and red spheres represent Mn, Sr, Nb and O, respectively. The modulated equatorial oxygen atom, O4, is labelled. b) Two different chequerboard ordering patterns, A and B, are possible when the pseudo-tetrahedral coordination sites are half occupied. c) The intergrowth of the two ordering patterns observed in the interlayer region of $MnSrNb_2O_7$.

intergrowth between the two local ordering patterns. The resulting structure contains distinct regions or domains of chequerboard order A and chequerboard order B, interconnected by either an unoccupied fault boundary or a doubly-occupied stripe boundary, orientated parallel to the *x*-axis. Although the intergrowth inevitably leads to the formation of short

Mn–Mn distances at the boundaries, the average distance between the manganese cations is optimised compared to a disordered model.

The incommensurate modulation of the manganese occupancy can be rationalised by considering that within $MnSrNb_2O_7$, there is a competition between minimising the repulsion between the Mn^{2+} cations and optimising the size of the *A*-site cation coordination site via octahedral tilting. Whilst a commensurate chequerboard ordering of the Mn^{2+}cations maximises the separation between the interlayer cations, it is not symmetry-compatible with the $a^-a^-c^+/a^-a^-c^+$ tilting pattern of the TaO_6 octahedra, which optimises the bonding environment of the strontium cations. This suggests that the incommensurate modulation of the Mn^{2+} site occupancy achieves the ideal compromise between both factors.

Further examination of the refined model revealed that the thermal parameters of the equatorial oxygen atoms (O4) sitting adjacent to the manganese cations were notably larger than the other atoms. This observation suggests that this position is also modulated. To investigate this further, the coordination site was split (O4 and O4'), and a crenel function was added to model a positional modulation. The fit to the data improved when this second modulation was added to the model, which implies that this particular oxygen atom responds to the presence or absence of an adjacent manganese cation within the intralayer region.

The observed, calculated and difference plots from the refinement of the incommensurate $A2_1am(0\beta0)000$ model of $MnSrNb_2O_7$ against the bank 2 and bank 4 NPD data collected at 80 K are shown in Figure 4.5. As can be seen, there is a considerable discrepancy between the observed and calculated plots which results from an inability of the model to account for the irregular peak shapes inherited from the precursor phase $Li_2SrNb_2O_7$. Full details of the refined structure are given in Table 4.1. Selected bond lengths and bond valence sum values for the cations are reported in Table 4.2.

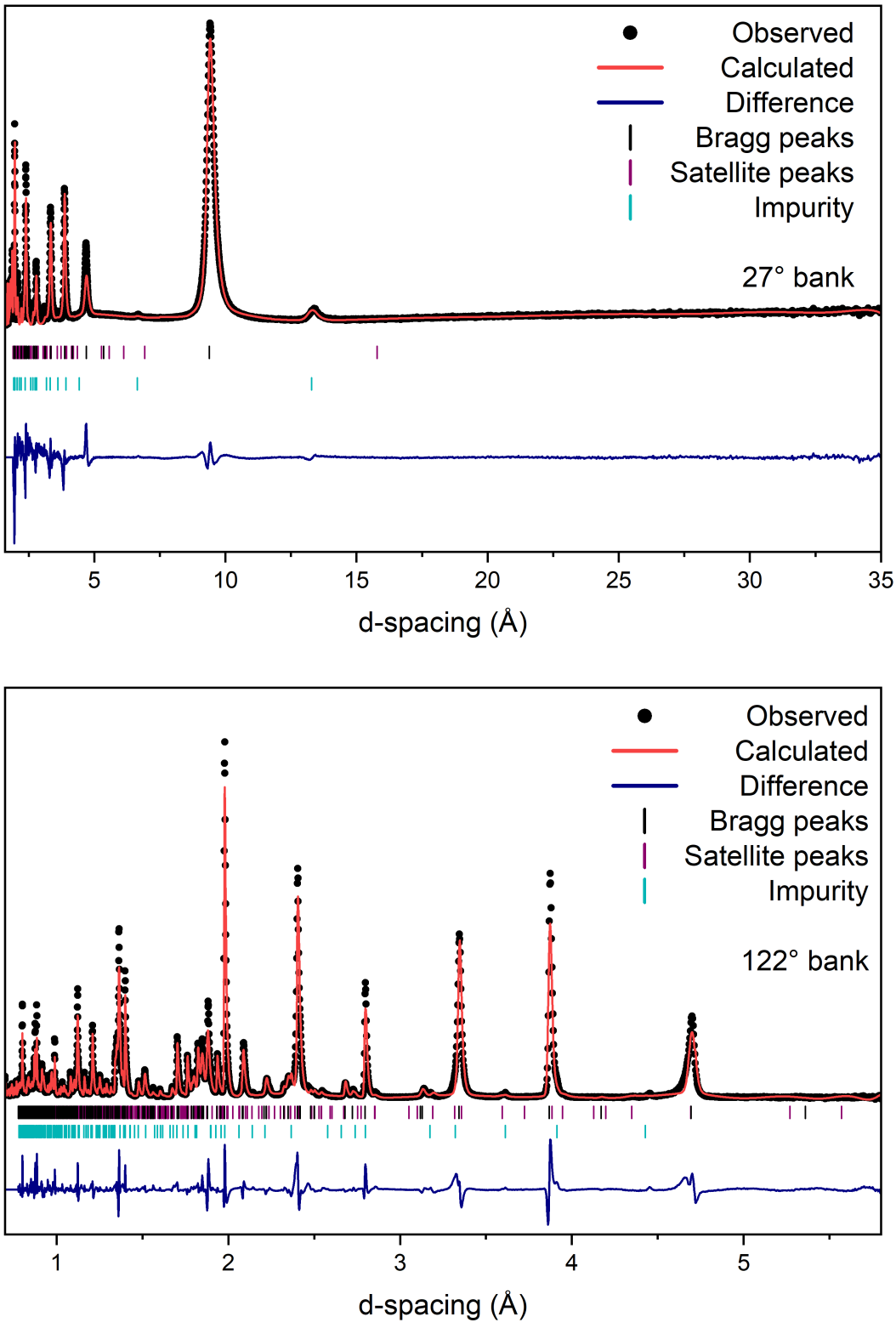


Figure 4.5 Observed, calculated and difference plots from the structural refinement of the $A2_1am(0\beta0)000$ model of $MnSrNb_2O_7$ against the NPD data collected from bank 1-10 (27°) and bank 4-7 (122°) of the WISH diffractometer at 80 K.

Table 4.1 Parameters from the structural refinement of the $A2_1am(0\beta0)000$ model of $MnSrNb_2O_7$ against the NPD data collected at 80 K.

Atom	Site	*x*	*y*	*z*	Occ.	B_{iso} / Å^2
Mn1	8*b*	0.5432(18)	0.488(3)	0.2530(7)	1.0	-0.030(2)*
Sr1	4*a*	0.2331(15)	0.230(2)	0	1.0	0.022(2)
Nb1	8*b*	0.7585(11)	0.2606(12)	0.1102(1)	1.0	0.013(8)
O1	4*a*	0.7362(19)	0.2181(15)	0	1.0	0.015(2)
O2	8*b*	0.7258(15)	0.2702(10)	0.2099(1)	1.0	0.006(1)
O3	8*b*	0.9863(13)	0.5002(15)	0.0954(2)	1.0	0.011(2)
O4	8*b*	0.0097(12)	0.009(2)	0.1033(7)	1.0	0.015(2)
O4'	8*b*	0.0097(12)	0.009(2)	0.1096(6)	1.0	0.015(2)

$MnSrNb_2O_7$ - Superspace group $A2_1am(0\beta0)000$ q2 = 0.814(2)

a = 5.5934(3) Å, *b* = 5.5892(3) Å, *c* = 18.7763(9) Å

Volume = 587.00(7) Å^3

Formula weight = 440.37 g mol^{-1}, Z = 4

Radiation source: Neutron Time of Flight, Instrument: WISH

Temperature: 80 K

R_p = 10.56 % $_wR_p$ = 12.35 %

* Negative value of B_{iso} suggests intensity is not being correctly accounted for by this model.

Table 4.2. Selected bond lengths and cation bond valence sums from the structural refinement of the $A2_1am(0\beta0)000$ model of $MnSrNb_2O_7$ against the NPD data collected at 80 K.

Cation	Anion	Bond length	BVS
Mn1	O2 × 1	1.81181(6)	+ 1.970
	O2 × 1	2.07427(8)	
	O2 × 1	2.31435(9)	
	O2 × 1	2.32160(9)	
	O4 × 1	2.71090(12)	
Sr1	O1 × 1	2.50494(14)	+ 2.261
	O4 × 2	2.61713(8)	
	O3 × 2	2.71943(8)	
	O3 × 2	2.73653(8)	
	O1 × 1	2.77986(15)	
	O1 × 1	2.81452(1)	
	O4 × 2	2.81782(9)	
Nb1	O3 × 1	1.86930(7)	+ 5.000
	O2 × 1	1.88169(8)	
	O4 × 1	1.99215(8)	
	O3 × 1	2.04517(8)	
	O4 × 1	2.05530(8)	
	O1 × 1	2.08650(9)	

4.3.2.3 Magnetisation data

Magnetisation data were collected from $MnSrNb_2O_7$ in an applied field of 100 Oe in the temperature range $5 \leq T/K \leq 300$ K. The zero-field-cooled (ZFC) and field-cooled (FC) data, shown in Figure 4.6, can be fit to the Curie-Weiss law in the region $100 \leq T/K \leq 300$ K, yielding a Curie constant of $C = 5.41$ cm^3 K mol^{-1} and a Weiss constant of $\theta_{CW} = -184.7$ K. The Curie constant was used to calculate the effective magnetic moment, $\mu_{eff} = 6.58$ μ_B, which can be directly compared to the calculated moment for Mn^{2+} (5.92 μ_B) and is higher than the spin-only moment expected for a single tetrahedral Mn^{2+} (S=5/2) ion per formula unit. The observed moment exceeds the calculated moment, but unlike tetrahedrally coordinated Fe^{2+} and Co^{2+}, this observation cannot be attributed to second-order spin-orbit

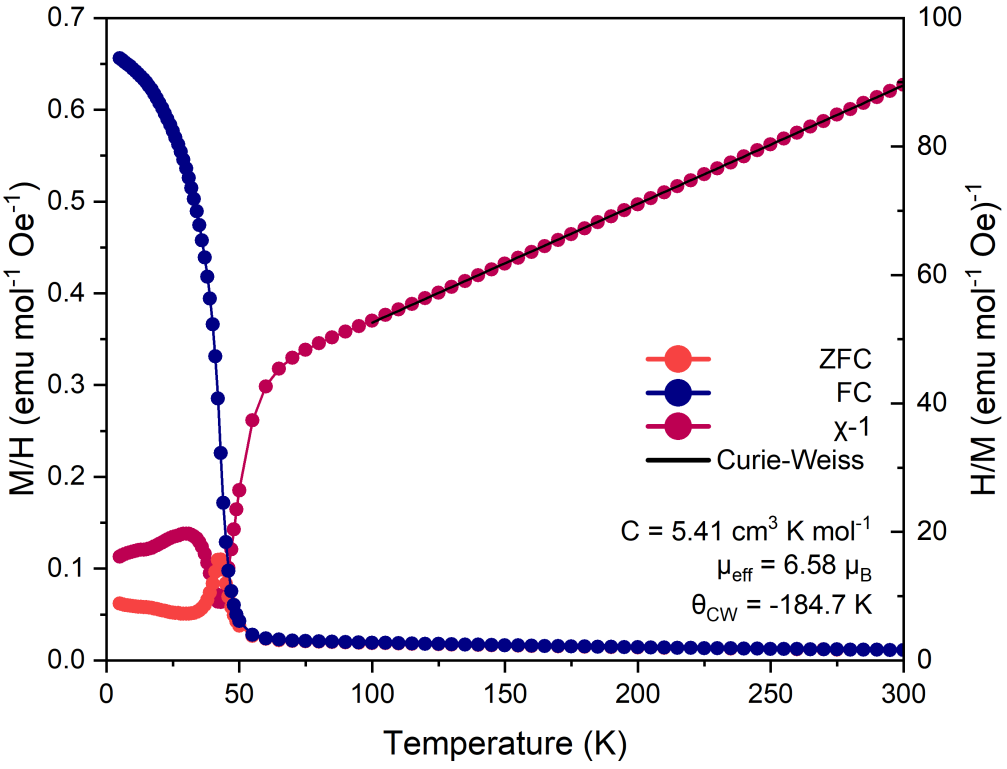


Figure 4.6 Zero-field-cooled and field-cooled magnetisation data collected from $MnSrNb_2O_7$ as a function of temperature in an applied field of 100 Oe.

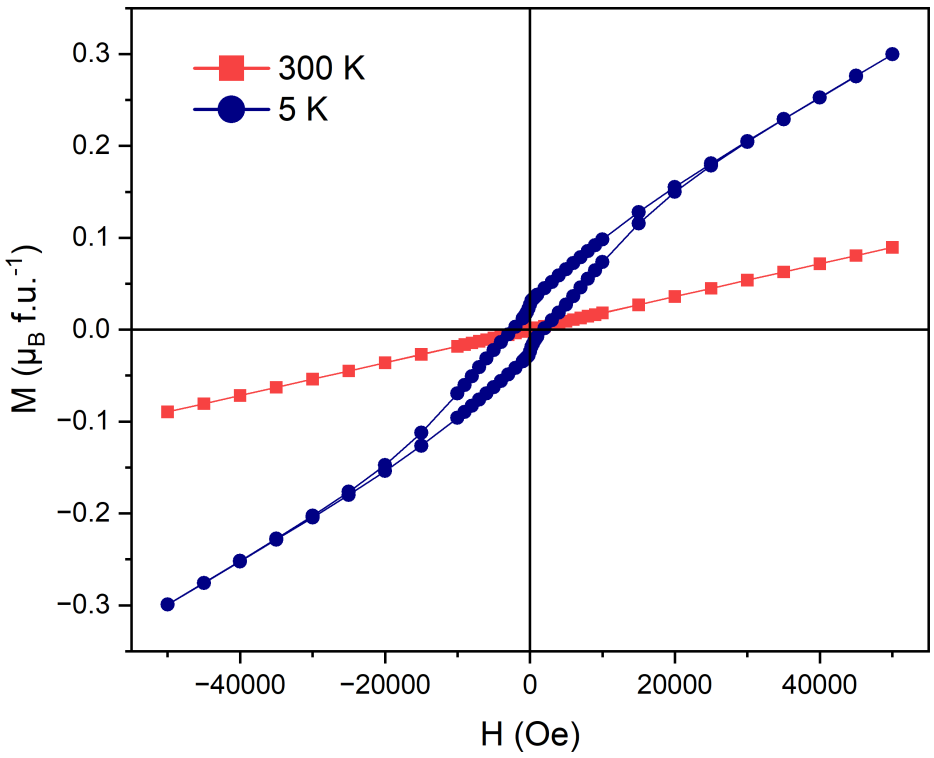


Figure 4.7 Magnetisation-field data collected from $MnSrNb_2O_7$ at 300 K and 5 K.

coupling, since the excited state that mixes with the ground state is spin forbidden. An incomplete quenching of the orbital angular momentum remains a plausible explanation, however, as the local environment of Mn^{2+} in $MnSrNb_2O_7$ deviates from an ideal tetrahedral geometry. The pseudo-tetrahedral coordination will alter the crystal field splitting, and therefore orbital contributions to the effective magnetic moment might be expected. The negative value of the Weiss constant is indicative of antiferromagnetic interactions between spins. The ZFC and FC data sharply diverge at approximately $T_N = 40$ K (antiferromagnetic in character). The magnetisation-field isotherm collected at 300 K is linear and passes through the origin, with data collected at 5 K exhibiting a weak hysteresis (Figure 4.7). This suggests that the Mn^{2+} ions adopt a canted antiferromagnetic arrangement below the transition temperature.

It should be noted that as a final step in the synthesis of $MnSrNb_2O_7$ and prior to magnetisation measurements, the sample was heated under a flow of hydrogen gas in order to reduce any manganese oxide impurity that may have been present in the sample but undetected by diffraction. This precaution was necessary because Mn_3O_4 undergoes a transition to ferrimagnetic state at T_C = 43 K, which is close to the magnetic transition temperature of $MnSrNb_2O_7$.[124,125] This step ensures that the observed magnetic ordering is not due to an Mn_3O_4 impurity.

4.3.2.4 Low temperature (1.5 K) neutron powder diffraction data

Neutron powder diffraction data collected from $MnSrNb_2O_7$ at 1.5 K exhibit a series of additional diffraction peaks not present in the data collected at 80 K, which can be attributed to magnetic order in the phase (Figure 4.8). These additional diffraction features appear as pairs and can be indexed using a single magnetic propagation vector (**k** = 0, 0, 0) of the incommensurately modulated crystallographic unit cell. This evidence further confirms that the manganese ions are modulated in this phase since they are the only magnetic ions present. A series of possible magnetic models were constructed based on the $A2_1am(0\beta0)000$ symmetry-modulated crystal structure using the ISODISTORT software package and were refined against the 1.5 K neutron diffraction data. The best fit was obtained using an $A2_1a'm'(0\beta0)000$ symmetry magnetic model, which can be constructed by applying the $m\Gamma2$ distortion mode to the $A2_1am(0\beta0)000$ crystallographic structure. This mode permits magnetic moments to be orientated along the *x*-, *y*- and *z*-directions, so these three parameters were allowed to refine freely. Both the ordered moment along the *x*- and *y*-directions converged to zero within error and henceforth were constrained to be zero in the refinement. The moment along the *z*-direction refined to a value of 3.90(2) μ_B, approximately 80% of the spin-only moment expected for a single S=5/2 tetrahedral Mn^{2+} cation. The refined magnetic model shows that the Mn cations adopt a G-type

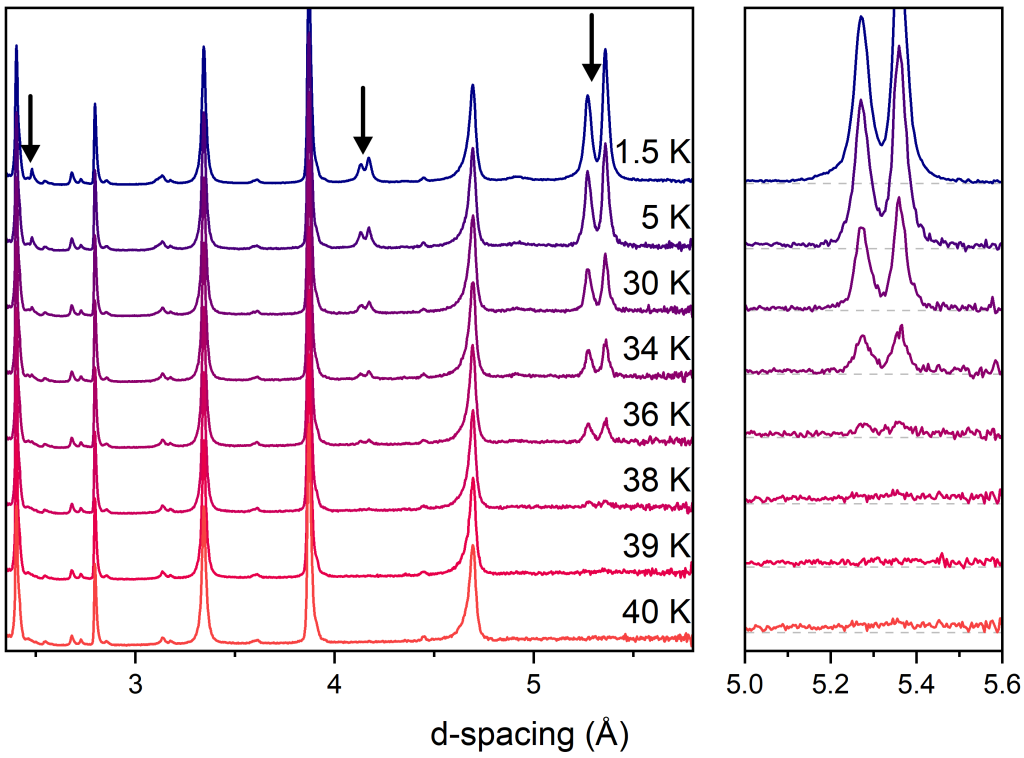


Figure 4.8 NPD data collected from $MnSrNb_2O_7$ as a function of temperature. Black arrows indicate magnetic scattering peaks. The right-hand image shows the region around the magnetic peaks at ~ 5.3 Å at a greater magnification. The grey-line is used to guide the reader's eye.

antiferromagnetic arrangement with moments orientated along the *z*-axis (Figure 4.9). Magnetisation data indicate that there is a ferromagnetic component (canting) to the magnetic structure; however, this could not be observed in the NPD data due to its small size. The observed, calculated, and difference plots of the refinement of the incommensurate $A2_1a'm'(0\beta0)000$ model of $MnSrNb_2O_7$ against the bank 1 and bank 4 NPD data collected at 1.5 K are shown in Figure 4.10. Full details of the refined structure are given in Table 4.3. Selected bond lengths and bond valence sum values for the cations are reported in Table 4.4.

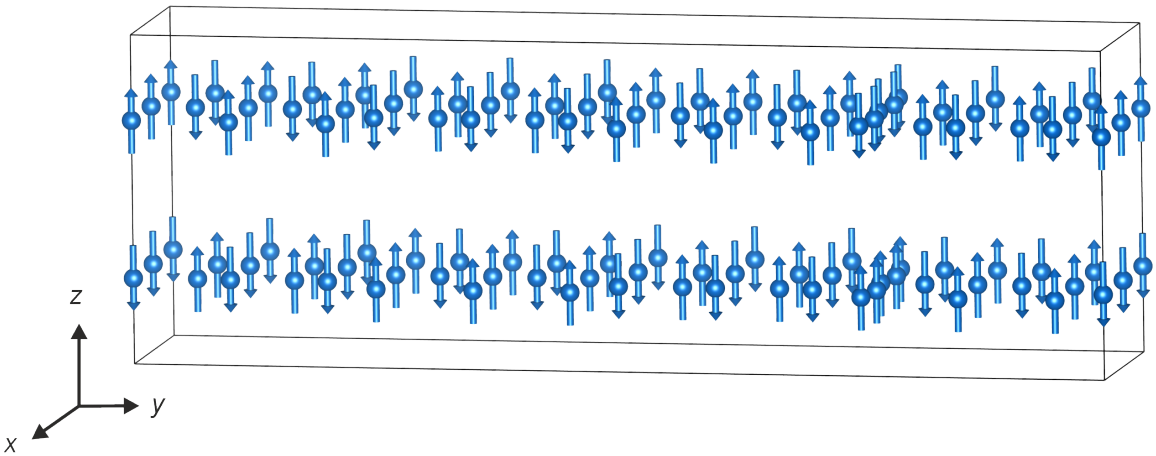


Figure 4.9 The G-type antiferromagnetic arrangement of Mn^{2+} ions adopted by $MnSrNb_2O_7$. The supercell depicted is an approximate structure, not a unit cell.

Table 4.3 Parameters from the structural and magnetic refinement of the magnetically ordered $A2_1a'm'(0\beta0)000$ model of $MnSrNb_2O_7$ against the NPD data collected at 1.5 K.

Atom	Site	*x*	*y*	*z*	Occ.	B_{iso} / Å^2
Mn1	8*b*	0.505(3)	0.522(2)	0.2522(10)	0.5	0.001(1)
		$M_x = 0$	$M_y = 0$	$M_z = 3.90(2)$		
Sr1	4*a*	0.2272(17)	0.237(2)	0	1.0	0.019(2)
Nb1	8*b*	0.7689(13)	0.2608(15)	0.1094(1)	1.0	0.009(1)
O1	4*a*	0.7148(17)	0.2186(19)	0	1.0	0.001(2)
O2	8*b*	0.7473(14)	0.2701(12)	0.2089(1)	1.0	0.014(1)
O3	8*b*	-0.9977(17)	0.4949(15)	0.0951(2)	1.0	0.015(2)
O4	8*b*	0.0087(16)	0.0009(17)	0.1012(6)	0.5	0.019(2)
O4'	8*b*	0.0087(16)	0.0009(17)	0.1132(5)	0.5	0.019(2)

$MnSrNb_2O_7$ – Magnetic superspace group $A2_1a'm'(0\beta0)000$ (#31.127) q2 = 0.808154

a = 5.5903(3) Å, b = 5.5909(3) Å, c = 18.7701(9) Å

Volume = 586.7(15) Å^3

Formula weight = 440.37 g mol^{-1}, Z = 4

Radiation source: Neutron Time of Flight, Instrument: WISH

Temperature: 1.5 K

R_p = 10.98 % $_wR_p$ = 12.91 %

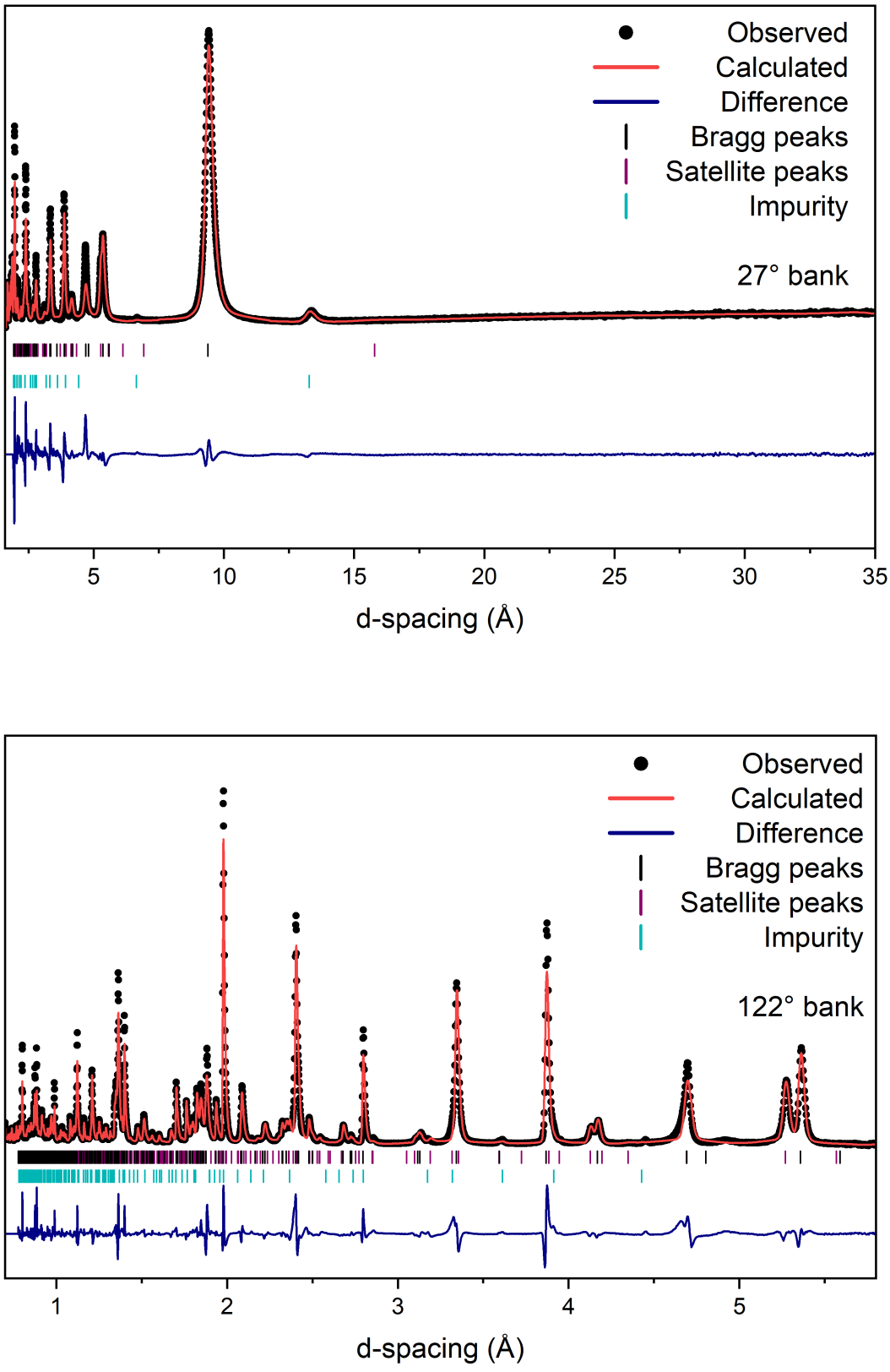


Figure 4.10 Observed, calculated and difference plots from the structural refinement of the magnetically ordered $A2_1a'm'(0\beta0)000$ model of $MnSrNb_2O_7$ against the NPD data collected from bank 1-10 (27°) and bank 4-7 (122°) of the WISH diffractometer at 1.5 K.

Table 4.4 Selected bond lengths and cation bond valence sums from the structural refinement of the magnetically ordered $A2_1a'm'(0\beta0)000$ model of $MnSrNb_2O_7$ against the NPD data collected at 1.5 K.

Cation	Anion	Bond length	BVS
Mn1	O2 × 1	1.77599(8)	+ 2.140
	O2 × 1	1.9976(1)	
	O2 × 1	2.3584(1)	
	O2 × 1	2.3788(1)	
	O4 × 1	2.5996(1)	
Sr1	O1 × 1	2.5043(2)	+ 2.504
	O4 × 2	2.5595(1)	
	O3 × 2	2.6711(1)	
	O3 × 2	2.6942(1)	
	O4 × 2	2.7569(1)	
	O1 × 1	2.7744(2)	
	O1 × 1	2.8192(3)	
Nb1	O2 × 1	1.80642(9)	+ 5.405
	O3 × 1	1.8653(1)	
	O4 × 1	1.9912(1)	
	O1 × 1	2.0025(1)	
	O3 × 1	2.0514(1)	
	O4 × 1	2.0554(1)	

4.3.2.5 Variable temperature neutron powder diffraction data

Neutron powder diffraction data was collected from $MnSrNb_2O_7$ at 1.5 K, 5 K, 10 K, 15 K, 20 K, 25 K, 30 K to 45 K at 1 K temperature increments, 50 K, 60 K, and 80 K. A magnetically ordered $A2_1a'm'(0\beta0)000$ model was sequentially refined against the data collected at each temperature, where the output file from the first refinement becomes the input file for the next. After the first refinement, all variables were turned off, and only the lattice parameters and the magnetic moment along the *z*-direction were allowed to vary freely in subsequent refinements. Figure 4.11 illustrates the evolution of the neutron powder diffraction data as a function of temperature. The intensity of the magnetic Bragg peaks, indicated by white arrows, decreases as the temperature increases, completely disappearing above 38 K.

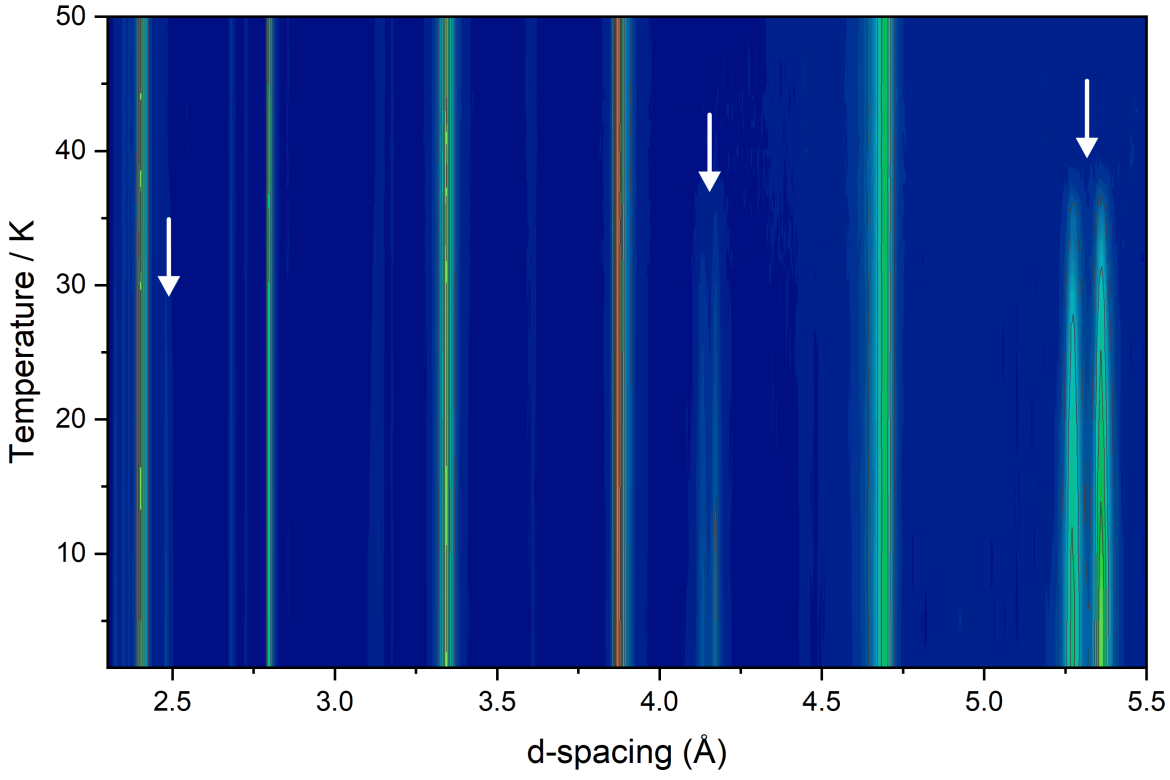


Figure 4.11 Evolution of the intensity of the neutron diffraction data collected from $MnSrNb_2O_7$ as a function of temperature. Magnetic peaks are labelled with arrows.

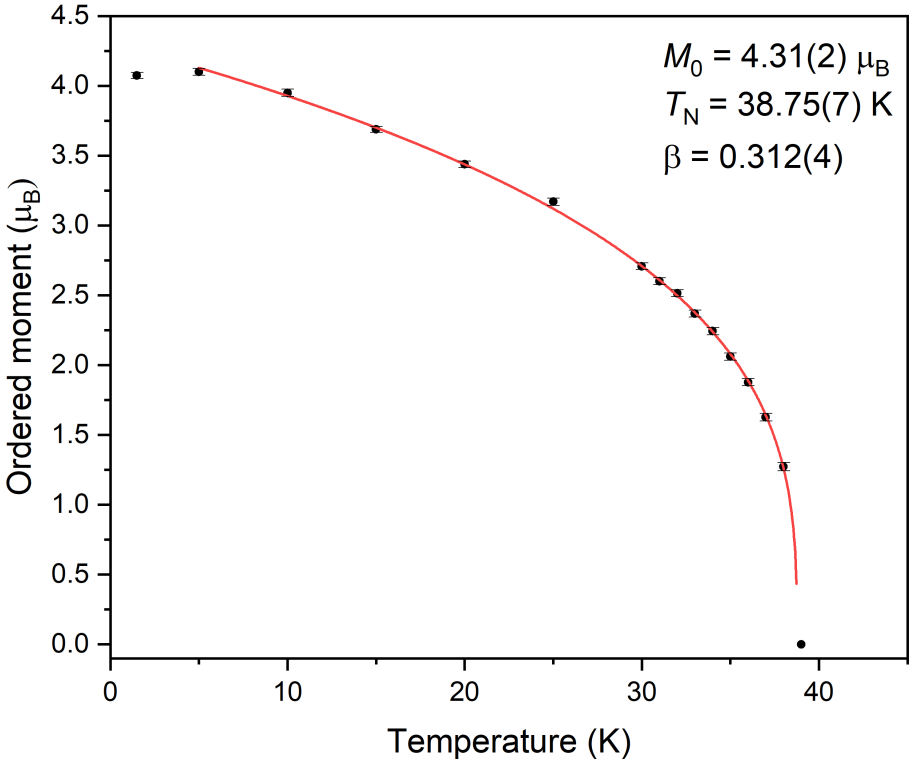


Figure 4.12 The ordered magnetic moment extracted from the refinement of an incommensurately modulated A2$_1$*a*'*m*'(0β0)000 model against NPD data collected from $MnSrNb_2O_7$ in the temperature range 1.5 K ≤ *T*/K ≤ 39 K.

Figure 4.12 shows the temperature dependence of the ordered moment obtained from the neutron powder diffraction data. This can be approximately fit to a power law, $M = M_0(1 - \frac{T}{T_N})^{\beta}$, to yield a transition temperature, T_N, of 38.75(7) K, which is in good agreement with the value obtained from magnetometry.[121] The extracted value of the exponential term (β = 0.312(4)) is indicative of strong 3D magnetic interactions. Interestingly, for the analogous compounds $MnSrTa_2O_7$ and $MnCaTa_2O_7$, a significant broadening of the magnetic diffraction peaks and the presence of diffuse scattering in this region was observed above the magnetic transition temperature, attributed to the onset of weak 2D magnetic correlations above this temperature. Figure 4.8 highlights that a similar behaviour was not observed in $MnSrNb_2O_7$, where no diffuse scattering is seen above T_N.

This suggests that the onset of long-range three-dimensional magnetic order occurs instantaneously at T_N and not over a broader temperature range as in the tantalum phases.

The evolution of the lattice parameters as a function of temperature is shown in Figure 4.13. The *c* lattice parameter increases with temperature, and both the *a* and *b* lattice parameters

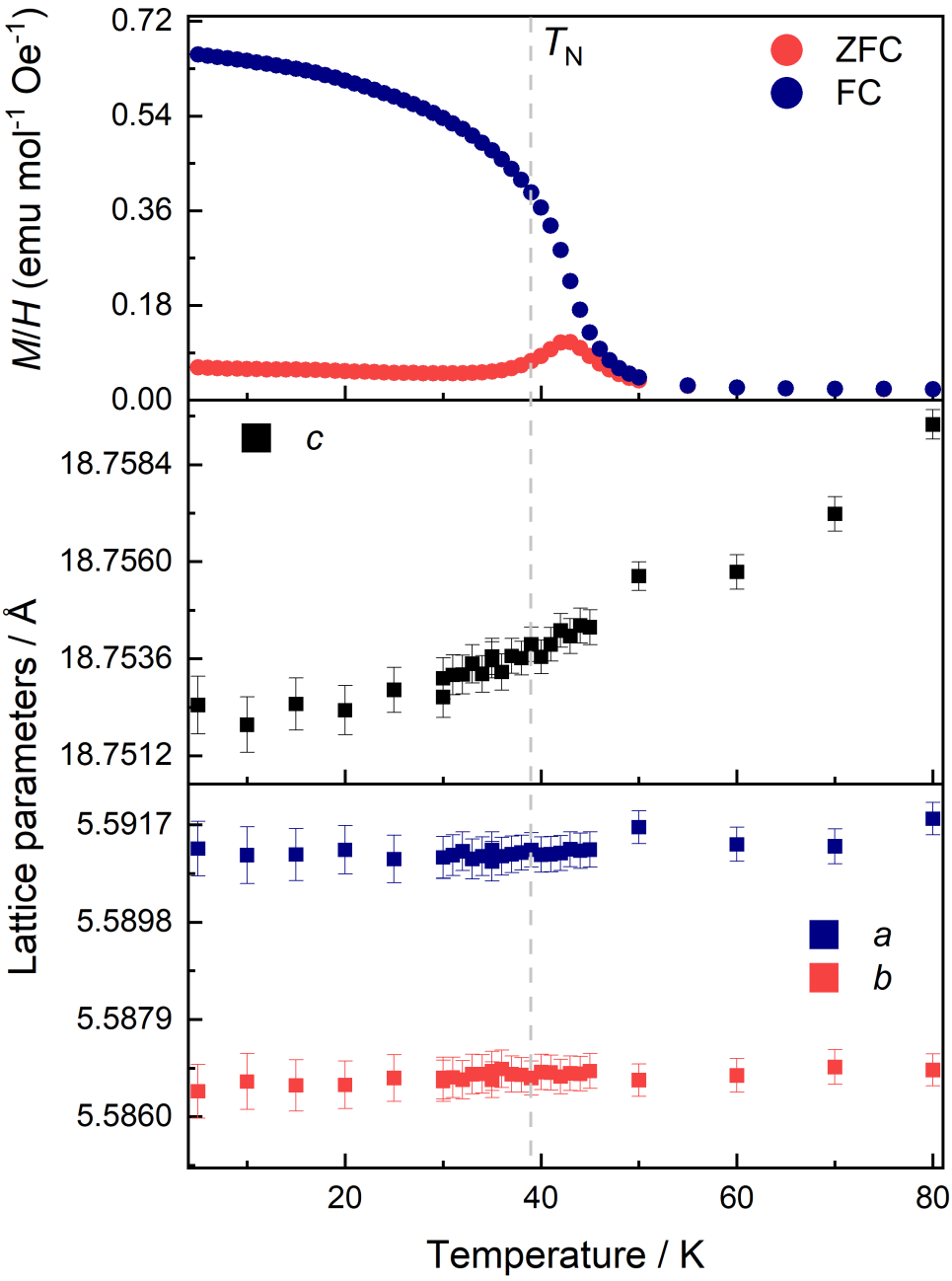


Figure 4.13 Zero-field cooled and field cooled magnetisation data and the lattice parameters extracted from NPD data collected from $MnSrNb_2O_7$, plotted as a function of temperature in the range $5 \leq T/K \leq 80$.

remain approximately constant across the measured temperature range. Furthermore, $MnSrNb_2O_7$ does not exhibit any apparent lattice parameter anomalies that coincide with the onset of magnetic order, which indicates that the electric and magnetic polarisations are not strongly coupled within $MnSrNb_2O_7$, unlike the analogous $MnSrTa_2O_7$ phase, which displays this signature of magnetoelectric coupling.[120]

4.3.2.6 Muon spectroscopy

A series of zero-field muon spin resonance measurements were performed over the temperature range $1 \leq T/K \leq 42$ K, with a particular focus around T_N. The asymmetry data of $MnSrNb_2O_7$ at 1 K, 30 K and 39 K are shown in Figure 4.14. A strong oscillatory signal can be observed below the magnetic ordering temperature, indicative of long-range magnetic order. Above the ordering temperature, a weak relaxing signal was observed, consistent with spin fluctuations but not magnetic order.

The asymmetry signals can be fit to an expression given by $A(t) = A_{relax}P(t) + A_{baseline}$ where $P(t)$ is given by $\cos(\omega_L t)\, e^{-\lambda_1 t}$. Here ω_L is the Larmor frequency of the muon, A_{relax} is an oscillating and relaxing term, and $A_{baseline}$ is a non-relaxing term. The temperature dependence of the relaxation rate, λ, shown in Figure 4.14, remains approximately temperature-independent across the measured temperature range.

The muon precession frequencies follow a typical temperature dependence, smoothly decreasing from approximately 30 MHz before rapidly falling to zero above T_N = 39 K (Figure 4.15). The temperature dependence of the precession frequency can be fit to the expression $v = v_0 \left[1 - \left(\frac{T}{T_N}\right)^{\alpha}\right]^{\beta}$ where $\alpha > 1$ and $\beta < 1$ are numbers, to yield a magnetic ordering temperature of T_N = 39.086 K, which is in excellent agreement with the value extracted from magnetisation measurements and NPD data.

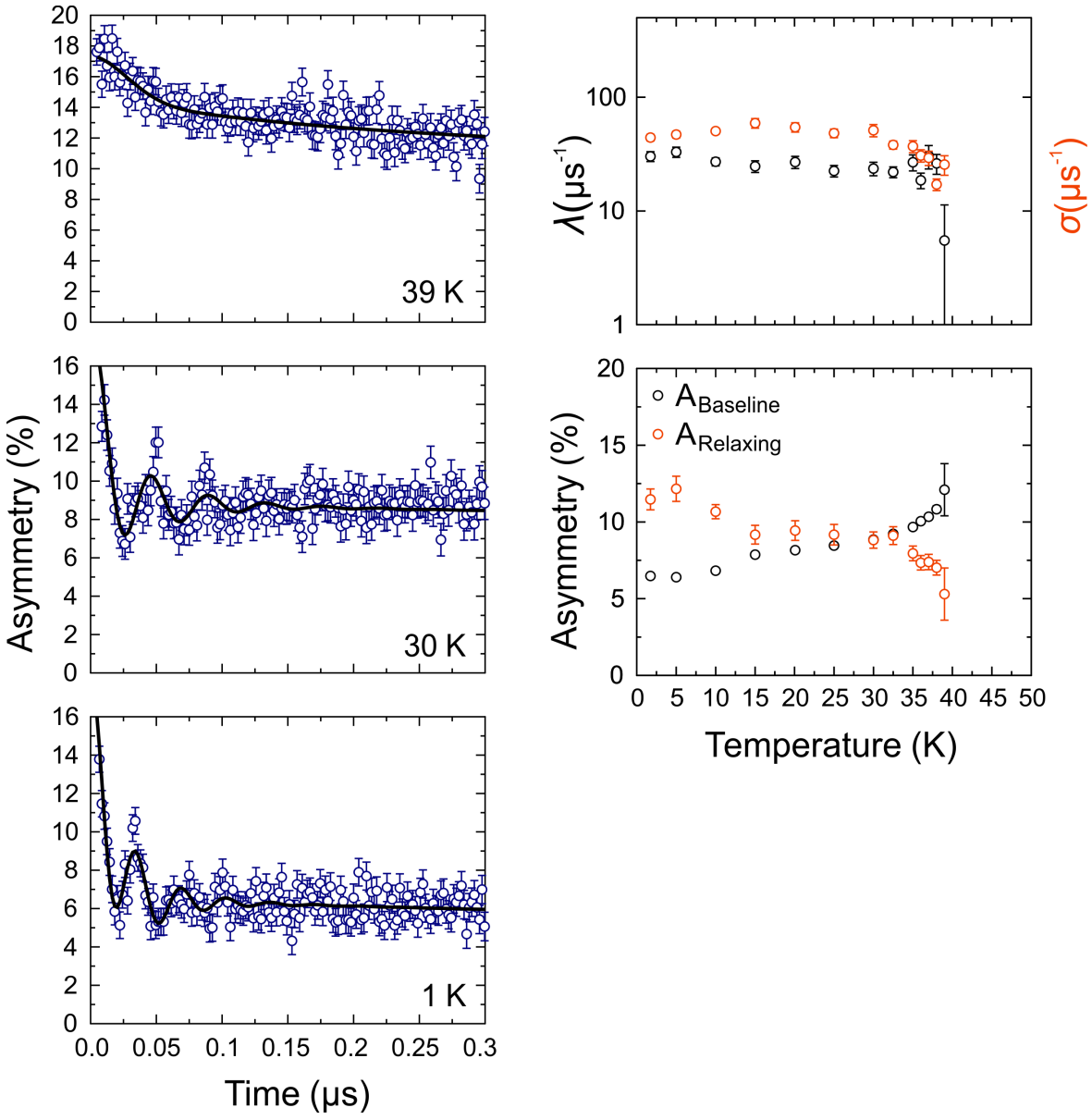


Figure 4.14 The zero-field muon SR asymmetry data for $MnSrNb_2O_7$ measured at T = 1 K, 30 K and 39 K. The temperature dependence of relaxation rate (λ and σ) and the baseline asymmetry and relaxing asymmetry are shown.

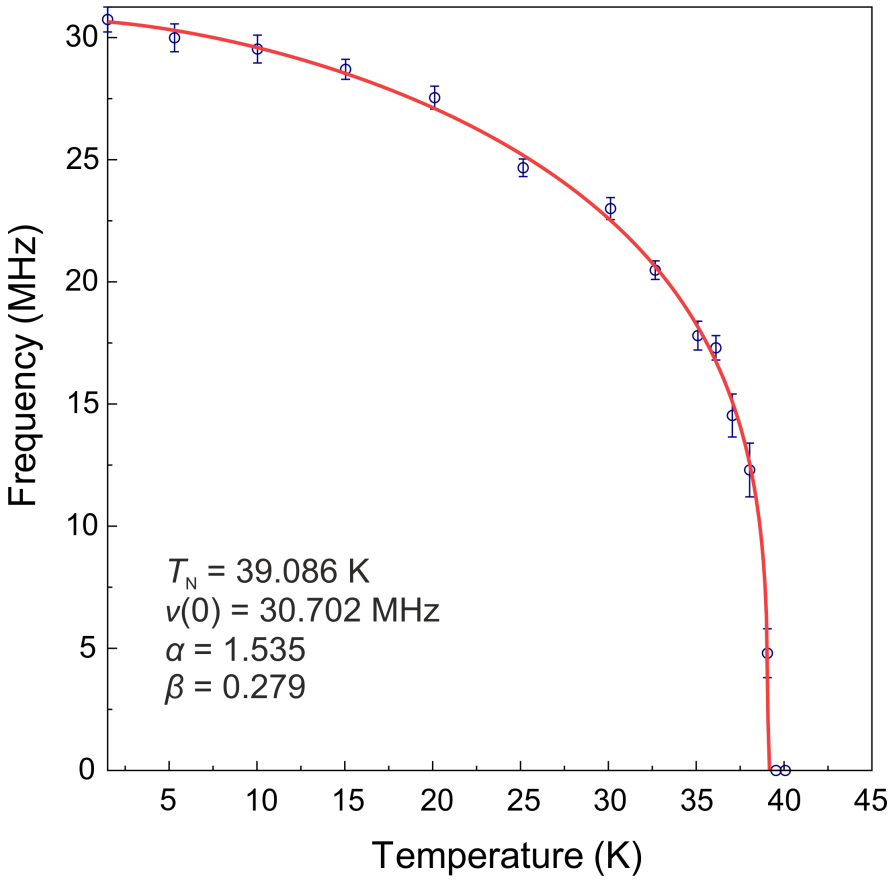


Figure 4.15 Temperature evolution of the muon precession frequency of $MnSrNb_2O_7$.

4.4 Discussion

The reaction of $Li_2SrNb_2O_7$ with anhydrous manganese chloride results in the topochemical cation exchange of the host lattice and the formation of $MnSrNb_2O_7$. At room temperature, $MnSrNb_2O_7$ adopts an incommensurately modulated, polar $A2_1am(0\beta0)000$ $n = 2$ Ruddlesden-Popper structure described by an $a^-a^-c^+/a^-a^-c^+$ tilting distortion. This symmetry is established by applying the X_2^+ (a;0) and the X_3^- (b;0) irreducible representations, which describe the $a^0a^0c^+/a^0a^0c^+$ and $a^-a^-c^0/a^-a^-c^0$ tilting distortions, respectively, along with a polar distortion mode that transforms like the irrep Γ_5^-, to the undistorted $I4/mmm$ aristotype structure. $MnSrNb_2O_7$ retains the same noncentrosymmetric structure as its precursor phase, $Li_2SrNb_2O_7$. Although the manganese coordination site occupancy is incommensurately modulated, the average structure of $MnSrNb_2O_7$ remains consistent with that of $Li_2SrNb_2O_7$. Therefore, the Mn for Li cation exchange does not affect the $a^-a^-c^+/a^-a^-c^+$ tilting distortion of the $SrTa_2O_7$ layers. This observation can be rationalised on the basis of Li^+ and Mn^{2+} cations sharing a similar ionic radius. This behaviour is analogous to the related tantalum phase, $MnSrTa_2O_7$, which also adopts an $A2_1am(0\beta0)000$ structure. The magnitudes of the tilts along each direction were measured. It was found that the tilt along the a direction was 2.0415(3)°, while the tilt along the c direction was 1.4246(0)°. Although these rotations are small, they are larger than the calculated errors, which confirms that the rotations are real and that $MnSrNb_2O_7$ does indeed adopt a $A2_1am$ structure at 80 K.

The cation-exchange reactions of the related phases $Li_2SrTa_2O_7$ and $Li_2CaTa_2O_7$ have also been extensively studied.[119,120] As previously noted, $MnSrTa_2O_7$ adopts a polar structure described in an $A2_1am$ space group, consistent with an $a^-a^-c^+/a^-a^-c^+$ tilting pattern. On cooling to $T_N = 43$ K, $MnSrTa_2O_7$ undergoes a transition to a canted antiferromagnetic state.

The onset of magnetic order is observed in the NPD data, with a large lattice parameter anomaly seen upon further cooling to T_A = 38 K, coinciding with a significant increase in the ferromagnetic moment of the phase. Detailed analysis of the crystal structure reveals that the lattice parameter anomaly occurs due to a substantial change in the magnitude of the polar distortion mode of $MnSrTa_2O_7$. These observations of a coincident change in both the magnetic and electric polarisations demonstrate the existence of magnetoelectric coupling in $MnSrTa_2O_7$. This is in contrast to $MnSrNb_2O_7$, where no such anomaly is observed in the lattice parameters.

The analogous phase $MnCaTa_2O_7$ is also polar but crystalises in the $P2_1nm$ space group, adopting a subtly different tilting distortion of the TaO_6 octahedra ($a^-b^-c^+/b^-a^-c^+$). Upon cooling, $MnCaTa_2O_7$ also undergoes a transition to an antiferromagnetic state. However, unlike $MnSrTa_2O_7$, a ferromagnetic component to the magnetic order is not observed, despite a canting of the moments being compatible with the symmetry of the system. Critically, although $MnCaTa_2O_7$ exhibits a lattice parameter anomaly and a step change in the magnitude of its polar distortion, this is not accompanied by an increase in the ferromagnetic moment of the phase, clearly demonstrating that the magnetoelectric coupling in this class of materials is strongly dependent on the exact symmetry of the structural distortions and magnetic ordering modes.

Structurally, $MnSrNb_2O_7$, $MnSrTa_2O_7$ and $MnCaTa_2O_7$ differ in several ways. As previously discussed, $MnSrNb_2O_7$ and $MnSrTa_2O_7$ both adopt incommensurately modulated, polar structures characterised by an $a^-a^-c^+/a^-a^-c^+$ tilting pattern described in the superspace group $A2_1am(0\beta0)000$. In comparison, $MnCaTa_2O_7$ adopts a commensurate, polar structure described in space group $P2_1nm$ with an $a^-b^-c^+/b^-a^-c^+$ tilting pattern (Figure 4.16). Interestingly, the $P2_1nm$ structure can be related to the

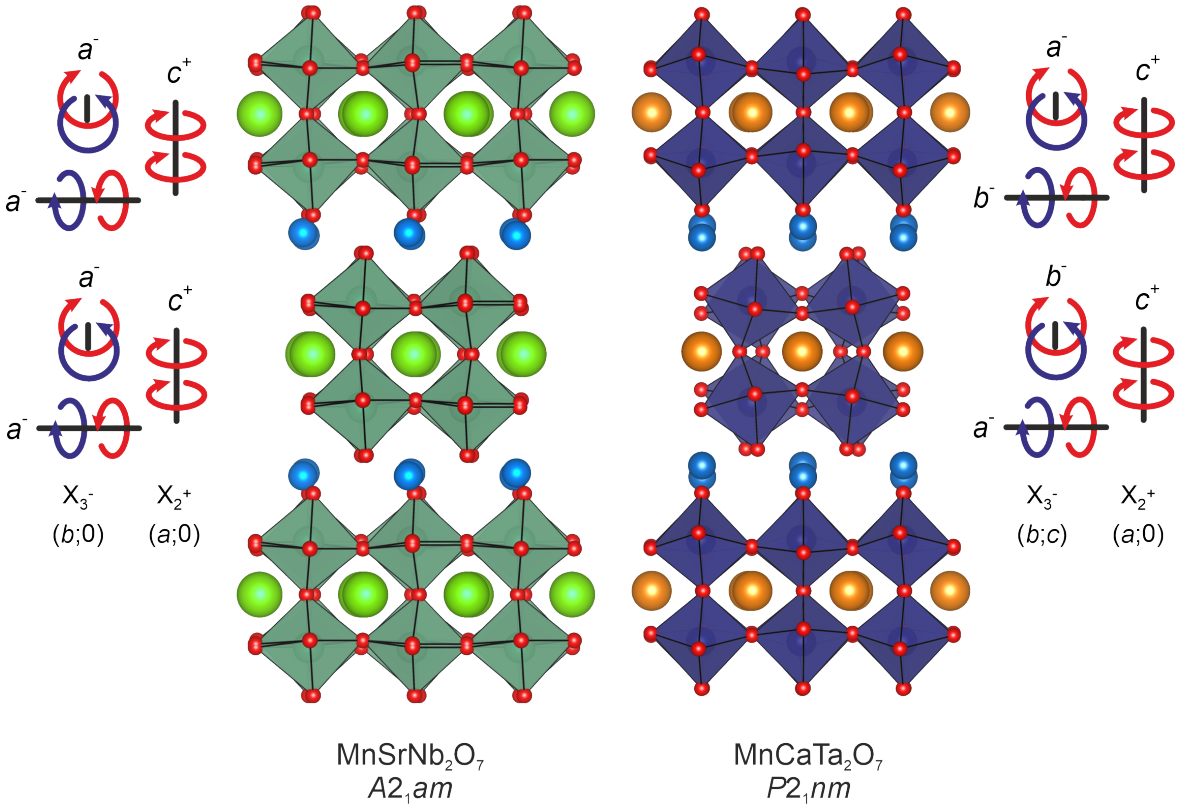


Figure 4.16 The crystal structures of $MnSrNb_2O_7$ ($A2_1am$) and $MnCaTa_2O_7$ ($P2_1nm$) alongside the direction and magnitude of the octahedral tilting distortions and to corresponding irreducible representations which can be used to describe each structure when applied to the *I*4/*mmm* aristotype. Blue, lime, green, navy, orange and red spheres represent Mn, Sr, Nb, Ta and Ca and O, respectively.

undistorted *I*4/*mmm* aristotype structure via the same three irreps as the $A2_1am$ structure: X_2^+ (*a*;0), X_3^- (*b*;c) octahedral rotations and the polar distortion mode Γ_5^-, where the order parameter of the X_3^- mode differs from that in $A2_1am$. The symmetries of these structural distortion modes are consistent with a trilinear-coupled hybrid improper mechanism and suggest that the mechanism by which the electronic polarisation is stabilised in this series of materials is identical. The precursor phases $Li_2SrNb_2O_7$ and $Li_2SrTa_2O_7$ both adopt structures described in the space group $A2_1am$, which is conserved upon cation exchange. In contrast, substituting Li^+ with Mn^{2+} in $Li_2CaTa_2O_7$ induces a structural transition from $Pna2_1$ to $P2_1nm$.

In all three phases, the manganese cations are ordered in a chequerboard pattern within the pseudo-tetrahedral coordination sites of the interlayer region. $MnSrNb_2O_7$ and $MnSrTa_2O_7$ adopt incommensurately modulated structures to achieve the optimal balance between minimising Mn–Mn repulsion and optimising Sr cation bonding via octahedral tilting. However, in the case of $MnCaTa_2O_7$, maximising the interatomic distance between manganese cations is prioritised, resulting in chequerboard ordering taking precedence over octahedral tilting.

The differing structures of $MnSrNb_2O_7$, $MnSrTa_2O_7$ and $MnCaTa_2O_7$ significantly influence their physical properties and behaviours. In each phase, the manganese cations adopt a G-type antiferromagnetic arrangement, with their magnetic moments orientated along the *z*-axis at low temperatures. Notably, the strontium-based phases display a significant ferromagnetic component to their magnetic structure, while the calcium analogue does not show evidence of ferromagnetism. Among the three phases, $MnSrNb_2O_7$ has the lowest magnetic ordering temperature. This is attributed to the presence of stacking faults within the material, which are expected to disrupt and delay the onset of long-range magnetic order by weakening the magnetic interactions between the manganese cations. Additionally, $MnSrTa_2O_7$ and $MnCaTa_2O_7$ demonstrate two-dimensional ordering above their respective magnetic ordering temperatures, indicated by the broadening of the magnetic diffraction peaks and the persistence of diffuse magnetic scattering above T_N. In contrast, no evidence of strong 2D interactions was observed in $MnSrNb_2O_7$. Furthermore, whilst the electronic and magnetic polarisations appear to be strongly coupled in $MnSrTa_2O_7$, there is no evidence of this phenomenon in $MnSrNb_2O_7$, even though both phases adopt the same, incommensurately modulated $A2_1am(0\beta0)000$ structure and display almost identical structural and magnetic behaviours.

Finally, the low-temperature cation exchange reactions of $Li_2SrNb_2O_7$ appear less robust and reliable than the equivalent reactions of the other precursor phases in this series. This will become more apparent in the following chapter, which further explores the cation exchange chemistry of $Li_2SrNb_2O_7$.

4.5 Conclusions

$MnSrNb_2O_7$ was successfully synthesised through the topochemical cation-exchange reaction of $Li_2SrNb_2O_7$ using anhydrous $MnCl_2$. Structural characterisation revealed that $MnSrNb_2O_7$ retains the polar Ruddlesden-Popper framework of the parent phase, adopting a distorted $a^-a^-c^+/a^-a^-c^+$ structure described in the superspace group $A2_1am(0\beta0)000$, with a propagation vector **q** = (0, 0.81, 0). The Mn^{2+} cations occupy the pseudo-tetrahedral sites of the intralayer region of the structure and are incommensurately modulated to optimise both the octahedral tilting and the Mn–Mn interatomic repulsion. $MnSrNb_2O_7$ undergoes a transition to an antiferromagnetically ordered state below T_N = 39 K, in which the magnetic moments are orientated parallel to the *z*-axis in a G-type arrangement. No lattice parameter anomalies coinciding with the onset of magnetic order are observed, indicating that the electric and magnetic polarisations are not strongly coupled in this phase.

Chapter 5: Synthesis and Characterisation of $M^{II}SrNb_2O_7$ (M = Fe, Co, Zn)

5.1 Introduction

Chapter 3 explored the synthesis of the metastable polar phases $FeCaTa_2O_7$, $CoCaTa_2O_7$ and $ZnCaTa_2O_7$ via topochemical cation exchange reactions from the thermodynamically stable precursor $Li_2CaTa_2O_7$ and demonstrated the feasibility of exchanging 3*d* transition metal cations with Li^+ in lithium-based pseudo-Ruddlesden-Popper phases. Building on these findings, the chapter that follows extends the investigation to the cation exchange reactions involving $Li_2SrNb_2O_7$, initially explored in Chapter 4, to synthesise and characterise the analogous $FeSrNb_2O_7$, $CoSrNb_2O_7$ and $ZnSrNb_2O_7$ phases.

5.2 Synthesis

5.2.1 Synthesis of $M^{II}SrNb_2O_7$ (M = Fe, Co, Zn)

Polycrystalline samples of $Li_2SrNb_2O_7$ were prepared according to the synthetic strategy described in Chapter 4. Polycrystalline samples of $M^{II}SrNb_2O_7$ (M = Fe, Co, Zn) were prepared via cation exchange reactions from $Li_2SrNb_2O_7$. 4.0 g of $Li_2SrNb_2O_7$ was combined with 10-molar equivalents of anhydrous $FeCl_2$ (99.5%), $CoCl_2$ (99.7%) or $ZnCl_2$ (99.99%). The mixtures were ground in an agate pestle and mortar in an argon-filled glovebox, loaded into Pyrex tubes and sealed under vacuum. The samples were heated at a ramp rate of 2 °C/min to 250 °C for six periods of 48 h, 300 °C for two periods of 48 h, and 250 °C for two periods of 48 hours, respectively, followed by cooling at 5 °C/min to room temperature. Between each heating cycle, the sample was washed with distilled water to

remove any unreacted chloride and LiCl byproduct and then combined with fresh anhydrous chloride for the following cycle.

5.3 Results

5.3.1 Optical SHG Measurements

The SHG signals from $CoSrNb_2O_7$, $FeSrNb_2O_7$, $ZnSrNb_2O_7$ and KDP were investigated under incident laser radiation of 1064 nm. The second harmonic efficiency of $CoSrNb_2O_7$, $FeSrNb_2O_7$ and $ZnSrNb_2O_7$ powders were compared to that of KDP powder with the same particle size. No SHG signal was observed in $CoSrNb_2O_7$ or $FeSrNb_2O_7$, indicating these phases adopt centrosymmetric crystal structures. $ZnSrNb_2O_7$ displayed a small SHG response in comparison to the KDP standard, which reveals that $ZnSrNb_2O_7$ adopts a non-centrosymmetric crystal structure.

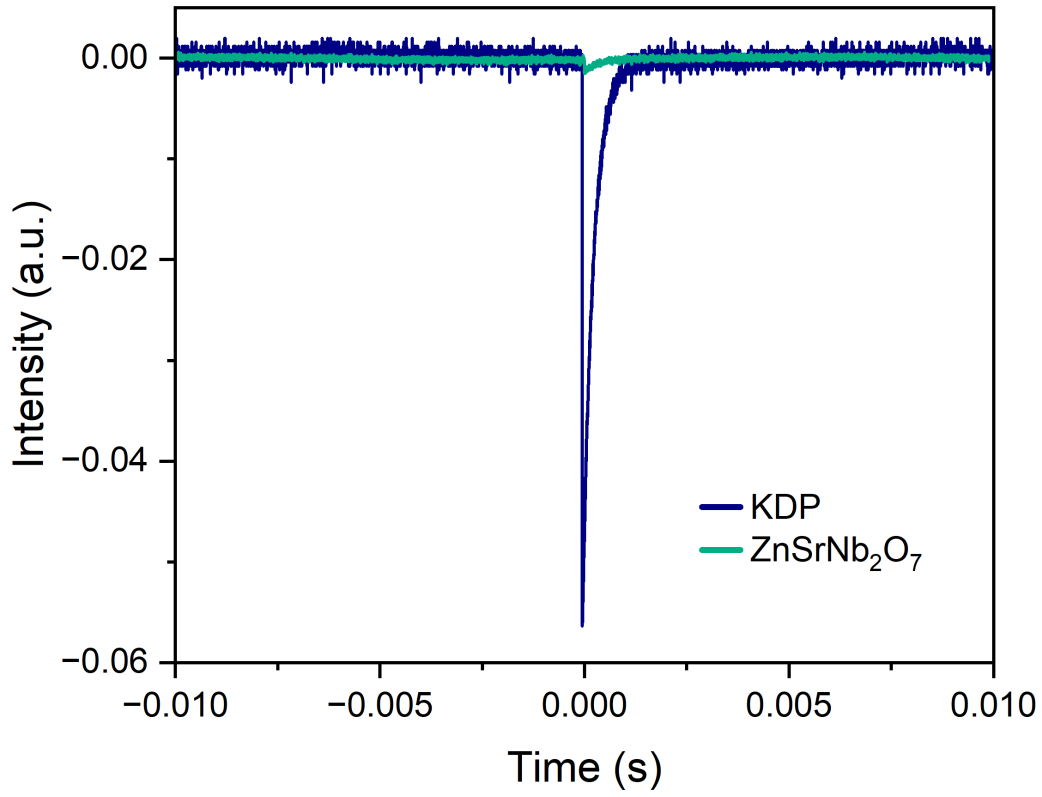


Figure 5.1 Plot of SHG intensity of $ZnSrNb_2O_7$ as a function of time under incident radiation of 1064 nm, compared to that of KDP standard.

5.3.2 Characterisation of $CoSrNb_2O_7$

5.3.2.1 Room temperature synchrotron X-ray diffraction data

Synchrotron X-ray diffraction data collected from $CoSrNb_2O_7$ at room temperature could be indexed using an orthorhombic unit cell (a = 5.5805(2) Å, b = 5.5836(2) Å, c = 18.5474(9) Å) consistent with a $\sim\sqrt{2} \times \sim\sqrt{2} \times 1$ geometric expansion of an undistorted n = 2 Ruddlesden-Popper unit cell (Figure 5.2). A close inspection of the Pawley refinement revealed a series of weak diffraction peaks, indicated with arrows in the bottom pane of Figure 5.2, that could not be indexed by the proposed unit cell, nor any expansion of the unit cells, or any logical impurities. Similar to the analogous manganese phase, these satellite peaks indicated a potential incommensurate modulation of the crystal structure of $CoSrNb_2O_7$.

5.3.2.2 50 K neutron powder diffraction data

5.3.2.2.1 Commensurate structural model

Neutron powder diffraction data collected from $CoSrNb_2O_7$ at 50 K could be indexed using an *A*-centred or primitive orthorhombic unit cell (a = 5.5772(2) Å, b = 5.5819(2) Å, c = 18.4423(4) Å) consistent with a $\sim\sqrt{2} \times \sim\sqrt{2} \times 1$ geometric expansion of an undistorted n = 2 Ruddlesden-Popper unit cell. A detailed symmetry analysis of the aristotype *I*4/*mmm* n = 2 Ruddlesden-Popper structure was used to generate a series of chemically plausible structural models, based on the tilting distortions of the Nb–O framework and to deduce their space groups. As noted above, $CoSrNb_2O_7$ is not SHG active and hence adopts a centrosymmetric crystal structure, and all non-centrosymmetric space groups could be eliminated from the list of potential space groups on this basis. Close inspection of the diffraction data revealed a number of possible candidate structures consistent with the observed reflection conditions: $a^0a^0c^+/a^0a^0c^+$ (*Acam*), $a^0a^0c^-/a^0a^0c^-$ (*Acaa*),

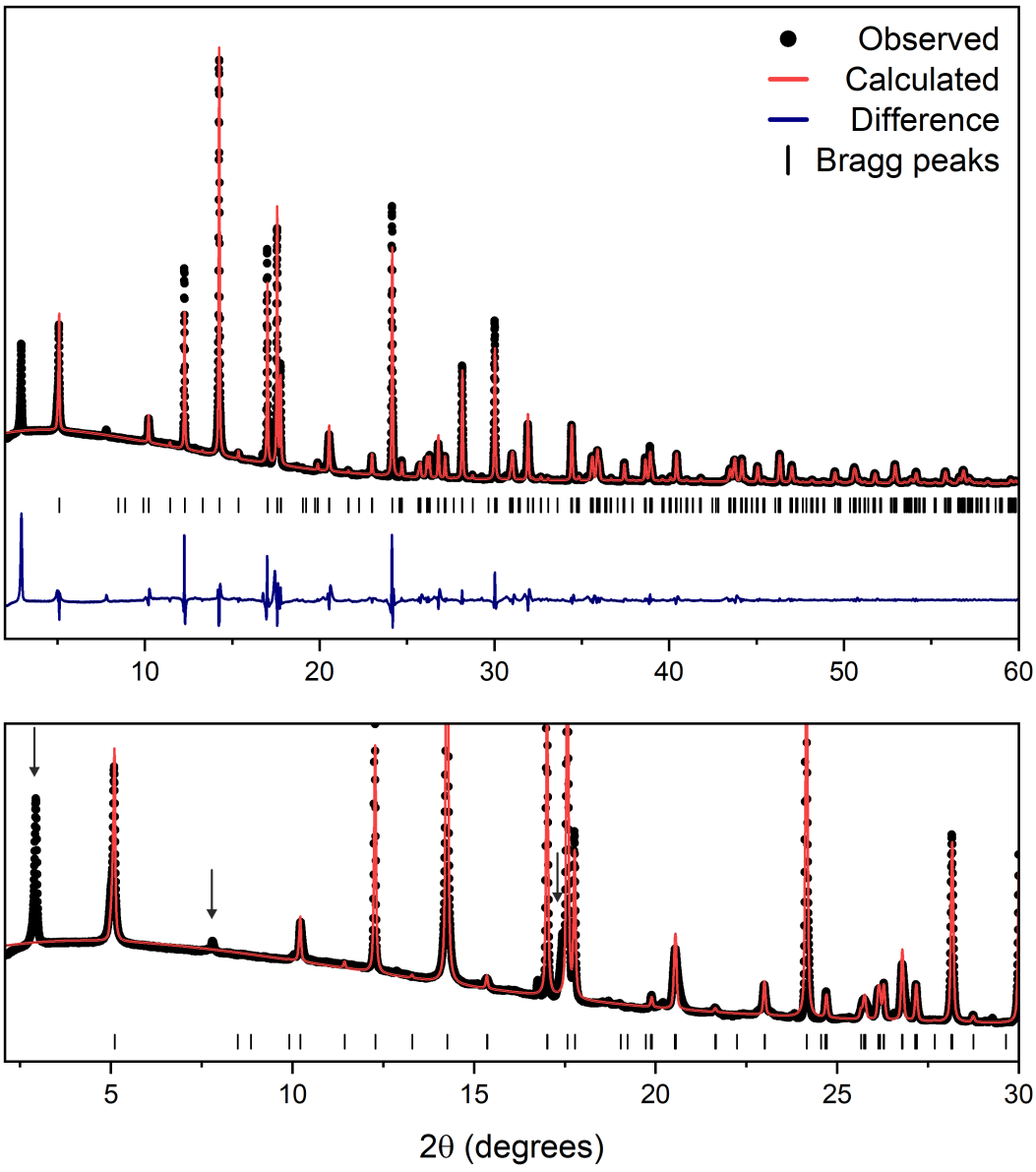


Figure 5.2 Observed, calculated and difference plots from the Pawley refinement of an primitive unit cell against SXRD data collected from $CoSrNb_2O_7$ at room temperature (top) and an expanded region showing weak diffraction peaks that cannot be accounted for with a commensurate expansion of the unit cell, labelled with black arrows (bottom).

$a^-a^-c^0/a^-a^-c^0$ (*Amam*), and $a^-a^-c^0/-(a^-a^-)c^0$ (*Acmm*). Structural models were constructed for $CoSrNb_2O_7$ with these tilting patterns and refined against the NPD data collected at 50 K. A reasonable fit to the observed data was achieved using an *Amam* symmetry model. The observed, calculated and difference plots from the refinement of the

Amam model of $CoSrNb_2O_7$ against the bank 1 and bank 4 NPD data collected at 60 K are shown in Figure 5.3.

Since divalent Co^{2+} cations are exchanged with monovalent Li^+ cations, the number of available coordination sites in the substituted phase is twice the number of transition metal cations present. Therefore, only half of the existing interlayer coordination sites between the perovskite double-layers of $CoSrNb_2O_7$ will be occupied by Co^{2+} cations. There is only one possible crystallographic Co coordination site (8*e*) in the *Amam* model, and as a result, Co can only adopt a disordered arrangement across this site to maintain the stoichiometry of the phase.

Analysis of the NPD data collected from $CoSrNb_2O_7$ and the analogous phase $MnSrNb_2O_7$ reveals the structures of the two compounds appear closely related. $MnSrNb_2O_7$ adopts a polar $a^-a^-c^+/a^-a^-c^+$ structure described in space group $A2_1am$ which can be related to the *I*4/*mmm* aristotype phase via two octahedral rotations that transform like the irreducible representations $X_3^-(a;0)$ and $X_2^+(b;0)$, along with the polar distortion mode Γ_5^-. In contrast, the centrosymmetric *Amam* model exhibits an $a^-a^-c^0/a^-a^-c^0$ tilting distortion that can be decomposed into the $X_3^-(a;0)$ mode. Consequently, $A2_1am$ is a non-centrosymmetric subgroup of *Amam*.

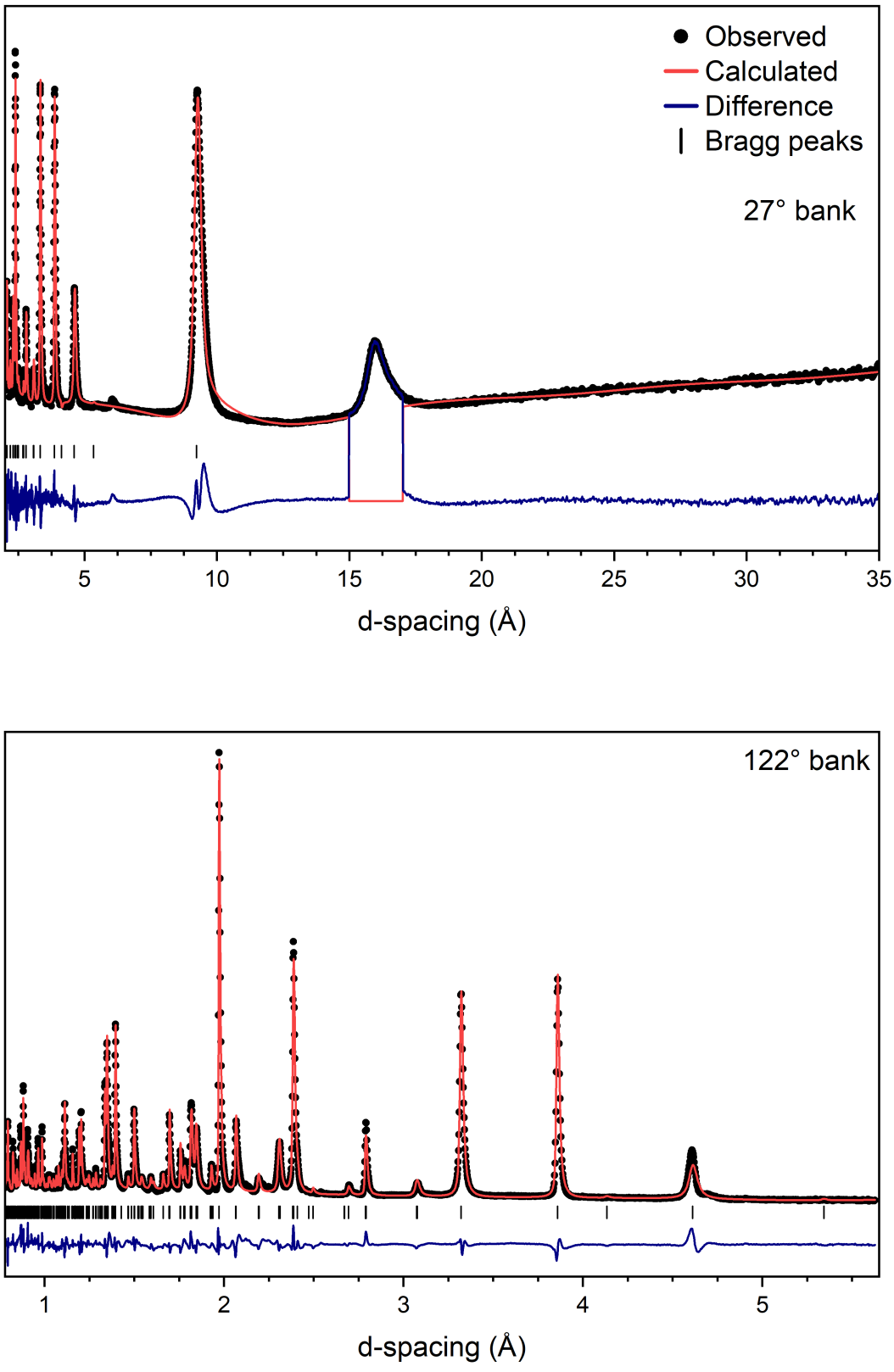


Figure 5.3 Observed, calculated and difference plots from the structural refinement of the unmodulated *Amam* model of $CoSrNb_2O_7$ against the NPD data collected from bank 1-10 (27°) and bank 4-7 (122°) at 50 K. Peak centred at 17 Å has been excluded from the refinement.

Closer inspection of the refinement of the commensurate model to the NPD data revealed a series of satellite peaks which could not be indexed by this unit cell or a rational expansion of the unit cell and could not be accounted for by any logical impurities. Instead, these peaks could be indexed by an incommensurate unit cell described in space group *Amam*(0β0)000 with a propagation vector **q** = (0, 0.82, 0), in which the translational symmetry has been broken along the *y*-axis. This behaviour is consistent with the related manganese-exchanged compound, $MnSrNb_2O_7$, which also adopts an incommensurately modulated structure with a structural modulation vector of **q** = (0, 0.81, 0). The observed, calculated and difference plots from the Pawley refinement of an *Amam*(0β0)000 unit cell against the bank 1 and bank 4 NPD data collected at 60 K are shown in Figure 5.4.

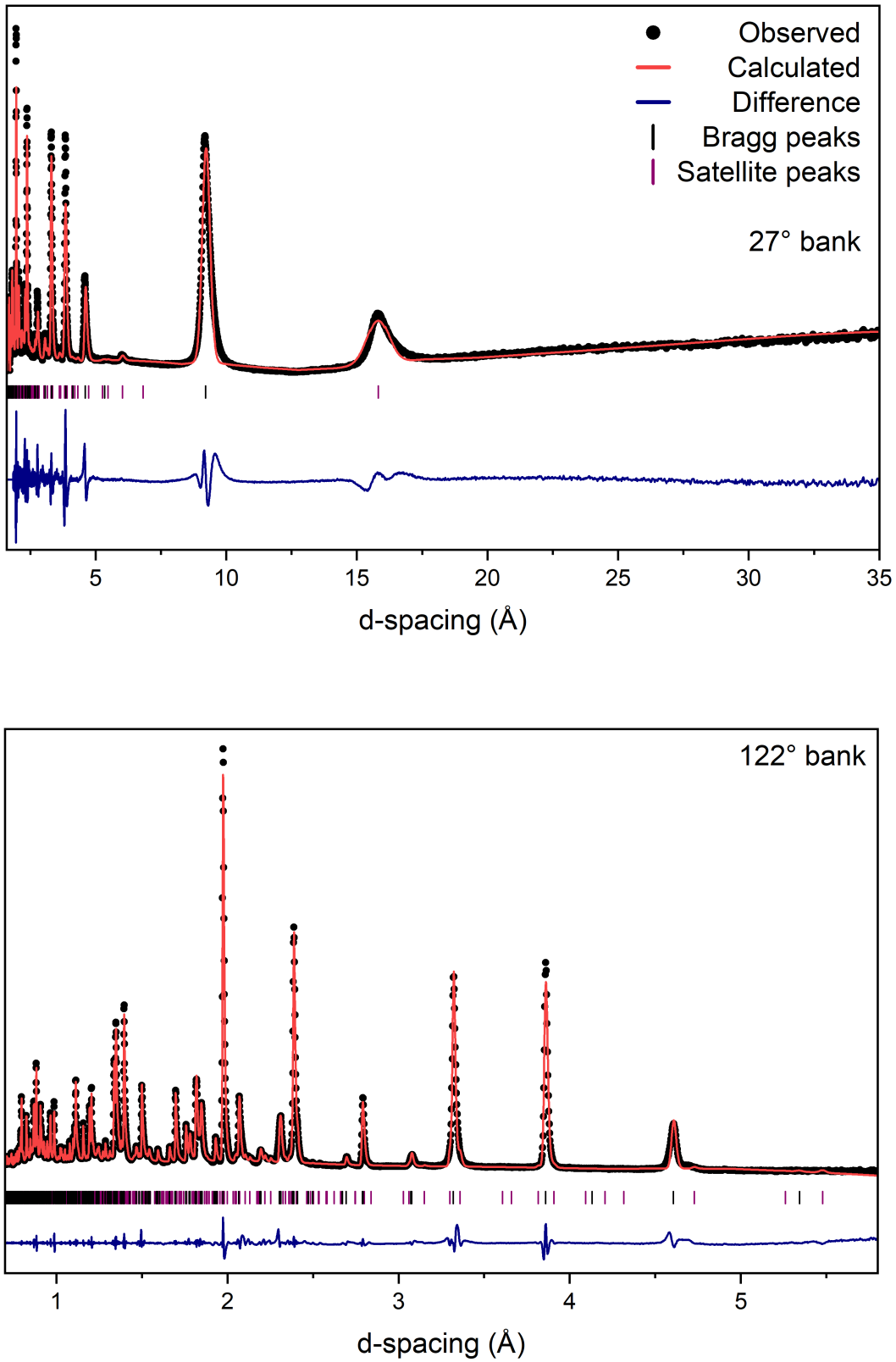


Figure 5.4 Observed, calculated and difference plots from the Pawley refinement of an incommensurately modulated *Amam*(0β0)000 unit cell against the NPD data collected from $CoSrNb_2O_7$ from 1-10 (27°) bank and 4-7 (122°) bank at 50 K.

5.3.2.2.2 Incommensurate structural model

A structural model was constructed with an $a^{-}a^{-}c^{0}/a^{-}a^{-}c^{0}$ tilting distortion, described in space group *Amam*(0β0)000, and refined against the NPD data collected at 50 K to establish which constituents of $CoSrNb_2O_7$ contribute to the structural modulation. A modulation wave for each atomic position was applied to the model in succession and refined. Neither a positional nor occupational modulation of the Sr or Nb sites visibly improved the fit to the observed data.

A visual inspection of the NPD data collected from $CoSrNb_2O_7$ and $MnSrNb_2O_7$ revealed that the two relatively strong satellite peaks, labelled (011-1) and (013-1), are observed in the $CoSrNb_2O_7$ diffraction data but are absent in the $MnSrNb_2O_7$ data(Figure 5.5). This suggests that the origin of the incommensurate modulation differs between the two phases. To explore this, a discontinuous variation (crenel function) was applied to the Co^{2+} site occupancy of the model in an attempt to replicate the occupational modulation of the Mn^{2+} site observed in $MnSrNb_2O_7$. As anticipated, refinement of the cobalt modulation wave did not improve the fit to the data.

Finally, models were constructed to investigate a potential modulation of the oxygen anion sites. Each oxygen site was split into two distinct positions, with atomic coordinates refined independently, and a discontinuous crenel function was applied to model the occupancy across both sites. Modulating the occupancy of the O2 anion site significantly improved the fit in the high *d*-spacing region, predicting intensity at the (011-1) reflection. However, this improvement was accompanied by an unreasonably large increase in the intensity of predicted peaks in the low *d*-spacing region, often causing the refinement to diverge. This observation suggests that the position of the O2 anion site is modulated and strongly correlated with the modulation of another site, likely cobalt. Initial attempts to correlate the

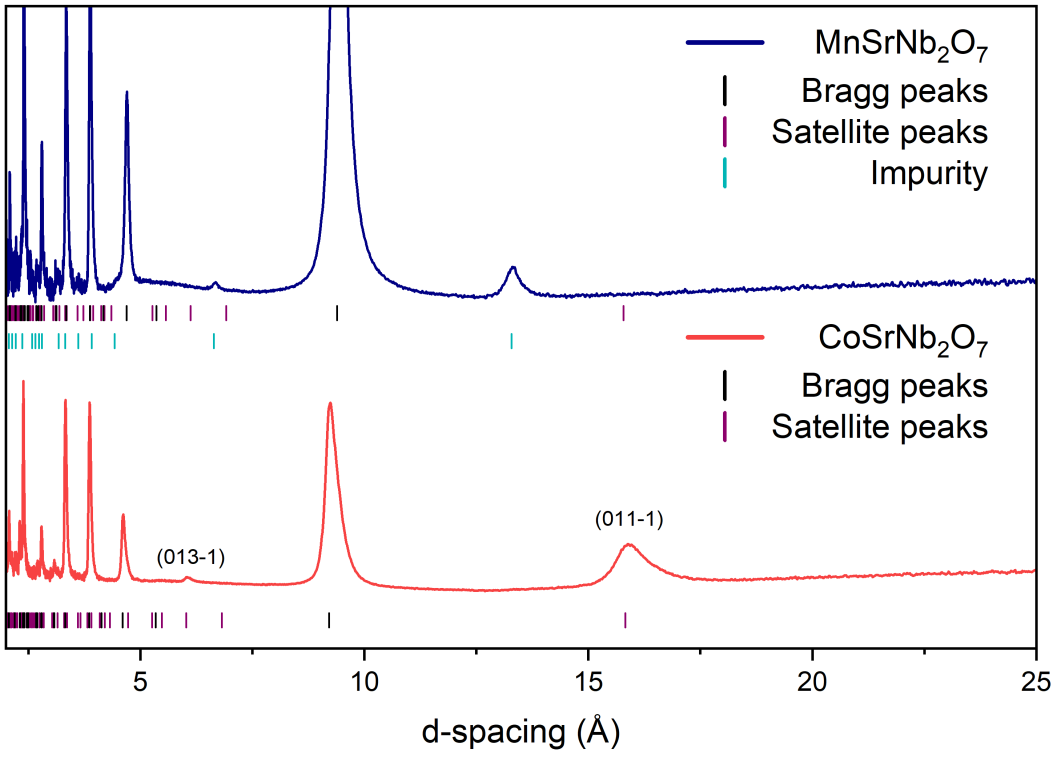


Figure 5.5 Comparison of the NPD data collected from $MnSrNb_2O_7$ and $CoSrNb_2O_7$, highlighting the difference between the observed incommensurate satellite peaks.

modulation of the O2 site with the cobalt site did not successfully model the intensity of the low *d*-spacing peaks.

The satellite peaks may be a consequence of an incomplete cation exchange reaction and the coexistence of both lithium and cobalt within the tetrahedral coordination sites of the interlayer region. If this were the case, complex interlayer cation ordering may be further complicated by the modulation of the lithium site. Given that the neutron scattering lengths of Co and Li are 2.49 fm, and Li -1.90 fm, respectively, the combined neutron scattering power of a site containing approximately equal amounts of Co and Li would be effectively zero. This makes it challenging to determine the precise locations of these ions in a structure where the NPD data is dominated by scattering from Sr, Nb and O. Chemical analysis, such as energy-dispersive X-ray (EDX) analysis, would be a useful technique to aid in the determination of the elemental composition of the material.

At this time, it was not possible to determine the precise origin of the structural modulation and to account for the satellite peaks, and only a relatively poor fit to the observed data was achieved using an uncorrelated model.

5.3.2.3 Magnetisation data

Magnetisation data were collected from $CoSrNb_2O_7$ in an applied field of 100 Oe in the temperature range $5 \leq T/K \leq 300$ K. The zero-field-cooled (ZFC) and field-cooled (FC) data, shown in Figure 5.6, can be fit to the modified form of the Curie-Weiss law, which includes a temperature independent term, χ_0, to account for the significant positive curvature of the χ^{-1} vs. T plot. The fit to the data in the region $100 \leq T/K \leq 300$ K yields a Curie constant of $C = 1.82$ cm^3 K mol^{-1} and a Weiss constant of $\theta_{CW} = -48.1$ K. The Curie constant was used

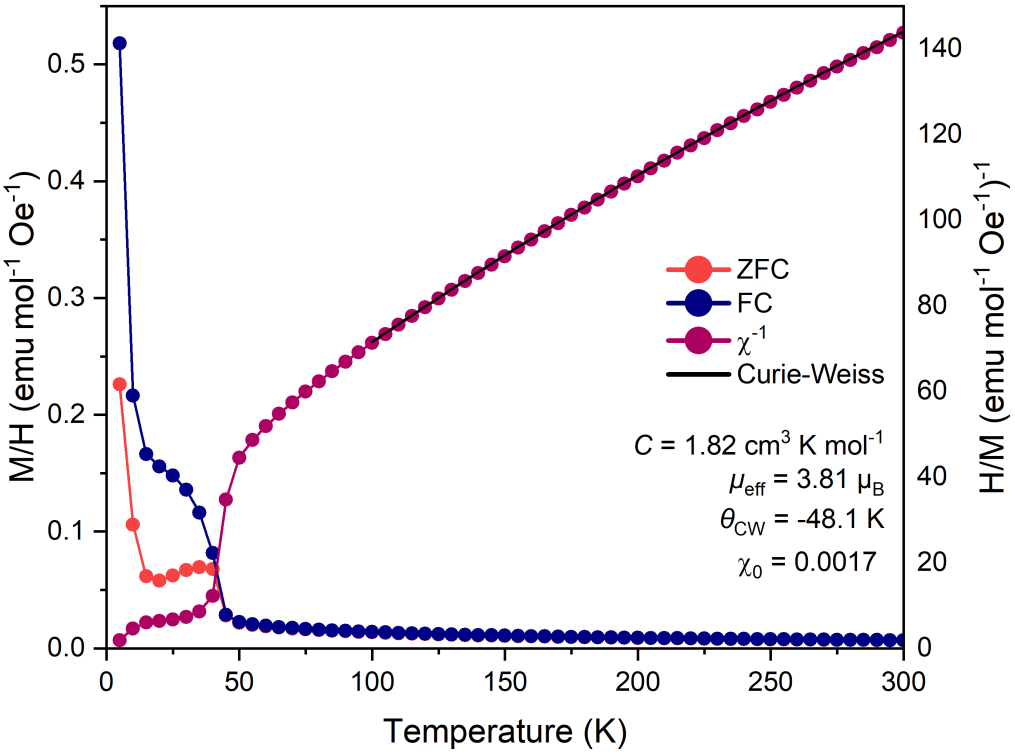


Figure 5.6 Zero-field-cooled and field-cooled magnetisation data collected from $CoSrNb_2O_7$ as a function of temperature in an applied field of 100 Oe.

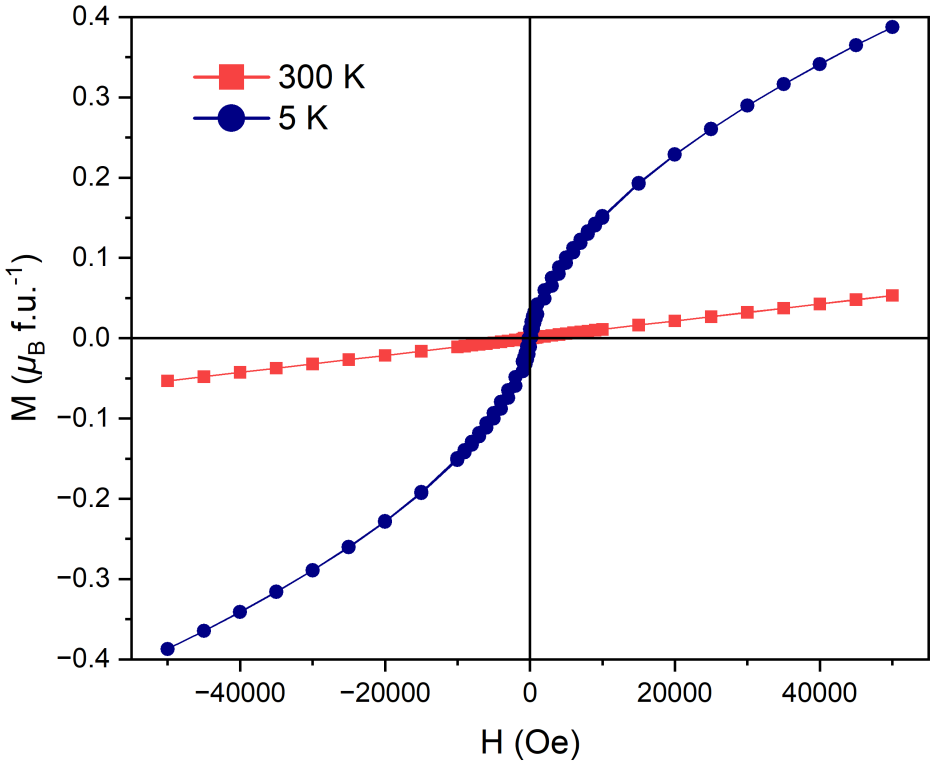


Figure 5.7 Magnetisation-field data collected from $CoSrNb_2O_7$ at 300 K and 5 K.

to calculate the effective magnetic moment, μ_{eff} = 3.81 μ_B, which agrees well with the expected spin-only moment for a single Co^{2+} (S=3/2) ion in a tetrahedral ligand field. However, due to second-order spin-orbit coupling, the observed magnetic moment is expected to be greater than the theoretical moment, typically in the range of 4.2-4.8 μ_B. Therefore, the calculated effective magnetic moment is smaller than anticipated, suggesting an incomplete cation exchange reaction.

The ZFC and FC data sharply diverge at approximately T_N = 40 K where the susceptibility shows a sharp cusp that is antiferromagnetic in character. The negative value of the Weiss constant is indicative of antiferromagnetic interactions and of the same magnitude as the magnetic ordering temperature. The magnetisation-field isotherm collected at 300 K is linear and passes through the origin, with data collected at 5 K also passing through the origin but

adopting a sigmoidal shape (Figure 5.7). This suggests that the Co^{2+} ions adopt an antiferromagnetic arrangement below the transition temperature.

5.3.2.4 Low temperature (1.5 K) neutron powder diffraction data

Neutron powder diffraction data collected from $CoSrNb_2O_7$ at 1.5 K were directly compared to data collected at 50 K and are presented in Figure 5.8. No new diffraction features were observed in the low-temperature data, and there was no additional scattering at nuclear Bragg peaks, indicating the absence of long-range magnetic order at 5 K or a structural phase transition.

The absence of long-range magnetic order at low temperatures, despite magnetisation data indicating the presence of antiferromagnetic interactions, suggests that magnetic interactions in $CoSrNb_2O_7$ are short-ranged. On the one hand, this is unsurprising, given the distance between the interlayer cobalt cations along the *z*-direction is approximately 9.5 Å, and the magnetism is, therefore, very two-dimensional in nature. However, weak 3D magnetic interactions are observed in other pseudo-Ruddlesden-Popper phases, such as the analogous material $CoCaTa_2O_7$, implying that another factor may be at play. For instance, residual lithium within the interlayer regions could disrupt long-range magnetic order. A significant contribution to the background is observed, particularly in the high *d*-spacing region of the data, which can be attributed to paramagnetic scattering from disordered moments in the paramagnetic phase above the magnetic transition temperature.

Refinement of the low temperature neutron diffraction data was not attempted at this stage because a satisfactory model had not been found and so no further structural information can be obtained.

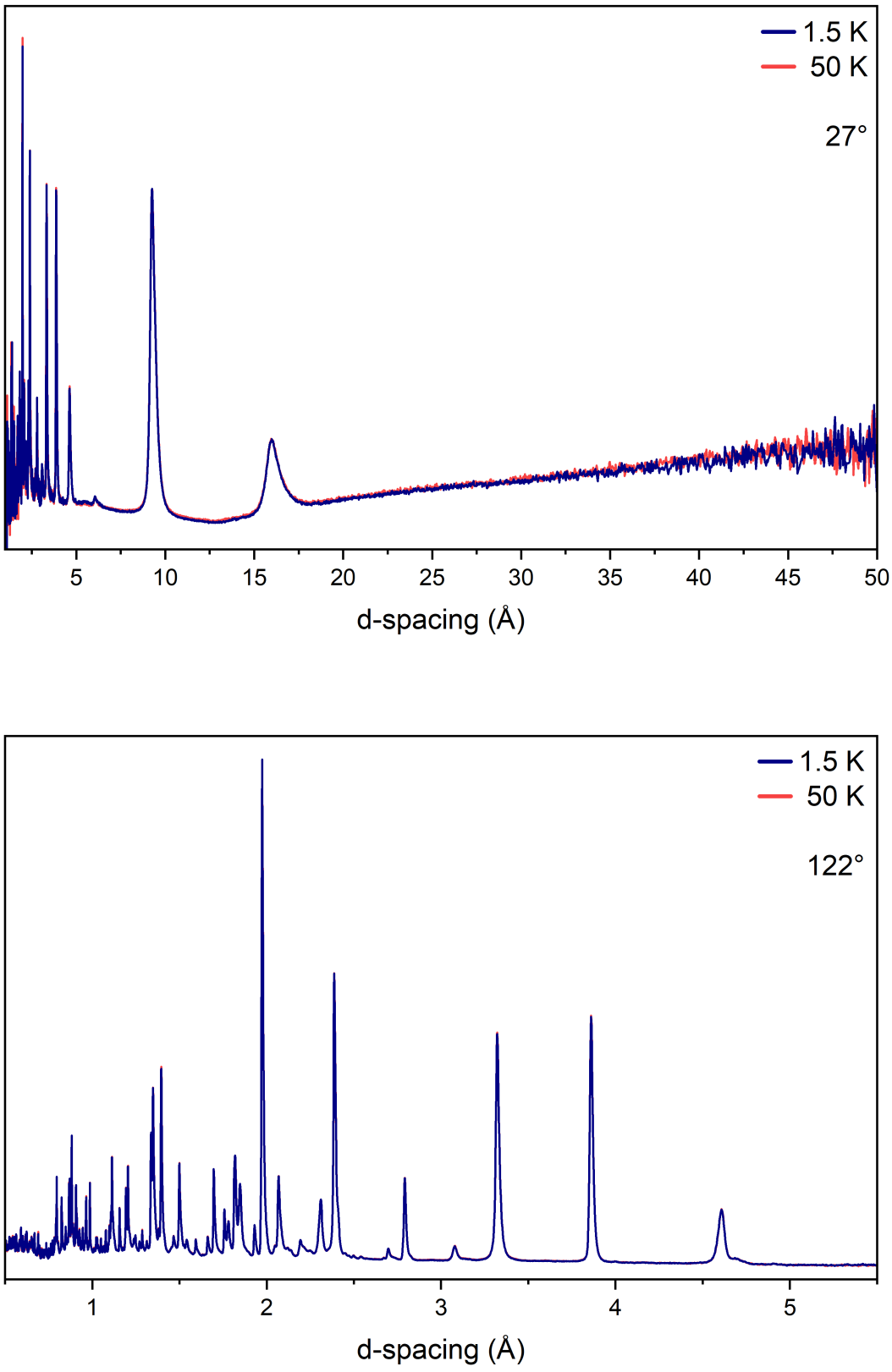


Figure 5.8 Comparison of the NPD data collected from $CoSrNb_2O_7$ at 1.5 K and 50 K using the 1-10 (27°) bank and 4-7 (122°) bank.

5.3.3 Characterisation of $ZnSrNb_2O_7$

5.3.3.1 Room temperature synchrotron X-ray diffraction data

Synchrotron X-ray diffraction data collected from $ZnSrNb_2O_7$ at room temperature could be indexed using a primitive, orthorhombic unit cell (a = 5.54097(7) Å, b = 5.55220(7) Å, c = 19.32268(19) Å), consistent with a $\sim\sqrt{2} \times \sim\sqrt{2} \times 1$ geometric expansion of an undistorted n = 2 Ruddlesden-Popper unit cell. Close inspection of the diffraction data revealed additional weak diffraction peaks which indicate a doubling of the c-axis, and extinction conditions consistent with a body-centred unit cell (Figure 5.9). As noted above, SHG measurements reveal that $ZnSrNb_2O_7$ is SHG active and, hence, adopts a non-centrosymmetric crystal structure. A detailed symmetry analysis of the aristotype n = 2 Ruddlesden-Popper structure was used to generate a series of chemically plausible structural models and to deduce their space groups, and three non-centrosymmetric candidate structures described in space groups consistent with the observed reflection conditions were identified: *Ima*2, $I2_12_12_1$ and *I*222. Structural models were constructed for $ZnSrNb_2O_7$ described in the *Ima*2, $I2_12_12_1$ and *I*222 space groups and refined against the SXRD data. The oxygen atomic positions were not refined at this stage due to poor X-ray scattering power and remained fixed at values generated by ISODISTORT.

Since divalent Zn^{2+} cations are exchanged with monovalent Li^+ cations, the number of available coordination sites in the substituted phase is twice the number of transition metal cations present. Therefore, only half of the existing interlayer coordination sites between the perovskite double-layers of $ZnSrNb_2O_7$ will be occupied by Zn^{2+} cations. During the initial refinement of each of the models against the SXRD data, the occupancies of the Zn^{2+} sites

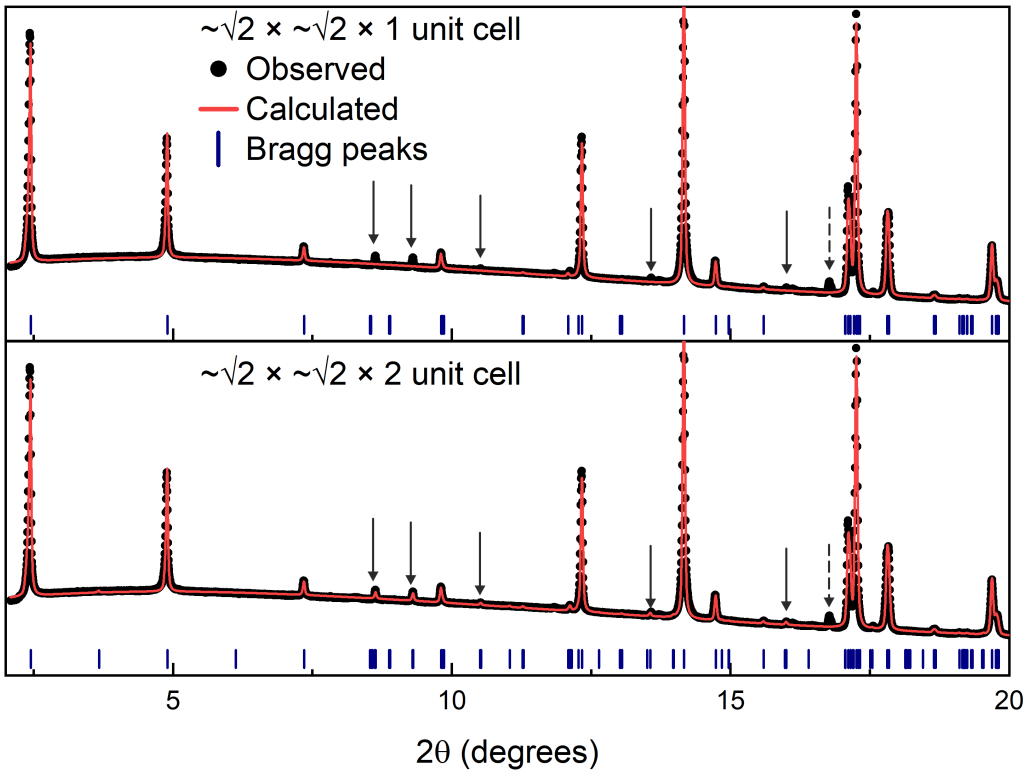


Figure 5.9 Observed and calculated plots from the Pawley refinement of (top) a primitive unit cell with a $\sim\sqrt{2} \times \sim\sqrt{2} \times 1$ and geometric expansion of the aristotype *I*4/*mmm* unit cell and (bottom) a body-centred unit cell with a $\sim\sqrt{2} \times \sim\sqrt{2} \times 2$ and geometric expansion against SXRD data collected from $ZnSrNb_2O_7$ at room temperature. Peaks marked by black arrows can only be indexed by a doubling of the *c*-axis, while peaks marked by dashed arrows correspond to an unknown impurity phase inherited from the precursor phase.

were constrained to be 0.5 to describe disorder across all zinc sites. Refinement of each of the Zn-site disordered *Ima*2, $I2_12_12_1$ and *I*222 models did not correctly describe the peak intensities of the superstructure reflections. However, refinement of the Zn-site occupancies vastly improved the fit to the data and demonstrated that there is a clear tendency for the zinc cations to order within the interlayer region.

5.3.3.2 100 K neutron powder diffraction data

Neutron powder diffraction data collected from $ZnSrNb_2O_7$ at 100 K could be indexed using a primitive orthorhombic unit cell (a = 5.5456(5) Å, b = 5.5301(5) Å, c = 38.5957(9) Å) consistent with a $\sim\sqrt{2} \times \sim\sqrt{2} \times 2$ geometric expansion of the aristotype *I*4/*mmm* unit cell.

The structural models described in space groups *Ima*2, $I2_12_12_1$ and *I*222 were each refined against the NPD data, initially by constraining the Zn^{2+} to adopt a disordered arrangement across the interlayer tetrahedral sites. The statistical and visual fits to the data and the refined models were compared, and it was found that the best fit to the observed data was achieved using the *I222* symmetry model. The observed, calculated and difference plots from the refinement of the *I222* model of $ZnSrNb_2O_7$ against the bank 1 and bank 4 NPD data collected at 100 K are shown in Figure 5.10. A close inspection of the refined model revealed the $SrNb_2O_7$ framework is chemically sensible.

There are six crystallographically distinct Zn^{2+} interlayer coordination sites: 2*a*, 2*b*, 2*c*, 2*d*, 4*e* and 4*f* in the *I222* model. Refinement of the Zn-site occupancies led to a clear ordering of the zinc cations, where the Zn occupancy of the 4*e* and 4*f* site refined to 0.16(1) and 0.03(1)Å, respectively. However, the occupancy of the remaining tetrahedral coordination sites did not refine to a value close to 1, which is necessary to maintain the stoichiometry of the phase. This suggests that the cation exchange reaction is incomplete, and that lithium remains in the material. The refined I*222* model indicates that Zn cations occupy the interlayer region in an alternating pattern of partially filled and empty layers, illustrated in Figure 5.11. This behaviour is unusual and does not represent an energetically favourable arrangement or chemically sensible ordering of Zn^{2+} cations. It is possible that while the *I222* crystal model accurately describes the $SrNb_2O_7$ framework, it does not correctly account for the interlayer cation order.

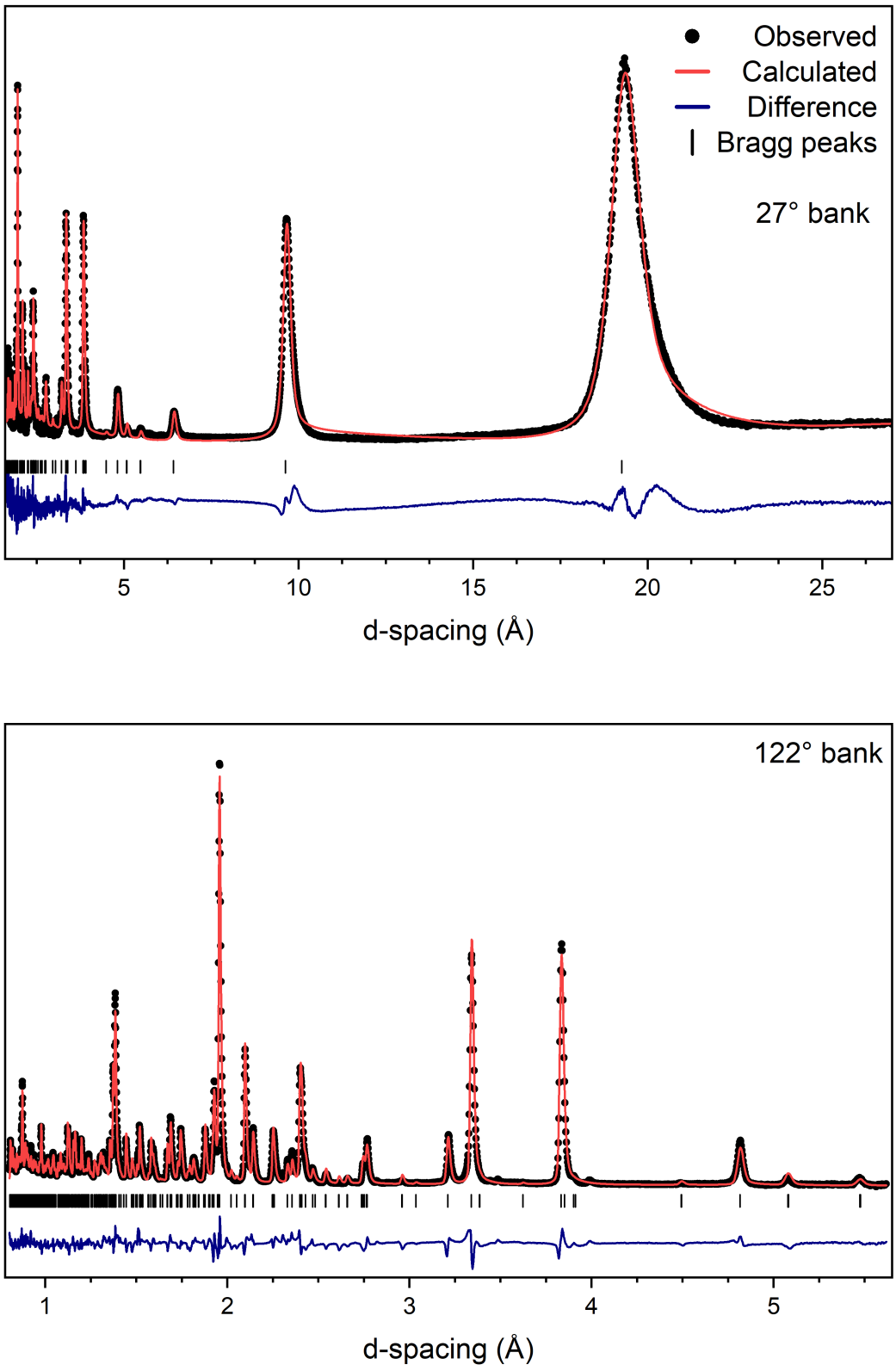


Figure 5.10 Observed, calculated and difference plots from the structural refinement of the *I*222 model of $ZnSrNb_2O_7$ against the NPD data collected from 1-10 (27°) bank and 4-7 (122°) bank at 100 K.

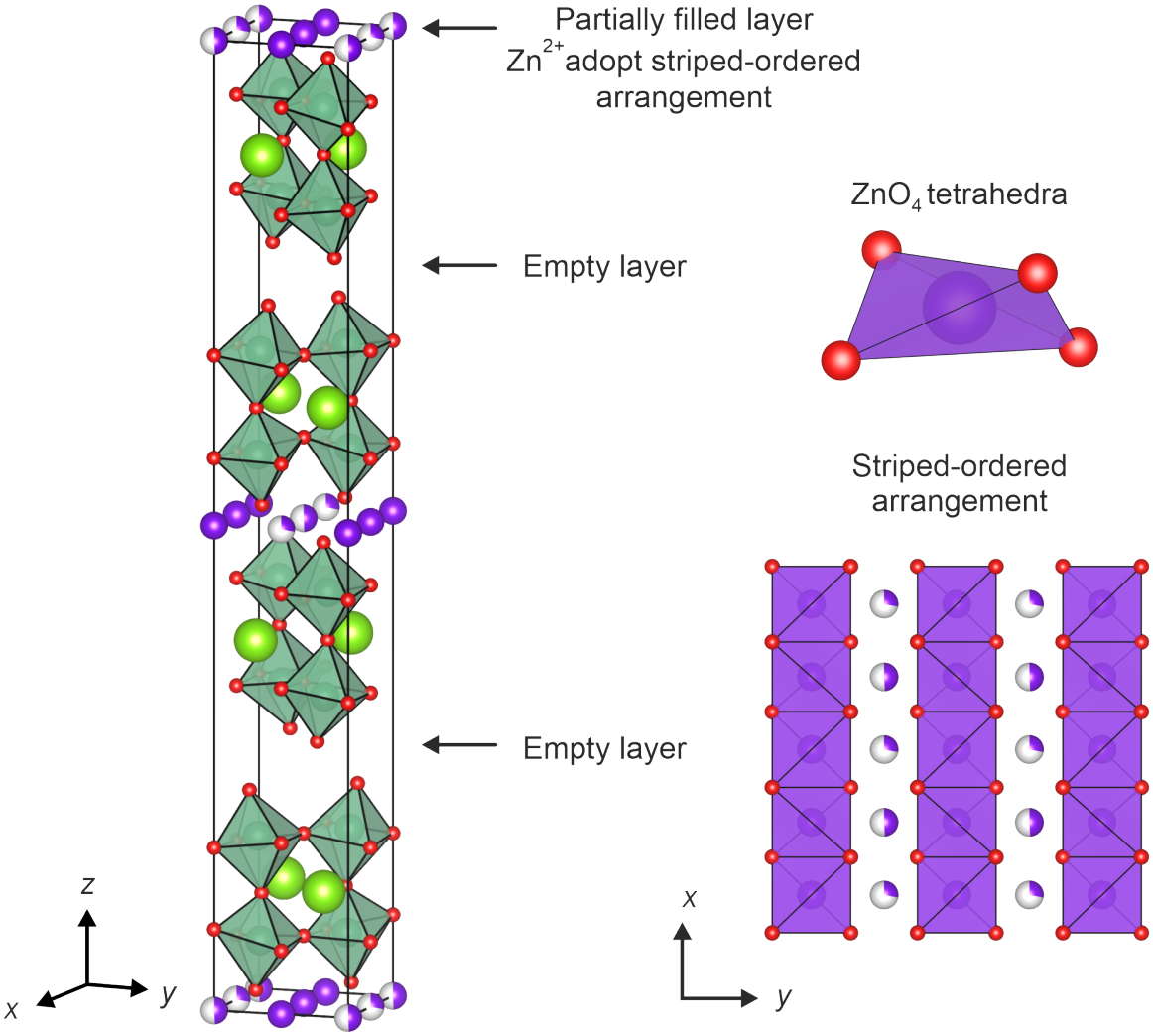


Figure 5.11 The refined *I*222 model of $ZnSrNb_2O_7$, illustrating the alternating empty and partially filled layers. The Zn^{2+} cations adopt a striped-order arrangement within the interlayer tetrahedral coordination sites in each partially filled layer. Purple, lime green, deep green and red spheres represent Zn, Sr, Ta and O atoms, respectively.

Further studies are necessary to acertain the complex crystal structure of $ZnSrNb_2O_7$. Advanced techniques such as electron diffraction and electron microscopy would provide detailed insights into the stacking arrangement and origin of the expansion of the *c*-axis. Although the structure of $ZnSrNb_2O_7$ is unknown at this stage, we can hypothesise as to the reason why this phase appears to behave differently, that is to say, why is this the only compound in the series to not adopt an incommensurately modulated crystal structure? Previous studies of $MnSrNb_2O_7$, $MnSrTa_2O_7$ and $MnCaTa_2O_7$ have demonstrated that there

is a competition between optimising the octahedral tilting of the BO_6 octahedra and optimising the *A*'-cation ordering in this family of materials.[119,120] In $CoSrNb_2O_7$ and $MnSrNb_2O_7$, the optimization of octahedral tilting prevails, leading these materials to adopt an incommensurately modulated crystal structure that represents a compromise in the ordering of transition metal cations. This modulation describes a chequerboard-ordered arrangement of the interlayer cations. However, for $ZnSrNb_2O_7$, it is more energetically favourable for the zinc cations to adopt a striped-ordered arrangement, which the incommensurate modulation cannot accommodate. As a result, $ZnSrNb_2O_7$ instead adopts a structure characterized by a doubling of the *c*-axis in order to achieve to optimal compromise between the ordering of the Zn^{2+} cations and octahedral tilting.

5.3.4 Characterisation of $FeSrNb_2O_7$

5.3.4.1 Room temperature synchrotron X-ray diffraction data

Synchrotron X-ray diffraction data collected from $FeSrNb_2O_7$ at room temperature could be indexed using a primitive, orthorhombic unit cell (a = 5.5320(2) Å, b = 5.5547(1) Å, c = 19.2528(5) Å), consistent with a $\sim\sqrt{2} \times \sim\sqrt{2} \times 1$ geometric expansion of an undistorted n = 2 Ruddlesden-Popper unit cell. Close inspection of the diffraction data revealed additional weak diffraction peaks which indicate a doubling of the *c*-axis, and extinction conditions consistent with a body-centred space group (Figure 5.12). A Pawley fitting revealed that the sample was not single-phase, and contained an iron oxide (Fe_3O_2) impurity. Similar to the analogous cobalt phase described previously, the presence of satellite peaks indicated a potential incommensurate modulation of the crystal structure of $FeSrNb_2O_7$.

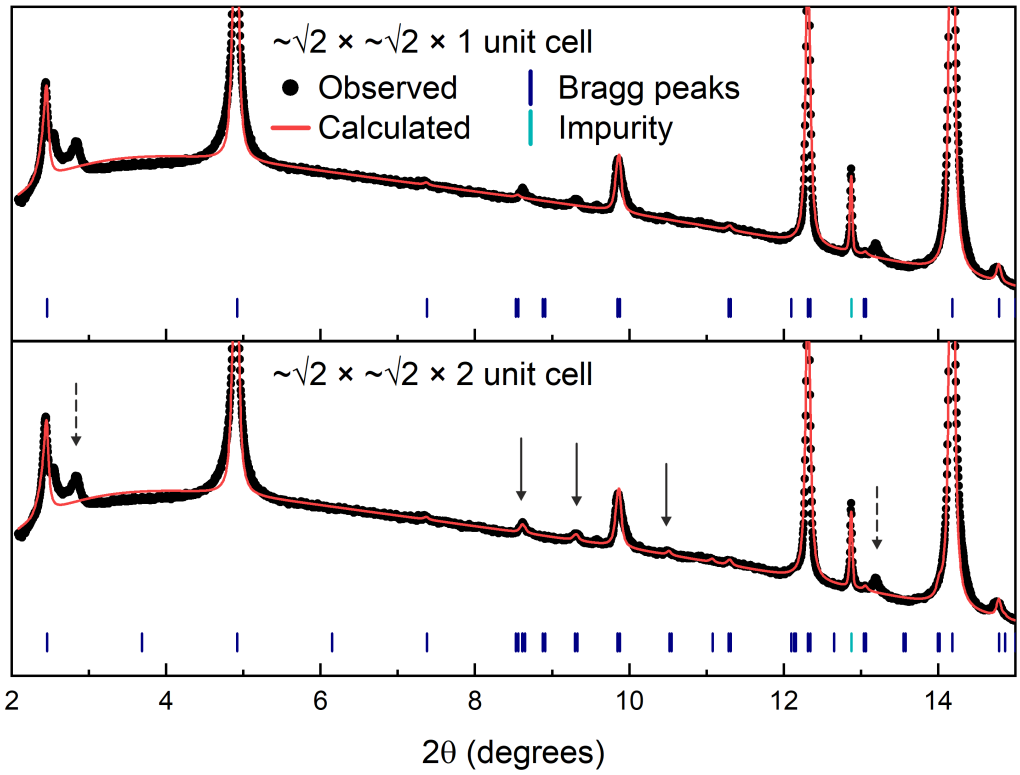


Figure 5.12 Observed and calculated plots from the Pawley refinement of (top) a primitive unit cell with a $\sim\sqrt{2} \times \sim\sqrt{2} \times 1$ and geometric expansion of the aristotype *I*4/*mmm* unit cell and (bottom) a body-centred unit cell with a $\sim\sqrt{2} \times \sim\sqrt{2} \times 2$ and geometric expansion against SXRD data collected from $FeSrNb_2O_7$ at room temperature. Peaks marked by black arrows can only be indexed by a doubling of the *c*-axis. Peaks marked by dashed arrows cannot be indexed by a commensurate unit cell.

As noted above, SHG measurements reveal that $FeSrNb_2O_7$ is not SHG active and, hence, adopts a centrosymmetric crystal structure. A detailed symmetry analysis of the aristotype $n = 2$ Ruddlesden-Popper structure was used to generate a series of chemically plausible structural models and to deduce their space groups. Two centrosymmetric candidate structures described in space groups consistent with the observed reflection conditions were identified: *Imcb* and *Icmm*. Structural models were constructed for $FeSrNb_2O_7$ described in the *Imcb* and *Icmm* space groups and refined against the SXRD data to establish a commensurate crystal structure. The oxygen atomic positions were not refined at this stage due to poor X-ray scattering power and remained fixed at values generated by

ISODISTORT. The refinements proceeded smoothly, but provided relatively poor fits to the observed data.

Since divalent Fe^{2+} cations are exchanged with monovalent Li^{+} cations, the number of available coordination sites in the substituted phase is twice the number of transition metal cations present. Therefore, only half of the existing interlayer tetrahedral coordination sites between the perovskite double-layers of $FeSrNb_2O_7$ will be occupied by Fe^{2+} cations. In the *Imcb* model, there are three possible crystallographically distinct tetrahedral coordination sites (*8*g, 4*b* and 4*a*). Therefore, Fe^{2+} can adopt an ordered or disordered arrangement across these sites to maintain the stoichiometry of the phase. An ordering across these sites results in an alternation between filled and empty layers. A disordered arrangement of the interlayer cations (half-occupied sites) was maintained when the Fe^{2+} site occupancy was refined.

In contrast, there are two distinct interlayer tetrahedral coordination sites in the *Icmm* model (8*f* and 8*f*), and an ordering over these sites would describe a striped arrangement of Fe^{2+} cations. Once again, the *Icmm* model retained a disordered arrangement of Fe^{2+} cations when the site occupancy was refined. These observations suggest the Fe^{2+} cations have a tendency to adopt a disordered or a chequerboard-ordered arrangement across the interlayer tetrahedral coordination sites, and are consistent with findings from Chapter 3, where Fe^{2+} cations of the related phase $FeCaTa_2O_7$ are ordered in a chequerboard pattern. Therefore, it is unlikely that either of the *Imcb* or *Iccm* models correctly describe the average crystal structure adopted by $FeSrNb_2O_7$.

5.3.4.2 60 K neutron powder diffraction data

Neutron powder diffraction data collected from $FeSrNb_2O_7$ at 60 K could be indexed using a primitive or *A*-centred orthorhombic unit cell (a = 5.5410(3) Å, b = 5.5562(3) Å, c = 38.436(2) Å) consistent with a $\sim\sqrt{2} \times \sim\sqrt{2} \times 2$ geometric expansion of an undistorted n = 2 Ruddlesden-Popper unit cell. Further symmetry analysis is necessary to establish a second list of candidate structures generated by applying two independent irreducible representations. Therefore, at this stage, further structural analysis of this phase has been conducted using a $P\bar{1}$ model of $FeSrNb_2O_7$.

Magnetic Bragg peaks corresponding to the antiferromagnetic impurity phase Fe_2O_3 (T_N = 264 K) were observed in the NPD data.[126,127] To account for the antiferromagnetic ordering of Fe_2O_3, an $R\bar{3}c.1$ magnetic model was added to the refinement.

The satellite peaks could be indexed by an incommensurate unit cell described in space group $P\bar{1}(\alpha\beta\gamma)0$ with a propagation vector **q** = (0, 0.82, 0), in which the translational symmetry has been broken along the *y*-axis. This behaviour is consistent with the analogous phase $CoSrNb_2O_7$ and the related compound, $MnSrNb_2O_7$, which also adopt incommensurately modulated structures with comparable structural modulation vectors. The observed, calculated and difference plots from the Pawley refinement of a $P\bar{1}(\alpha\beta\gamma)0$ unit cell against the bank 1 and bank 4 NPD data collected at 60 K are shown in Figure 5.13. There is a large contribution to background of the data collected from bank 1, making it somewhat difficult to discern the superstructure peaks from the noise of the background, and accounts for the relatively poor fit to the observed data at low *d*-spacing. The fit to the two broad peaks centred at 17 Å is also poor, and it is clearer from high resolution SXRD data that there are three peaks present. It is unlikely that the peak corresponds to an impurity

phase, since it would have a very large *d*-spacing, and may instead suggest that a more complicated superspace group is necessary to describe the crystal structure (e.g. α or $\gamma \neq 0$).

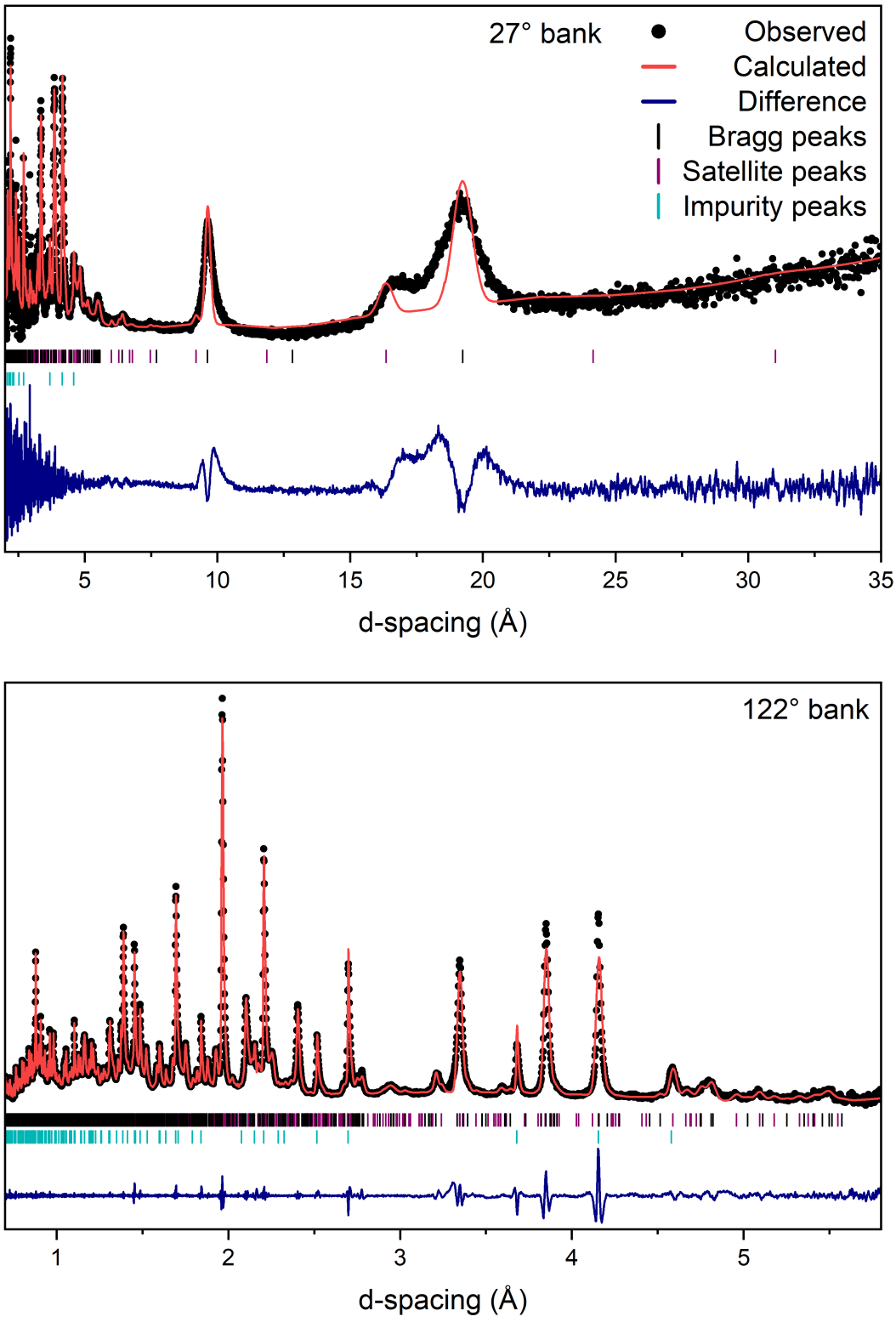


Figure 5.13 Observed, calculated and difference plots from the Pawley refinement of a $P\bar{1}(\alpha\beta\gamma)0$ unit cell against the NPD data collected from $FeSrNb_2O_7$ from 1-10 (27°) bank and 4-7 (122°) bank at 60 K.

5.3.4.3 Magnetisation data

Magnetisation data were collected from $FeSrNb_2O_7$ in an applied field of 100 Oe in the temperature range $5 \leq T/K \leq 300$ K. However, due to the unavoidable presence of small amounts of iron oxide in the sample concealing the magnetic properties of $FeSrNb_2O_7$, it became necessary to perform a ferromagnetic subtraction. This method exploits the fact that the magnetisation of a ferromagnetic impurity saturates at a relatively low field. The paramagnetic susceptibility of a bulk sample can be measured in the presence of ferromagnetic impurities by measuring the gradient of magnetization-field isotherms in applied fields larger than 2 T. The magnetisation of the sample was measured in a series of five fields between $3 \leq H/T \leq 5$ from 5 K to 300 K at 5 K temperature intervals. The magnetization vs. field data were fit to a linear function, the gradient of which is the paramagnetic susceptibility of the bulk sample and the *y*-intercept is the saturated ferromagnetic moment of the sample. The temperature-dependent paramagnetic susceptibility and saturated magnetic moment of the sample are shown in Figure 5.14.

The paramagnetic susceptibility data (Figure 5.14, bottom), can be fit to the Curie-Weiss law in the region $275 \leq T/K \leq 300$ K, yielding a Curie constant of $C = 3.45$ cm^3 K mol^{-1} and a Weiss constant of $\theta_{CW} = -289.64$ K. The Curie constant was used to calculate the effective magnetic moment, $\mu_{eff} = 5.25$ μ_B, which exceeds the expected spin-only moment for a single Fe^{2+} (S=2) ion in a tetrahedral ligand field ($\mu = 4.90$ μ_B). This discrepancy can be attributed to second-order spin-orbit coupling. The negative value of the Weiss constant is indicative of the antiferromagnetic interactions within the sample. However, the magnetisation is not a reliable indicator of the magnetic interactions in this phase because the Curie-Weiss law can only be fit to a small region of data as it shows a considerable curvature. This suggests that the behaviour of $FeSrNb_2O_7$ cannot be accurately described using the Curie-Weiss law, particularly since the value of $|\theta|$ is of the order of the maximum value of the measured

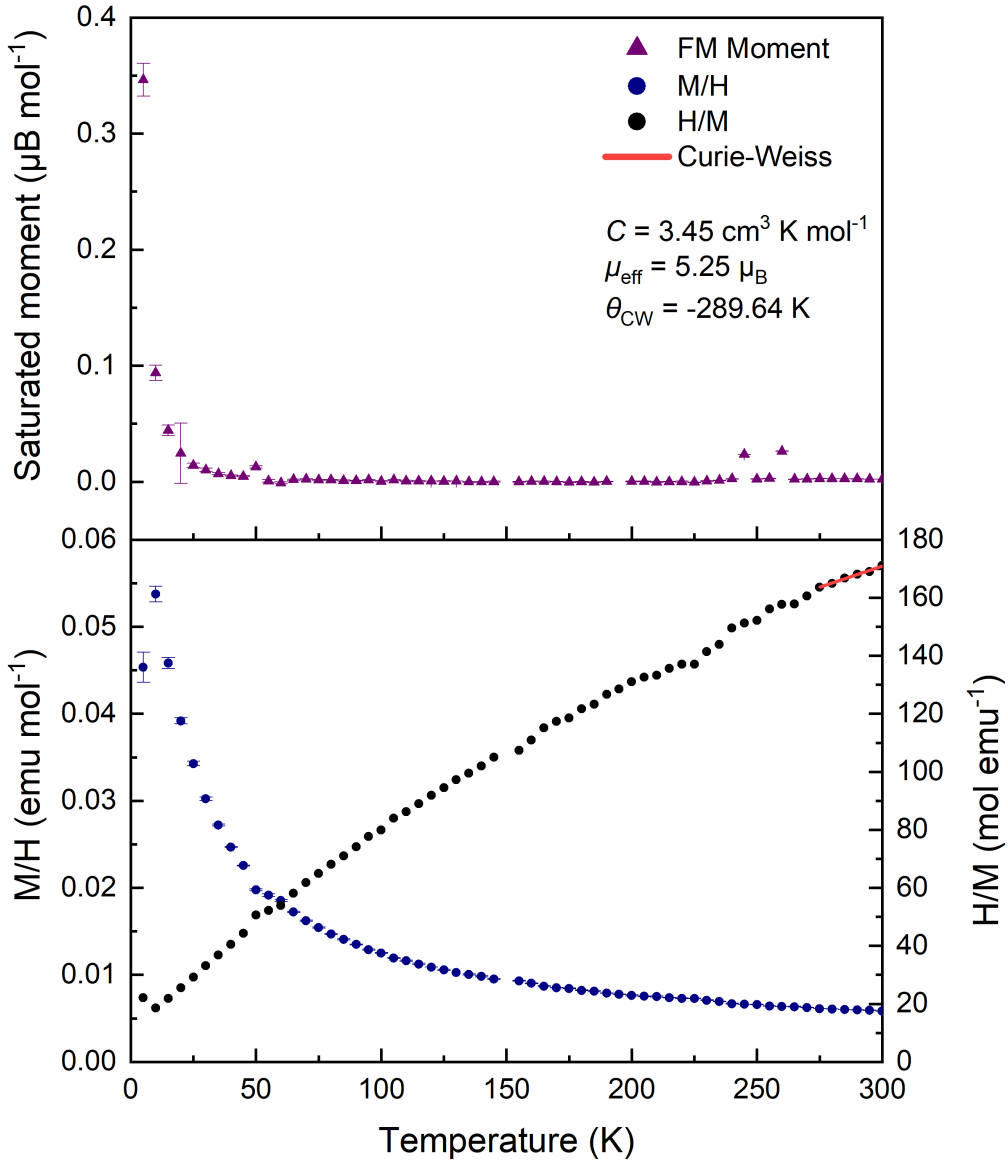


Figure 5.14 The saturated ferromagnetic moment (top), paramagnetic susceptibility, inverse susceptibility of $FeSrNb_2O_7$ as a function of temperature (bottom), and fit to the Curie-Weiss law in the temperature range $275 \leq T/K \leq 300$ K.

temperature range, and therefore one should be wary of the values of C and θ_{CW} extracted from this fitting. Below ~ 25 K, a sharp increase in the saturated moment of the sample is observed, which suggests the onset of magnetic order in the phase (Figure 5.14, top).

5.3.4.4 Low temperature (1.5 K) neutron powder diffraction data

Neutron powder diffraction data collected from $FeSrNb_2O_7$ at 1.5 K were directly compared to data collected at 60 K and are presented in Figure 5.15. No new diffraction features were observed in the low-temperature data, and there was no additional scattering at nuclear Bragg peaks, indicating the absence of long-range magnetic order at 5 K or a structural phase transition. A significant contribution to the background is observed, particularly in the high *d*-spacing region, which can be attributed to paramagnetic scattering arising from the disordered moments in the paramagnetic phase above the magnetic transition temperature.

Refinement of the low temperature neutron diffraction data was not attempted at this stage because a satisfactory model had not been found and so no further structural information can be obtained.

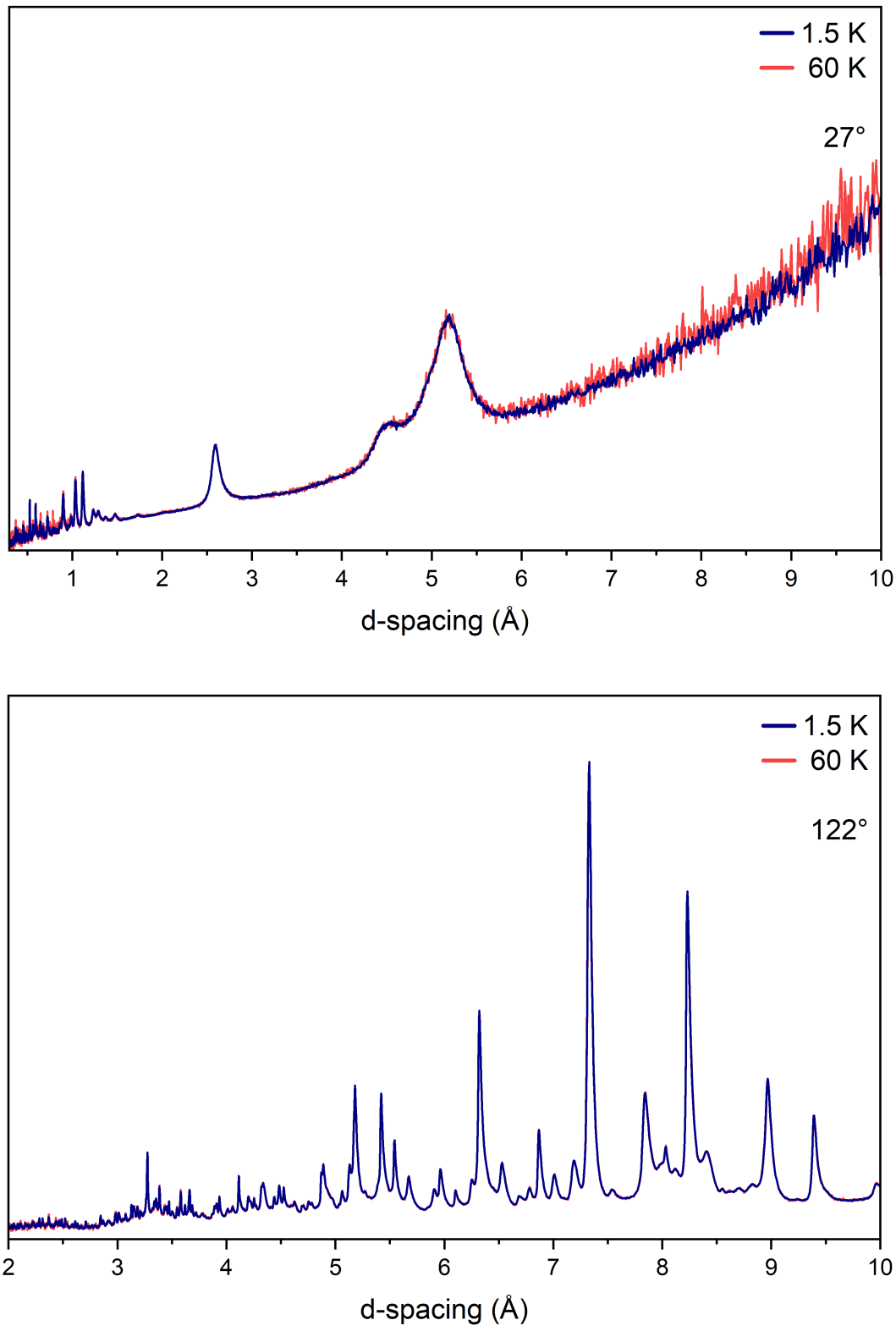


Figure 5.15 Comparison of the NPD data collected from $FeSrNb_2O_7$ at 1.5 K and 60 K using the 1-10 (27°) bank and 4-7 (122°) bank.

5.4 Discussion

The reaction between $Li_2SrNb_2O_7$ and anhydrous $FeCl_2$, $CoCl_2$, and $ZnCl_2$ results in the topochemical exchange of divalent transition metal cations with lithium ions and the synthesis of the metastable phases $FeSrNb_2O_7$, $CoSrNb_2O_7$, and $ZnSrNb_2O_7$. At this stage, it is not possible to unambiguously determine the crystal structures of the phases studied. The complexity of the structures necessitates further investigation, particularly through electron diffraction, to probe the superstructures and elucidate the origins of the axis doubling observed in $FeSrNb_2O_7$ and $ZnSrNb_2O_7$. Elemental analysis and complexometric titrations would also be useful to determine whether lithium remains in the structures. This combined approach might provide the detailed structural information required to understand the subtleties of these materials.

Although the exact crystal structures of these phases are not known at this point, it is possible to compare and contrast the structural information we do have to draw meaningful conclusions about the cation exchange chemistry of $Li_2SrNb_2O_7$.

Given that manganese, iron and cobalt adopt similar chequerboard arrangements in the MCaTa$_2$O$_7$ series, it is reasonable to assume that Fe and Co cations in MSrNb$_2$O$_7$ would adopt analogous local coordination environments to the related phase $MnSrNb_2O_7$. $MnSrNb_2O_7$ presents a unique case in which its superstructure is characterized by a local chequerboard ordering of the manganese cations. This arrangement minimizes interatomic cation-cation repulsion between manganese ions in the interlayer region, but necessitates an incommensurate modulation of the manganese site occupancy. Therefore, the interlayer cations of $CoSrNb_2O_7$ and $FeSrNb_2O_7$ might be expected to adopt a similar local chequerboard-ordered arrangement, by either (1) adopting a structure where a chequerboard

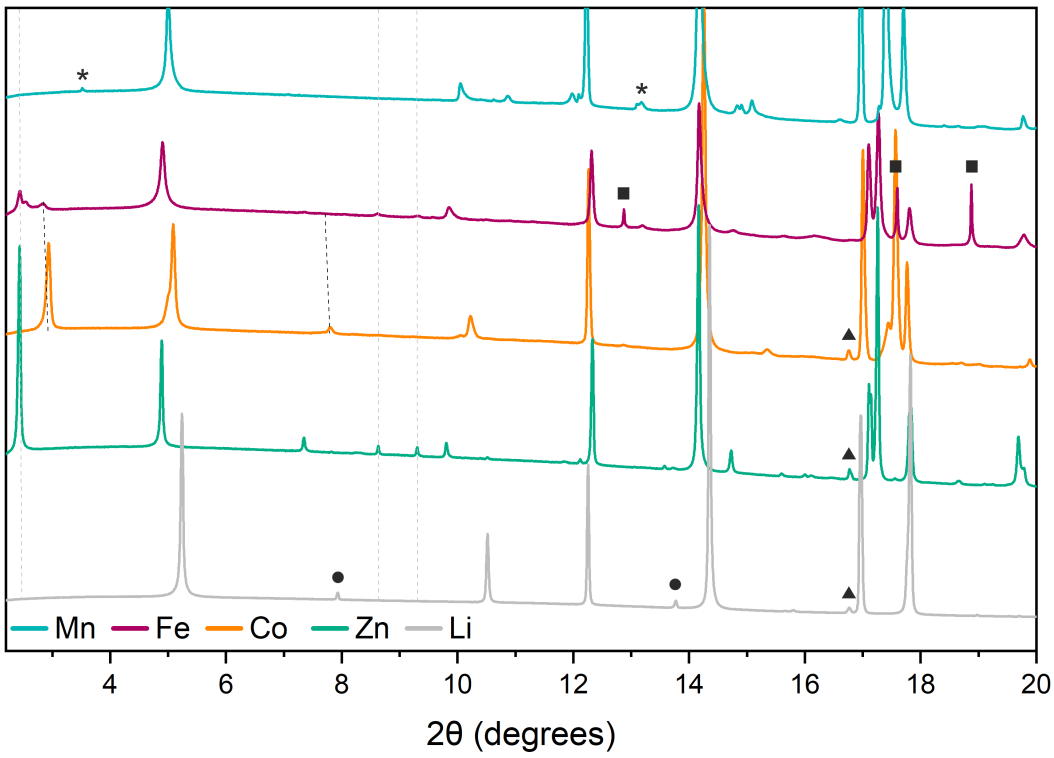


Figure 5.16 Raw SXRD data collected from MSrNb$_2$O$_7$ (M = Mn, Fe, Co, Zn and Li$_2$) at room temperature. Grey dashed lines are used to indicate reflections consistent with a doubling of the c-axis and black dashed lines are used to indicate satellite peaks. Stars, squares, circles and triangles mark peaks corresponding to an unknown n = 3 Ruddlesden-Popper impurity, Fe$_2$O$_3$, Li$_3$O$_4$, and an unknown impurity inherited from the precursor material.

ordering of the interlayer cations is permitted by symmetry or (2) adopting an incommensurately modulated structure that represents the optimal compromise between octahedral tilting and cation ordering.

Indeed, the diffraction data collected from CoSrNb$_2$O$_7$ and FeSrNb$_2$O$_7$ (Figure 5.16) show evidence of an incommensurate structural modulation. However, the satellite peaks corresponding to the modulation differ from those observed in the diffraction data of MnSrNb$_2$O$_7$ and it is therefore plausible to conclude that the nature or origin of the structural modulation in CoSrNb$_2$O$_7$ and FeSrNb$_2$O$_7$ is distinct from that in MnSrNb$_2$O$_7$. If the cation-exchange reaction in these phases is incomplete, the remaining lithium ions and transition metal cations in the interlayer region could create complex interlayer cation ordering.

Consequently, the observed satellite peaks may arise from a modulation of the lithium cations, a factor not considered in the models tested in this chapter.

SXRD and NPD data indicate that $FeSrNb_2O_7$ and $ZnSrNb_2O_7$ adopt analogous average structures with a doubling of the *c*-axis (Figure 5.16). The expansion of the unit cell could arise from the ordering of the interlayer cations in an arrangement whereby the layers are no longer stacked primitively with respect to one another, as illustrated in Figure 5.17. A doubling of the *c*-axis may also be a consequence of localised ordering of lithium and transition metal cations to alternating layers. Although $ZnSrNb_2O_7$ and $FeSrNb_2O_7$ appear to be isostructural, SHG reveals that the former adopts a non-centrosymmetric crystal structure, whereas $FeSrNb_2O_7$ adopts a centrosymmetric structure.

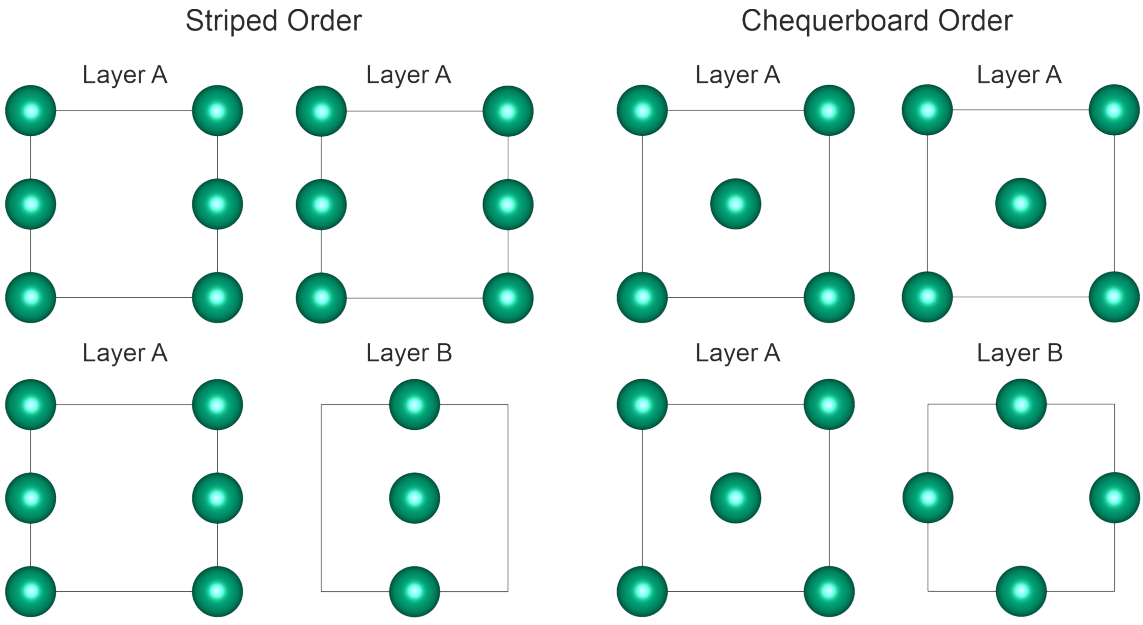


Figure 5.17 A comparison of the possible striped and chequerboard ordering arrangements of the transition metal cations occupying the interlayer region of the pseudo-Ruddlesden-Popper structure, where the layers are stacked primitively with respect to the subsequent layer (AA), or shifted by half a unit cell along *x* (AB).

The magnetic properties of $CoSrNb_2O_7$ and $FeSrNb_2O_7$ provide additional layers of complexity. While both phases exhibit evidence of antiferromagnetic interactions in their magnetization data, no long-range magnetic order is observed in the low-temperature neutron powder diffraction data. This discrepancy suggests that the magnetic interactions are confined to short-range order, possibly due to the structural disorder introduced through the existence of lithium in the interlayer region, or competing interactions within the lattice.

As discussed in the previous chapter, the cation exchange chemistry of $Li_2SrNb_2O_7$ appears to be less robust than that of the analogous phase $Li_2CaTa_2O_7$. This reduced robustness likely stems from the inherent instability of $Li_2SrNb_2O_7$, which does not serve as a sufficiently stable starting material for topochemical exchange reactions. This observation aligns with the difficulties encountered in the cation exchange reactions of $Li_2SrTa_2O_7$. Zhu's research demonstrated the challenges in synthesizing $FeSrTa_2O_7$ and $NiSrTa_2O_7$, as these compounds could not be successfully produced.[128] Additionally, the cation exchange processes in the synthesis of $CuSrTa_2O_7$ and $CoSrTa_2O_7$ were found to be incomplete, and complex interlayer cation order existed due to the presence of both lithium and transition metal cations. This further highlights the limitations and challenges associated with the cation exchange approach in this particular Ruddlesden-Popper family of materials.

Finally, this chapter demonstrates that the ease of cation exchange varies depending on the type of transition metal cation. The substitution of Li^+ for Mn^{2+} and synthesis of $MnSrNb_2O_7$ reached 100% completion, but diffraction data indicates that exchange reactions involving Co^{2+}, Fe^{2+} and Zn^{2+} may not have reached full completion, with residual Li^+ ions potentially remaining in the phases. This discrepancy can be attributed to crystal field effects. Since high-spin Co^{2+} (d^7) ions and Fe^{2+} (d^6) ions generally prefer octahedral coordination environments, forcing these ions into the five-coordinate, pseudo-tetrahedral coordination

sites between the $SrNb_2O_7$ layers incurs an energy penalty. As a result of this, the fully exchanged products may not be kinetically stable. In contrast, high-spin Mn^{2+}cations with a d^5 electronic configuration, do not exhibit a strong geometric preference, which facilitates complete cation exchange.

While significant progress has been made in understanding these complex phases, further studies, particularly utilizing electron microscopy, energy-dispersive X-ray analysis (EDX) or X-ray absorption spectroscopy (XAS), are necessary to fully elucidate their structures and to explain their observed physical behaviours. The insights gained from comparing and contrasting these phases, as well as from examining their cation exchange chemistry and magnetic properties, will contribute to the broader understanding of these and related layered materials.

5.5 Conclusions

Although detailed structural characterisation of the cation-exchanged phases explored in this chapter was not feasible at this time, it is clear that the topochemical exchange of diamagnetic Li^+ *A*'-cations in the $n = 2$ Ruddlesden-Popper phase $Li_2SrNb_2O_7$ with various divalent, first-row transition metal cations has been achieved with varying degrees of success. $CoSrNb_2O_7$ and $FeSrNb_2O_7$ adopt non-polar superstructures characterised by an incommensurate modulation, the origin of which is not yet understood. However, evidence suggests that it differs from the analogous phase $MnSrNb_2O_7$. While both phases exhibit signs of antiferromagnetic interactions upon cooling to low temperatures, neither displays evidence of long-range magnetic order, which may be a consequence of incomplete cation exchange and structural disorder within the interlayer region. $FeSrNb_2O_7$ and $ZnSrNb_2O_7$ adopt structures consistent with a $\sim\sqrt{2} \times \sim\sqrt{2} \times 2$ geometric expansion of an undistorted $n = 2$ Ruddlesden-Popper unit cell, possibly a result of complex interlayer cation ordering.

Despite the promising methodology, the cation exchange reactions of $Li_2SrNb_2O_7$ presented unforeseen challenges and phases with complex structures. This chapter critically examines these difficulties, providing insights and implications for future research in the field of topochemical cation exchange reactions.

Chapter 6: Computational Studies of $Li_2AB_2O_7$ (*A* = Ca, Sr; *B* = Nb, Ta)

6.1 Introduction

The *n* = 2 pseudo-Ruddlesden-Popper phases $Li_2SrTa_2O_7$ and $Li_2CaTa_2O_7$ have been shown experimentally to adopt polar $a^-a^-c^+/a^-a^-c^+$ and $a^-a^-c^+/a^-a^--c^+$ distorted structures described in space groups $A2_1am$ and $Pna2_1$ at room temperature, respectively.[129,130] An $a^-a^-c^+/a^-a^-c^+$ distortion pattern can be decomposed into an in-phase octahedral rotation ($a^0a^0c^+/a^0a^0c^+$) that transforms like the irreducible representation (irrep) $X_2^+(a;0)$, an out-of-phase octahedral rotation ($a^-a^-c^0/a^-a^-c^0$) that transforms like the irrep $X_3^-(b;0)$ and a polar distortion mode orientated in the *ab* plane which transforms like Γ_5^-. This combination of irreducible representations is consistent with a trilinear-coupled stabilisation of the polar, non-centrosymmetric structure. In contrast, the $a^-a^-c^+/a^-a^--c^+$ distortion pattern described in space group $Pna2_1$ can be decomposed into the same out-of-phase octahedral rotation ($a^-a^-c^0/a^-a^-c^0$) that transforms like the irrep $X_3^-(a;0)$, an in-phase octahedral rotation ($a^0a^0c^+/a^0a^0-c^+$) which transforms like the irrep $X_2^+(0;b)$, where the sense of the rotation is inverted between each layer, and a polar distortion mode along the [001] direction which transforms like Γ_3^-. However, unlike $A2_1am$ symmetry, the rotation pattern that establishes the $Pna2_1$ symmetry is not consistent with a trilinear-coupled mechanism, since the two non-polar rotation modes together cannot stabilise a polar structure and the Γ_3^- mode is essential to establish the symmetry. Instead, a second-order Jahn-Teller distortion is thought to stabilise the polar phase. This observation of a switch between the two different stabilisation mechanisms as a function of *A*-site cation

size (Sr/Ca) suggests that the two stabilisation mechanisms are in close competition in this family of materials.

The structure of the closely related niobium phase $Li_2SrNb_2O_7$ is debated. Uppulri *et al.* report a structural transition from a polar structure described in the $A2_1am$ space group at room temperature to an antipolar structure described in space group *Pnam* upon cooling below 90 K. The *Pnam* structure described by Uppulri is closely related to $Pna2_1$, and can be decomposed into the same $X_3^-(a;0)$ and $X_2^+(0;b)$ irreducible representations, plus an antipolar distortion mode M_5^-. In contrast, Nagai *et al.* report the phase transition from a non-polar *Amam* structure (which can be decomposed into the $X_3^-(a;0)$ octahedral rotation) at room temperature to a polar $Pna2_1$ structure at low temperature.[131–133] A summary of each of the experimentally proposed ground state crystal structures of $Li_2AB_2O_7$ is given in Figure 6.1.

This chapter explores the structures and structural distortions of $Li_2SrNb_2O_7$, $Li_2SrTa_2O_7$ and $Li_2CaTa_2O_7$ from a theoretical perspective to rationalise their compositional and structural behaviours. First-principles density functional theory calculations, symmetry principles and crystal-chemical models were used to explore the descent in symmetry from the undistorted $I4/mmm$ parent structure to the ground state. The structural distortions of these phases were investigated using a symmetry-mode approach, where distorted structures are related to their higher-symmetry parent structure by atomic displacement patterns (or modes) which transform like irreducible representations, as described in Chapter 2.[134] First-principles calculations were then used to determine which distortions are energetically favourable, which provides an indication as to probable ground-state structures and possible phase-transition pathways.

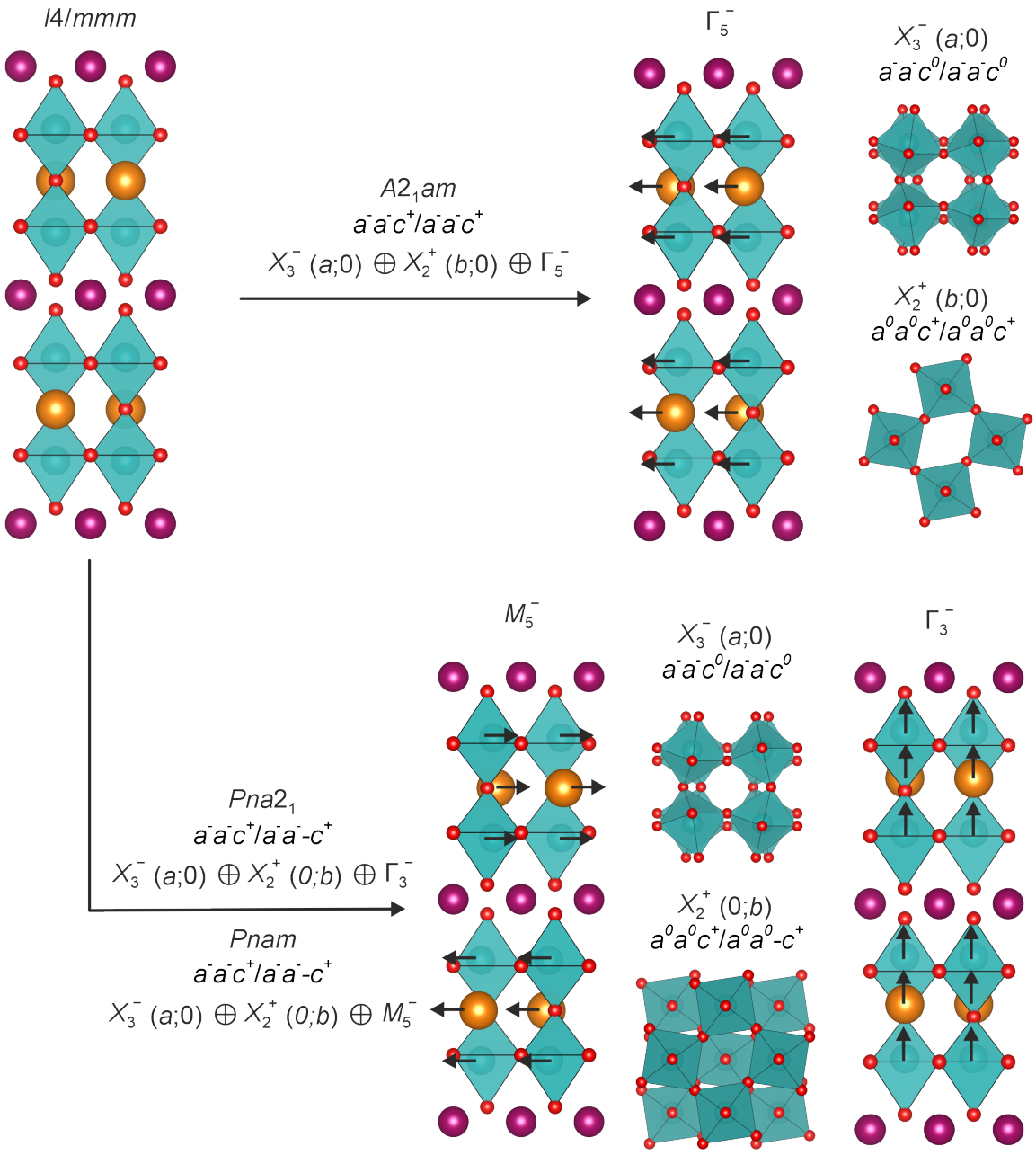


Figure 6.1 A schematic of the atomic displacements of the structural distortion modes extracted from the decomposition of each of the reported ground state structures, $A2_1am$, *Pnam* and $Pna2_1$, with respect to the *I*4/*mmm* high symmetry $Li_2AB_2O_7$ (*A* = Ca, Sr and *B* = Nb, Ta) structure. Purple, orange, teal and red spheres represent Li, *A*, *B* and O atoms, respectively.

6.2 Methods

The first-principles calculations presented in this chapter were performed using the Vienna Ab initio Simulation Package (VASP). The PBEsol exchange-correlation functional and projector-augmented wave (PAW) potentials were used for all calculations. The valence electron configurations for each pseudopotential were as follows: $1s^2 2s^1$ for Li, $3s^2 3p^6 4s^2$ for Ca, $4s^2 5s^2 4p^6$ for Sr, $4s^2 4p^6 4d^4 5s^1$ for Nb, $5p^6 6s^1 5d^4$ for Ta and $2s^2 2p^4$ for O. A force convergence tolerance of 2.5 meV/Å was used, and the lattice constants converged to within 0.001 Å with a planewave cutoff of 900 eV and a $5 \times 5 \times 3$ *k*-point mesh for $Li_2CaTa_2O_7$ and $Li_2SrTa_2O_7$, and a planewave cutoff of 1100 eV and a $6 \times 6 \times 2$ *k*-point mesh for $Li_2SrNb_2O_7$. Force-constant matrices were calculated using finite differences, and the results were validated against calculations performed using density functional perturbation theory.

6.3 Results

6.3.1 $Li_2CaTa_2O_7$

6.3.1.1 Density functional perturbation theory calculations

Density functional perturbation theory (DFPT) was used to calculate the phonons at the Γ-point of the conventional unit cell, and a $2 \times 2 \times 1$ supercell, of the high-symmetry *I*4/*mmm* reference structure of $Li_2CaTa_2O_7$. It was necessary to create a $2 \times 2 \times 1$ supercell to investigate the octahedral rotations which arise at the zone-boundary of the parent *I*4/*mmm* structure, since these modes will be folded back to the Γ-point in the supercell. The results of these calculations are reported in Table 6.1. Two instabilities were identified at the Γ-point of the conventional unit cell, corresponding to the M_5^- mode and the Γ_5^- mode. An imaginary phonon frequency corresponds to an instability and indicates that the given

distortion will lower the energy of the parent structure. In total, a further five instabilities were observed at the Γ-point of the supercell: $X_2^+, X_1^-, X_4^-, X_3^-$ and SM.

Table 6.1 Frequencies, degeneracies and resulting space groups of the unstable modes identified in the supercell of the *I*4/*mmm* aristotype structure of $Li_2CaTa_2O_7$ and the irreducible representations corresponding to each mode.

Frequency / THz	Degeneracy	Space group	Mode
1.7719i	2	$P2_1/m$ (#11)	M_5^- (*a*,*b*)
2.0395i	2	*Cm* (#8)	Γ_5^- (*a*,*b*)
3.6554i	2	*Cmca* (#64)	X_2^+(*a*;0)
3.9172i	2	*Pcna* (#50)	X_1^-(*a*;*b*)
4.1369i	2	*Pccm* (#49)	X_4^-(*a*;0)
4.2227i	4	*Pm* (#6)	SM
4.8657i	2	*Pnnm* (#58)	X_3^- (*a*,*b*)

6.3.1.2 Frozen phonon calculations

The symmetry-adapted modes of each of the instabilities of the *I*4/*mmm* reference structure of $Li_2CaTa_2O_7$ identified in the DFPT calculations were constructed and used to calculate the force constants of each mode. Table 6.2 shows that $Li_2CaTa_2O_7$ is unstable to each of the X_2^+, X_1^-, X_3^-, and M_5^- modes, which is in agreement with the results of the DFPT calculations.

Table 6.2 Calculated frequencies and force constants for the Γ_3^-, X_2^+, X_1^-, X_3^-, and M_5^- modes in the *I*4/*mmm* reference structure of $Li_2CaTa_2O_7$.

	Γ_3^-	X_2^+	X_1^-	X_3^-	M_5^-
Frequency / THz	5.0783	3.6577i	3.9202i	4.8809i	1.8288i
Force constant / eV A^{-2}	1.3788	-0.8749	-1.0051	-1.5721	-0.5266

The X_3^- mode was frozen into the *I*4/*mmm* system along the (*a*;0) direction ([100] crystallographic direction) to establish *Amam* (#63) symmetry and this structure was then relaxed. The energy surface around the relaxed *Amam* structure was explored by constructing a new set of symmetry-adapted modes for each of the following irreps: Γ_2^-, which would establish *A*2$_1$*am* (#36) symmetry, Y_2^+ and Y_2^-, which would establish *Pnam* (#62) symmetry and finally Y_4^+, which would establish *Pnab* (#60) symmetry, noting that the irreducible representations are labelled according to the *Amam* space group and not *I*4/*mmm*. The frequencies and force constants of each of these modes are presented in Table 6.3. A negative force indicates that the given distortion will lower the energy of the *Amam* structure. The *Amam* structure is unstable to the Γ_2^-, Y_2^- and Y_4^+ modes, although the force constant of the Y_4^+ mode is much smaller in magnitude than the Γ_2^- and Y_2^-modes and only just negative.

Table 6.3 Calculated frequencies and force constants for Γ_2^-, Y_2^+, Y_2^- and Y_4^+ modes in the $Li_2CaTa_2O_7$ *Amam* reference structure.

	Γ_2^-	Y_2^+	Y_2^-	Y_4^+
Frequency / THz	2.9103i	1.8163	2.8994i	0.4737i
Force constant / eV A^{-2}	-0.7101	0.5612	-0.7185	-0.0160
Resulting space group	*A*2$_1$*am*	*Pnam*	*Pnam*	*Pnab*

Initially, the Γ_2^- mode was frozen into the *Amam* system along the (*a*) direction to establish *A*2$_1$*am* symmetry and this structure was then relaxed. The energy surface around the relaxed *A*2$_1$*am* structure was explored by constructing a further set of symmetry-adapted modes for the Y_2 irrep which would establish the experimentally observed *Pna*2$_1$ (#33) symmetry, noting that the irreducible representation is labelled according to the *A*2$_1$*am* space group and not *I*4/*mmm*. Table 6.4 shows the calculated frequency and force constant of the Y_2 mode.

The positive value of the force constant indicates that the $A2_1am$ structure is stable with respect to the Y_2 mode. DFPT calculations were used to calculate the phonons at the Γ-point of $A2_1am$ to investigate whether any instabilities were present. The results show that there are no instabilities in the $A2_1am$ symmetry structure and it is therefore dynamically stable.

Table 6.4 Calculated frequency and force constant for the Y_2 mode in the $Li_2CaTa_2O_7$ $A2_1am$ reference structure.

	Y_2
Frequency / THz	2.0149
Force constant / eV A^{-2}	0.7168

For comparison, the Y_2^- mode was frozen into the *Amam* system along the (*a*) direction to establish *Pnam* symmetry and this structure was then relaxed. The experimentally observed polar $Pna2_1$ structure of $Li_2CaTa_2O_7$ can be derived from *Pnam* by the application of a polar distortion that transforms like the irreducible representation Γ_4^- labelled according to the *Pnam* space group (or Γ_3^- if labelled according to $I4/mmm$). The energy surface around the relaxed *Pnam* structure was explored by constructing a further set of symmetry-adapted modes for the Γ_4^- irrep.

Table 6.5 shows the calculated frequency and force constant of the Γ_4^- mode. The positive value of the force constant indicates that the *Pnam* structure is stable with respect to the Γ_4^- mode. Indeed, when frozen into the *Pnam* structure, the amplitude of the Γ_4^- mode is zero when the $Pna2_1$ structure is relaxed. This can be visualised by observing that the Γ_4^- mode is pushed out of the system, and $Li_2CaTa_2O_7$ relaxes to a structure described in space group *Pnam.* DFPT calculations were used to calculate the phonons at the Γ-point of *Pnam* to check whether any instabilities were present. The results show that there are no instabilities in *Pnam* and the structure is therefore dynamically stable.

Table 6.5 Calculated frequency and force constant for the Γ_4^- mode in the $Li_2CaTa_2O_7$ *Pnam* reference structure.

	Γ_4^-
Frequency / THz	2.0594
Force constant / eV A^{-2}	0.6269

Finally, the Y_4^+ mode was frozen into the *Amam* system along the (a) direction to establish *Pnab* symmetry and this structure was then relaxed. The *Pnab* structure is related to the undistorted *I*4/*mmm* aristotype structure by two nonpolar rotation modes transforming like the irreducible representations X_3^- and X_1^-. The energy surface around the relaxed *Pnab* structure was explored by constructing a further set of symmetry-adapted modes for the Γ_3^- irrep which would establish the experimentally observed *Pna*2$_1$ symmetry, noting that the irreducible representation is labelled according to the *Pnab* space group and not *I*4/*mmm*. Table 6.6 shows the calculated frequency and force constant of the Γ_3^- mode. The negative value of the force constant indicates that the *Pnab* structure is unstable with respect to the Γ_3^- mode.

Table 6.6 Calculated frequency and force constant for the Γ_3^- mode in the $Li_2CaTa_2O_7$ *Pnab* reference structure.

	Γ_3^-
Frequency / THz	2.8945i
Force constant / eV A^{-2}	-0.7144

The results of these first-principles calculations and the descent in symmetry from *I*4/*mmm* to the ground state *Pna*2$_1$ structure of $Li_2CaTa_2O_7$ are summarised in Table 6.7 and visually presented in Figure 6.2. The energy differences listed are with respect to the high-symmetry *I*4/*mmm* structure.

Table 6.7 The calculated force constants of the listed modes for $Li_2CaTa_2O_7$ and the energy difference per formula unit between the fully relaxed *I*4/*mmm* structure and the distorted structures. The irreducible representation labels refer to the reference structure given in the row above, not to *I*4/*mmm*.

	Force constant eV/A^{-2}	**ΔE / meV/f.u.**	**Resulting Space Group**
*I*4/*mmm*			
X_3^- (*a*;0)	-1.5721	-594.11497	*Amam*
Amam			
Γ_2^-	-0.7101	-725.14046	$A2_1am$
Y_2^-	-0.7185	-736.99873	*Pnam*
Y_2^+	0.5612	-	*Pnam*
Y_4^+	-0.0160	-594.14211	*Pnab*
$A2_1am$			
Y_2	0.7168	-	$Pna2_1$
Pnam			
Γ_4^-	0.6269	-	$Pna2_1$
Pnab			
Γ_3^-	-0.7144	-737.00139	$Pna2_1$

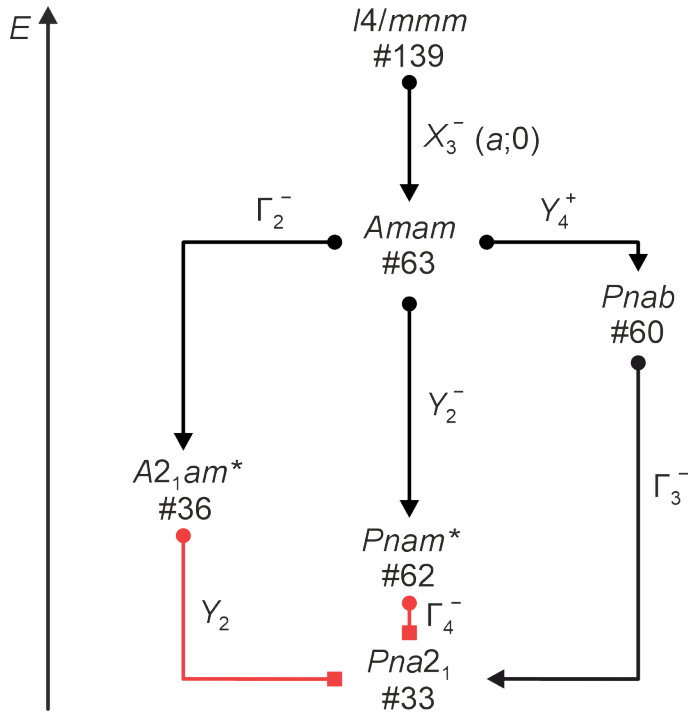


Figure 6.2 Summary of the phonon mode exploration of $Li_2CaTa_2O_7$. The irreducible representation labels refer to the reference structure (e.g. the structure from which the arrow originates), not to *I*4/*mmm*. Black and red arrows indicate whether a particular mode is unstable or stable in the reference structure, respectively. An asterisk is used to indicate when a structure is dynamically stable.

6.3.2 $Li_2SrTa_2O_7$

6.3.2.1 Density functional perturbation theory calculations

DFPT was used to calculate the phonons at the Γ-point of the conventional unit cell, and a $2 \times 2 \times 1$ supercell of the high-symmetry *I*4/*mmm* reference structure of $Li_2SrTa_2O_7$. The results of these calculations are reported in Table 6.8. No instabilities were identified at the Γ-point of the conventional unit cell, and one set of unstable degenerate modes was found at the Γ-point of the supercell, corresponding to X_3^- modes.

Table 6.8 Frequencies, degeneracies and resulting space groups of the unstable modes identified in the supercell of the *I*4/*mmm* aristotype structure of $Li_2SrTa_2O_7$ and the irreducible representations corresponding to each mode.

Frequency / THz	Degeneracy	Space group	Mode
2.8260i	2	*Pnnm* (#58)	X_3^-

6.3.2.2 Frozen phonon calculations

The symmetry-adapted modes of the X_3^-, X_2^+ and Γ_5^- irreducible representations were constructed and used to calculate the force constants for each mode. Table 6.9 shows that $Li_2SrTa_2O_7$ is unstable with respect to the X_3^- distortion, which is in agreement with the results of the DFPT calculations.

Table 6.9 Calculated frequencies and force constants for the Γ_5^-, X_2^+ and X_3^-, modes in the *I*4/*mmm* reference structure of $Li_2SrTa_2O_7$.

	Γ_5^-	X_2^+	X_3^-
Frequency / THz	1.4766	2.2499	2.8676i
Force constant / eV A^{-2}	3.2271	0.3304	-0.5038

The X_3^- mode was frozen into the *I*4/*mmm* system along the (*a*;0) direction ([100] crystallographic direction) to establish *Amam* symmetry and this structure was then relaxed. The energy surface around the relaxed *Amam* structure was explored by constructing a new set of symmetry-adapted modes for each of the following irreps: Γ_2^-, which would establish $A2_1am$ symmetry, and Y_2^+ and Y_2^-, which would establish *Pnam* symmetry, noting that the irreducible representations are labelled according to *Amam* symmetry and not *I*4/*mmm*. The frequencies and force constants of each of these modes are presented in Table 6.10. The positive values of the force constants indicate that the *Amam* structure is stable to the Γ_2^-, Y_2^- and Y_2^+ modes. These results were checked using DFPT calculations which confirmed that the *Amam* structure is dynamically stable and has no further instabilities.

Table 6.10 Calculated frequencies and force constants for Γ_2^-, Y_2^+ and Y_2^- modes in the *Amam* reference structure of $Li_2SrTa_2O_7$.

	Γ_2^-	Y_2^+	Y_2^-
Frequency / THz	2.1595	1.9914	1.0915
Force constant / eV A^{-2}	0.4045	0.7936	0.3631
Resulting space group	$A2_1am$	*Pnam*	*Pnam*

Finally, the X_3^- mode was frozen into the *I*4/*mmm* system along the (*a*;*b*) direction ([110] crystallographic direction) to establish *Pnnm* (#58) symmetry and this structure was then relaxed. The energy surface around the relaxed *Pnnm* structure was explored by constructing a new set of symmetry-adapted modes for the Γ_3^- and Γ_4^- irreps, which would each establish $P2_1nm$ (#31) symmetry, noting that the irreducible representations are labelled according to the *Pnnm* space group and not *I*4/*mmm*. The frequencies and force constants of each of these modes are presented in Table 6.11. The positive values of the force constants indicate that the *Pnnm* structure is stable to both the Γ_3^- mode and Γ_4^- mode.

Table 6.11 Calculated frequency and force constant for the Γ_3^- and Γ_4^- modes in the *Pnnm* structure of $Li_2SrTa_2O_7$.

	Γ_3^-	Γ_4^-
Frequency / THz	1.2558	1.0926
Force constant / eV A^{-2}	0.4047	0.3647

The results of these first-principles calculations and the descent in symmetry from *I*4/*mmm* to the *Amam* ground state structure of $Li_2SrTa_2O_7$ are summarised in Table 6.12 and visually in Figure 6.3. The energy differences listed are with respect to the high symmetry *I*4/*mmm* structure.

Table 6.12 The calculated force constants of the listed modes for $Li_2SrTa_2O_7$ and the energy difference per formula unit between the fully relaxed *I*4/*mmm* structure and the distorted structures. The irreducible representation labels refer to the reference structure given in the row above, not to *I*4/*mmm*.

	Force constant eV/A^{-2}	**ΔE / meV/f.u.**	**Resulting Space Group**
*I*4/*mmm*			
X_3^- (*a*;0)	-0.5038	-77.5200	*Amam*
Amam			
Γ_2^-	0.4045	-	$A2_1am$
Y_2^-	0.3631	-	*Pnam*
Y_2^+	0.7936	-	*Pnam*
Pnnm			
Γ_3^-	0.4047	-	$P2_1nm$
Γ_4^-	0.3647	-	$P2_1nm$

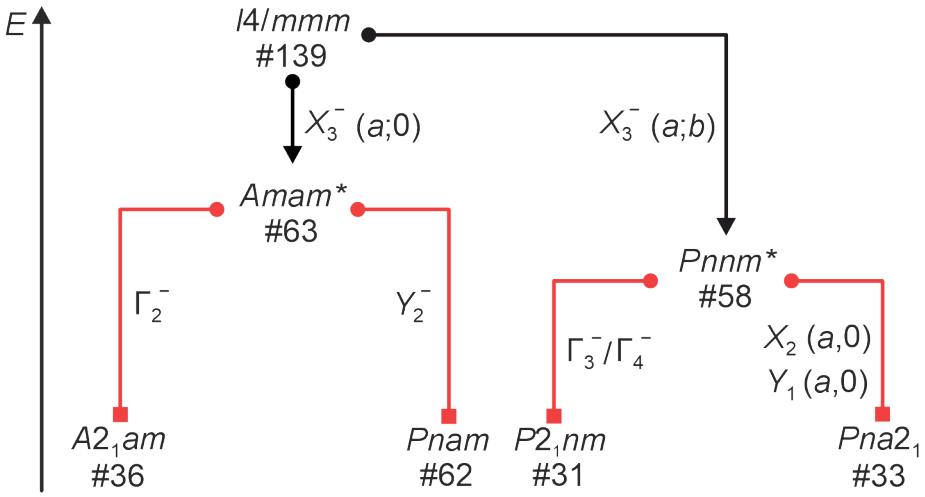


Figure 6.3 Summary of the phonon mode exploration of $Li_2SrTa_2O_7$. The irreducible representation labels refer to the reference structure (e.g. the structure from which the arrow originates), not to *I*4/*mmm*. Black and red arrows indicate whether a particular mode is unstable or stable in the reference structure, respectively. An asterisk is used to indicate when a structure is dynamically stable.

6.3.2.3 Varying the exchange-correlation functional

Up until this point, the calculations in this thesis have strictly used the PBEsol exchange-correlation functional. The LDA and PBE exchange-correlation functionals systematically underestimate and overestimate the unit cell volume of a phase. Both the *I*4/*mmm* and *Amam* structures of $Li_2SrTa_2O_7$ were relaxed using the LDA and PBE exchange-correlation functionals. The lattice parameters are presented in Table 6.13.

DFPT calculations were repeated using the over- and underestimated unit cells to investigate whether any distortion modes become unstable in either the *I*4/*mmm* structure or *Amam* structure of $Li_2SrTa_2O_7$. No new instabilities were observed in calculations using either LDA or PBE exchange-correlation functionals.

Table 6.13 Calculated lattice parameters of $Li_2SrTa_2O_7$ in the fully relaxed *I*4/*mmm* and *Amam* space groups using the LDA, PBEsol and PBE exchange-correlation functionals.

		Exchange-correlation functional		
Space group	Lattice parameter	LDA	PBEsol	PBE
*I*4/*mmm*	*a*	3.9194	3.9470	3.9779
	c	17.8350	18.1943	18.5122
Amam	*a*	5.5293	5.5731	5.6210
	b	5.5468	5.5849	5.6301
	c	17.7781	18.1068	18.3830

6.3.3 $Li_2SrNb_2O_7$

6.3.3.1 Density functional perturbation theory calculations

DFPT was used to calculate the phonons at the Γ-point of the conventional unit cell and a $2 \times 2 \times 1$ supercell of the high-symmetry *I*4/*mmm* reference structure of $Li_2SrNb_2O_7$. The results of these calculations are reported in Table 6.14. Two instabilities were identified at the Γ-point of the conventional cell, corresponding to Γ_5^- and M_5^- modes, and one set of unstable degenerate modes was found at the Γ-point of the supercell, corresponding to X_3^- modes.

Table 6.14 Frequencies, degeneracies and resulting space groups of the unstable modes identified in the supercell of the *I*4/*mmm* aristotype structure of $Li_2SrNb_2O_7$ and the irreducible representations corresponding to each mode.

Frequency / THz	Degeneracy	Space group	Mode
0.5826i	4	*Pm*	SM
1.4335i	2	$P2_1/m$	M_5^-
2.1005i	2	*Cm*	Γ_5^-
3.0228i	2	*Pnnm*	X_3^-

6.3.3.2 Frozen phonon calculations

The symmetry-adapted modes of each of the instabilities of the *I*4/*mmm* reference structure of $Li_2SrNb_2O_7$ identified in the DFPT calculations were constructed and used to calculate the force constants for each mode. Table 6.15 shows that $Li_2SrNb_2O_7$ is unstable to each of the Γ_5^-, X_3^-, and M_5^- modes, which is in agreement with the results of the DFPT calculations.

Table 6.15 Calculated frequencies and force constants for the Γ_5^-, X_3^-, and M_5^- modes in the *I*4/*mmm* reference structure of $Li_2SrNb_2O_7$.

	Γ_5^-	X_3^-	M_5^-
Frequency / THz	2.1021i	3.1936i	1.4760i
Force constant / eV A^{-2}	-0.7022	-0.6006	-0.6761

Initially, the X_3^- mode was frozen into the *I*4/*mmm* system along the (*a*;0) direction ([100] crystallographic direction) to establish *Amam* symmetry and this structure was then relaxed. The energy surface around the relaxed *Amam* structure was explored by constructing a further set of symmetry-adapted modes for each of the following irreps: Γ_2^-, which would establish $A2_1am$ symmetry, and Y_2^+ and Y_2^-, which would establish *Pnam* symmetry, noting that the irreducible representations are labelled according to the *Amam* space group and not *I*4/*mmm*. The frequencies and force constants of each of these modes are presented in Table 6.16. The *Amam* structure is unstable with respect to the Γ_2^- and Y_2^- modes.

Table 6.16 Calculated frequencies and force constants for Γ_2^-, Y_2^+ and Y_2^- modes in the *Amam* reference structure of $Li_2SrNb_2O_7$.

	Γ_2^-	Y_2^+	Y_2^-
Frequency / THz	2.1560i	1.3079	1.4800i
Force constant / eV A^{-2}	-0.6788	0.5305	-0.6128
Resulting space group	$A2_1am$	*Pnam*	*Pnam*

Secondly, the Γ_2^- mode was frozen into the *Amam* system along the (*a*) direction to establish $A2_1am$ symmetry and this structure was then relaxed. The energy surface around the relaxed $A2_1am$ structure was explored by constructing a further set of symmetry-adapted modes for the Y_2 mode which would establish the experimentally observed $Pna2_1$ symmetry, noting that the irreducible representation is labelled according to the $A2_1am$ space group and not

*I*4/*mmm*. Table 6.17 shows the calculated frequency and force constant of the Y_2 mode. The positive value of the force constant indicates that the $A2_1am$ structure is stable with respect to the Y_2 mode.

Table 6.17 Calculated frequency and force constant for the Y_2 mode in the $A2_1am$ structure of $Li_2SrNb_2O_7$.

	Y_2
Frequency / THz	2.3803
Force constant / eV A^{-2}	0.7584

For comparison, the Y_2^- mode was frozen into the *Amam* system along the (*a*) direction to establish *Pnam* symmetry and this structure was then relaxed. The energy surface around the relaxed *Pnam* structure was explored by constructing a further set of symmetry-adapted modes for the Γ_4^- irrep which would establish the experimentally observed $Pna2_1$ symmetry, noting that the irreducible representation is labelled according to the *Pnam* space group and not *I*4/*mmm*. Table 6.18 shows the calculated frequency and force constant of the Γ_4^- mode. The positive value of the force constant indicates that the Γ_4^- mode is stable in the *Pnam* structure.

Table 6.18 Calculated frequency and force constant for the Γ_4^- mode in the *Pnam* structure of $Li_2SrNb_2O_7$.

	Γ_4^-
Frequency / THz	2.4169
Force constant / eV A^{-2}	0.5336

Finally, the X_3^- mode was frozen into the *I*4/*mmm* system along the (*a*;*b*) direction ([110] crystallographic direction) to establish *Pnnm* symmetry and this structure was then relaxed. The energy surface around the relaxed *Pnnm* structure was explored by constructing a new set of symmetry-adapted modes for the Γ_3^- and Γ_4^- irreps, which would each establish $P2_1nm$

symmetry, and the X_2 and Y_1 irreps, which would each establish $Pna2_1$ symmetry, noting that the irreducible representations are labelled according to the *Pnnm* space group and not *I*4/*mmm*. The frequencies and force constants of each of these modes are presented in Table 6.19. The *Pnnm* structure is unstable to both the Γ_3^- mode and Γ_4^- mode.

Table 6.19 Calculated frequency and force constant for the Γ_3^-, Γ_4^- X_2 and Y_1 modes in the *Pnnm* structure of $Li_2SrNb_2O_7$.

	Γ_3^-	Γ_4^-	X_2	Y_1
Frequency / THz	2.3991i	1.7009i	2.9262	2.6529
Force constant / eV A^{-2}	-0.8635	-0.7915	1.0176	0.8092

The Γ_3^- and Γ_4^- modes were frozen into the *Pnnm* system along the (*a*) direction to establish $P2_1nm$ symmetry and these structures were then relaxed. DFPT was then used to calculate the Γ-point phonon frequencies. No further instabilities were identified in either of the $P2_1nm$ structures, and the structures are therefore dynamically stable. In both $P2_1nm$ structures, the polarisation is orientated in the *ab* plane.

The results of these first-principles calculations and the descent in symmetry from *I*4/*mmm* to the *Pnam* ground state structure of $Li_2SrNb_2O_7$ are summarised in Table 6.20 and visually in Figure 6.4. The energy differences listed are with respect to the high symmetry *I*4/*mmm* structure.

Table 6.20 The calculated force constants of the listed modes for $Li_2SrNb_2O_7$ and the energy difference per formula unit between the fully relaxed *I*4/*mmm* structure and the distorted structures. The irreducible representation labels refer to the reference structure given in the row above, not to *I*4/*mmm*.

	Force constant eV/A^{-2}	**ΔE / meV/f.u.**	**Resulting Space Group**
*I*4/*mmm*			
X_3^- (*a*;0)	-0.6006	-106.3512	*Amam*
X_3^- (*a*;*b*)	-	-109.0893	*Pnnm*
Amam			
Γ_2^-	-0.6788	-113.2025	$A2_1am$
Y_2^-	-0.6128	-114.7980	*Pnam*
Y_2^+	0.5305	-	*Pnam*
$A2_1am$			
Y_2	0.7584	-	$Pna2_1$
Pnam			
Γ_4^-	0.5336	-	$Pna2_1$
Pnnm			
Γ_3^-	-0.8635	-111.8377	$P2_1nm$
Γ_4^-	-0.7915	-113.6225	$P2_1nm$
$X_2(a,0)$	1.0176	-	$Pna2_1$
$Y_1(a,0)$	0.8092	-	$Pna2_1$

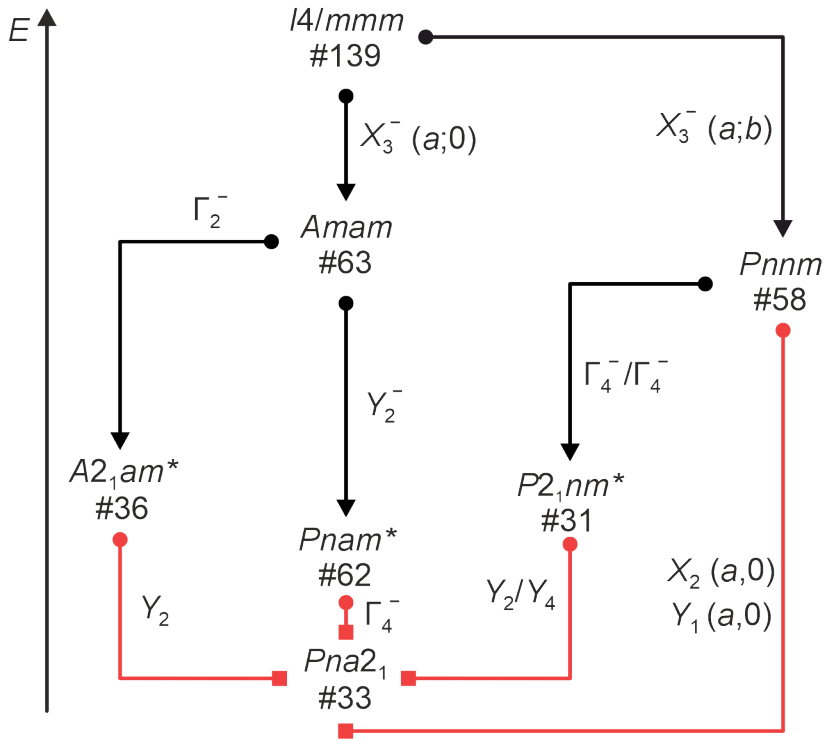


Figure 6.4 Summary of the phonon mode exploration of $Li_2SrNb_2O_7$. The irreducible representation labels refer to the reference structure (e.g. the structure from which the arrow originates), not to *I*4/*mmm*. Black and red arrows indicate whether a particular mode is unstable or stable in the reference structure, respectively. An asterisk is used to indicate when a structure is dynamically stable.

6.3.4 Influence of Artificial Strain

Imposing artificial strain on the $Li_2AB_2O_7$ systems may be an effective strategy towards tuning the relative energies of different phases. In particular, the influence of strain on the magnitude of various distortion modes was investigated by focusing on dynamically stable structures which were expected to be unstable to further distortions that would establish the experimentally observed ground state structures.

Strain was manually applied to the *ab* plane of each structure by constraining the lattice parameters to predetermined values corresponding to a chosen value of applied strain. The atomic positions were allowed to relax and respond to the applied strain by changing their positions slightly, but the lattice parameters themselves, and therefore the unit cell shape, were constrained to prevent the imposed strain being relaxed out of the cell. For each value of applied strain, a range of new structures where the *c*-axis length was manually varied were generated. Here a positive strain (+) implies a compressive strain in the *ab* plane, and hence an elongation of the *c*-axis. Once again, the atomic positions were allowed to relax, but the lattice parameters were kept at a fixed value. The total energy of each structure was then plotted against *c*-axis length, where the minimum of the parabola corresponded to the optimised *c*-axis length for the given strain applied to the *ab* plane. As a final step, the *c*-axis length was set to the optimised value and an atomic relaxation was performed. The resulting structures were fully optimised for the applied strain. The force constants of the modes of interest in the structure were then calculated for each of the new structures to investigate how the applied strain affects the instabilities in each phase. The force constants of the Γ_2^- mode in the *Amam* structure of $Li_2SrTa_2O_7$ and the Γ_4^- mode in the *Pnam* structure of $Li_2CaTa_2O_7$ and $Li_2SrNb_2O_7$ as a function of applied strain are presented in Table 6.21, Table 6.22 and Table 6.23.

Table 6.21 The lattice parameters and calculated force constant of the Γ_2^- mode in the $Li_2SrTa_2O_7$ *Amam* structure.

Strain / %	*a*	*b*	*c*	Force constant / eV/A^{-2}
+1.5	5.4897	5.5013	18.3926	-0.0693
+1	5.5176	5.5292	18.2974	0.0975
0	5.5733	5.5851	18.1091	0.4045
-1	5.6291	5.6409	17.9338	0.5128
-1.5	5.6569	5.6688	17.8471	0.2811

Table 6.22 The lattice parameters and calculated force constant of the Γ_4^- mode in the $Li_2CaTa_2O_7$ *Pnam* structure.

Strain / %	*a*	*b*	*c*	Force constant / eV/A^{-2}
+1.5	5.4328	5.3602	18.4334	0.7716
+1	5.4604	5.3874	18.3520	0.7414
0	5.5155	5.4418	18.1887	0.6269
-1	5.5707	5.4962	18.0407	0.5169
-1.5	5.5983	5.5234	17.9650	0.4645

Table 6.23 The lattice parameters and calculated force constant of the Γ_4^- mode in the $Li_2SrNb_2O_7$ *Pnam* structure.

Strain / %	*a*	*b*	*c*	Force constant / eV/A^{-2}
+1.5	5.4987	5.5091	18.2435	0.2787
+1	5.5266	5.5370	18.1400	0.3016
0	5.5824	5.5930	17.9368	0.5336
-1	5.6382	5.6489	17.7527	0.6679
-1.5	5.6661	5.6769	17.6574	0.7016

Each of the modes of interest were frozen into each system under strain and the atomic positions were allowed to relax. The energy of the resulting structures and the distortion mode amplitudes extracted from each phase are presented in Figure 6.5, Figure 6.6 and Figure 6.7.

Table 6.21 shows an applied compressive strain of 1.5% to the *Amam* phase of $Li_2SrTa_2O_7$ induces a Γ_2^- instability. This suggests that for compressive strain of 1.5%, the Γ_2^- mode would lower the energy of the *Amam* structure and establish the $A2_1am$ symmetry of the experimentally observed ground state structure. Indeed, Figure 6.5a and b show that the energy of the *Amam* phase and the $A2_1am$ phase remain equal for small values of strain until a compressive strain of 1.5%, where the $A2_1am$ phase becomes slightly more stable. Figure 6.5c demonstrates that the X_3^- distortion mode increases slightly as a function of strain from tensile to compressive. The X_2^+ and Γ_5^- modes remain constant and approximately zero as a function of strain until a compressive strain > 1%, at which point they become nonzero. It is not possible to infer which mode is driving the transition from the *Amam* structure to the $A2_1am$ structure, but both distortion modes are necessary to establish the correct symmetry.

Table 6.22 shows that the Γ_4^- mode becomes increasingly soft moving from compressive to tensile strain in $Li_2CaTa_2O_7$. Interestingly, the opposite behaviour is observed for $Li_2SrNb_2O_7$, where the Γ_4^- mode becomes harder moving from a compressive to tensile strain (Table 6.23). For both compounds, the *Pnam* structure does not become unstable with respect to the Γ_4^- mode within the values of compressive and tensile strain explored in the calculations. Figure 6.6a and b, and Figure 6.7a and b illustrate that the energy of the *Pnam* and $Pna2_1$ structures of both $Li_2CaTa_2O_7$ and $Li_2SrNb_2O_7$ remain equal within the values of applied strain, which suggests that $Pna2_1$ is relaxing back to *Pnam* and the Γ_4^- mode is being pushed out of the structure.

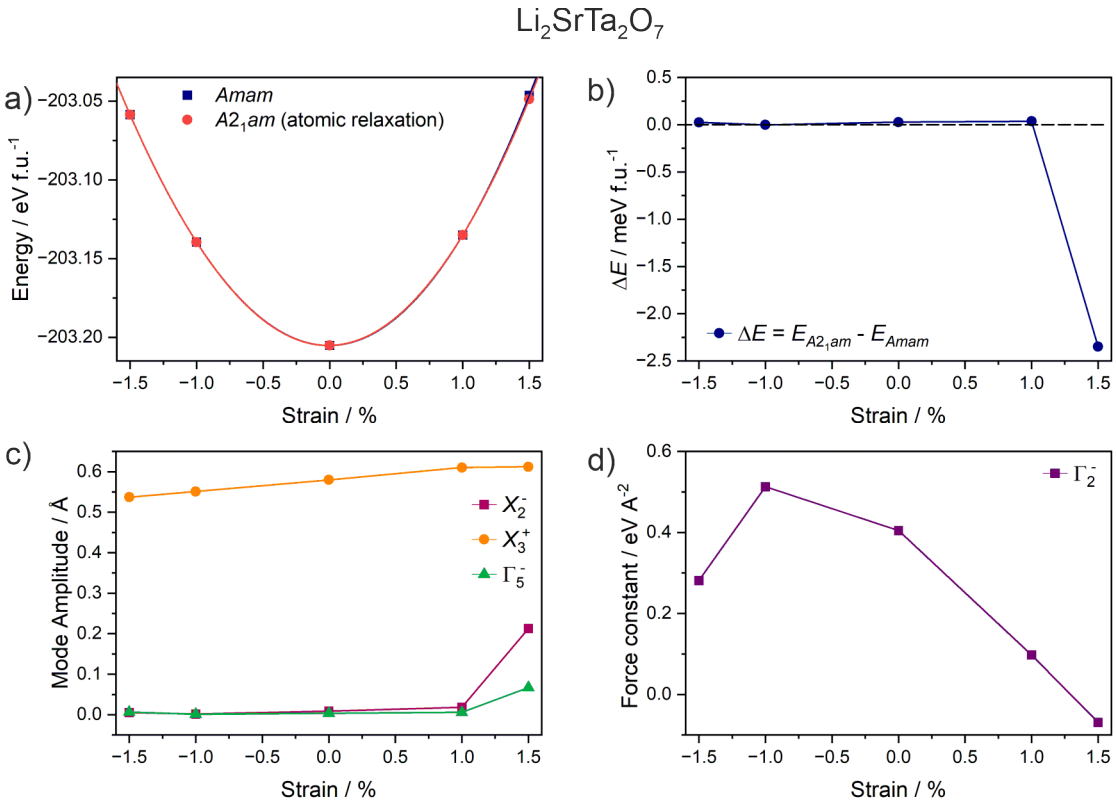


Figure 6.5 a) The total energy of the *Amam* and *A*2$_1$*am* structures, b) the energy difference between the *Amam* and *A*2$_1$*am* structures and c) the amplitude of structural distortion modes of *Amam* and d) the force constant of the Γ_2^- mode in the *Amam* structure as a function of applied strain of $Li_2SrTa_2O_7$. The energies and mode amplitudes reported are normalised to the high symmetry *I*4/*mmm* reference cell (e.g. for a 24-atom cell).

Figure 6.6c and Figure 6.7c show the evolution of the structural distortion modes as a function of strain. For $Li_2CaTa_2O_7$, the X_3^- distortion mode appears to very slightly decrease with increasing amplitudes of both compressive and tensile strain, whereas the M_5^- mode slightly increases with increasing amplitudes of compressive and tensile strain. The X_2^+ mode rapidly increases as a function of strain from tensile to compressive strain. This same trend is observed in the value of the force constant of the Γ_4^- mode, which indicates that the rotational modes, in particular the X_2^+ mode, is in competition with, and potentially supressing, the polar Γ_4^- distortion mode. In $Li_2SrNb_2O_7$, the X_3^- distortion slightly increases moving from tensile to compressive strain. The X_2^+ mode remains approximately constant from tensile to compressive strain, until a compressive strain of > 1%, after which the

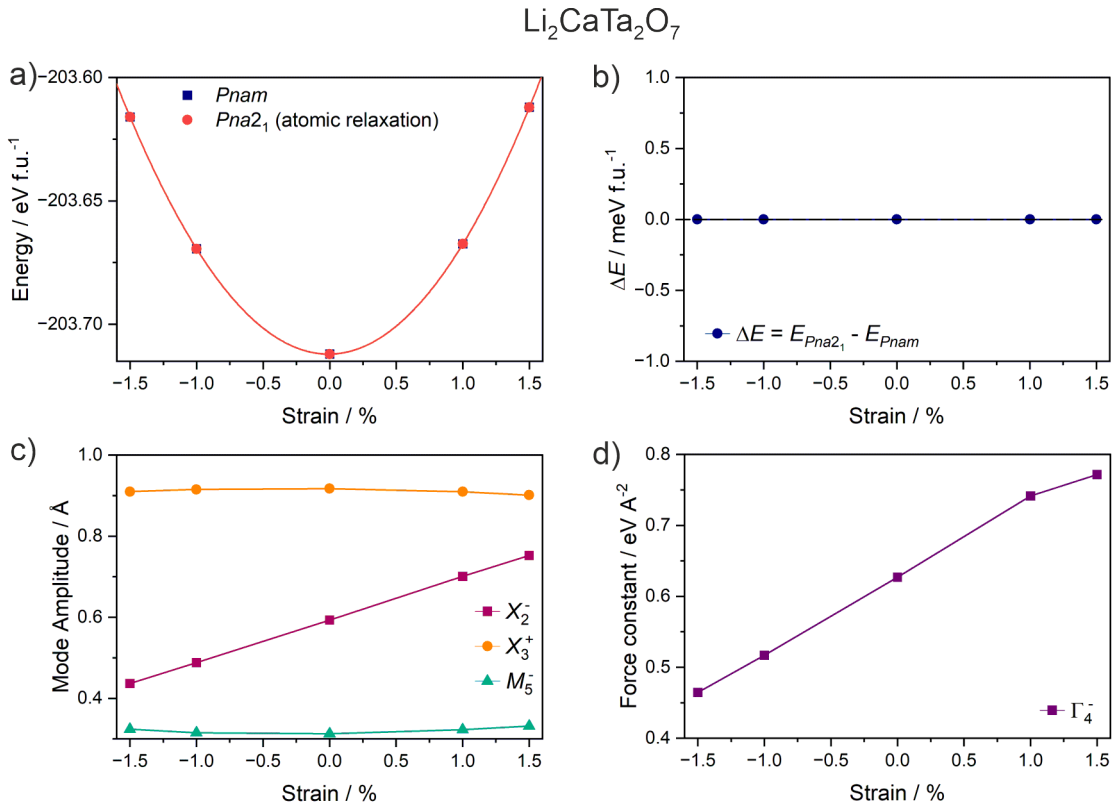


Figure 6.6. a) The total energy of the *Pnam* and *Pna*2$_1$ structures, b) the energy difference between the *Pnam* and *Pna*2$_1$ structures, c) the amplitude of structural distortion modes of the *Pnam* structure and d) the force constant of the Γ_4^- mode as a function of applied strain in the *Pnam* structure of $Li_2CaTa_2O_7$. The energies and mode amplitudes reported are normalised to the high symmetry *I*4/*mmm* reference cell (e.g. for a 24-atom cell).

amplitude of the mode rapidly increases. The M_5^- mode decreases from tensile to compressive strain. The decrease in the magnitude of this mode is consistent with the softening of the Γ_4^- mode moving from tensile to compressive strain and suggests that in $Li_2SrNb_2O_7$, the M_5^- mode may be competing with the Γ_4^- mode. These observations are consistent with those previously reported by Hasin and Nowadnick.[135]

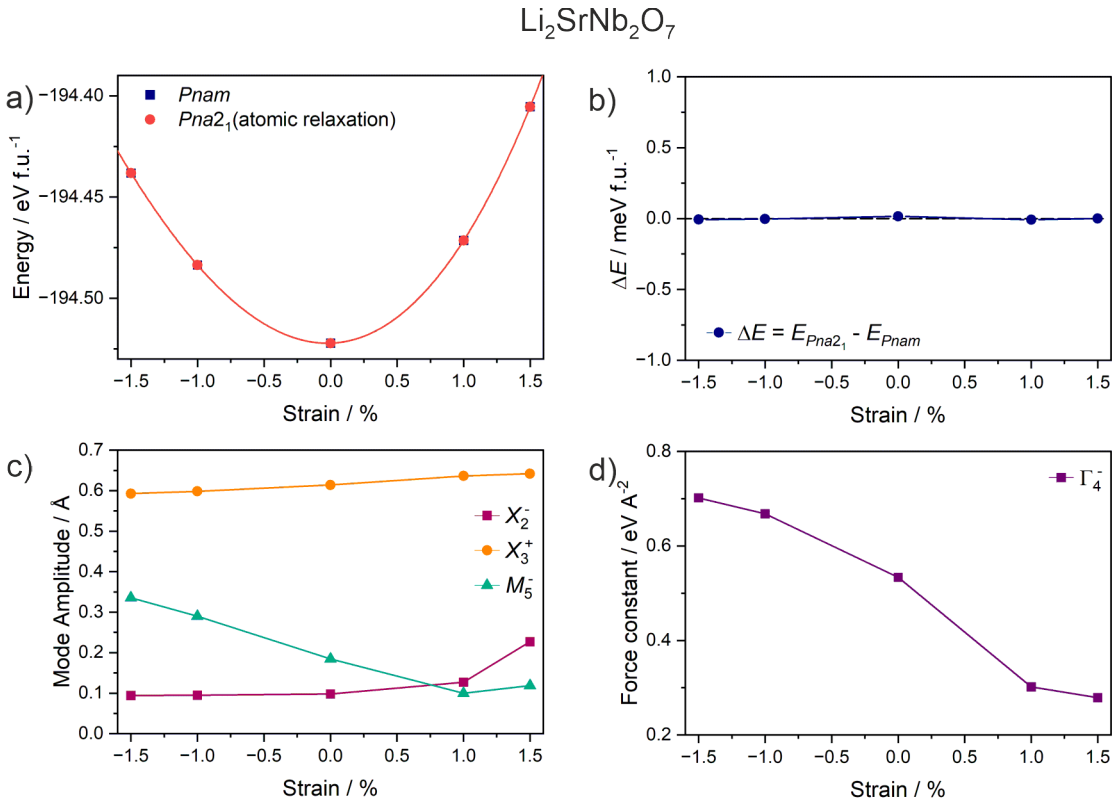


Figure 6.7. a) The total energy of the *Pnam* and *Pna*2$_1$ structures, b) the energy difference between the *Pnam* and *Pna*2$_1$ structures, c) the amplitude of structural distortion modes of the *Pnam* structure and d) the force constant of the Γ_4^- mode as a function of applied strain in the *Pnam* structure of $Li_2SrNb_2O_7$. The energies and mode amplitudes reported are normalised to the high symmetry *I*4/*mmm* reference cell (e.g. for a 24-atom cell).

6.4 Discussion

Structural relaxations of each of the experimentally reported structures (*Amam, Pnam, Pna*2$_1$ and *A*2$_1$*am*) of $Li_2AB_2O_7$ were performed for each member of the series. The energy differences between the *I*4/*mmm* high symmetry reference structure and the distorted structures are presented in Table 6.24. For $Li_2CaTa_2O_7$ and $Li_2SrNb_2O_7$, *Pnam* is the lowest energy structure, but is only approximately 0.01 meV/f.u. lower in energy than the *Pna*2$_1$ structure. Additionally, the *Pna*2$_1$ structure relaxes back to the *Pnam* structure for both $Li_2CaTa_2O_7$ and $Li_2SrNb_2O_7$. In contrast, the *Amam* structure of $Li_2SrTa_2O_7$ is marginally lower in energy than *Pnam, Pna*2$_1$ and *A*2$_1$*am* (< 0.03 meV/f.u.), which all relax back to the

Table 6.24 The energy difference per formula unit between the fully relaxed *I*4/*mmm* structure and the distorted structures.

		ΔE / meV/f.u.		
Space group	**Irreducible Representation**	**$Li_2CaTa_2O_7$**	**$Li_2SrTa_2O_7$**	**$Li_2SrNb_2O_7$**
Amam	X_3^- (*a*;0)	-595.2311	-78.9229	-108.4664
Pnam	X_3^- (*a*;0) ⊕ X_2^+(0;*b*) ⊕ M_5^-	-737.6593	-78.8956	-115.7869
*Pna*2$_1$	X_3^- (*a*;0) ⊕ X_2^+(*0*;*b*) ⊕ Γ_3^-	-737.6496	-78.9149	-115.7722
*A*2$_1$*am*	X_3^- (*a*;0) ⊕ X_2^+(*b*;0) ⊕ Γ_5^-	-725.8142	-78.9019	-114.2702

Amam structure. These findings support those of previous theoretical studies, but are not consistent with the experimentally reported structures, where SHG measurements conclude all three phases adopt non-centrosymmetric structures at low temperatures.[120,135–139] This suggests these calculations are unable to correctly account for the onset of polarity in this family of materials.

Our findings demonstrate that all three materials are unstable to at least the X_3^- mode in the undistorted *I*4/*mmm* reference structure, and that the *Amam* structure is lower in energy than the *I*4/*mmm* structure. Both $Li_2CaTa_2O_7$ and $Li_2SrNb_2O_7$ are also unstable to Γ_5^- and M_5^- polar distortions in the *I*4/*mmm* structure, but only $Li_2CaTa_2O_7$ is unstable to X_2^+. Interestingly, $Li_2SrTa_2O_7$ is not unstable to any zone-centre polar distortions in the *I*4/*mmm* structure, which suggests that this phase cannot be a proper ferroelectric.

Although DFT cannot be used to describe the dynamics of a phase transition, it can provide insights into possible phase transition pathways and intermediate phases. Galven and co-workers report the phase transition behaviour of $Li_2CaTa_2O_7$.[139] $Li_2CaTa_2O_7$ undergoes a

transition from a polar $Pna2_1$ phase to an antipolar *Pnam* phase at $T = 220$ °C, and a second transition to a non-polar *Amam* structure at 660 °C. As discussed previously in Section 6.3.1, the transition from the $I4/mmm$ reference structure to the polar ground state $Pna2_1$ structure of $Li_2CaTa_2O_7$ appears to proceed through the intermediate phases *Amam* and *Pnab*. If this were indeed true, it would suggest that the transition from *Pnam* to $Pna2_1$ is a first-order, discontinuous phase transition, since the system would need to 'reverse' from *Pnam* because calculations indicate that the transition pathway from *Pnam* to $Pna2_1$ via the Γ_4^- mode is stable. In order to investigate this further, it is necessary to collect high-resolution synchrotron X-ray diffraction data from $Li_2CaTa_2O_7$ through the phase transitions to study the lattice parameter changes. One might expect a discontinuous variation in the lattice parameters as a function of temperature at the phase transition temperature if the transition from *Pnam* to $Pna2_1$ is truly first-order.[140]

6.4.1 Structure Decomposition

The experimental structures of $Li_2CaTa_2O_7$, $Li_2SrTa_2O_7$ and $Li_2SrNb_2O_7$ can be decomposed using ISODISTORT to obtain the magnitude of each structural distortion mode and compared with the theoretical values of the DFT-relaxed structures. The distortion mode amplitudes obtained from the decomposition of the DFT-relaxed and experimental structures for each of the phases listed are reported in Table 6.25, Table 6.26 and Table 6.27.

Table 6.25 Structural distortion mode decomposition of the experimental (when reported) and DFT-relaxed structures of $Li_2CaTa_2O_7$ with respect to the high-symmetry *I*4/*mmm* reference structure. The distortion mode amplitudes given are normalised to the reference cell in Å (e.g. for a 24-atom cell).

		Irreducible Representation							
Space group		X_3^-	X_2^+	M_5^-	M_5^+	Γ_5^-	Γ_3^-	X_1^-	X_4^+
Amam	Expt.	0.641	-	-	-	-	-	-	-
	DFT	0.971	-	-	-	-	-	-	-
Pnam	Expt.	0.794	0.417	0.191	-	-	-	-	-
	DFT	0.916	0.596	0.313	-	-	-	-	-
$Pna2_1$	Expt.	0.824	0.542	0.242	0.058	-	0.198	0.081	0.161
	DFT	0.917	0.593	0.312	0.000	-	0.000	0.000	0.000
$A2_1am$	Expt.	-	-	-	-	-	-	-	-
	DFT	0.911	0.579	-	-	0.301	-	-	-
Pnab	Expt.	-	-	-	-	-	-	-	-
	DFT	0.969	-	-	0.020	-	-	0.046	-

Table 6.26 Structural distortion mode decomposition of the experimental (when reported) and DFT-relaxed structures of $Li_2SrTa_2O_7$ with respect to the high-symmetry *I*4/*mmm* reference structure. The distortion mode amplitudes given are normalised to the reference cell in Å (e.g. for a 24-atom cell).

		Irreducible Representation			
Space group		X_3^-	X_2^+	M_5^-	Γ_5^-
Amam	Expt.	0.415	-	-	-
	DFT	0.584	-	-	-
Pnam	Expt.	-	-	-	-
	DFT	0.579	0.005	0.004	-
$A2_1am$	Expt.	0.536	0.085	-	0.281
	DFT	0.580	0.009	-	0.003

Table 6.27 Structural distortion mode decomposition of the experimental (when reported) and DFT-relaxed structures of $Li_2SrNb_2O_7$ with respect to the high-symmetry *I*4/*mmm* reference structure. The distortion mode amplitudes given are normalised to the reference cell in Å (e.g. for a 24-atom cell).

		Irreducible Representation						
Space group		X_3^-	X_2^+	M_5^-	Γ_5^-	Γ_3^-	X_1^-	X_4^+
Amam	Expt.	0.497	-	-	-	-	-	-
	DFT	0.617	-	-	-	-	-	-
Pnam	Expt.	0.591	0.213	0.270	-	-	-	-
	DFT	0.617	0.099	0.183	-	-	-	-
$Pna2_1$	Expt.	0.568	0.084	0.352	-	0.041	0.029	0.016
	DFT	0.614	0.098	0.185	-	0.002	0.000	0.000
$A2_1am$	Expt.	0.547	0.068	-	0.474	-	-	-
	DFT	0.618	0.097	-	0.141	-	-	-
$P2_1nm$	Expt.	-	-	-	-	-	-	-
	DFT	0.617	0.094	0.002	0.140	-	0.000	-

In all three systems, in both the experimental and DFT-relaxed structures, the amplitude of the X_2^+ mode is consistently smaller than the X_3^- mode. The X_3^- structural distortion mode consists of oxygen and lithium displacements and a comparatively small displacement of the *A* and *B*-site cations. The X_2^+ mode involves the motion of only lithium and oxygen, where the oxygen ion displacements are the most significant contributor to the magnitude of the mode. The Γ_3^- and Γ_5^- polar distortion modes involve the motion of the *A* and *B*-site cations against the oxygen lattice and result in a net macroscopic polarisation. These displacements are in opposite directions in the M_5^- antipolar mode, and therefore lead to a cancellation of the layer polarisations to yield a net zero macroscopic polarisation.

When comparing the values from experiment with those obtained theoretically, it is clear that DFT greatly overestimates the magnitude of the rotational distortions, particularly the X_3^- and X_2^+ modes. This observation might explain the discrepancy between the ground state

structures predicted by theory and those obtained from experiment. It is possible that these rotational modes compete with, or suppress, the polar mode in the calculations, and an overestimation of the X_3^- and X_2^+ modes results in an underestimation of the polar modes. To investigate this further, strain calculations probed the interplay between the magnitude of the rotational modes and the polar distortions. In particular, the X_2^+ mode, which describes the $a^0a^0c^+/a^0a^0c^+$ distortion and displacement of atoms perpendicular to the *c*-axis, may be significantly influenced by the application of strain in the *ab* plane. A softening of the Γ_4^- mode is observed in the *Pnam* structure of $Li_2CaTa_2O_7$, which would establish the experimentally observed $Pna2_1$ structure, as the magnitude of the X_2^+ mode decreases. This suggests that the X_2^+ mode competes with the polar distortion mode in *Pnam*. However, $Li_2SrNb_2O_7$ does not display the same behaviour. The magnitude of the X_2^+ mode remains mostly constant within the strain values of the calculations whereas the M_5^- mode decreases from tensile to compressive strain. This could indicate that the mechanisms that stabilises the polar structures in these materials are different.

Finally, the consequences of the chemical substitution of the *A* and *B* sites are explored. Substitution of larger Sr^{2+} for smaller Ca^{2+} reduces the tolerance factor and enhances instabilities to octahedral rotations. The amplitudes of the octahedral rotation modes (e.g. X_3^- and X_2^+) vary systematically with composition and are greater in the calcium phase than in either of the strontium phases. Additionally, the X_2^+ mode is unstable in the *I*4/*mmm* structure of $Li_2CaTa_2O_7$, but hardens as a function of cation size from Ca to Sr, becoming stable in both $Li_2SrTa_2O_7$ and $Li_2SrNb_2O_7$.

Given that Nb^{5+} and Ta^{5+} are almost identical in size (ionic radius of octahedral Ta^{5+} = 0.64 Å, octahedral Nb^{5+} = 0.64 Å), $Li_2SrTa_2O_7$ and $Li_2SrNb_2O_7$ might be expected to behave similarly, assuming that an ionic packing model is dominant. However, the magnitude of

the octahedral distortions in $Li_2SrNb_2O_7$ are greater than in $Li_2SrTa_2O_7$, despite the tolerance factors of each phase being the same. Experimental data show that $Li_2SrTa_2O_7$ adopts an $A2_1am$ structure, in contrast to $Li_2SrNb_2O_7$, which has a $Pna2_1$ ground state. This preference for the $Pna2_1$ phase of $Li_2SrNb_2O_7$ reflects the stronger SOJT interaction of Nb–O vs. Ta–O.[26,141]

A displacement of the Ta cations is observed in the *Pnam* and $Pna2_1$ structures of $Li_2CaTa_2O_7$, but the displacement of the Ca cation has the greatest contribution to the magnitude of the polar distortion mode. This suggests that a large polarisation arises from the *A*–O layers, which has been previously observed in Ruddlesden-Popper hybrid-improper ferroelectrics.[61] The layer-resolved polarisations for each material should be calculated to confirm this. Since the Ta–O layers do not appear to significantly contribute to the polarisation, it is likely that ferroelectricity in these phases is not induced by the hybridisation of Ta and O orbitals via the SOJT effect, that is, it is not a result of a proper ferroelectric mechanism. BVS calculations indicate that Ca is under-bonded in *Pnam* (BVS = 1.731) and that this under-bonding is relieved in $Pna2_1$ (BVS = 1.969), suggesting that the transition from the antipolar *Pnam* structure to the polar $Pna2_1$ structure is driven by the optimisation of the Ca cation bonding environment.

In contrast, the opposite behaviour is observed in $Li_2SrNb_2O_7$, where the displacement of the Nb cations in the *Pnam,* $Pna2_1$ and $A2_1am$ structures is greater in magnitude than that of the Sr cations, and suggests a large polarisation arises from the Nb–O layers. BVS calculations reveal that the bonding environment of Sr has been optimised in the *Pnam* structure (BVS = 2.069). This may indicate that the origin of ferroelectricity in these phases is different and although the experimentally reported ground state structures are the same for both phases, the primary driver for the structural distortions may differ.

The calculated lattice parameters of $Li_2CaTa_2O_7$, $Li_2SrTa_2O_7$ and $Li_2SrNb_2O_7$ are reported in Table 6.28. When available, the experimental lattice parameters are also reported. It is clear that there are significant discrepancies between the lattice parameters calculated using DFT and those determined experimentally. Firstly, DFT calculations systematically underestimate the magnitude of the lattice parameters of $Li_2CaTa_2O_7$. This is unsurprising, since DFT calculations are performed at zero kelvin, and therefore the lattice parameters reported for higher temperature phases e.g. *Amam* and *Pnam* are larger. In comparison, the lattice parameters of the DFT-relaxed structures of $Li_2SrTa_2O_7$ are much closer to the experimentally reported values, particularly in the *a* and *b* directions, whilst the *c* lattice parameter is consistently underestimated.

Table 6.28 The lattice parameters (Å) of experimental structures (when reported) and DFT-relaxed structures of $Li_2CaTa_2O_7$, $Li_2SrTa_2O_7$ and $Li_2SrNb_2O_7$.

		$Li_2CaTa_2O_7$		**$Li_2SrTa_2O_7$**		**$Li_2SrNb_2O_7$**	
Space group	**Lattice parameter**	Expt.	DFT	Expt.	DFT	Expt.	DFT
*I*4/*mmm*	*a*	-	3.9229	3.9531[142]	3.9470	-	3.9470
	b	-	3.9229	3.9531	3.9470	-	3.9470
	c	-	18.2010	18.3102	18.1943	-	18.0141
Amam	*a*	5.5510[143]	5.5295	5.5797[142]	5.5731	5.5990[144]	5.5848
	b	5.5580	5.5096	5.5844	5.5849	5.6056	5.5707
	c	18.5042	18.0865	18.1822	18.1068	18.0241	17.9742
Pnam	*a*	5.5326[143]	5.5155	-	5.5735	5.5890[145]	5.5824
	b	5.5047	5.4418	-	5.5852	5.5942	5.5931
	c	18.3524	18.1887	-	18.1069	17.9331	17.9365
$A2_1am$	*a*	-	5.5164	5.5784[146]	5.5734	5.5918[145]	5.5820
	b	-	5.4458	5.5842	5.5850	5.5987	5.5915
	c	-	18.1841	18.1845	18.1064	18.0102	17.9423
$Pna2_1$	*a*	5.5123[147]	5.5157	-	-	5.5937[144]	5.5928
	b	5.4637	5.4426	-	-	5.5986	5.5830
	c	18.2321	18.1874	-	-	17.9230	17.9349
$P2_1nm$	*a*	-	-	-	-	-	5.5817
	b	-	-	-	-	-	5.5920
	c	-	-	-	-	-	17.9410

6.4.2 Future Work

Several questions about these phases still remain to be answered, and additional work is necessary to establish why the ground state structures determined using theory are not consistent with the experimentally reported ground state structures. It might be insightful to further investigate the interplay between the magnitudes of the rotational modes and the

polar distortion modes, perhaps in a more robust way than through the application of strain, by manually freezing in different amplitudes of the modes and observing how this changes the magnitude of the polar distortion modes.

This work could be further extended to study how the different structural distortion modes evolve across the $Li_2Sr_xCa_{1-x}Ta_2O_7$ ($0 \leq x \leq 1$) compositional series. Substitution of Sr into $Li_2CaTa_2O_7$ leads to an increase in the *a* and *b* lattice parameters, accompanied by a decrease in *c*. This suggests that applying a compressive pressure in the *ab*-plane should stabilise the $Pna2_1$ phase of $Li_2SrTa_2O_7$ with respect to the $A2_1am$ phase. Likewise, applying a tensile pressure to $Li_2CaTa_2O_7$ should stabilise the $A2_1am$ phase with respect to the $Pna2_1$ phase. These calculations might further shed light on the switch from a trilinear-coupled stabilisation to a conventional SOJT coupling as a function of the *A*-cation size.

Finally, a similar symmetry mode approach could be taken to study the cation-exchanged materials discussed in Chapters 3, 4 and 5 of this thesis.

6.5 Conclusions

The objective of this chapter was to explore the energy surface of the $n = 2$ pseudo-Ruddlesden-Popper phases $Li_2AB_2O_7$ (*A* = Sr, Ca and *B* = Nb, Ta) to rationalise their compositional and structural behaviours. This investigation revealed that the energy landscapes of these systems are incredibly shallow, and many phases are in close competition. In particular, these findings suggest it should be possible to tune between the competing polar $Pna2_1$ and antipolar *Pnam* phases of $Li_2SrNb_2O_7$ and $Li_2CaTa_2O_7$. However, this work has not been able to account for the experimentally observed ground state structures and further work is necessary to understand this discrepancy.

Chapter 7: Conclusions

Topochemical cation-exchange reactions of layered perovskites have been extensively studied for their use in the synthesis of metastable phases which are otherwise inaccessible via traditional high-temperature solid-state methods. This thesis explores the use of low-temperature cation exchange reactions in the synthesis of novel, layered perovskite oxide phases. Specifically, it focuses on a series of polar $n = 2$ pseudo-Ruddlesden-Popper oxide phases as precursor materials to explore the synthesis of new ferroelectric and magnetoelectric materials by incorporating ferromagnetism into the phase through the substitution of paramagnetic first-row transition metal cations with diamagnetic Li^+ cations. Beyond the synthesis of novel ferroelectric and multiferroic materials, this work seeks to understand the chemical principles that dictate their structural and physical behaviours.

Chapter three examines the cation exchange chemistry of $Li_2CaTa_2O_7$ to probe the relationship between the *A*'-site cation and structural distortions. The compounds $FeCaTa_2O_7$, $CoCaTa_2O_7$, and $ZnCaTa_2O_7$ were synthesised and their structural distortions characterised using a combination of symmetry analysis, NPD data and SHG. These phases, synthesised via topochemical exchange from the thermodynamically stable precursor phase, are kinetically stable and retain the polar, $n = 2$ Ruddlesden-Popper framework of the precursor host phase, adopting noncentrosymmetric crystal structures. Structural analysis reveals that the interlayer *A*'-cations of $FeCaTa_2O_7$ and $CoCaTa_2O_7$ adopt a chequerboard-order arrangement, while in $ZnCaTa_2O_7$, they adopt a striped arrangement. This behaviour can be rationalised on the basis of the competition between minimising the cation-cation repulsion of the *A*'-cations and optimising the size of the *A*'-cations coordination sites via octahedral tilting. The striped and chequerboard ordering schemes represent the optimal solutions for smaller and larger cations, respectively.

Upon cooling, $FeCaTa_2O_7$ and $CoCaTa_2O_7$ adopt G-type antiferromagnetically ordered structures below their respective magnetic transition temperatures, however, no evidence of magnetoelectric coupling was observed for either compound.

Chapters four and five explore the synthesis of $M^{II}SrNb_2O_7$ (M = Mn, Fe, Co and Zn) from $Li_2SrNb_2O_7$. $MnSrNb_2O_7$ adopts a noncentrosymmetric structure characterised by an incommensurately modulated ordering of the Mn^{2+} cations over the pseudo-tetrahedral interlayer coordination sites which represents the optimum compromise between cation ordering and octahedral tilting. No lattice parameter anomalies coinciding with the onset of magnetic order were observed, indicating that the electric and magnetic polarisations are not strongly coupled in this phase. Both $FeSrNb_2O_7$ and $CoSrNb_2O_7$ adopt centrosymmetric crystal structures but display some structural similarities to $MnSrNb_2O_7$, most notably the presence of an incommensurate modulation of the crystal structure, although the chemical origin of this modulation appears to differ from that of $MnSrNb_2O_7$. Likewise, $ZnSrNb_2O_7$ adopts a noncentrosymmetric structure consistent with a $\sim\sqrt{2} \times \sim\sqrt{2} \times 2$ geometric expansion of an undistorted n = 2 Ruddlesden-Popper unit cell. These added structural complexities likely arise as a result of an incomplete cation exchange and the persistence of lithium within the interlayer tetrahedral coordinate sites. A comprehensive summary of the key structural and physical behaviours of the phases studied in this thesis are reported in Table 7.1.

This study has revealed that the octahedral tilting distortions adopted by the $M^{II}AB_2O_7$ (M = Mn, Fe, Co, Zn; A = Ca, Sr; B = Nb, Ta) series of n = 2 Ruddlesden-Popper oxides depends on the tolerance factor (size mismatch between the A-site and B-site cations) and the size of the interlayer A' cation. In situations such as these, where divalent A'-cations are exchanged with monovalent Li^+ cations, ordering of the cations within the interlayer tetrahedral

Table 7.1 Summary of the structural and physical behaviours of the compounds studied in this work, with $MnCaTa_2O_7$ and $MnSrTa_2O_7$ included for comparison.

Compound	Space Group	Glazer Tilt	NCS?	Commensurate?	Magnetic Order	T_N / K	T_A / K	FM Component?	Magnetoelectric Coupling?
$FeCaTa_2O_7$	$P2_1nm$	$a^-b^-c^+/b^-a^-c^+$	Y	Y	G-type	37	-	Y	N
$CoCaTa_2O_7$	$P2_1nm$	$a^-b^-c^+/b^-a^-c^+$	Y	Y	G-type	25	-	Y	N
$ZnCaTa_2O_7$	$P2cm$	$a^-b^-c^+/-(a^-b^-)c^+$	Y	Y	-	-	-	-	-
$MnCaTa_2O_7$[119]	$P2_1nm$	$a^-b^-c^+/b^-a^-c^+$	Y	Y	G-type	55	50	N	N
$MnSrTa_2O_7$[120]	$A2_1am$	$a^-a^-c^+/a^-a^-c^+$	Y	N	G-type	43	38	Y	Y
$MnSrNb_2O_7$	$A2_1am$	$a^-a^-c^+/a^-a^-c^+$	Y	N	G-type	39	-	Y	N
$FeSrNb_2O_7$	?	?	N	N	Unknown	25	-	N	N
$CoSrNb_2O_7$	$Amam$	$a^-a^-c^0/a^-a^-c^0$	N	N	Unknown	40	-	N	N
$ZnSrNb_2O_7$	?	?	Y	Y	-	-	-	-	-

coordination sites can occur, thus, there is an added competition between the cation order and optimum octahedral tilting distortion.

Table 7.1 demonstrates that the size of the *A*-cation of the host lattice plays a crucial role in determining the octahedral tilting distortion of the phase. Substitution of the larger Sr^{2+} cations for smaller Ca^{2+} cations results in a reduction of the tolerance factor and a change from a native distortion of a^-a^-/a^-a^- to a^-b^-/b^-a^-.

$MnSrNb_2O_7$ and $MnSrTa_2O_7$ are isostructural, both adopting an average structure described in an $A2_1am$ space group. The onset of polarity in an $A2_1am$ structure is stabilised by a hybrid improper mechanism rather than a SOJT-driven proper mechanism, making it sensitive to the magnitude of structural distortions dictated by the size mismatch of the *A* and *B*-site cations. Given that the ionic radii of octahedral Nb^{5+} and Ta^{5+} are approximately equal, it is unsurprising that their crystal structures are broadly similar. Despite their related structures, only $MnSrTa_2O_7$ displays a strong coupling between the magnetic and electric polarisations, which perhaps suggests that although the dominant stabilisation mechanism is HIP, the SOJT distortion may still play a role in the coupling.

Although $FeCaTa_2O_7$ and $CoCaTa_2O_7$ are isostructural with the previously reported manganese phase $MnCaTa_2O_7$, they exhibit subtle differences in their physical behaviours. While a ferromagnetic component of the magnetic moment is symmetry compatible with the $a^-b^-c^+/b^-a^-c^+$ tilting distortion of the $P2_1nm$ structure, symmetry allowance alone is not sufficient to guarantee the emergence of a ferromagnetic component. For instance, in the case of $MnCaTa_2O_7$, although minima in the *a*, *b* and *c* lattice parameters and discontinuities in the magnitudes of the $X_2^+(0;a)$ and Γ_5^- modes were observed, these did not coincide with any notable change in the magnetisation data. In contrast, no lattice parameter anomalies were observed in $FeCaTa_2O_7$ and $CoCaTa_2O_7$ despite the observation of a ferromagnetic

component in the magnetisation data. These differences in the physical behaviour may be attributed to the varying crystal field effects of the interlayer *A*'-cations. Collectively, these observations suggest that achieving the magnetoelectric coupling seen in $MnSrTa_2O_7$ requires strict conditions to be met. Whilst being symmetry allowed is necessary, there appear to be additional subtleties needed to ensure strong coupling between the electrical and magnetic polarisations, which remain to be fully understood.

The exchange chemistry of the niobium-based material $Li_2SrNb_2O_7$ is less reliable than that of the tantalum phases, showing inconsistent outcomes that do not systematically vary with composition. This unreliability likely arises from the inability to synthesise $Li_2CaNb_2O_7$, and suggests that $Li_2SrNb_2O_7$ is on the edge of phase stability and therefore not a robust host lattice for cation exchange reactions. Previously, Mallick observed that it is not possible to substitute more than 10% Ca^{2+} into $Li_2SrNb_2O_7$, highlighting its instability in conformational space, and suggesting the tolerance factor is near its lower limit.[148] In contrast, the tolerance factor of the tantalum-based compound can be varied to a greater extent, as both extremes of the compositional series exist. This is consistent with the observation that the exchange chemistry of the niobium-based phase does not work as well as the tantalum compounds.

Finally, chapter six investigated the structures and structural distortions of the thermodynamically stable precursor phases $Li_2SrNb_2O_7$, $Li_2SrTa_2O_7$ and $Li_2CaTa_2O_7$ from a theoretical perspective using symmetry analysis and first-principles calculations. Calculations revealed a shallow energy landscape between competing structures and were not able to account for the macroscopic polarisation that is experimentally observed in these phases. Further work is necessary to understand the transition from a trilinear-coupled

stabilization of the polar structure to a ‘conventional’ SOJT mechanism as a function of the *A*-cation in this family of materials.

The successful low-temperature synthesis of these polar, magnetically ordered phases demonstrates that cation exchange reactions can act as a viable route to prepare new ferroelectric and potentially magnetoelectric materials. This research demonstrates the feasibility of topochemical cation exchange reactions to synthesize novel materials with tailored properties and highlights the rich cation exchange chemistry inherent in Ruddlesden-Popper phases, which warrants further exploration. Additionally, this work underscores the challenges associated with structurally characterizing distorted, layered oxide materials and emphasises the importance of using a combination of complementary techniques. These include synchrotron X-ray diffraction, neutron powder diffraction, second-harmonic generation, symmetry analysis, and magnetisation, all of which were crucial for unequivocally determining the crystal and magnetic structures of the phases studied. Future studies should focus on optimising low temperature cation exchange methods to synthesise new metastable phases and to further investigate the interplay between structural distortions and material properties. A natural progression of this work might be to explore the use of $n = 3$ Ruddlesden-Popper oxides as polar precursor phases in topochemical cation exchange reactions to synthesise complex ferroelectric and multiferroic materials, since they can exhibit additional tilting distortion modes not possible in their $n = 2$ analogues.

Appendix 1 – Index of Figures and Tables

Figure 1.1 The cubic ABO_3 perovskite crystal structure, where the orange *A*-cation sits in a 12-coordinate site formed by the BO_6 octahedra shown in blue. 2

Figure 1.2 The general crystal structure of the aristotype A_2BO_4 n = 1 and $A_3B_2O_7$ and $A'_2AB_2O_7$ n = 2 Ruddlesden-Popper oxides. Orange, green, pink, blue and red spheres represent *A*, *A*', *B* and O atoms, respectively.....3

Figure 1.3 The cubic perovskite structure and a cooperative octahedral rotation of the BO_6 octahedra.....4

Figure 1.4 a) The in-phase and out-of-phase tilting distortions of the BO_6 octahedra of a 3D perovskite around the [001] axis. b) The *I*2*cm* structure adopted by $RbNdNb_2O_7$, exhibiting an $a-a-c+/-(a-a-c+)$ tilting distortion, where pink, orange, blue and red are used to represent Rb, Nd, Nb and O ions, respectively.....7

Figure 1.5 The high-temperature paraelectric *Pm*3*m* and ferroelectric tetragonal *P*4*mm* structures of $PbTiO_3$. Orange, blue and red are used to represent Pb, Ti and O ions, respectively. 11

Figure 1.6 The non-polar *I*4/*mmm* aristotype structure of $Ca_3Mn_2O_7$ can be related to $A2_1am$ by the application of the two non-polar modes, $X2^+$ and the $X3^-$, which together couple to the polar $\Gamma5^-$ mode to generate a macroscopic polarisation. The net polarisation arises from the non-cancellation of *A*-site cation displacements in inequivalent *A*O layers. Orange, blue and red are used to represent Ca, Mn and O ions, respectively. 13

Figure 1.7 The change in energy per formula unit of the *I*4/*mmm* phase of $Ca_3Mn_2O_7$ as a function of the amplitude of a) the non-polar $X2^+$ and $X3^-$ modes b) the polar $\Gamma5^-$ mode c) the polar $\Gamma5^-$ mode in the presence of the hybrid order parameter, $QX23 = \lambda QX3 - QX2^+$. d) shows a magnification of the region around ΔE = 0. Figure is taken with permission from Reference 43. 14

Figure 1.8 The topochemical cation exchange reaction of $Na_2La_2Ti_3O_{10}$ using a molten mixture of $CoCl_2$ and KCl results in the exchange of the 9-coordinate Na^+ ions with Co^{2+} ions, which occupy 50% of the available tetrahedral coordination sites. Orange, blue, green, mint and red are used to represent La, Ti, Na, Co and O ions, respectively.....21

Figure 2.1 Schematic of the furnace setup used for air-sensitive cation-exchange reactions performed in sealed Pyrex tubes, where the furnace is orientated a) horizontally and b)

vertically, for reactions involving reagents with melting points below the reaction temperature ($ZnCl_2$). 28
Figure 2.2 Schematic representation of the flowing tube apparatus used in cation-exchange reactions taking place under flowing argon gas. 29
Figure 2.3 Schematic representation of Bragg's Law. 30
Figure 2.4 The atomic scattering factor of Li, O and Ca atoms as a function of scattering angle....33
Figure 2.5 X-ray optics of the Debye-Scherrer transmission geometry and Bragg-Brentano reflection geometry. 35
Figure 2.6 Left: Schematic diagram of the dipole magnets used to accelerate electrons inside a synchrotron. **V** represents the direction of travel of an electron, **H** is the magnetic field, and **F** is the force experienced by the electron. Right: Schematic diagram of a typical synchrotron. 36
Figure 2.7 Schematic representation of the SQUID component of a magnetometer.....43
Figure 2.8 Schematic top view of the detector arrangement of the GPS instrument at PSI. The up detector is not shown because it sits above the sample. Figure adapted from Reference 100. 49
Figure 2.9 Schematic representation of a modified Kurtz-Powder Laser system adapted from Reference 101. 50
Figure 3.1 a) Plot of SHG intensity of $ZnCaTa_2O_7$ as a function of time under incident radiation of 1064 nm, compared to that of KDP standard. b) Plot of SHG intensity of $FeCaTa_2O_7$ and $CoCaTa_2O_7$ as a function of time under incident radiation of 2090 nm, compared to that of $AgGaS_2$ standard....60
Figure 3.2 Observed, calculated and difference plots from the Pawley fitting of a primitive unit cell against SXRD data collected from $ZnCaTa_2O_7$ at room temperature. 61
Figure 3.3 The two possible ordering schemes adopted by the interlayer cations in the $P2_1nm$ (left) and $P2cm$ (right) Ruddlesden-Popper structure of $A'CaTa_2O_7$. Mint and red spheres represent A' and O, respectively. Grey spheres represent the positions of empty A'-sites. 63
Figure 3.4 Observed, calculated and difference plots from the structural refinement of the ordered $P2cm$ model of $ZnCaTa_2O_7$ against the NPD data collected from 2-9 (58°) and bank 4-7 (122°) of the WISH diffractometer at 100 K....65

Figure 3.5 A comparison between the refinements of the disordered (top) and ordered (bottom) Zn-site *P*2*cm* models against SXRD data collected from $ZnCaTa_2O_7$ at room temperature. Black arrows indicate peaks which correspond to the ordering of Zn^{2+} ions. 68
Figure 3.6 Observed, calculated and difference plots from the Pawley fitting of a primitive unit cell against SXRD data collected from $FeCaTa_2O_7$ at room temperature. 69
Figure 3.7 Observed, calculated and difference plots from the structural refinement of the $P2_1nm$ model of $FeCaTa_2O_7$ against the NPD data collected from bank 2-9 (58°) and bank 4-7 (122°) of the WISH diffractometer at 200 K.....72
Figure 3.8 Zero-field-cooled and field-cooled magnetisation data collected from $FeCaTa_2O_7$ as a function of temperature in an applied field of 100 Oe. 75
Figure 3.9 Magnetisation-field data collected from $FeCaTa_2O_7$ at 300 K and 5 K. The inset shows an expanded view of the origin.....76
Figure 3.10 AC susceptibility data collected from $FeCaTa_2O_7$, showing the frequency dependence of the magnetic transition temperature, T_N, from 10 Hz to 500 Hz. 77
Figure 3.11 NPD data collected from $FeCaTa_2O_7$ at 1.5 K, 41 K and 200 K, where additional magnetic scattering can be seen below the magnetic diffraction peak at 5.3 Å, labelled with an arrow. Grey lines are used to guide the reader's eye. 78
Figure 3.12 Observed, calculated and difference plots from the structural refinement of the magnetically ordered $P2_1n'm'$ model of $FeCaTa_2O_7$ against the NPD data collected from bank 2-9 (58°) and bank 4-7 (122°) of the WISH diffractometer at 1.5 K.....79
Figure 3.13 The G-type antiferromagnetic arrangement of Fe^{2+} ions adopted by $FeCaTa_2O_7$. 82
Figure 3.14 Evolution of the intensity of the neutron diffraction data collected from $FeCaTa_2O_7$ as a function of temperature. Magnetic peaks are labelled with arrows.....83
Figure 3.15 NPD data collected from $FeCaTa_2O_7$ as a function of temperature, from bank 4-7 (122°). Black arrows indicate magnetic scattering peaks. The right-hand image shows the region around the magnetic peak at ~ 5.3 Å at a greater magnification. The grey-line is used to guide the reader's eye.....84
Figure 3.16 The ordered magnetic moment extracted from the refinement of the ordered $P2_1n'm'$ model against NPD data collected from $FeCaTa_2O_7$ in the temperature range 1.5 K $\leq$ T/K $\leq$ 60 K.....85
Figure 3.17 Zero-field cooled and field cooled magnetisation data and the lattice parameters extracted from NPD data collected from $FeCaTa_2O_7$, plotted as a function of temperature in the range $1.5 \leq T/K \leq 60$. 86

Figure 3.18 Observed, calculated and difference plots from the Pawley fitting of a primitive unit cell against SXRD data collected from $CoCaTa_2O_7$ at room temperature. 87
Figure 3.19 Observed, calculated and difference plots from the structural refinement of the ordered $P2_1nm$ model of $CoCaTa_2O_7$ against the NPD data collected from bank 2-9 (58°) and bank 4-7 (122°) of the WISH diffractometer at 100 K. 91
Figure 3.20 Zero-field-cooled and field-cooled magnetisation data collected from $CoCaTa_2O_7$ as a function of temperature in an applied field of 100 Oe. 93
Figure 3.21 Magnetisation-field data collected from $CoCaTa_2O_7$ at the indicated temperatures. 94
Figure 3.22 Observed, calculated and difference plots from the structural refinement of the magnetically ordered $P2_1n$'m' model of $CoCaTa_2O_7$ against the NPD data collected from bank 2-9 (58°) and bank 4-7 (122°) of the WISH diffractometer at 1.5 K. 96
Figure 3.23 Evolution of the intensity of the neutron diffraction data collected from $CoCaTa_2O_7$ as a function of temperature. Magnetic peaks are labelled with arrows. 99
Figure 3.24 NPD data collected from $CoCaTa_2O_7$ as a function of temperature (bank 4-7 (122°)). Black arrows indicate magnetic scattering peaks. The right-hand image shows the region around the magnetic peak at ~ 5.3 Å at a greater magnification. The grey line is used to guide the reader's eye. 100
Figure 3.25 The ordered magnetic moment extracted from the refinement of the ordered $P2_1n$'m' model against NPD data collected from $CoCaTa_2O_7$ in the temperature range 1.5 K $\leq T/K \leq$ 40 K. 101
Figure 3.26 Zero-field cooled and field cooled magnetisation data and the lattice parameters extracted from NPD data collected from $CoCaTa_2O_7$, plotted as a function of temperature in the range $1.5 \leq T/K \leq 55$. 102
Figure 3.27 Crystal structures and the coordination environments of the A' cations in $FeCaTa_2O_7$ and $ZnCaTa_2O_7$. Pink, mint, orange, blue and red spheres represent Fe, Zn, Ca, Ta and O, respectively. 103
Figure 3.28 The ordering schemes adopted by Fe and Co (left) and Zn (right) within the interlayer coordination sites. Pink, mint and red spheres represent Fe/Co, Zn and O, respectively. Grey spheres represent the positions of empty A'-sites. 105
Figure 3.29 Crystal field splitting of d-orbitals in a tetrahedral coordination environment. The ground state electronic configuration of Fe^{2+} (left), Co^{2+} (middle) and Zn^{2+} (right) are compared. 107

Figure 4.1 Plot of SHG intensity of $MnSrNb_2O_7$ as a function of time under incident radiation of 2090 nm, compared to that of $AgGaS_2$ standard. The inset shows the region around $t = 0$ at greater magnification.....114
Figure 4.2 Observed, calculated and difference plots from the Pawley refinement of an *A*-centred unit cell against SXRD data collected from $MnSrNb_2O_7$ at room temperature (top) and an expanded region showing weak diffraction peaks that cannot be accounted for with a commensurate expansion of the unit cell, labelled with black arrows (bottom). 115
Figure 4.3 Plots of raw SXRD data collected from $MnSrNb_2O_7$ and $Li_2SrNb_2O_7$.....116
Figure 4.4 a) The average incommensurately modulated crystal structure of $MnSrNb_2O_7$, described in the superspace group $A2_1am(0\beta0)000$. Blue, lime, green and red spheres represent Mn, Sr, Nb and O, respectively. The modulated equatorial oxygen atom, O4, is labelled. b) Two different chequerboard ordering patterns, A and B, are possible when the pseudo-tetrahedral coordination sites are half occupied. c) The intergrowth of the two ordering patterns observed in the interlayer region of $MnSrNb_2O_7$. 119
Figure 4.5 Observed, calculated and difference plots from the structural refinement of the $A2_1am(0\beta0)000$ model of $MnSrNb_2O_7$ against the NPD data collected from bank 1-10 (27°) and bank 4-7 (122°) of the WISH diffractometer at 80 K. 121
Figure 4.6 Zero-field-cooled and field-cooled magnetisation data collected from $MnSrNb_2O_7$ as a function of temperature in an applied field of 100 Oe.....124
Figure 4.7 Magnetisation-field data collected from $MnSrNb_2O_7$ at 300 K and 5 K.....125
Figure 4.8 NPD data collected from $MnSrNb_2O_7$ as a function of temperature. Black arrows indicate magnetic scattering peaks. The right-hand image shows the region around the magnetic peaks at ~ 5.3 Å at a greater magnification. The grey-line is used to guide the reader's eye.....127
Figure 4.9 The G-type antiferromagnetic arrangement of Mn^{2+} ions adopted by $MnSrNb_2O_7$. The supercell depicted is an approximate structure, not a unit cell.....128
Figure 4.10 Observed, calculated and difference plots from the structural refinement of the magnetically ordered $A2_1a'm'(0\beta0)000$ model of $MnSrNb_2O_7$ against the NPD data collected from bank 1-10 (27°) and bank 4-7 (122°) of the WISH diffractometer at 1.5 K. 129
Figure 4.11 Evolution of the intensity of the neutron diffraction data collected from $MnSrNb_2O_7$ as a function of temperature. Magnetic peaks are labelled with arrows. 131

Figure 4.12 The ordered magnetic moment extracted from the refinement of an incommensurately modulated $A2_1a'm'(0\beta0)000$ model against NPD data collected from $MnSrNb_2O_7$ in the temperature range 1.5 K ≤ *T*/K ≤ 39 K. 132
Figure 4.13 Zero-field cooled and field cooled magnetisation data and the lattice parameters extracted from NPD data collected from $MnSrNb_2O_7$, plotted as a function of temperature in the range 5 ≤ T/K ≤ 80.....133
Figure 4.14 The zero-field muon SR asymmetry data for $MnSrNb_2O_7$ measured at *T* = 1 K, 30 K and 39 K. The temperature dependence of relaxation rate (λ and σ) and the baseline asymmetry and relaxing asymmetry are shown. 135
Figure 4.15 Temperature evolution of the muon precession frequency of $MnSrNb_2O_7$...136
Figure 4.16 The crystal structures of $MnSrNb_2O_7$ ($A2_1am$) and $MnCaTa_2O_7$ ($P2_1nm$) alongside the direction and magnitude of the octahedral tilting distortions and to corresponding irreducible representations which can be used to describe each structure when applied to the $I4/mmm$ aristotype. Blue, lime, green, navy, orange and red spheres represent Mn, Sr, Nb, Ta and Ca and O, respectively.....139
Figure 5.1 Plot of SHG intensity of $ZnSrNb_2O_7$ as a function of time under incident radiation of 1064 nm, compared to that of KDP standard. 143
Figure 5.2 Observed, calculated and difference plots from the Pawley refinement of an primitive unit cell against SXRD data collected from $CoSrNb_2O_7$ at room temperature (top) and an expanded region showing weak diffraction peaks that cannot be accounted for with a commensurate expansion of the unit cell, labelled with black arrows (bottom). 145
Figure 5.3 Observed, calculated and difference plots from the structural refinement of the unmodulated *Amam* model of $CoSrNb_2O_7$ against the NPD data collected from bank 1-10 (27°) and bank 4-7 (122°) at 50 K. Peak centred at 17 Å has been excluded from the refinement. 147
Figure 5.4 Observed, calculated and difference plots from the Pawley refinement of an incommensurately modulated $Amam(0\beta0)000$ unit cell against the NPD data collected from $CoSrNb_2O_7$ from 1-10 (27°) bank and 4-7 (122°) bank at 50 K. 149
Figure 5.5 Comparison of the NPD data collected from $MnSrNb_2O_7$ and $CoSrNb_2O_7$, highlighting the difference between the observed incommensurate satellite peaks. 151
Figure 5.6 Zero-field-cooled and field-cooled magnetisation data collected from $CoSrNb_2O_7$ as a function of temperature in an applied field of 100 Oe.....152
Figure 5.7 Magnetisation-field data collected from $CoSrNb_2O_7$ at 300 K and 5 K. 153

Figure 5.8 Comparison of the NPD data collected from $CoSrNb_2O_7$ at 1.5 K and 50 K using the 1-10 (27°) bank and 4-7 (122°) bank. 155
Figure 5.9 Observed and calculated plots from the Pawley refinement of (top) a primitive unit cell with a $\sim\sqrt{2} \times \sim\sqrt{2} \times 1$ and geometric expansion of the aristotype *I*4/*mmm* unit cell and (bottom) a body-centred unit cell with a $\sim\sqrt{2} \times \sim\sqrt{2} \times 2$ and geometric expansion against SXRD data collected from $ZnSrNb_2O_7$ at room temperature. Peaks marked by black arrows can only be indexed by a doubling of the *c*-axis, while peaks marked by dashed arrows correspond to an unknown impurity phase inherited from the precursor phase. ... 157
Figure 5.10 Observed, calculated and difference plots from the structural refinement of the *I*222 model of $ZnSrNb_2O_7$ against the NPD data collected from 1-10 (27°) bank and 4-7 (122°) bank at 100 K. 159
Figure 5.11 The refined *I*222 model of $ZnSrNb_2O_7$, illustrating the alternating empty and partially filled layers. The Zn^{2+} cations adopt a striped-order arrangement within the interlayer tetrahedral coordination sites in each partially filled layer. Purple, lime green, deep green and red spheres represent Zn, Sr, Ta and O atoms, respectively. 160
Figure 5.12 Observed and calculated plots from the Pawley refinement of (top) a primitive unit cell with a $\sim\sqrt{2} \times \sim\sqrt{2} \times 1$ and geometric expansion of the aristotype *I*4/*mmm* unit cell and (bottom) a body-centred unit cell with a $\sim\sqrt{2} \times \sim\sqrt{2} \times 2$ and geometric expansion against SXRD data collected from $FeSrNb_2O_7$ at room temperature. Peaks marked by black arrows can only be indexed by a doubling of the *c*-axis. Peaks marked by dashed arrows cannot be indexed by a commensurate unit cell. 162
Figure 5.13 Observed, calculated and difference plots from the Pawley refinement of a *P*1(αβγ)0 unit cell against the NPD data collected from $FeSrNb_2O_7$ from 1-10 (27°) bank and 4-7 (122°) bank at 60 K. 165
Figure 5.14 The saturated ferromagnetic moment (top), paramagnetic susceptibility, inverse susceptibility of $FeSrNb_2O_7$ as a function of temperature (bottom), and fit to the Curie-Weiss law in the temperature range $275 \leq T/K \leq 300$ K. 167
Figure 5.15 Comparison of the NPD data collected from $FeSrNb_2O_7$ at 1.5 K and 60 K using the 1-10 (27°) bank and 4-7 (122°) bank. 169
Figure 5.16 Raw SXRD data collected from $MSrNb_2O_7$ (*M* = Mn, Fe, Co, Zn and Li_2) at room temperature. Grey dashed lines are used to indicate reflections consistent with a doubling of the *c*-axis and black dashed lines are used to indicate satellite peaks. Stars, squares, circles and triangles mark peaks corresponding to an unknown *n* = 3 Ruddlesden-

Popper impurity, Fe_2O_3, Li_3O_4, and an unknown impurity inherited from the precursor material. 171
Figure 5.17 A comparison of the possible striped and chequerboard ordering arrangements of the transition metal cations occupying the interlayer region of the pseudo-Ruddlesden-Popper structure, where the layers are stacked primitively with respect to the subsequent layer (AA), or shifted by half a unit cell along *x* (AB).....172
Figure 6.1 A schematic of the atomic displacements of the structural distortion modes extracted from the decomposition of each of the reported ground state structures, $A2_1am$, *Pnam* and $Pna2_1$, with respect to the $I4/mmm$ high symmetry $Li_2AB_2O_7$ (*A* = Ca, Sr and *B* = Nb, Ta) structure. Purple, orange, teal and red spheres represent Li, *A*, *B* and O atoms, respectively. 178
Figure 6.2 Summary of the phonon mode exploration of $Li_2CaTa_2O_7$. The irreducible representation labels refer to the reference structure (e.g. the structure from which the arrow originates), not to $I4/mmm$. Black and red arrows indicate whether a particular mode is unstable or stable in the reference structure, respectively. An asterisk is used to indicate when a structure is dynamically stable.....185
Figure 6.3 Summary of the phonon mode exploration of $Li_2SrTa_2O_7$. The irreducible representation labels refer to the reference structure (e.g. the structure from which the arrow originates), not to $I4/mmm$. Black and red arrows indicate whether a particular mode is unstable or stable in the reference structure, respectively. An asterisk is used to indicate when a structure is dynamically stable.....189
Figure 6.4 Summary of the phonon mode exploration of $Li_2SrNb_2O_7$. The irreducible representation labels refer to the reference structure (e.g. the structure from which the arrow originates), not to $I4/mmm$. Black and red arrows indicate whether a particular mode is unstable or stable in the reference structure, respectively. An asterisk is used to indicate when a structure is dynamically stable.....196
Figure 6.5 a) The total energy of the *Amam* and $A2_1am$ structures, b) the energy difference between the *Amam* and $A2_1am$ structures and c) the amplitude of structural distortion modes of *Amam* and d) the force constant of the $\Gamma 2^-$ mode in the *Amam* structure as a function of applied strain of $Li_2SrTa_2O_7$. The energies and mode amplitudes reported are normalised to the high symmetry $I4/mmm$ reference cell (e.g. for a 24-atom cell). 200
Figure 6.6. a) The total energy of the *Pnam* and $Pna2_1$ structures, b) the energy difference between the *Pnam* and $Pna2_1$ structures, c) the amplitude of structural distortion modes of the *Pnam* structure and d) the force constant of the $\Gamma 4^-$ mode as a function of applied strain

in the *Pnam* structure of $Li_2CaTa_2O_7$. The energies and mode amplitudes reported are normalised to the high symmetry *I*4/*mmm* reference cell (e.g. for a 24-atom cell).....201
Figure 6.7. a) The total energy of the *Pnam* and *Pna*2_1 structures, b) the energy difference between the *Pnam* and *Pna*2_1 structures, c) the amplitude of structural distortion modes of the *Pnam* structure and d) the force constant of the Γ4 − mode as a function of applied strain in the *Pnam* structure of $Li_2SrNb_2O_7$. The energies and mode amplitudes reported are normalised to the high symmetry *I*4/*mmm* reference cell (e.g. for a 24-atom cell).....202

Table 2.1 The chemically plausible distortions of the $n = 2$ Ruddlesden-Popper structure. 53
Table 3.1 Parameters from the structural refinement of the ordered *P*2*cm* model of $ZnCaTa_2O_7$ against the NPD data collected at 100 K.....66
Table 3.2 Selected bond lengths and cation bond valence sums from the structural refinement of the *P*2*cm* model of $ZnCaTa_2O_7$ against the NPD data collected at 100 K....67
Table 3.3 Parameters from the structural refinement of the ordered *P*2_1*nm* model of $FeCaTa_2O_7$ against the NPD data collected at 200 K. 73
Table 3.4 Selected bond lengths and cation bond valence sums from the structural refinement of the ordered *P*2_1*nm* model of $FeCaTa_2O_7$ against the NPD data collected at 200 K. 74
Table 3.5 Parameters from the structural refinement of the magnetically ordered *P*2_1*n*'*m*' model of $FeCaTa_2O_7$ against the NPD data collected at 1.5 K.....80
Table 3.6 Selected bond lengths and cation bond valence sums from the structural refinement of the magnetically ordered *P*2_1*n*'*m*' model of $FeCaTa_2O_7$ against the NPD data collected at 1.5 K.....81
Table 3.7 Parameters from the structural refinement of the ordered *P*2_1*nm* model of $CoCaTa_2O_7$ against the NPD data collected at 100 K. 90
Table 3.8 Selected bond lengths and cation bond valence sums from the structural refinement of the ordered *P*2_1*nm* model of $CoCaTa_2O_7$ against the NPD data collected at 100 K. 92
Table 3.9 Parameters from the structural refinement of the magnetically ordered *P*2_1*n*'*m*' model of $CoCaTa_2O_7$ against the NPD data collected at 1.5 K. 97
Table 3.10 Selected bond lengths and cation bond valence sums from the structural refinement of the magnetically ordered *P*2_1*n*'*m*' model of $CoCaTa_2O_7$ against the NPD data collected at 1.5 K.....98

Table 3.11 A comparison of the calculated modified tolerance factor, *t*', and the magnitude *a*, *b* and *c,* of the rotations around each axis extracted from the $P2_1nm$ and $P2cm$ crystal structure models of $FeCaTa_2O_7$, $CoCaTa_2O_7$ and $ZnCaTa_2O_7$.....104
Table 3.12 Ionic radii of Li^+ and M^{2+} cations in a tetrahedral coordination geometry.....107
Table 4.1 Parameters from the structural refinement of the $A2_1am(0\beta0)000$ model of $MnSrNb_2O_7$ against the NPD data collected at 80 K.....122
Table 4.2. Selected bond lengths and cation bond valence sums from the structural refinement of the $A2_1am(0\beta0)000$ model of $MnSrNb_2O_7$ against the NPD data collected at 80 K. 123
Table 4.3 Parameters from the structural and magnetic refinement of the magnetically ordered $A2_1a'm'(0\beta0)000$ model of $MnSrNb_2O_7$ against the NPD data collected at 1.5 K. 128
Table 4.4 Selected bond lengths and cation bond valence sums from the structural refinement of the magnetically ordered $A2_1a'm'(0\beta0)000$ model of $MnSrNb_2O_7$ against the NPD data collected at 1.5 K. 130
Table 6.1 Frequencies, degeneracies and resulting space groups of the unstable modes identified in the supercell of the *I*4/*mmm* aristotype structure of $Li_2CaTa_2O_7$ and the irreducible representations corresponding to each mode. 180
Table 6.2 Calculated frequencies and force constants for the $\Gamma3-$, $X2+$, $X1-$, $X3-$, and $M5-$modes in the *I*4/*mmm* reference structure of $Li_2CaTa_2O_7$. 180
Table 6.3 Calculated frequencies and force constants for $\Gamma2-$, $Y2+$, $Y2-$ and $Y4+$ modes in the $Li_2CaTa_2O_7$ *Amam* reference structure. 181
Table 6.4 Calculated frequency and force constant for the *Y*2 mode in the $Li_2CaTa_2O_7$ $A2_1am$ reference structure. 182
Table 6.5 Calculated frequency and force constant for the $\Gamma4-$ mode in the $Li_2CaTa_2O_7$ *Pnam* reference structure. 183
Table 6.6 Calculated frequency and force constant for the $\Gamma3-$ mode in the $Li_2CaTa_2O_7$ *Pnab* reference structure. 183
Table 6.7 The calculated force constants of the listed modes for $Li_2CaTa_2O_7$ and the energy difference per formula unit between the fully relaxed *I*4/*mmm* structure and the distorted structures. The irreducible representation labels refer to the reference structure given in the row above, not to *I*4/*mmm*. 184

Table 6.8 Frequencies, degeneracies and resulting space groups of the unstable modes identified in the supercell of the *I*4/*mmm* aristotype structure of $Li_2SrTa_2O_7$ and the irreducible representations corresponding to each mode. 186
Table 6.9 Calculated frequencies and force constants for the $\Gamma 5^-$, $X2^+$ and $X3^-$, modes in the *I*4/*mmm* reference structure of $Li_2SrTa_2O_7$. 186
Table 6.10 Calculated frequencies and force constants for $\Gamma 2^-$, $Y2^+$ and $Y2^-$ modes in the *Amam* reference structure of $Li_2SrTa_2O_7$. 187
Table 6.11 Calculated frequency and force constant for the $\Gamma 3^-$ and $\Gamma 4^-$ modes in the *Pnnm* structure of $Li_2SrTa_2O_7$. 188
Table 6.12 The calculated force constants of the listed modes for $Li_2SrTa_2O_7$ and the energy difference per formula unit between the fully relaxed *I*4/*mmm* structure and the distorted structures. The irreducible representation labels refer to the reference structure given in the row above, not to *I*4/*mmm*. 188
Table 6.13 Calculated lattice parameters of $Li_2SrTa_2O_7$ in the fully relaxed *I*4/*mmm* and *Amam* space groups using the LDA, PBEsol and PBE exchange-correlation functionals. 190
Table 6.14 Frequencies, degeneracies and resulting space groups of the unstable modes identified in the supercell of the *I*4/*mmm* aristotype structure of $Li_2SrNb_2O_7$ and the irreducible representations corresponding to each mode. 191
Table 6.15 Calculated frequencies and force constants for the $\Gamma 5^-$, $X3^-$, and $M5^-$ modes in the *I*4/*mmm* reference structure of $Li_2SrNb_2O_7$. 192
Table 6.16 Calculated frequencies and force constants for $\Gamma 2^-$, $Y2^+$ and $Y2^-$ modes in the *Amam* reference structure of $Li_2SrNb_2O_7$. 192
Table 6.17 Calculated frequency and force constant for the $Y2$ mode in the $A2_1am$ structure of $Li_2SrNb_2O_7$. 193
Table 6.18 Calculated frequency and force constant for the $\Gamma 4^-$ mode in the *Pnam* structure of $Li_2SrNb_2O_7$. 193
Table 6.19 Calculated frequency and force constant for the $\Gamma 3^-$, $\Gamma 4^-$ $X2$ and $Y1$ modes in the *Pnnm* structure of $Li_2SrNb_2O_7$. 194
Table 6.20 The calculated force constants of the listed modes for $Li_2SrNb_2O_7$ and the energy difference per formula unit between the fully relaxed *I*4/*mmm* structure and the distorted structures. The irreducible representation labels refer to the reference structure given in the row above, not to *I*4/*mmm*. 195

Table 6.21 The lattice parameters and calculated force constant of the Γ2 − mode in the $Li_2SrTa_2O_7$ *Amam* structure. 198
Table 6.22 The lattice parameters and calculated force constant of the Γ4 − mode in the $Li_2CaTa_2O_7$ *Pnam* structure. 198
Table 6.23 The lattice parameters and calculated force constant of the Γ4 − mode in the $Li_2SrNb_2O_7$ *Pnam* structure. 198
Table 6.24 The energy difference per formula unit between the fully relaxed *I*4/*mmm* structure and the distorted structures. 203
Table 6.25 Structural distortion mode decomposition of the experimental (when reported) and DFT-relaxed structures of $Li_2CaTa_2O_7$ with respect to the high-symmetry *I*4/*mmm* reference structure. The distortion mode amplitudes given are normalised to the reference cell in Å (e.g. for a 24-atom cell). 205
Table 6.26 Structural distortion mode decomposition of the experimental (when reported) and DFT-relaxed structures of $Li_2SrTa_2O_7$ with respect to the high-symmetry *I*4/*mmm* reference structure. The distortion mode amplitudes given are normalised to the reference cell in Å (e.g. for a 24-atom cell). 205
Table 6.27 Structural distortion mode decomposition of the experimental (when reported) and DFT-relaxed structures of $Li_2SrNb_2O_7$ with respect to the high-symmetry *I*4/*mmm* reference structure. The distortion mode amplitudes given are normalised to the reference cell in Å (e.g. for a 24-atom cell). 206
Table 6.28 The lattice parameters (Å) of experimental structures (when reported) and DFT-relaxed structures of $Li_2CaTa_2O_7$, $Li_2SrTa_2O_7$ and $Li_2SrNb_2O_7$. 210
Table 7.1 Summary of the structural and physical behaviours of the compounds studied in this work, with $MnCaTa_2O_7$ and $MnSrTa_2O_7$ included for comparison. 214

Appendix 2 – Additional Data

A2.1 Additional data from the structural refinements in Chapter 3

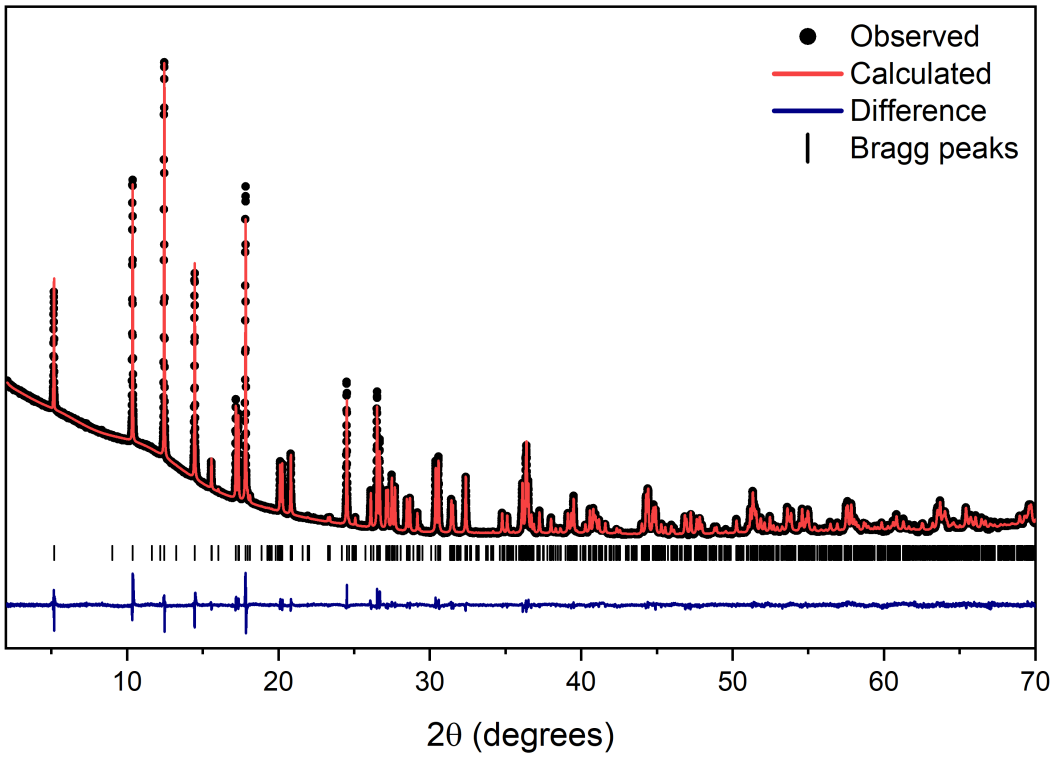


Figure A2.1.1 Observed, calculated and difference plots from the structural refinement of the *Pna*2_1 model of $Li_2CaTa_2O_7$ against SXRD data collected at room temperature.

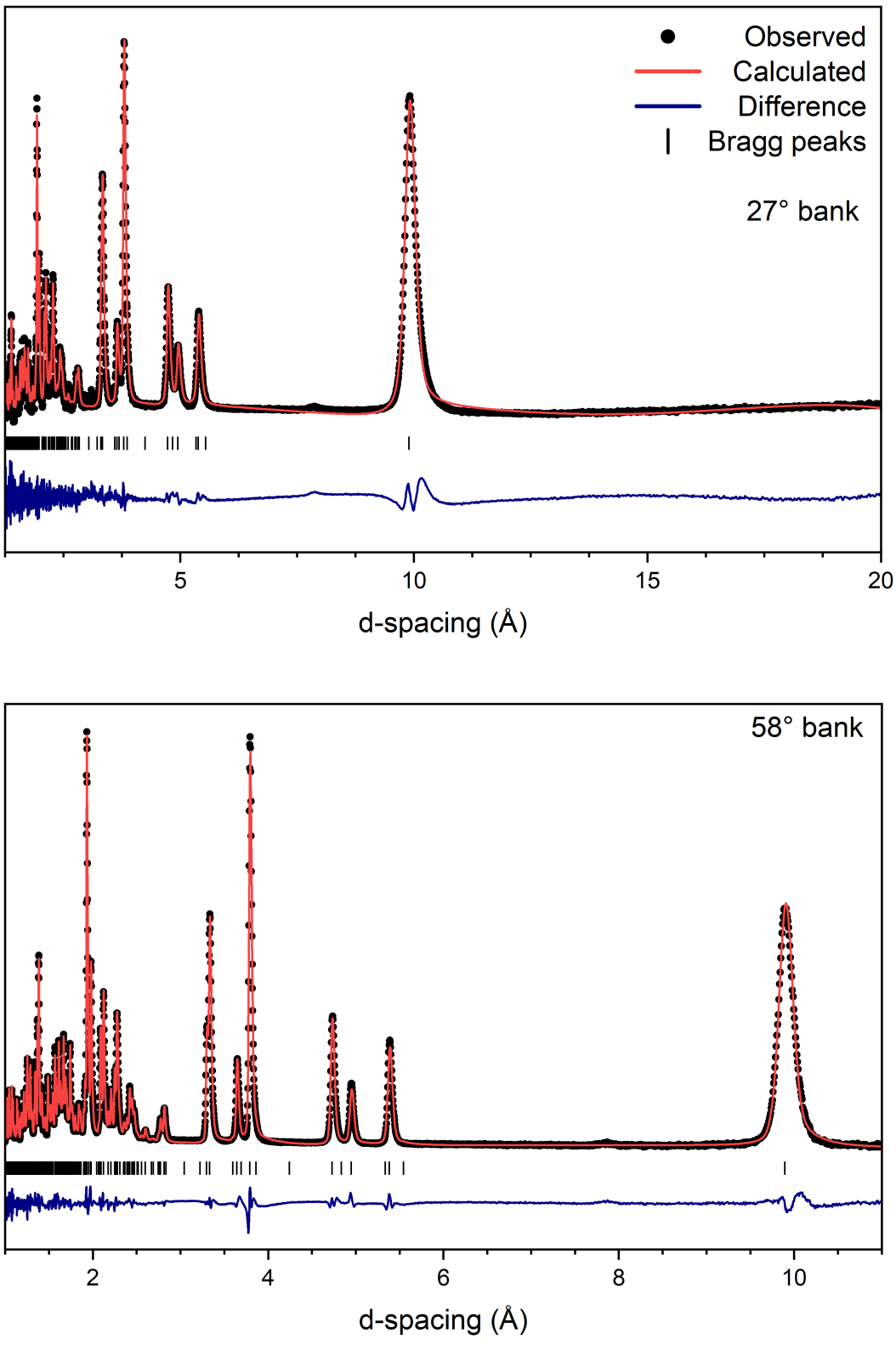


Figure A2.1.2 Observed, calculated and difference plots from the structural refinement of the ordered *P*2*cm* model of $ZnCaTa_2O_7$ against the NPD data collected from bank 1-10 (27°) and bank 2-9 (58°) on the WISH diffractometer at 100 K.

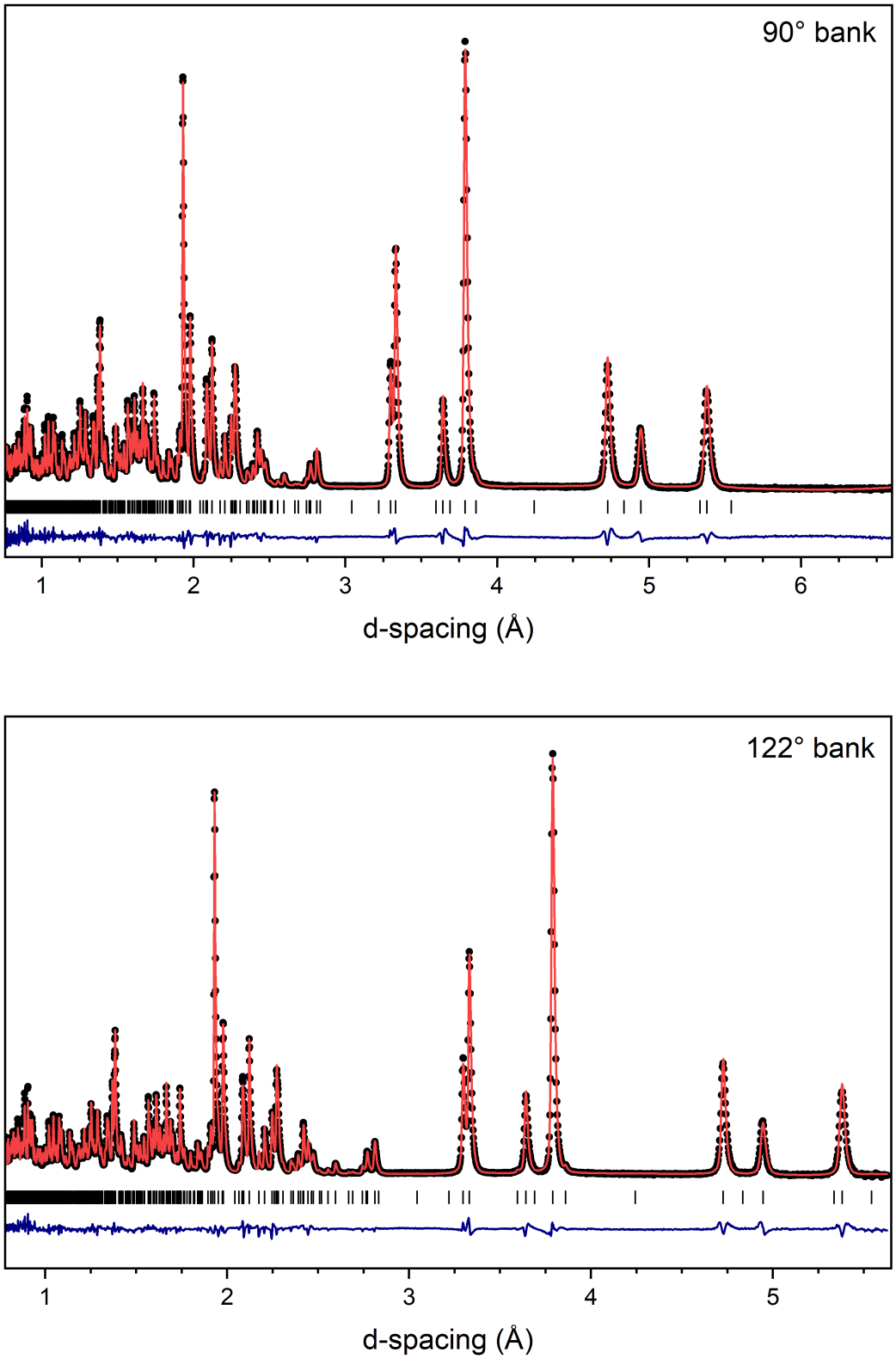


Figure A2.1.3 Observed, calculated and difference plots from the structural refinement of the ordered *P*2*cm* model of $ZnCaTa_2O_7$ against the NPD data collected from bank 3-8 (90°) and bank 4-7 (122°) on the WISH diffractometer at 100 K.

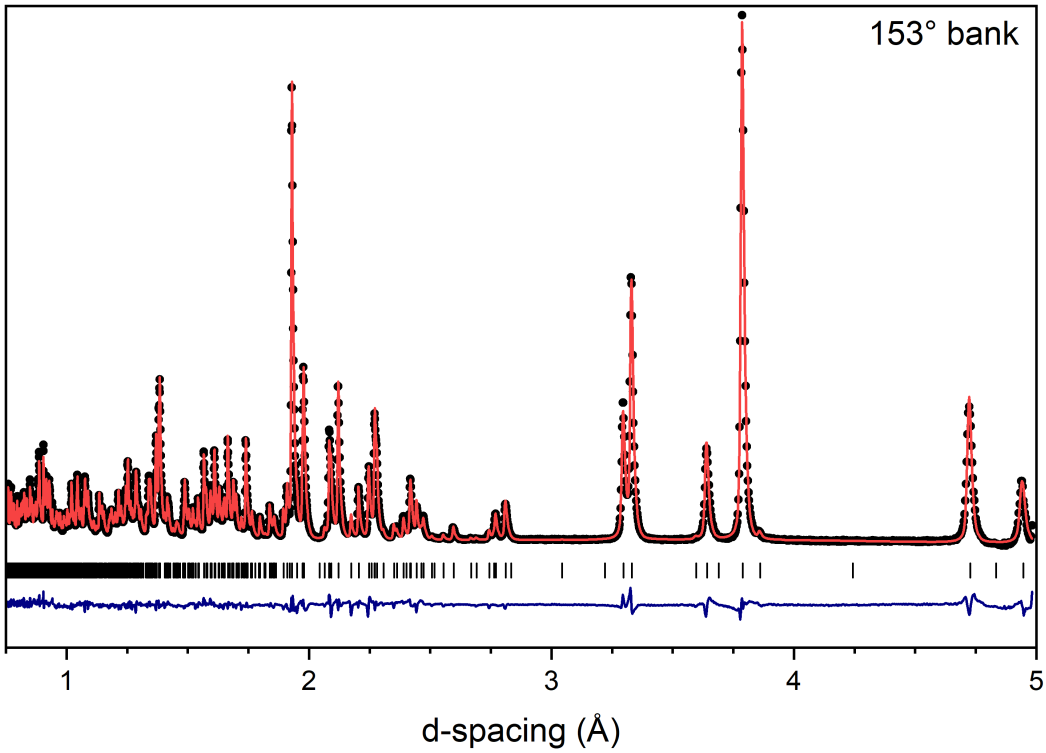


Figure A2.1.4 Observed, calculated and difference plots from the structural refinement of the ordered *P*2*cm* model of $ZnCaTa_2O_7$ against the NPD data collected from bank 5-6 (153°) on the WISH diffractometer at 100 K.

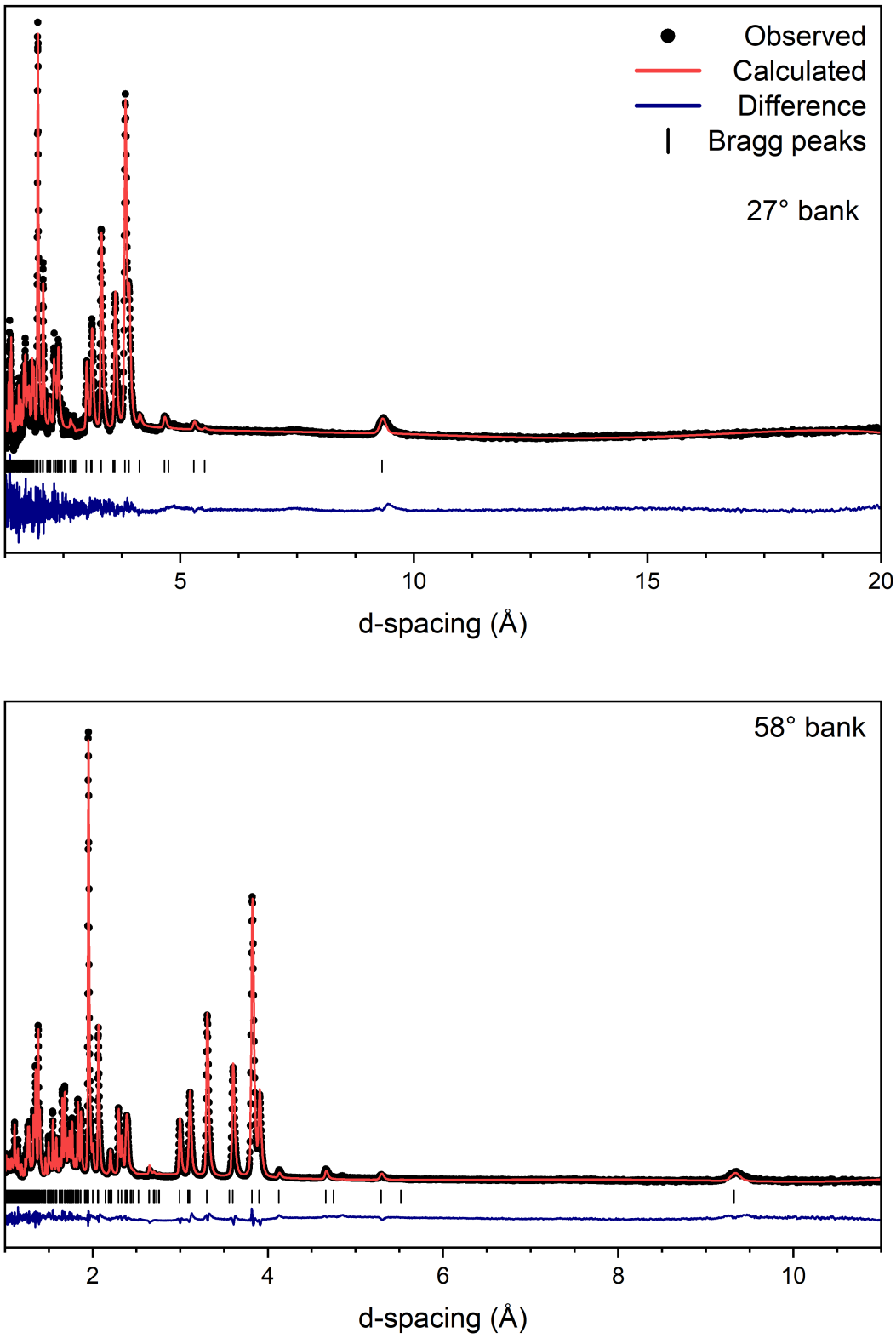


Figure A2.1.5 Observed, calculated and difference plots from the structural refinement of the *P*2$_1$*nm* model of $FeCaTa_2O_7$ against the NPD data collected from bank 1-10 (27°) and bank 2-9 (58°) on the WISH diffractometer at 200 K.

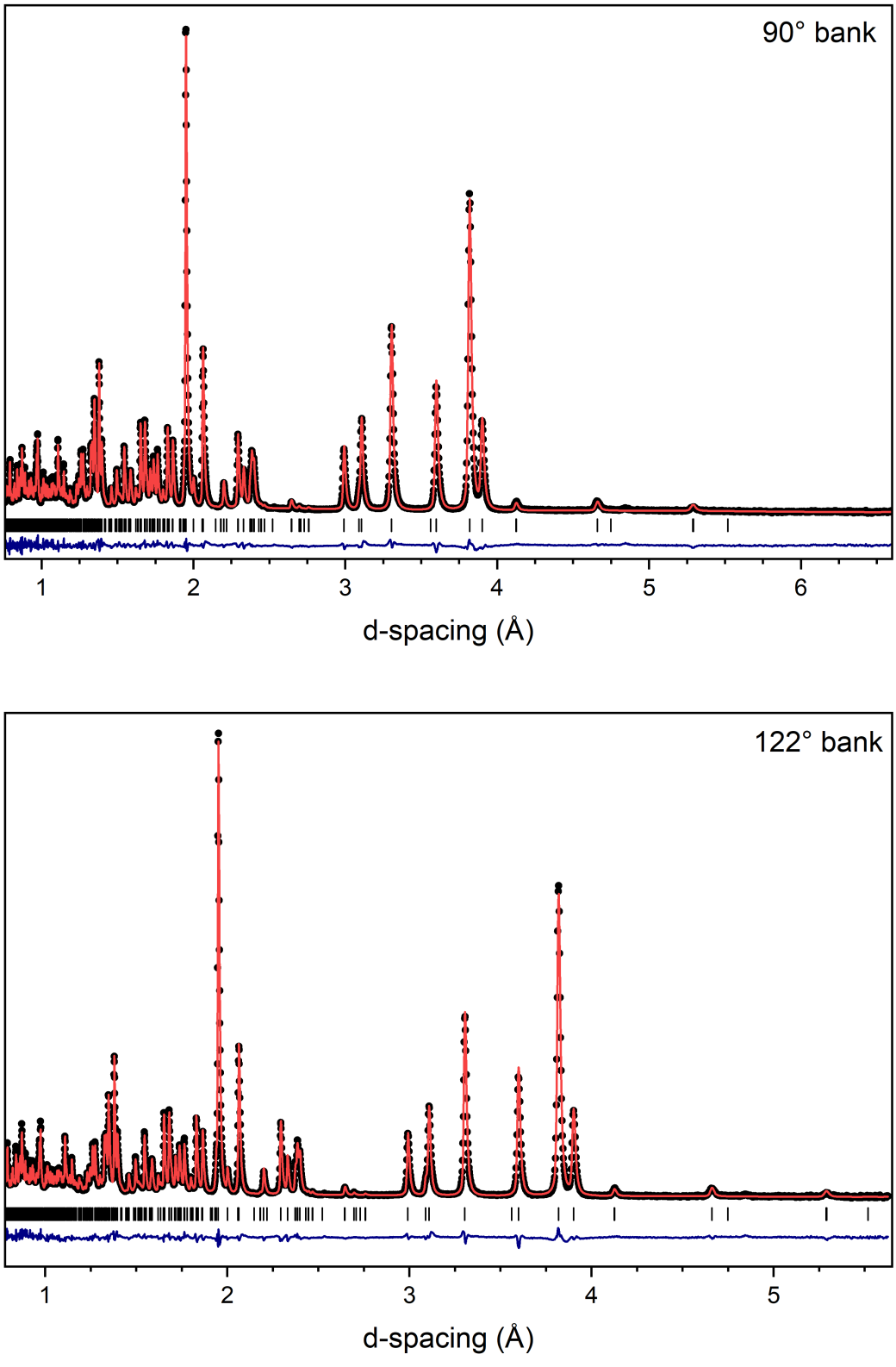


Figure A2.1.6 Observed, calculated and difference plots from the structural refinement of the $P2_1nm$ model of $FeCaTa_2O_7$ against the NPD data collected from bank 3-8 (90°) and bank 4-7 (122°) on the WISH diffractometer at 200 K.

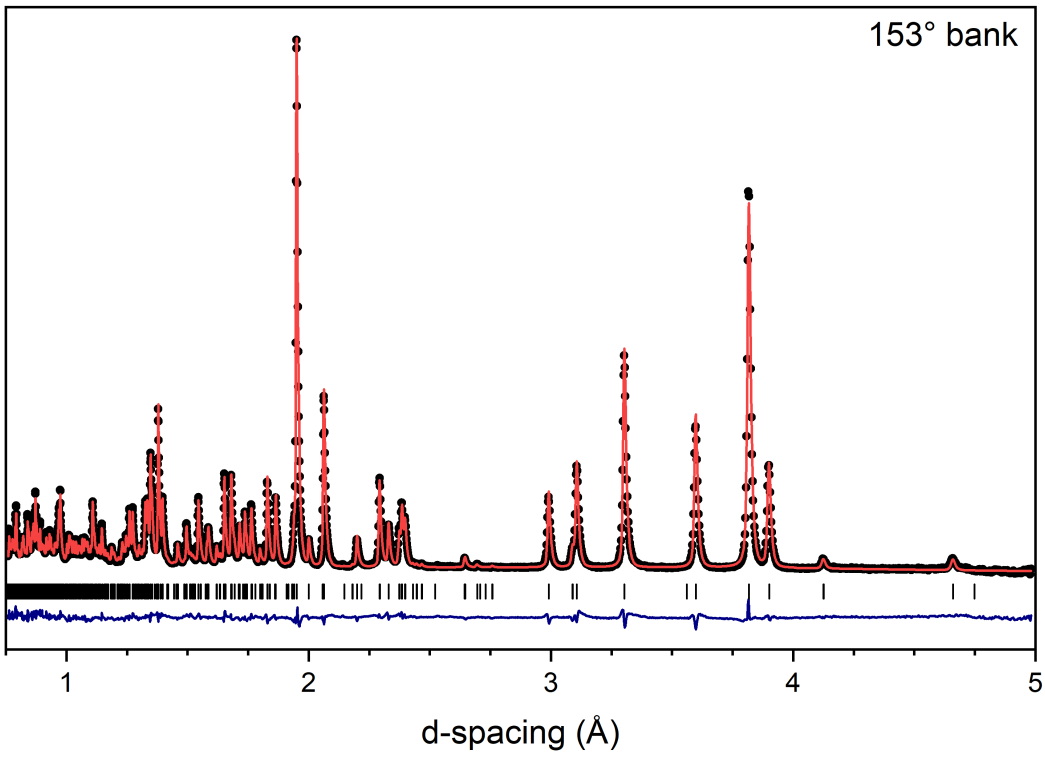


Figure A2.1.7 Observed, calculated and difference plots from the structural refinement of the $P2_1nm$ model of $FeCaTa_2O_7$ against the NPD data collected from bank 5-6 (153°) on the WISH diffractometer at 200 K.

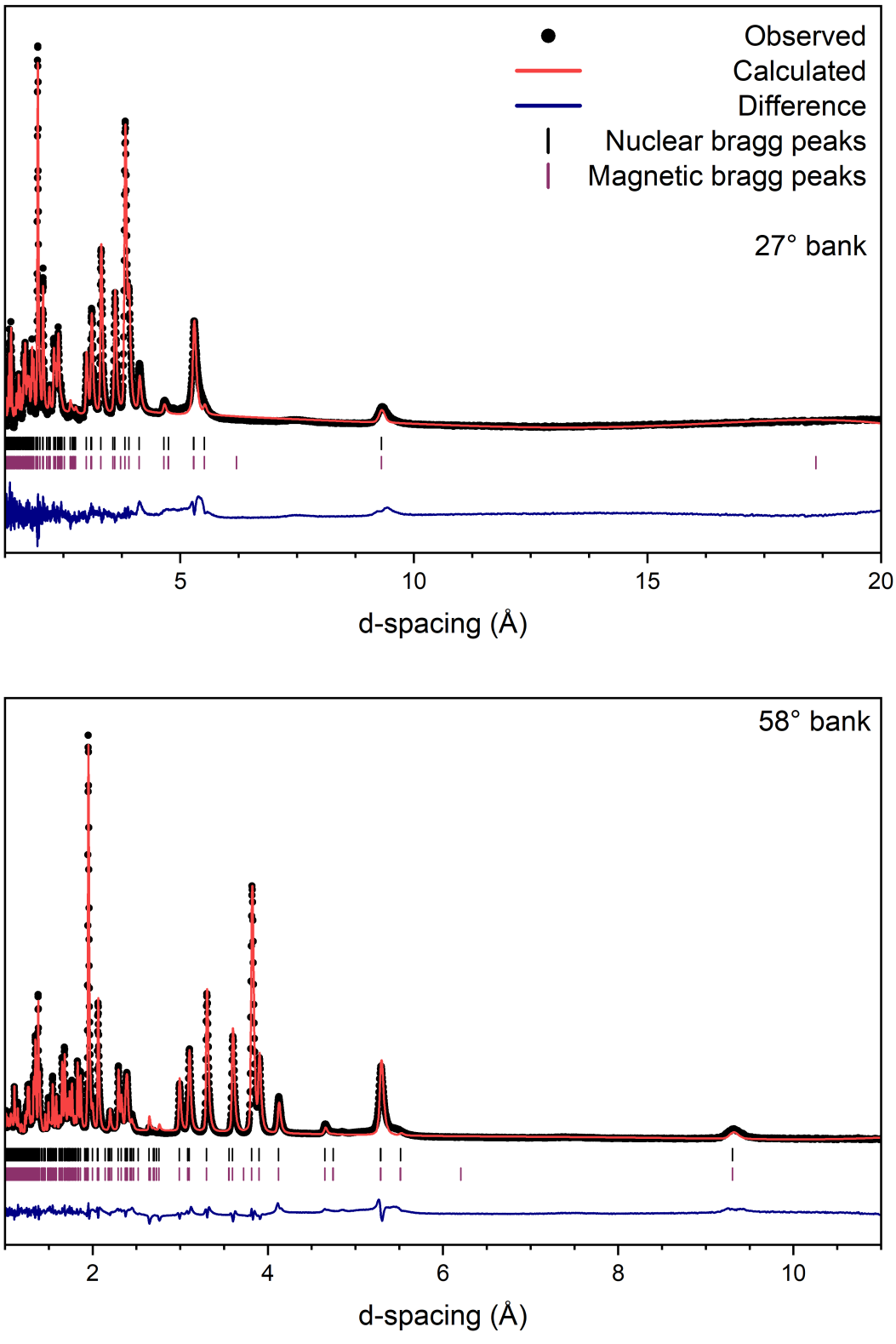


Figure A2.1.8 Observed, calculated and difference plots from the structural refinement of the $P2_1n'm'$ model of $FeCaTa_2O_7$ against the NPD data collected from bank 1-10 (27°) and bank 2-9 (58°) on the WISH diffractometer at 1.5 K.

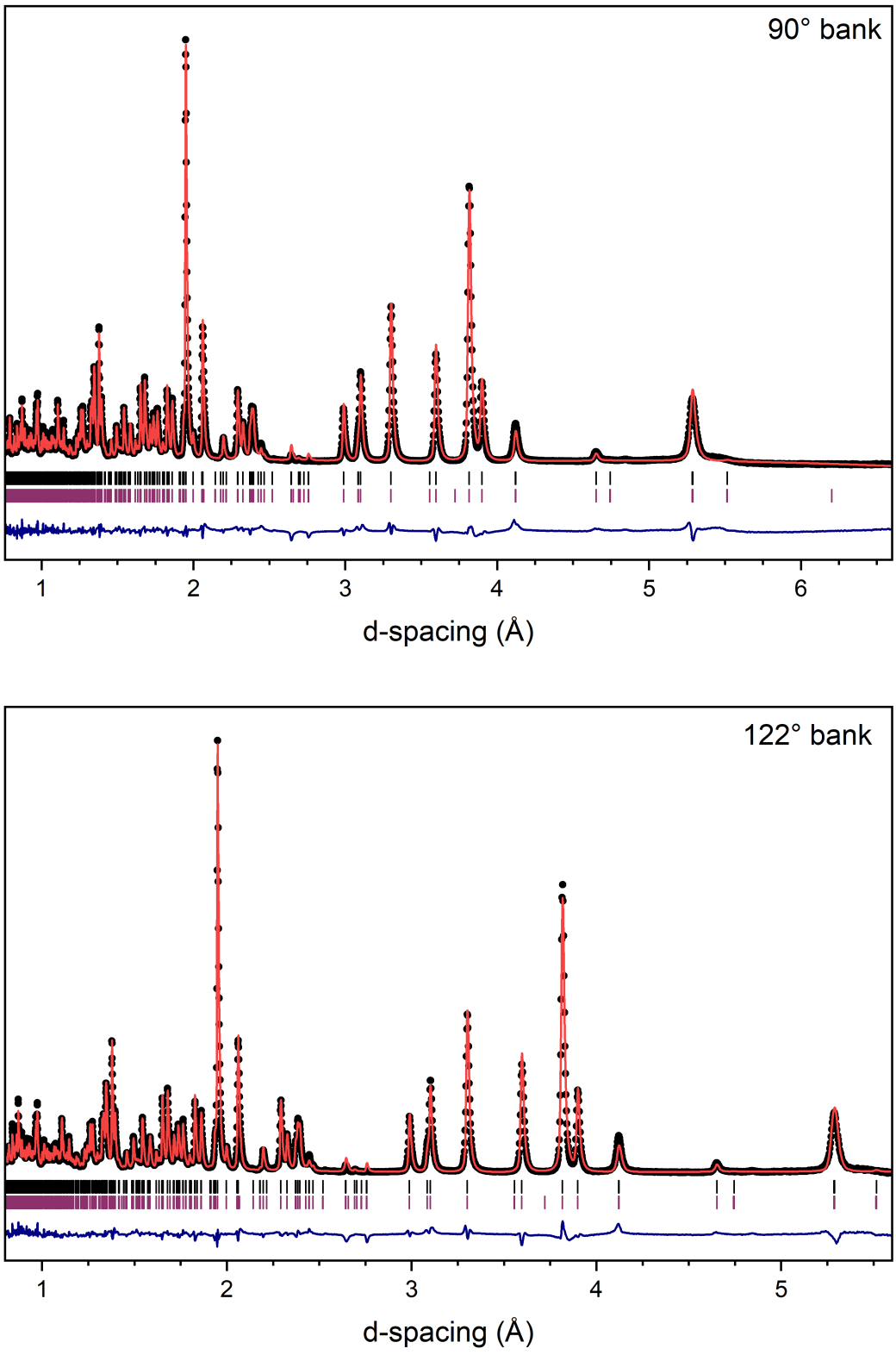


Figure A2.1.9 Observed, calculated and difference plots from the structural refinement of the $P2_1n'm'$ model of $FeCaTa_2O_7$ against the NPD data collected from bank 3-8 (90°) and bank 4-7 (122°) on the WISH diffractometer at 1.5 K.

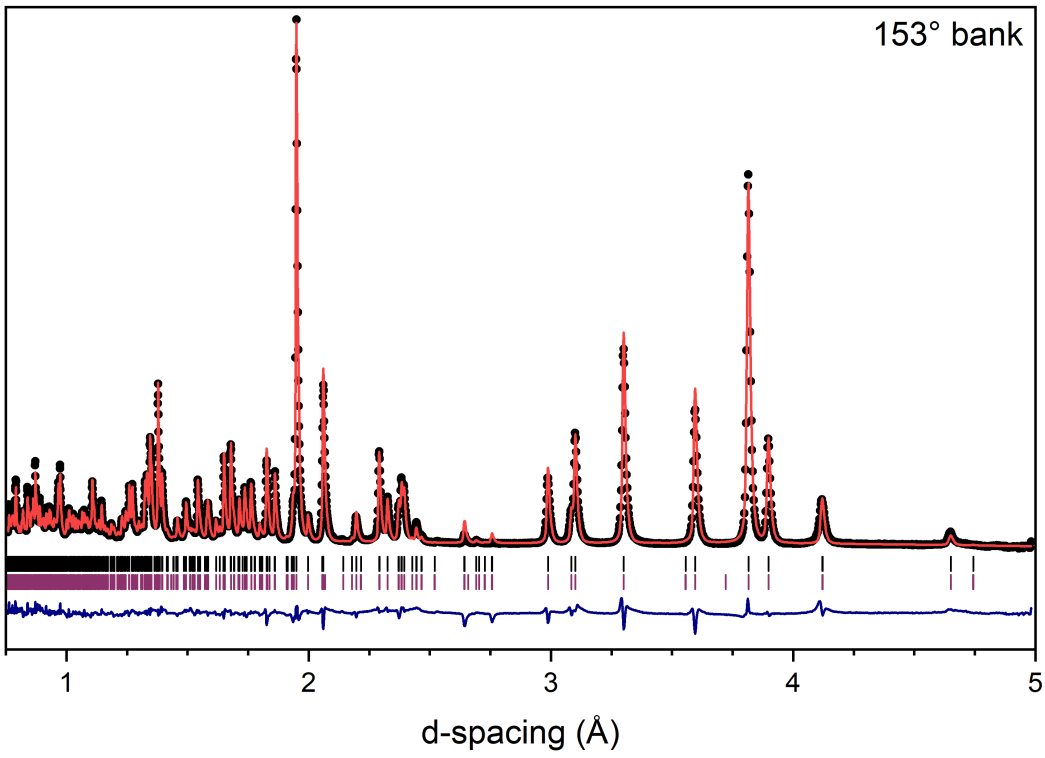


Figure A2.1.10 Observed, calculated and difference plots from the structural refinement of the $P2_1n'm'$ model of $FeCaTa_2O_7$ against the NPD data collected from bank 5-6 (153°) on the WISH diffractometer at 1.5 K.

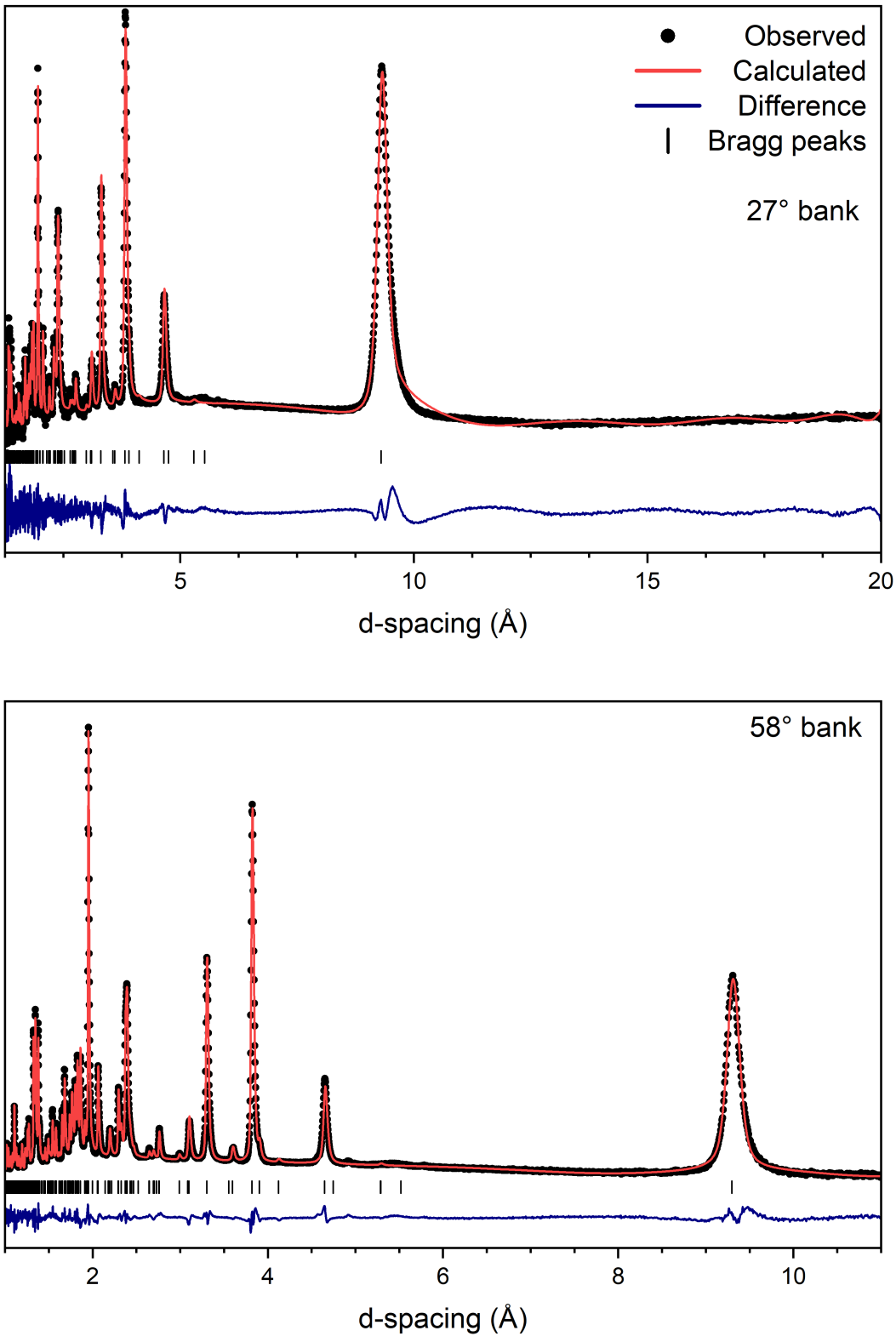


Figure A2.1.11 Observed, calculated and difference plots from the structural refinement of the $P2_1nm$ model of $CoCaTa_2O_7$ against the NPD data collected from bank 1-10 (27°) and bank 2-9 (58°) on the WISH diffractometer at 100 K.

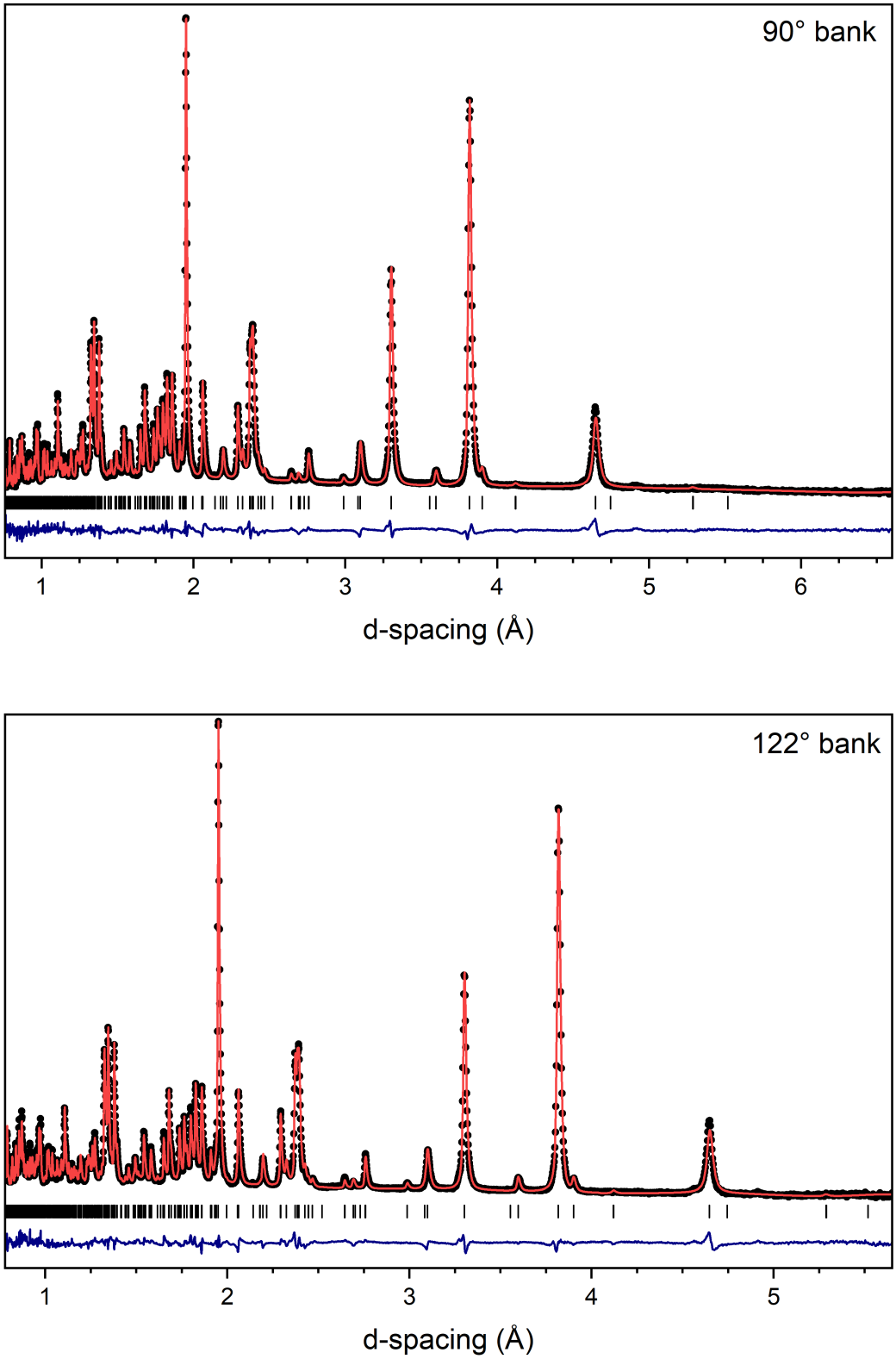


Figure A2.1.12 Observed, calculated and difference plots from the structural refinement of the $P2_1nm$ model of $CoCaTa_2O_7$ against the NPD data collected from bank 3-8 (90°) and bank 4-7 (122°) on the WISH diffractometer at 100 K.

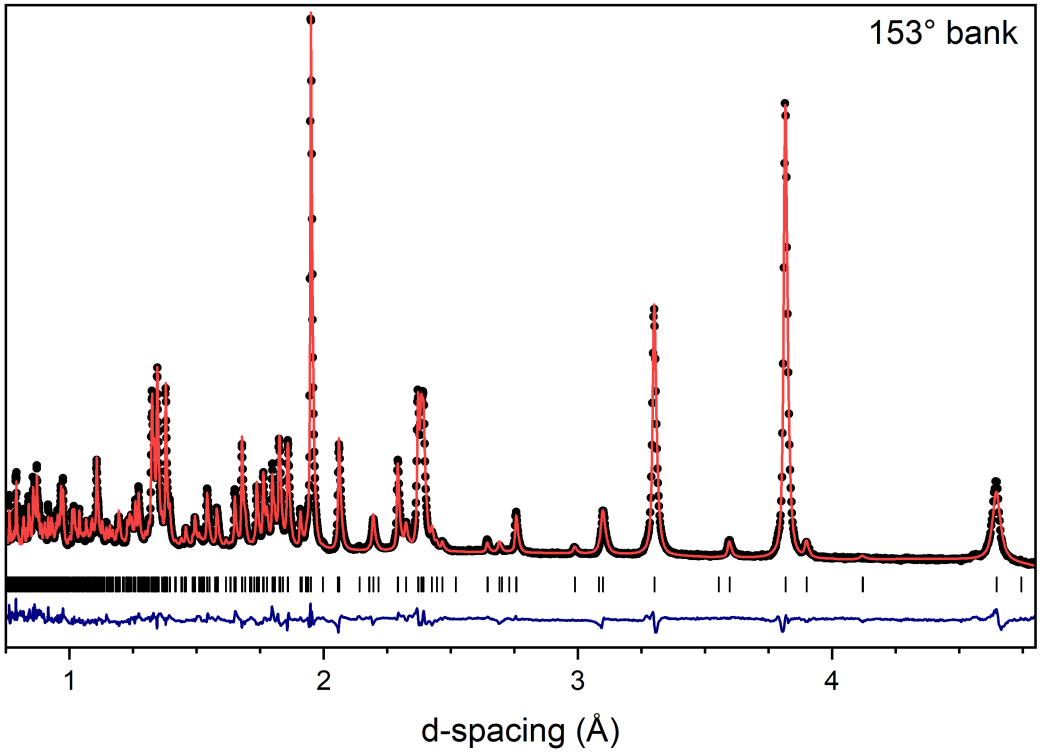


Figure A2.1.13 Observed, calculated and difference plots from the structural refinement of the *P*2$_1$*nm* model of $CoCaTa_2O_7$ against the NPD data collected from bank 5-6 (153°) on the WISH diffractometer at 100 K.

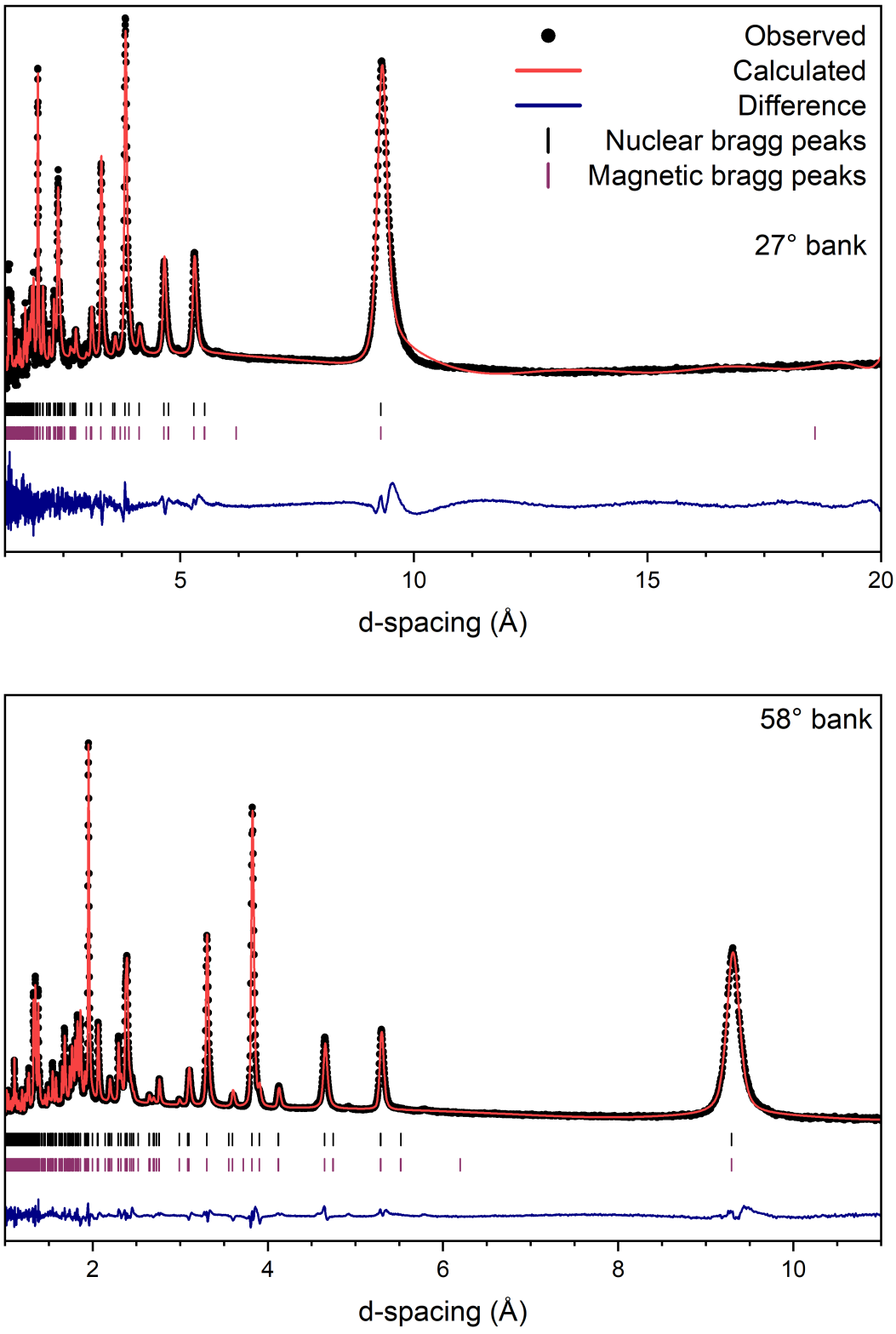


Figure A2.1.14 Observed, calculated and difference plots from the structural refinement of the $P2_1n'm'$ model of $CoCaTa_2O_7$ against the NPD data collected from bank 1-10 (27°) and bank 2-9 (58°) on the WISH diffractometer at 1.5 K.

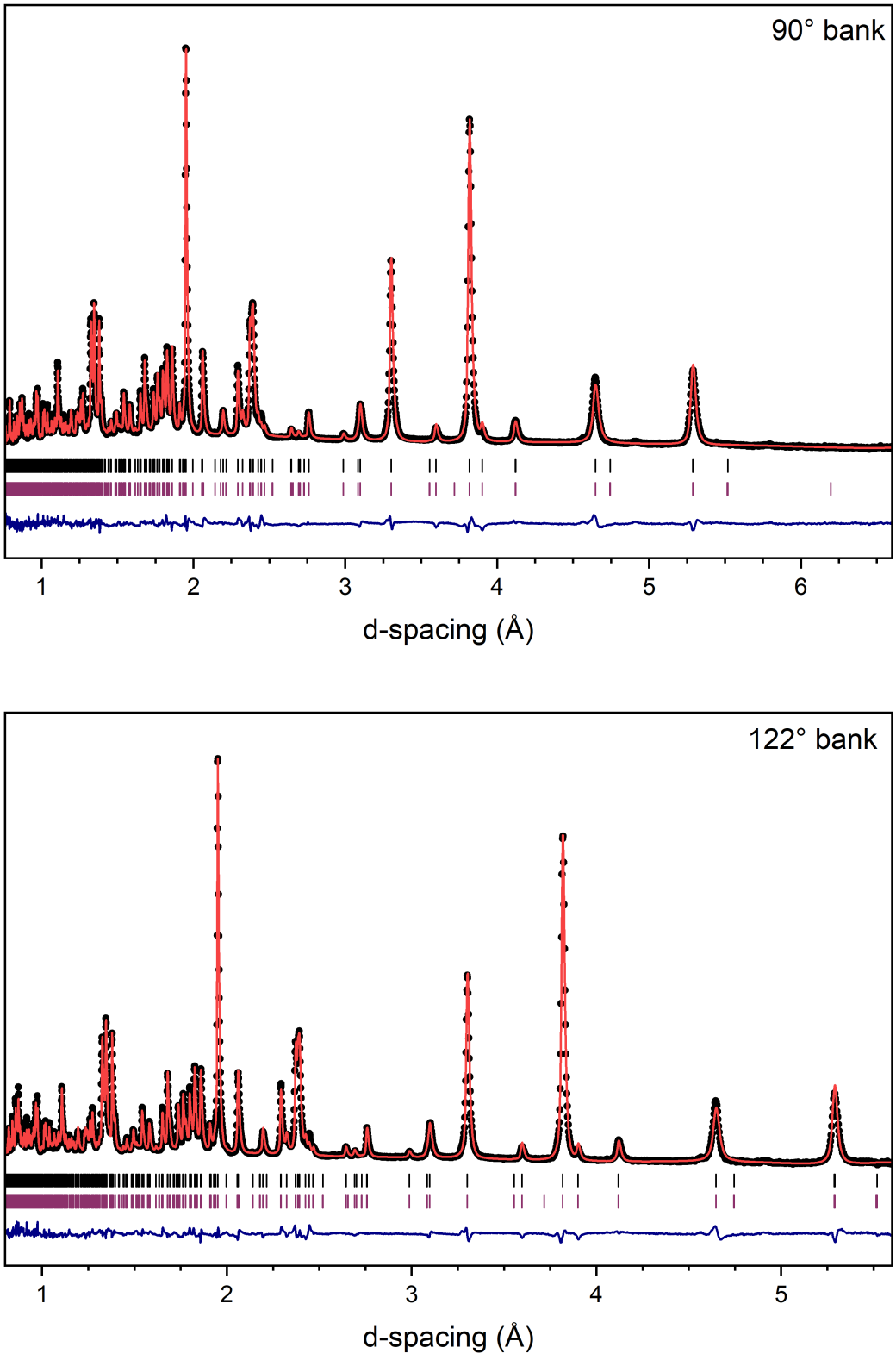


Figure A2.1.15 Observed, calculated and difference plots from the structural refinement of the $P2_1n'm'$ model of $CoCaTa_2O_7$ against the NPD data collected from bank 3-8 (90°) and bank 4-7 (122°) on the WISH diffractometer at 1.5 K.

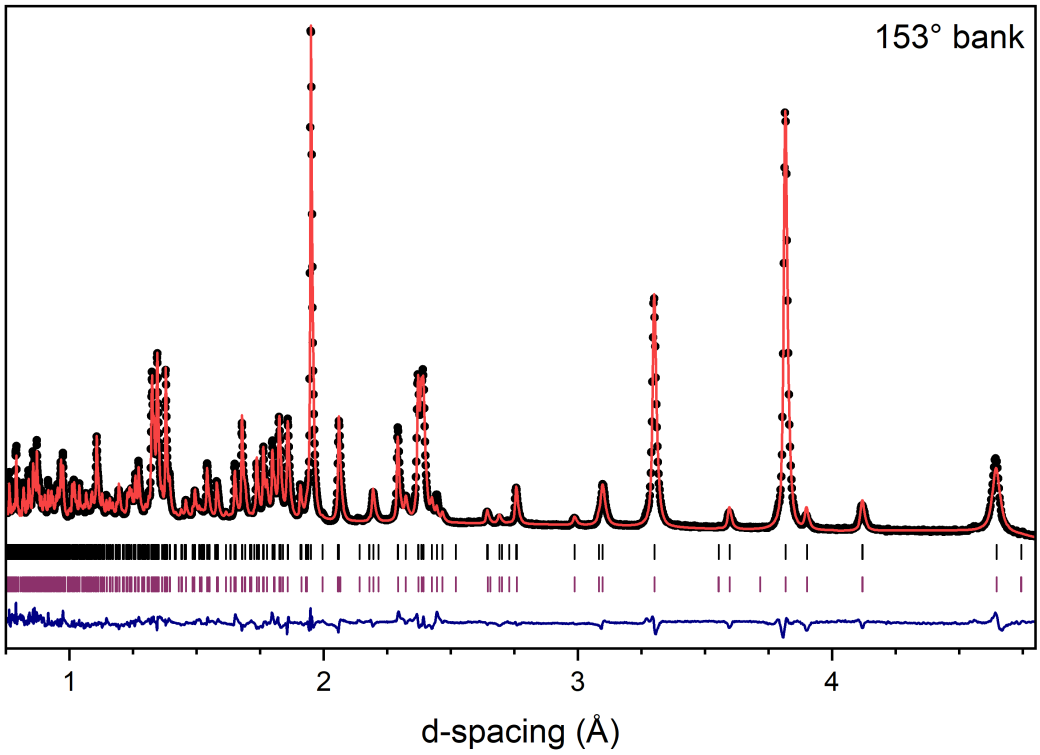


Figure A2.1.16 Observed, calculated and difference plots from the structural refinement of the $P2_1n'm'$ model of $CoCaTa_2O_7$ against the NPD data collected from bank 5-6 (153°) on the WISH diffractometer at 1.5 K.

A2.2 Additional data from the structural refinements in Chapter 4

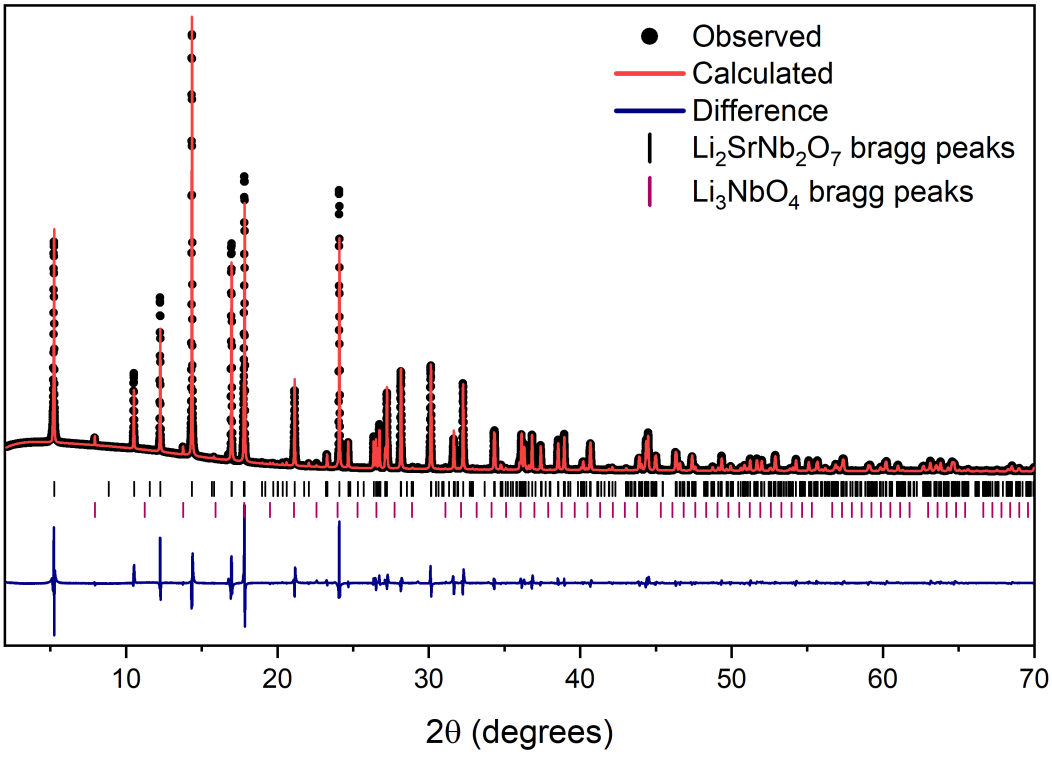


Figure A2.2.1 Observed, calculated and difference plots from the structural refinement of the *A*2$_1$*am* model of $Li_2SrNb_2O_7$ against SXRD data collected at room temperature.

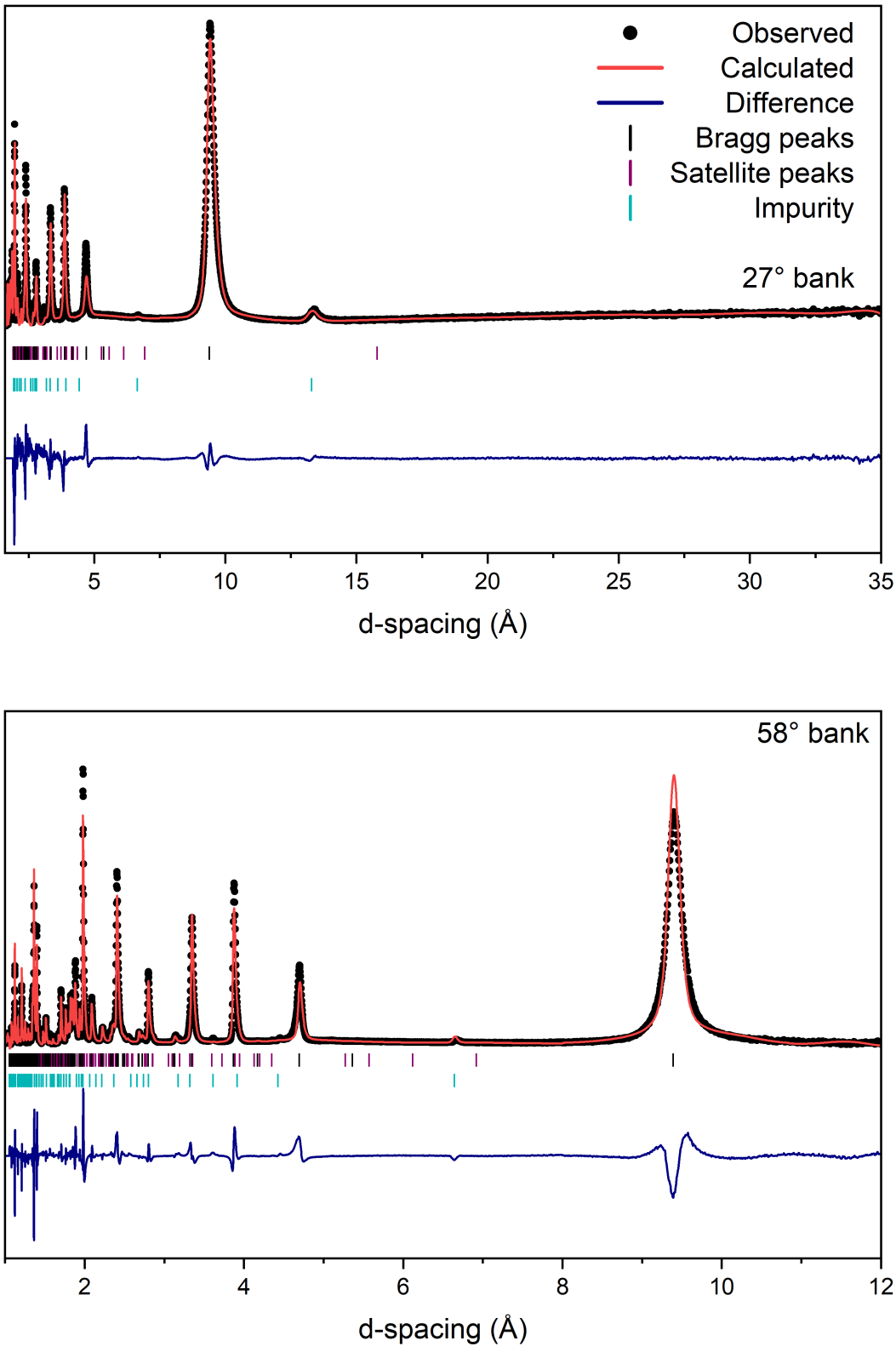


Figure A2.2.2 Observed, calculated and difference plots from the structural refinement of the $A2_1am(0\beta0)000$ model of $MnSrNb_2O_7$ against the NPD data collected from bank 1-10 (27°) and bank 2-9 (58°) on the WISH diffractometer at 80 K.

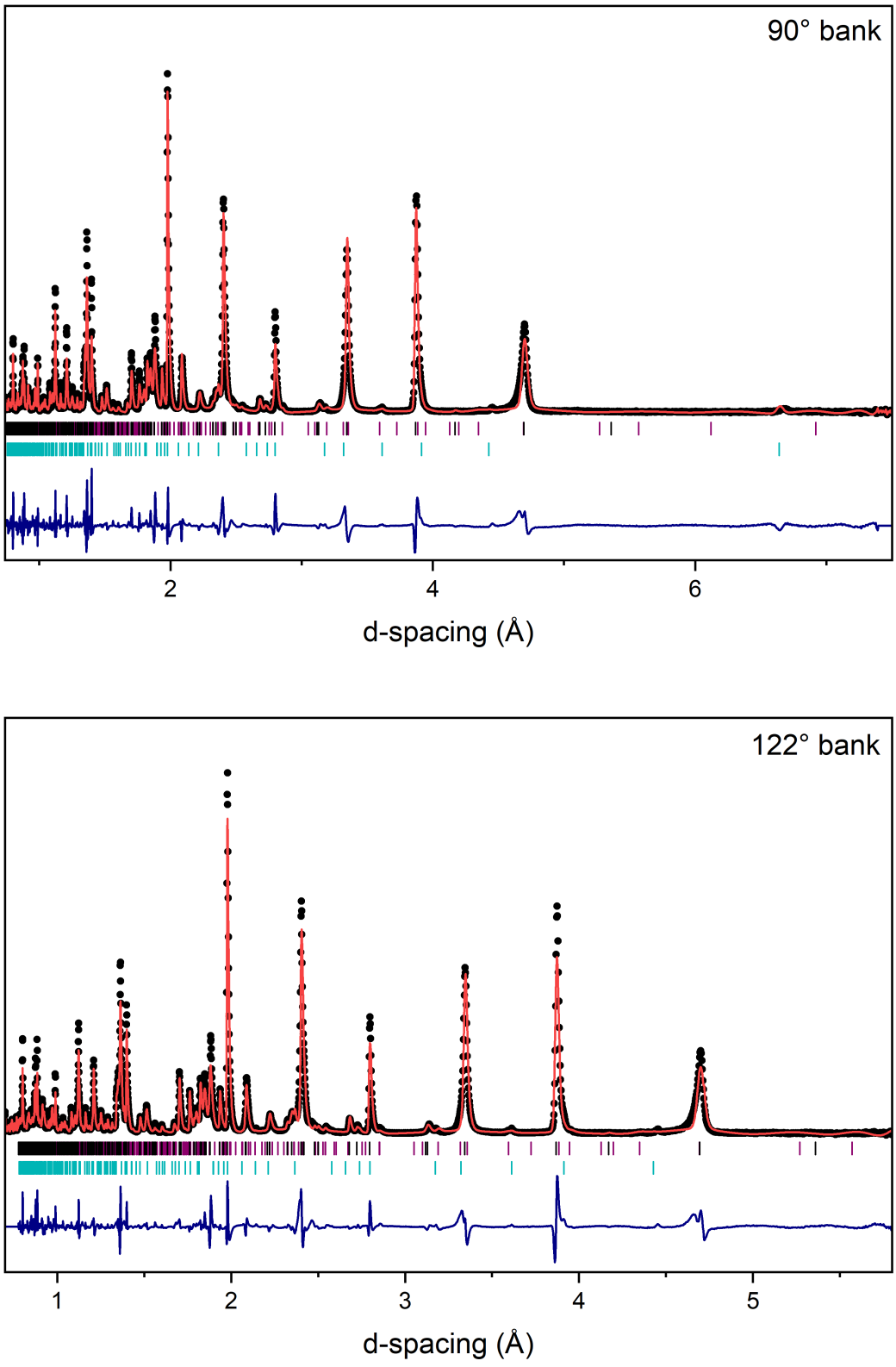


Figure A2.2.3 Observed, calculated and difference plots from the structural refinement of the $A2_1am(0\beta0)000$ model of $MnSrNb_2O_7$ against the NPD data collected from bank 3-8 (90°) and bank 4-7 (122°) on the WISH diffractometer at 80 K.

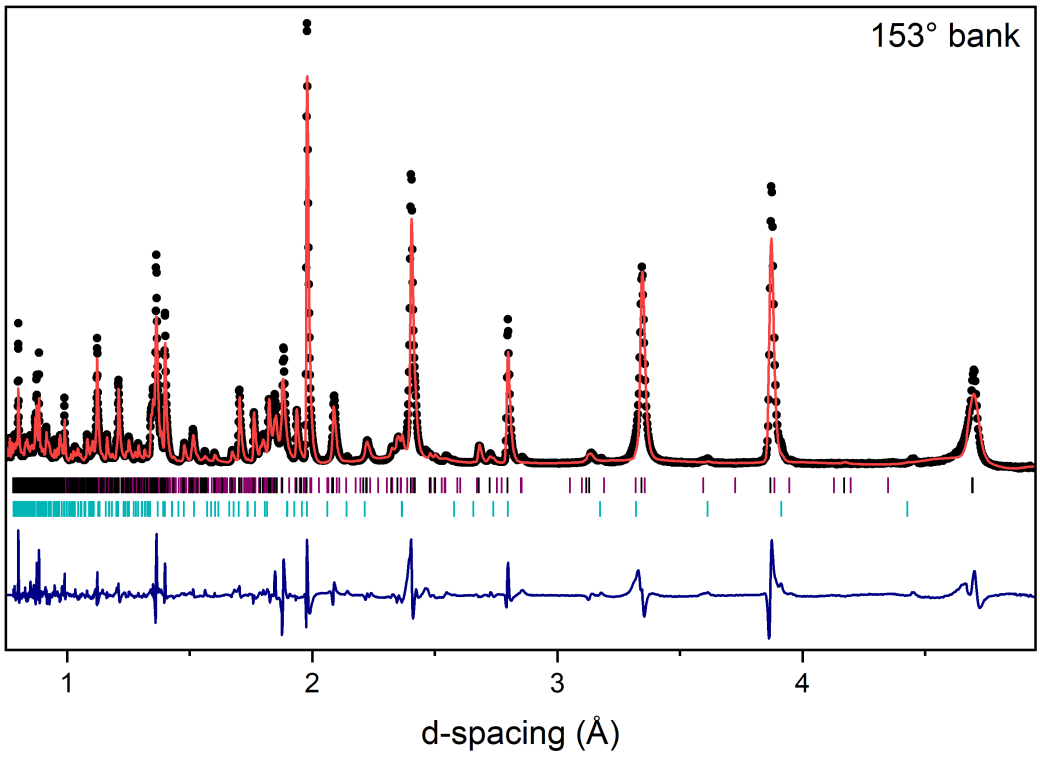


Figure A2.2.4 Observed, calculated and difference plots from the structural refinement of the $A2_1am(0\beta0)000$ model of $MnSrNb_2O_7$ against the NPD data collected from bank 5-6 (153°) on the WISH diffractometer at 80 K.

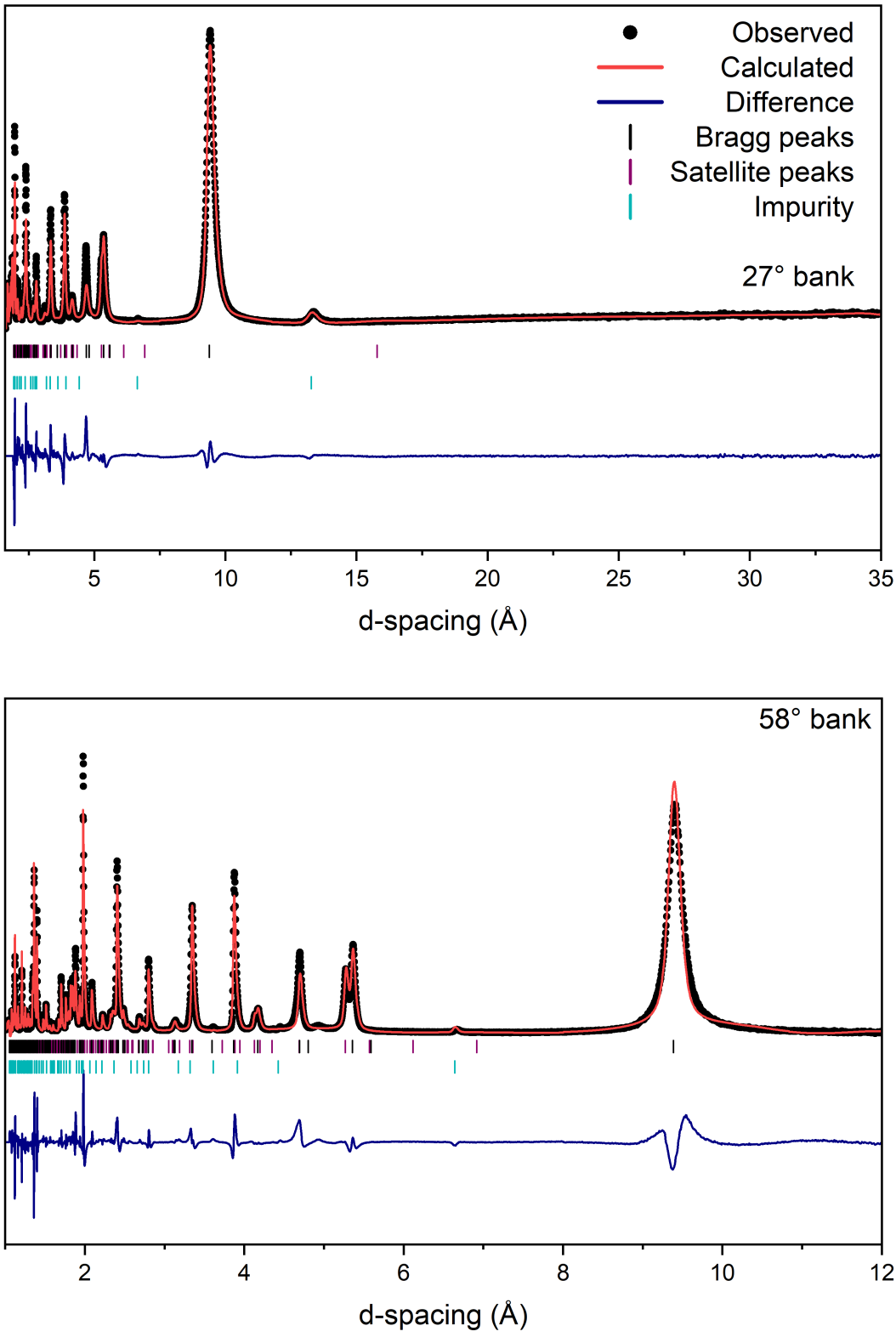
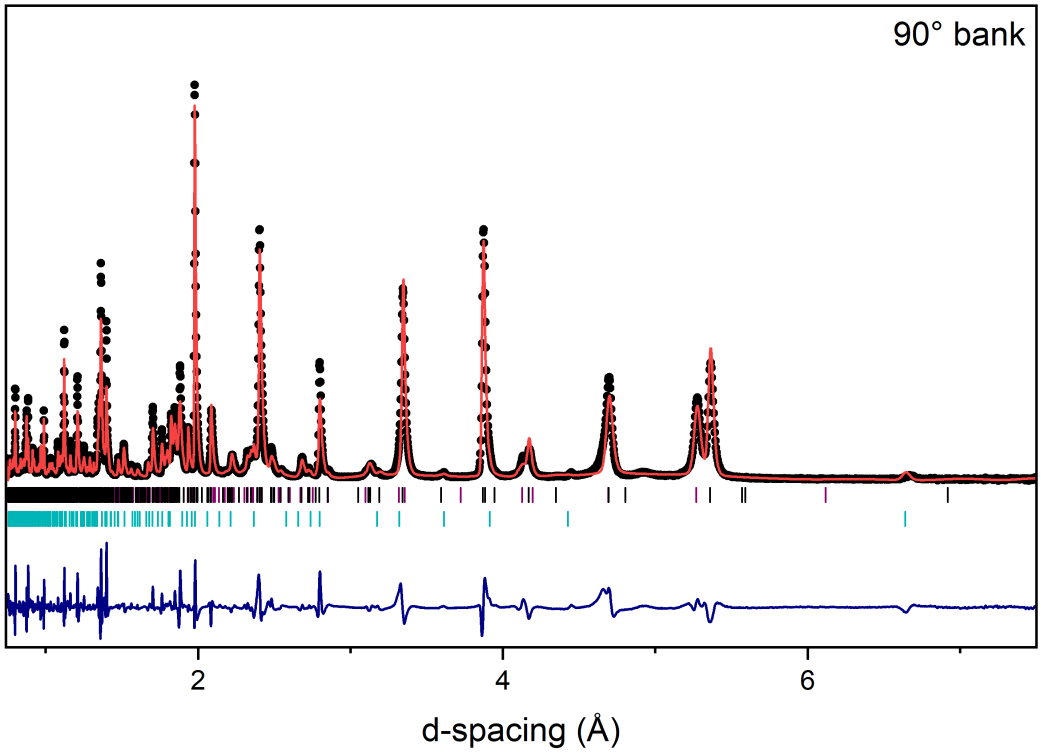


Figure A2.2.5 Observed, calculated and difference plots from the structural refinement of the $A2_1am(0\beta0)000$ model of $MnSrNb_2O_7$ against the NPD data collected from bank 1-10 (27°) and bank 2-9 (58°) on the WISH diffractometer at 1.5 K.



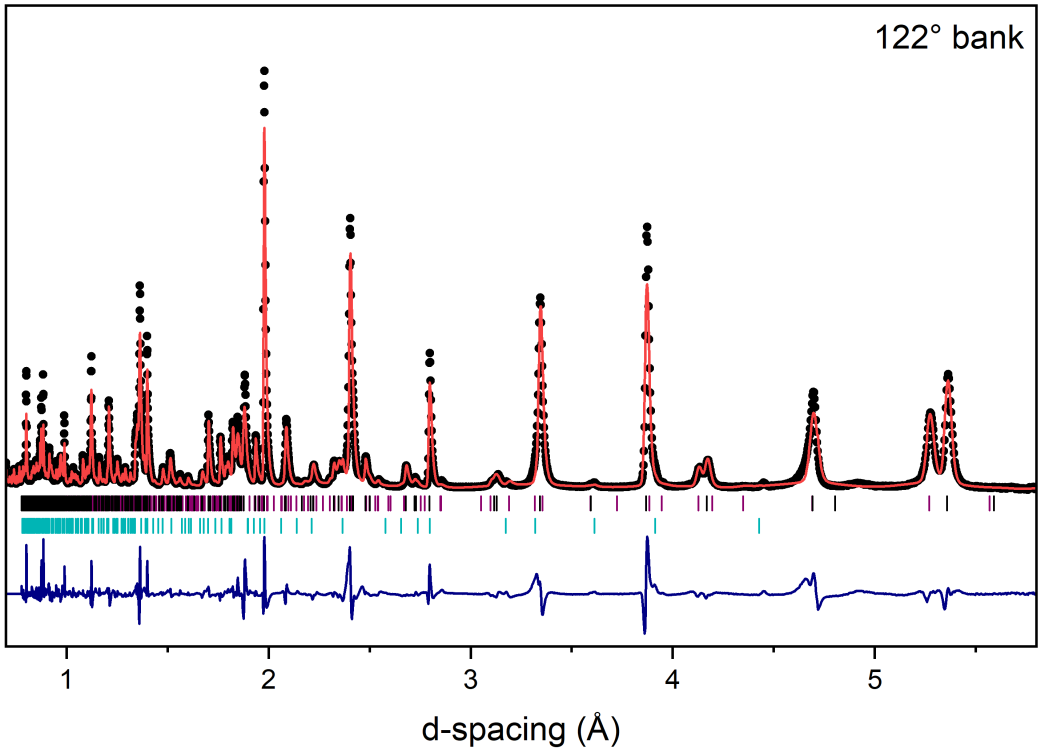


Figure A2.2.6 Observed, calculated and difference plots from the structural refinement of the $A2_1am(0\beta0)000$ model of $MnSrNb_2O_7$ against the NPD data collected from bank 3-8 (90°) and bank 4-7 (122°) on the WISH diffractometer at 1.5 K.

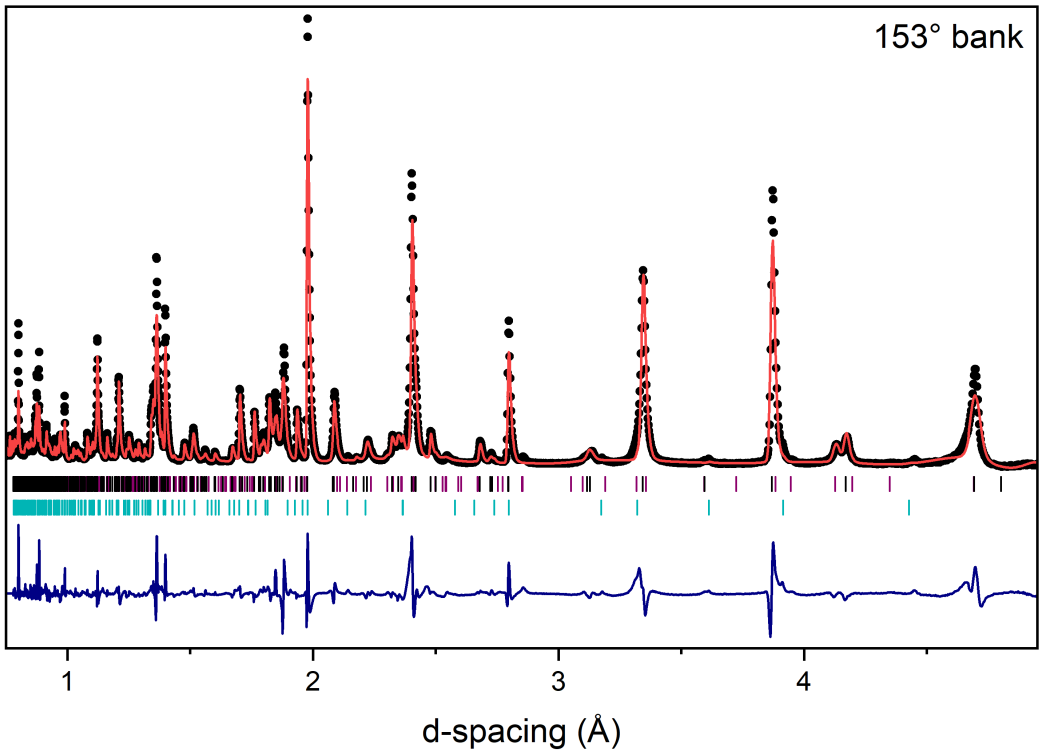


Figure A2.2.7 Observed, calculated and difference plots from the structural refinement of the $A2_1am(0\beta0)000$ model of $MnSrNb_2O_7$ against the NPD data collected from bank 5-6 (153°) on the WISH diffractometer at 1.5 K.

A2.3 Additional data from the first principles calculations of Chapter 6

Table A2.3.1 Lattice parameters and atomic coordinates of $A2_1am$ $Li_2CaTa_2O_7$ from first principles calculations.

Atom	Site	*x*	*y*	*z*
Li1	8*b*	0.24934	0.00596	0.26263
Ca1	4*a*	0.04316	0.75121	0
Ta1	8*b*	0.00622	0.24853	0.88796
O1	8*b*	0.27828	0.03226	0.08460
O2	8*b*	0.70566	0.45780	0.11841
O3	8*b*	0.00155	0.20118	0.78592
O4	4*a*	0.97489	0.33041	0
a = 5.51635 Å, b = 5.44579 Å, c = 18.18411 Å				

Table A2.3.2 Lattice parameters and atomic coordinates of *Pnam* $Li_2CaTa_2O_7$ from first principles calculations.

Atom	Site	*x*	*y*	*z*
Li1	8*d*	0.49001	0.75208	0.01255
Ca1	4*c*	0.29680	0.00159	1/4
Ta1	8*d*	0.75939	0.00137	0.13795
O1	8*d*	0.46812	0.71728	0.83454
O2	8*d*	0.04248	0.29350	0.86858
O3	8*d*	0.75755	0.04960	0.03599
O4	4*c*	0.72827	0.91928	1/4
a = 5.51566 Å, b = 5.44176 Å, c = 18.18767 Å				

Table A2.3.3 Lattice parameters and atomic coordinates of *Pna*2$_1$ $Li_2CaTa_2O_7$ from first principles calculations.

Atom	Site	*x*	*y*	*z*
Li1	4*a*	0.99011	0.74785	0.73742
Li2	4*a*	0.51009	0.24804	0.76255
Ca1	4*a*	0.20323	0.50159	0.00000
Ta1	4*a*	0.25941	0.49862	0.61204
Ta2	4*a*	0.25936	0.49861	0.38795
O1	4*a*	0.96819	0.78263	-0.08454
O2	4*a*	0.54239	0.20661	0.88141
O3	4*a*	0.96813	0.78266	0.08454
O4	4*a*	0.54239	0.20657	0.11859
O5	4*a*	0.2576	0.45036	0.71401
O6	4*a*	0.25754	0.45034	0.28598
O7	4*a*	0.22826	0.58072	0.50000
a = 5.51570 Å, b = 5.44216 Å, c = 18.18744 Å				

Table A2.3.4 Lattice parameters and atomic coordinates of *Amam* $Li_2SrTa_2O_7$ from first principles calculations.

Atom	Site	*x*	*y*	*z*
Li1	8*e*	0	0	0.73945
Sr1	4*c*	3/4	0.25507	0
Ta1	8*g*	3/4	0.25364	0.38513
O1	8*e*	0	0	0.90563
O2	8*e*	0	0	0.61500
O3	8*g*	3/4	0.28189	0.28198
O4	4*c*	3/4	0.70572	0
a = 5.57310 Å, *b* = 5.58492 Å, *c* = 18.10681 Å				

Table A2.3.5 Lattice parameters and atomic coordinates of *Pnnm* $Li_2SrTa_2O_7$ from first principles calculations.

Atom	Site	*x*	*y*	*z*
Li1	4*e*	0	0	0.26054
Li2	4*f*	0	1/2	0.23946
Sr1	4*g*	0.75000	0.74496	0
Ta1	8*h*	0.75000	0.74636	0.38514
O1	4*e*	0	0	0.0944
O2	4*e*	0	0	0.38505
O3	4*f*	0	1/2	0.11495
O4	4*f*	0	1/2	0.40559
O5	8*h*	0.75000	0.71823	0.28199
O6	4*g*	0.25002	0.70587	0
a = 5.57285 Å, *b* = 5.58542 Å, *c* = 18.10842 Å				

Table A2.3.6 Lattice parameters and atomic coordinates of $A2_1am$ $Li_2SrNb_2O_7$ from first principles calculations.

Atom	Site	*x*	*y*	*z*
Li1	8*b*	0.24782	0.00440	0.26180
Sr1	4*a*	0.01196	0.74483	0
Nb1	8*b*	0.01153	0.24611	0.88462
O1	8*b*	0.25308	0.00443	0.09458
O2	8*b*	0.74086	0.49373	0.11641
O3	8*b*	0.99488	0.21715	0.78149
O4	4*a*	0.99180	0.29654	0
a = 5.58200 Å, b = 5.59150 Å, c = 17.94235 Å				

Table A2.3.7 Lattice parameters and atomic coordinates of *Pnam* $Li_2SrNb_2O_7$ from first principles calculations.

Atom	Site	*x*	*y*	*z*
Li1	8*d*	0.50077	0.75471	0.01176
Sr1	4*c*	0.26853	0.99476	1/4
Nb1	8*d*	0.76801	0.00384	0.13462
O1	8*d*	0.49068	0.74519	0.84458
O2	8*d*	0.00398	0.25681	0.86643
O3	8*d*	0.75050	0.03264	0.03148
O4	4*c*	0.74719	0.95339	1/4
a = 5.58240 Å, b = 5.59307 Å, c = 17.93646 Å				

Table A2.3.8 Lattice parameters and atomic coordinates of $P2_1nm$ $Li_2SrNb_2O_7$ from first principles calculations.

Atom	Site	*x*	*y*	*z*
Li1	4*b*	0.24772	0.25437	0.76179
Li2	4*b*	0.24776	0.75441	0.73821
Sr1	2*a*	0.51182	0.00516	0
Sr2	2*a*	0.01178	0.49465	0
Nb1	4*b*	0.01151	0.99599	0.88462
Nb2	4*b*	0.5115	0.5038	0.88461
O1	4*b*	0.253	0.25437	0.59462
O2	4*b*	0.74124	0.74414	0.61637
O3	4*b*	0.2412	0.75607	0.61644
O4	4*b*	0.75297	0.24582	0.59458
O5	4*b*	0.99491	0.96723	0.78148
O6	4*b*	0.49471	0.53274	0.78148
O7	2*a*	0.99168	0.04644	0
O8	2*a*	0.49201	0.45347	0
a = 5.58167 Å, b = 5.59204 Å, c = 17.94094 Å				

Appendix 3 – Bibliography

1 B. Raveau, A. Maignan, C. Martin and M. Hervieu, *Chemistry of Materials*, 1998, 10, 2641–2652.

2 H. Müller-Buschbaum, *Angewandte Chemie International Edition in English*, 1989, 28, 1472–1493.

3 A. M. Abakumov, A. A. Tsirlin and E. V. Antipov, *Transition-Metal Perovskites*, Elsevier Ltd., 2013, vol. 2.

4 V. M. Goldschmidt, *Naturwissenschaften*, 1926, 14, 477–485.

5 H. D. Megaw, *Proceedings of the Physical Society*, 1946, 58, 133–152.

6 H. D. Megaw, *Nature*, 1945, 155, 484–485.

7 S. P. N. Nair and P. Murugavel, *Oxides: Their Properties and Uses*, Elsevier Ltd., 2013, vol. 4.

8 A. M. Abakumov, A. A. Tsirlin and E. V. Antipov, in *Comprehensive Inorganic Chemistry II (Second Edition): From Elements to Applications*, Elsevier Ltd, 2013, vol. 2, pp. 1–40.

9 N. A. Benedek and C. J. Fennie, *Journal of Physical Chemistry C*, 2013, 117, 13339–13349.

10 I. D. Brown and D. Altermatt, *Acta Crystallographica Section B*, 1985, 41, 244–247.

11 N. E. Brese and M. O'Keeffe, *Acta Crystallographica Section B*, 1991, 47, 192–197.

12 C. J. Howard and H. T. Stokes, *Crystallography Acta Crystallographica Section B Acta Cryst*.

13 C. Structure, C. Caotnta, C. Chothia, P. ; Pauling, P. Pauling, L. W. Coleman, O. E. Little, R. A. I. Bannard, D. T. Cromer, J. B. Mann, R. Guttormson, B. Robertson, R. F. Stewart, E. R. Davidson and W. T. Simpson, *The Classification of Tilted Octahedra in Perovskites*, FORDAP, 1970, vol. 225.

14 N. A. Hill, *Journal of Physical Chemistry B*, 2000, 104, 6694–6709.

15 N. A. Spaldin and R. Ramesh, *Nat Mater*, 2019, 18, 203–212.

16 N. A. Spaldin, *Magnetic Materials: Fundamentals and Applications*, Cambridge University Press, 2010.

17 M. M. Vopson, *Critical Reviews in Solid State and Materials Sciences*, 2015, 40, 223–250.

18 S. Blundell, *Magnetism in Condensed Matter*, Oxford University Press, 2001.

19 J. B. Goodenough, *Physical Review*, 1955, 100, 564–573.

20 J. Kanamori, *Progress of Theoretical Physics*, 1957, 17, 177–196.

21 P. W. Anderson, *Physical Review*, 1959, 115, 2–13.

22 P. S. Halasyamani and K. R. Poeppelmeier, *American Chemical Society*, 1998, preprint, DOI: 10.1021/cm980140w.

23 R. Zhang, M. S. Senn and M. A. Hayward, *Chemistry of Materials*, 2016, 28, 8399–8406.

24 X. Huai and T. T. Tran, *Annu Rev Mater Res*, 2023, 53, 253–274.

25 R. G. Pearson, *Journal of Molecular Structure: THEOCHEM*, 1983, 103, 25–34.

26 P. S. Halasyamani, 2004, preprint, DOI: 10.1021/cm049297g.

27 R. Seshadri and N. A. Hill, *Chemistry of Materials*, 2001, 13, 2892–2899.

28 M. W. Stoltzfus, P. M. Woodward, R. Seshadri, J.-H. Klepeis and B. Bursten, *Inorg Chem*, 2007, 46, 3839–3850.

29 M. Kunz and I. D. Brown, *J Solid State Chem*, 1995, 115, 395–406.

30 N. S. P. Bhuvanesh and J. Gopalakrishnan, *J Mater Chem*, 1997, 7, 2297–2306.

31 N. A. Benedek, A. T. Mulder and C. J. Fennie, *J Solid State Chem*, 2012, 195, 11–20.

32 I. B. Bersuker, *Physics Letters*, 1966, 20, 589–590.

33 I. B. Bersuker and B. G. Vekhter, *Ferroelectrics*, 1978, 19, 137–150.

34 J. K. Burdett, *Inorg Chem*, 1981, 20, 1959–1962.

35 R. E. Cohen, *Nature*, 1992, 358, 136–138.

36 N. A. Benedek and M. A. Hayward, DOI:10.1146/annurev-matsci-080819.

37 G. Catalan and J. F. Scott, *Advanced Materials*, 2009, 21, 2463–2485.

38 C.-Y. Kuo, Z. Hu, J. C. Yang, S.-C. Liao, Y. L. Huang, R. K. Vasudevan, M. B. Okatan, S. Jesse, S. V Kalinin, L. Li, H. J. Liu, C.-H. Lai, T. W. Pi, S. Agrestini, K. Chen, P. Ohresser, A. Tanaka, L. H. Tjeng and Y. H. Chu, *Nat Commun*, 2016, 7, 12712.

39 T. Kimura, T. Goto, H. Shintani, K. Ishizaka, T. Arima and Y. Tokura, *Nature*, 2003, 426, 55–58.

40 M. C. Knapp and P. M. Woodward, *J Solid State Chem*, 2006, 179, 1076–1085.

41 G. King and P. M. Woodward, *J Mater Chem*, 2010, 20, 5785–5796.

42 E. Bousquet, M. Dawber, N. Stucki, C. Lichtensteiger, P. Hermet, S. Gariglio, J.-M. Triscone and P. Ghosez, *Nature*, 2008, 452, 732–736.

43 N. A. Benedek and C. J. Fennie, *Phys Rev Lett*, DOI:10.1103/PhysRevLett.106.107204.

44 H. T. Stokes, E. H. Kisi, D. M. Hatch and C. J. Howard, *Acta Crystallographica Section B*, 2002, 58, 934–938.

45 N. A. Benedek, J. M. Rondinelli, H. Djani, P. Ghosez and P. Lightfoot, *Royal Society of Chemistry*, 2015, preprint, DOI: 10.1039/c5dt00010f.

46 M. M. Elcombe, E. H. Kisi, K. D. Hawkins, T. J. White, P. Goodman and S. Matheson, *Acta Crystallographica Section B*, 1991, 47, 305–314.

47 X. Q. Liu, J. W. Wu, X. X. Shi, H. J. Zhao, H. Y. Zhou, R. H. Qiu, W. Q. Zhang and X. M. Chen, *Appl Phys Lett*, 2015, 106, 202903.

48 Y. Yoshida, S.-I. Ikeda, H. Matsuhata, N. Shirakawa, C. H. Lee and S. Katano, *Phys Rev B*, 2005, 72, 54412.

49 M. V Lobanov, M. Greenblatt, E. ad N. Caspi, J. D. Jorgensen, D. V Sheptyakov, B. H. Toby, C. E. Botez and P. W. Stephens, *Journal of Physics: Condensed Matter*, 2004, 16, 5339–5348.

50 Y. S. Oh, X. Luo, F.-T. Huang, Y. Wang and S.-W. Cheong, *Nat Mater*, 2015, 14, 407–413.

51 M. Liu, Y. Zhang, L.-F. Lin, L. Lin, S. Yang, X. Li, Y. Wang, S. Li, Z. Yan, X. Wang, X.-G. Li, S. Dong and J.-M. Liu, *Appl Phys Lett*, 2018, 113, 22902.

52 T. Zhu, G. Khalsa, D. M. Havas, A. S. Gibbs, W. Zhang, P. S. Halasyamani, N. A. Benedek and M. A. Hayward, *Chemistry of Materials*, 2018, 30, 8915–8924.

53 N. A. Benedek, *Inorg Chem*, 2014, 53, 3769–3777.

54 T. Zhu, T. Cohen, A. S. Gibbs, W. Zhang, P. S. Halasyamani, M. A. Hayward and N. A. Benedek, *Chemistry of Materials*, 2017, 29, 9489–9497.

55 S. Asaki, H. Akamatsu, G. Hasegawa, T. Abe, Y. Nakahira, S. Yoshida, C. Moriyoshi and K. Hayashi, *Jpn J Appl Phys*, 2020, 59, SPPC04.

56 A. Snedden, K. S. Knight and P. Lightfoot, *J Solid State Chem*, 2003, 173, 309–313.

57 C. J. Fennie and K. M. Rabe, *Appl Phys Lett*, 2006, 88, 262902.

58 B.-W. Li, M. Osada, T. C. Ozawa and T. Sasaki, *Chemistry of Materials*, 2012, 24, 3111–3113.

59 S. Mallick, G. Khalsa, J. Z. Kaaret, W. Zhang, M. Batuk, A. S. Gibbs, J. Hadermann, P. S. Halasyamani, N. A. Benedek and M. A. Hayward, *Dalton Transactions*, 2021, 50, 15359–15369.

60 S. Roitti, *J Mater Sci Lett*, 1982, 1, 217–218.

61 A. T. Mulder, N. A. Benedek, J. M. Rondinelli and C. J. Fennie, *Adv Funct Mater*, 2013, 23, 4810–4820.

62 S. Yoshida, K. Fujita, H. Akamatsu, O. Hernandez, A. Sen Gupta, F. G. Brown, H. Padmanabhan, A. S. Gibbs, T. Kuge, R. Tsuji, S. Murai, J. M. Rondinelli, V. Gopalan and K. Tanaka, *Adv Funct Mater*, DOI:10.1002/adfm.201801856.

63 E. E. McCabe, E. Bousquet, C. P. J. Stockdale, C. A. Deacon, T. T. Tran, P. S. Halasyamani, M. C. Stennett and N. C. Hyatt, *Chemistry of Materials*, 2015, 27, 8298–8309.

64 V. A. Cascos, J. Roberts-Watts, C. Skingle, I. Levin, W. Zhang, P. S. Halasyamani, M. C. Stennett, N. C. Hyatt, E. Bousquet and E. E. McCabe, *Chemistry of Materials*, 2020, 32, 8700–8712.

65 M. Hayward, in *Comprehensive Inorganic Chemistry Second Edition*, Elsevier, 2013, pp. 417–453.

66 R. E. Schaak and T. E. Mallouk, *Chemistry of Materials*, 2002, 14, 1455–1471.

67 M. A. Hayward, *Semicond Sci Technol*, DOI:10.1088/0268-1242/29/6/064010.

68 K. G. Sanjaya Ranmohotti, E. Josepha, J. Choi, J. Zhang and J. B. Wiley, *Advanced Materials*, 2011, 23, 442–460.

69 J. Gopalakrishnan, *Chemistry of Materials*, 1995, 7, 1265–1275.

70 K.-A. Hyeon and S.-H. Byeon, *Chemistry of Materials*, 1999, 11, 352–357.

71 U. Müller, *Inorganic Structural Chemistry*, Wiley, 2007.

72 T. Janssen, A. Janner, A. Looijenga-Vos and P. M. de Wolff, *International Tables for Crystallography*, International Union of Crystallography, Chester, England, 2006, vol. C.

73 S. Van Smaalen, *Incommensurate crystallography*, OUP Oxford, 2007, vol. 21.

74 H. T. Stokes, B. J. Campbell and S. van Smaalen, *Acta Crystallographica Section A*, 2011, 67, 45–55.

75 S. van Smaalen, 2004, 219, 681–691.

76 G. Chapuis and A. Arakcheeva, *Rendiconti Lincei*, 2013, 24, 77–84.

77 D. Segal, *J Mater Chem*, 1997, 7, 1297–1305.

78 W. Clegg, A. J. Blake, J. M. Cole, J. S. O. Evans, P. Main, S. Parsons and D. J. Watkin, *Crystal Structure Analysis: Principles and Practice*, Oxford University Press, 2009, vol. 9780199219469.

79 D. E. Sands, *Introduction to Crystallography*, Dover Publications, 1993.

80 P. J. Brown, A. G. Fox, E. N. Maslen, M. A. O'Keefe and B. T. M. Willis, in *International Tables for Crystallography*, 2006.

81 B. D. Cullity, *Elements of X-ray Diffraction*, Addison-Wesley Publishing Company, 1956.

82 M. Attfield, P. Barnes, J. K. Cockcroft and H. Driessen, Instrument X-ray Optics I. Reflection Geometry http://pd.chem.ucl.ac.uk/pdnn/inst1/optics1.htm.

83 P. Barnes, J. K. Cockcroft, S. Jacques and M. Vickers, How do Synchrotrons Work? http://pd.chem.ucl.ac.uk/pdnn/inst2/work.htm.

84 S. P. Thompson, J. E. Parker, J. Potter, T. P. Hill, A. Birt, T. M. Cobb, F. Yuan and C. C. Tang, *Review of Scientific Instruments*, 2009, 80, 075107.

85 E. H. Kisi and C. J. Howard, *Applications of Neutron Powder Diffraction*, OUP Oxford, 2008.

86 V. F. Sears, *Neutron News*, 1992, 3, 26–37.

87 J. W. G. Thomason, *Nucl Instrum Methods Phys Res A*, 2019, 917, 61–67.

88 D. Duxbury, D. Khalyavin, P. Manuel, D. Raspino, N. Rhodes, E. Schooneveld and E. Spill, *Journal of Instrumentation*, 2014, 9, C12008–C12008.

89 L. C. Chapon, P. Manuel, P. G. Radaelli, C. Benson, L. Perrott, S. Ansell, N. J. Rhodes, D. Raspino, D. Duxbury, E. Spill and J. Norris, *Neutron News*, 2011, 22, 22–25.

90 H. M. Rietveld, *J Appl Crystallogr*, 1969, 2, 65–71.

91 J. S. O. Evans and I. R. Evans, *J Chem Educ*, 2021, 98, 495–505.

92 R. E. Dinnebier, A. Leineweber and J. S. O. Evans, *Rietveld Refinement*, De Gruyter, 2019.

93 A. A. Coelho, *J Appl Crystallogr*, 2018, 51, 210–218.

94 S. Cassidy, *Magnetic properties of solids*, 2024.

95 S. Mugiraneza and A. M. Hallas, *Nature Research*, 2022, preprint, DOI: 10.1038/s42005-022-00853-y.

96 S. J. Blundell, *Contemp Phys*, 1999, 40, 175–192.

97 H. Wallen, *Nature Reviews Methods Primers*, 2022, 2, 5.

98 S. Blundell, R. De Renzi, T. Lancaster and F. L. Pratt, *Muon Spectroscopy: An Introduction*, Oxford University Press, 2022.

99 G. J. W. Gill, *Site Characterisation and Data Analysis for μ ± SR Experiments. DPhil. thesis. University of Oxford*.

100 A. Amato, H. Luetkens, K. Sedlak, A. Stoykov, R. Scheuermann, M. Elender, A. Raselli and D. Graf, *Review of Scientific Instruments*, 2017, 88, 093301.

101 K. M. Ok, E. O. Chi and P. S. Halasyamani, *Chem Soc Rev*, 2006, 35, 710–717.

102 S. K. Kurtz and T. T. Perry, *J Appl Phys*, 1968, 39, 3798–3813.

103 B. J. Campbell, H. T. Stokes, D. E. Tanner and D. M. Hatch, *J Appl Crystallogr*, 2006, 39, 607–614.

104 H. T. Stokes, D. M. Hatch and B. J. Campbell, ISOTROPY Software Suite, iso.byu.edu.

105 H. T. Stokes, D. M. Hatch and B. J. Campbell, ISODISTORT, ISOTROPY Software Suite, iso.byu.edu.

106 F. Giustino, *Materials Modelling Using Density Functional Theory: Properties and Predictions*, Oxford University Press, 2014.

107 P. Hohenberg and W. Kohn, *Physical Review*, 1964, 136, B864–B871.

108 J. M. Perez-Mato, D. Orobengoa and M. I. Aroyo, *Acta Crystallographica Section A*, 2010, 66, 558–590.

109 G. Kresse and J. Hafner, *Phys Rev B*, 1993, 47, 558–561.

110 G. Kresse and J. Hafner, *Phys Rev B*, 1994, 49, 14251–14269.

111 G. Kresse and J. Furthmüller, *Phys Rev B*, 1996, 54, 11169–11186.

112 G. Kresse and J. Furthmüller, *Comput Mater Sci*, 1996, 6, 15–50.

113 G. Kresse and D. Joubert, *Phys Rev B*, 1999, 59, 1758–1775.

114 S. Mallick, A. S. Gibbs, W. Zhang, P. S. Halasyamani, N. A. Benedek and M. A. Hayward, *Chemistry of Materials*, 2020, 32, 7965–7972.

115 S. Mallick, A. D. Fortes, W. Zhang, P. S. Halasyamani and M. A. Hayward, *Chemistry of Materials*, 2021, 33, 2666–2672.

116 J. Gopalakrishnan, V. Bhat and B. Raveau, *Mater Res Bull*, 1987, 22, 413–417.

117 K. Toda and M. Sato, *J Mater Chem*, 1996, 6, 1067–1071.

118 E. A. Josepha, S. Farooq, C. M. Mitchell and J. B. Wiley, *J Solid State Chem*, 2014, 216, 85–90.

119 S. Mallick, F. Orlandi, P. Manuel, W. Zhang, P. S. Halasyamani and M. A. Hayward, *Chemistry of Materials*, 2023, 35, 7839–7846.

120 T. Zhu, F. Orlandi, P. Manuel, A. S. Gibbs, W. Zhang, P. S. Halasyamani and M. A. Hayward, *Nat Commun*, DOI:10.1038/s41467-021-25098-1.

121 S T Bramwell and P C W Holdsworth, *Journal of Physics: Condensed Matter*, 1993, 5, L53.

122 L. Pauling, *The Nature of the Chemical Bond and the Structure of Molecules and Crystals: An Introduction to Modern Structural Chemistry*, Cornell University Press, 1960.

123 M. J. Pitcher, P. Mandal, M. S. Dyer, J. Alaria, P. Borisov, H. Niu, J. B. Claridge and M. J. Rosseinsky, *Science (1979)*, 2015, 347, 420–424.

124 E. Jo, K. An, J. H. Shim, C. Kim and S. Lee, *Phys Rev B*, 2011, 84, 174423.

125 I. S. Jacobs, *Journal of Physics and Chemistry of Solids*, 1959, 11, 1–11.

126 N. Amin and S. Arajs, *Phys Rev B*, 1987, 35, 4810–4811.

127 F. J. Morin, *Physical Review*, 1950, 78, 819–820.

128 T. Zhu, *Soft chemical routes to ferroelectric and multiferroic materials. DPhil. thesis. University of Oxford*.

129 T. Zhu, F. Orlandi, P. Manuel, A. S. Gibbs, W. Zhang, P. Shiv. Halasyamani and M. A. Hayward, *Nat Commun*, 2021, 12, 1–8.

130 C. Galven, D. Mounier, B. Bouchevreau, E. Suard, A. Bulou, M.-P. Crosnier-Lopez and F. Le Berre, *Inorg Chem*, 2016, 55, 2309–2323.

131 T. Nagai, H. Shirakuni, A. Nakano, H. Sawa, H. Moriwake, I. Terasaki and H. Taniguchi, *Chemistry of Materials*, 2019, 31, 6257–6261.

132 R. Uppuluri, H. Akamatsu, A. Sen Gupta, H. Wang, C. M. Brown, K. E. Agueda Lopez, N. Alem, V. Gopalan and T. E. Mallouk, *Chemistry of Materials*, 2019, 31, 4418–4425.

133 Y. Mochizuki, T. Nagai, H. Shirakuni, A. Nakano, F. Oba, I. Terasaki and H. Taniguchi, *Chemistry of Materials*, 2021, 33, 1257–1264.

134 N. A. Benedek, *Inorg Chem*, 2014, 53, 3769–3777.

135 K.-E. Hasin and E. A. Nowadnick, *Phys Rev Mater*, 2023, 7, 124402.

136 Y. Mochizuki, T. Nagai, H. Shirakuni, A. Nakano, F. Oba, I. Terasaki and H. Taniguchi, *Chemistry of Materials*, 2021, 33, 1257–1264.

137 R. Uppuluri, H. Akamatsu, A. Sen Gupta, H. Wang, C. M. Brown, K. E. Agueda Lopez, N. Alem, V. Gopalan and T. E. Mallouk, *Chemistry of Materials*, 2019, 31, 4418–4425.

138 T. Nagai, H. Shirakuni, A. Nakano, H. Sawa, H. Moriwake, I. Terasaki and H. Taniguchi, *Chemistry of Materials*, 2019, 31, 6257–6261.

139 C. Galven, D. Mounier, B. Bouchevreau, E. Suard, A. Bulou, M. P. Crosnier-Lopez and F. Le Berre, *Inorg Chem*, 2016, 55, 2309–2323.

140 T. Zhu, A. S. Gibbs, N. A. Benedek and M. A. Hayward, *Chemistry of Materials*, 2020, 32, 4340–4346.

141 K. M. Ok, P. S. Halasyamani, D. Casanova, M. Llunell, P. Alemany and S. Alvarez, *Chemistry of Materials*, 2006, 18, 3176–3183.

142 T. Pagnier, N. Rosman, C. Galven, E. Suard, J. L. Fourquet, F. Le Berre and M. P. Crosnier-Lopez, *J Solid State Chem*, 2009, 182, 317–326.

143 C. Galven, D. Mounier, B. Bouchevreau, E. Suard, A. Bulou, M. P. Crosnier-Lopez and F. Le Berre, *Inorg Chem*, 2016, 55, 2309–2323.

144 T. Nagai, H. Shirakuni, A. Nakano, H. Sawa, H. Moriwake, I. Terasaki and H. Taniguchi, *Chemistry of Materials*, 2019, 31, 6257–6261.

145 R. Uppuluri, H. Akamatsu, A. Sen Gupta, H. Wang, C. M. Brown, K. E. Agueda Lopez, N. Alem, V. Gopalan and T. E. Mallouk, *Chemistry of Materials*, 2019, 31, 4418–4425.

146 T. Zhu, F. Orlandi, P. Manuel, A. S. Gibbs, W. Zhang, P. S. Halasyamani and M. A. Hayward, *Nat Commun*, DOI:10.1038/s41467-021-25098-1.

147 S. Mallick, F. Orlandi, P. Manuel, W. Zhang, P. S. Halasyamani and M. A. Hayward, *Chemistry of Materials*, 2023, 35, 7839–7846.

148 S. Mallick, *Cation exchange chemistry as a route to induce noncentrosymmetry in layered perovskite oxides. DPhil. thesis. University of Oxford*.